KINETIC ALGORITHMS FOR NON-EQUILIBRIUM GAS DYNAMICS

by

William Marcus Eppard

Dissertation submitted to the Faculty of the

Virginia Polytechnic Institute and State University

in partial fulfillment of the requirements for the degree of

DOCTOR OF PHILOSOPHY

in

Aerospace Engineering

APPROVED:

Bernard Grossman, Chairman

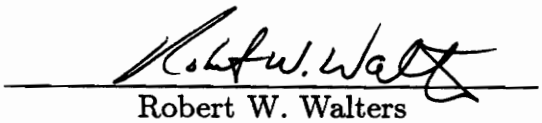

Robert W. Walters

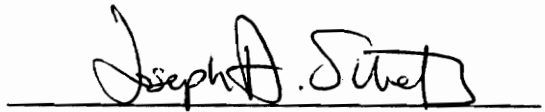

Joseph A. Schetz

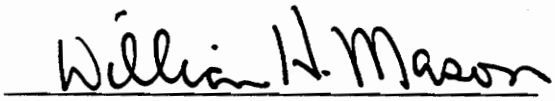

William H. Mason

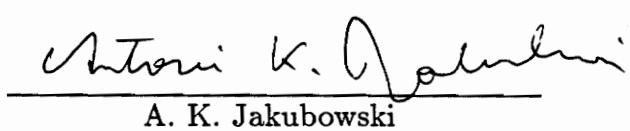

A. K. Jakubowski

April 1993

Blacksburg, Virginia

ABSTRACT

New upwind kinetic-difference schemes have been developed for flows with non-equilibrium thermodynamics and chemistry. These schemes are derived from the Boltzmann equation with the resulting Euler schemes developed as moments of the discretized Boltzmann scheme with a locally Maxwellian velocity distribution. Application of a directionally-split Courant-Isaacson-Rees (CIR) scheme at the Boltzmann level results in a flux-vector splitting scheme at the Euler level and is called Kinetic Flux-Vector Splitting (KFVS). Extension to flows with finite-rate chemistry and vibrational relaxation is accomplished utilizing non-equilibrium kinetic theory. Computational examples are presented comparing KFVS with the schemes of Van-Leer and Roe for quasi-one-dimensional flow through a supersonic diffuser, inviscid flow through two-dimensional inlet, viscous flow over a cone at zero angle-of-attack, and shock-induced combustion/detonation in a premixed hydrogen-air mixture. Calculations are also shown for the transonic flow over a bump in a channel and the transonic flow over an NACA 0012 airfoil. The results show that even though the KFVS scheme is a Riemann solver at the kinetic level, its behavior at the Euler level is more similar to the the existing flux-vector splitting algorithms than to the flux-difference splitting scheme of Roe.

A new approach toward the development of a genuinely multi-dimensional Riemann solver is also presented. The scheme is based on the same kinetic theory considerations used in the development of the KFVS scheme. The work has been motivated by the recent progress on multi-dimensional upwind schemes by the groups at the University of Michigan and the Von Karman Institute. These re-

searchers have developed effective upwind schemes for the multi-dimensional linear advection equation using a cell-vertex fluctuation-splitting approach on unstructured grids of triangles or tetrahedra. They have made preliminary applications to the Euler equations using several wave decomposition models of the flux derivative. The issue of the appropriate wave model does not appear to be adequately resolved. The approach taken in the present work is to apply these new multi-dimensional upwind schemes for the scalar advection equation at the Boltzmann level. The resulting Euler schemes are obtained as moments of the fluctuations in the Maxwellian distribution function. The development is significantly more complicated than standard (dimensionally-split) kinetic schemes in that the Boltzmann discretization depends upon the direction of the molecular velocities which must be accounted for in the limits of integration in velocity space. The theoretical issues have been solved through analytic quadrature and Euler schemes have been developed. For this formulation it was not necessary to prescribe any explicit wave decomposition model. Encouraging preliminary results have been obtained for perfect gases on uniform Cartesian meshes with first-order spatial accuracy. Results are presented for a 29° shock reflection, a 45° shear discontinuity, and Mach 3 flow over a step.

Finally, methods for obtaining accurate gas-dynamic simulations in the continuum transition regime are considered. In particular, large departures from translational equilibrium are modeled using algorithms based on the Burnett equations instead of the Navier-Stokes equations. Here, the same continuum formulation of the governing equations is retained, but new constitutive relations based on higher-order Chapman-Enskog theory are introduced. Both a rotational relaxation model and a bulk-viscosity model have been considered for simulating rotational non-equilibrium. Results are presented for hypersonic normal shock calculations

in argon and diatomic nitrogen and comparisons are made with Direct Simulation Monte Carlo (DSMC) results. The present work closely follows that of the group at Stanford, however, the use of upwind schemes and the bulk-viscosity model represent new contributions.

ACKNOWLEDGMENTS

I would like to express my sincerest thanks to my research advisor, Dr. Bernard Grossman, for providing constant support and understanding during this endevour. His vast knowledge of fluid dynamics and sharp mathematical skills have proved invaluable in this work. Any mistakes I have made or will make in the future are in no way a reflection upon him. I would also like to thank my parents and family for their constant support, encouragement and confidence. They have instilled in me the courage to persevere even when things seem the worst. Also, I must thank my fiancee Karen for her unending support and enduring patience during this sometimes trying experience. I am also indebted to my friends in the sun room for their companionship and enlightening discussions. They will always remain close to my thoughts, and I sincerely hope our paths will cross again in the future. This work would not have been possible without the financial support of the Fluid Physics Branch at NASA Langley Research Center under NASA grant NAG-1-776. Special thanks to the Branch Head, Ajay Kumar and the contract monitor, R. Charles Swanson. I would also like to thank Ajay for suggesting the bulk-viscosity study.

TABLE OF CONTENTS

LIST OF FIGURES

Chapter 1

Introduction

1.1 General Problem Description

The effective design of high performance aerospace vehicles and propulsion systems requires advanced algorithms that are capable of accurately computing the complex fluid phenomena occurring around the vehicle as well as within the inlets, combustors, and nozzles. The emphasis of this work is placed on numerical algorithms for hypersonic flows and supersonic/hypersonic combustion. Here, the high temperatures and large flow gradients brought on by either combustion processes or high speeds of flight result in finite-rate chemical and energy exchange phenomena. The primary complication associated with chemical and thermal non-equilibrium is the introduction of a wide range of time scales involved in the thermo-chemical processes that may be very different from the fluid-dynamic time scale. For the general case, the chemical rate processes, the non-equilibrium thermal state of the gas, and the fluid dynamics are strongly coupled. The accurate resolution of the many time scales present requires solving additional species mass conservation equations and non-equilibrium internal energy equations in a fully-coupled manner with the fluid-dynamic equations. Calculations of this type become very intense computationally and require large amounts of computer memory and computational time. In addition to the consideration of highly vectorized and parallel codes, emphasis must be placed on extremely accurate algorithms so that the important features of the flowfield may be resolved with as few grid points as possible. The primary

objective of this work is the development of advanced numerical algorithms for calculating hypersonic flows and supersonic/hypersonic combustion.

1.2 Upwind Methods

The major contribution of this work is the development of accurate and robust upwind methods for modeling the inviscid nature of the flowfield, while within the framework of general thermo-chemical considerations. The benefits of upwind schemes, where the discretization of the inviscid fluxes is accomplished by flux-vector or flux-difference splitting methods, have been fully documented, *e.g.,* see the review articles of Harten, Lax and Van Leer [1] and Roe [2]. These schemes are found to be very accurate and robust for transonic, supersonic and hypersonic flows and are known for their nearly oscillation-free behavior in shock capturing approaches. Several of the more popular upwind algorithms are the flux-vector splitting methods due to Steger and Warming [3] and to Van Leer [4] and the flux-difference splitting technique of Roe [5]. These schemes, initially developed for perfect gases, have been extended to flows with real gases, *e.g.*, Grossman and Walters [6,7] and to flows in chemical and thermal non-equilibrium, *e.g.*, Grossman and Cinnella [8].

1.2.1 Kinetic Flux-Vector Splitting

All of the previously mentioned upwind algorithms originate from the Euler equations for gas dynamics. The Euler equations, however, can be obtained as moments of the Boltzmann equation for the kinetic theory of gases provided the velocity distribution function is Maxwellian [9]. This connection between the Boltzmann equation and the Euler equations has lead to a new class of upwind kinetic schemes which are based on the principle that an upwind scheme at the Boltzmann level leads to an upwind scheme at the Euler level. Kinetic-difference schemes for

the Euler equations have been developed by Deshpande [10–13] and his coworkers. In their approach the resulting Euler schemes are developed as moments of the discretized Boltzmann scheme with a locally Maxwellian velocity distribution. Splitting the velocity distribution at the Boltzmann level in a Courant-Isaacson-Rees (CIR) sense, is seen to result in a flux-split Euler scheme called Kinetic Flux-Vector Splitting (KFVS) in Refs. [11], [12], and [13]. Similar differential-difference schemes with kinetic-based dissipation have been developed in Russia by Elizarova and Chetverushkin [14–16], where many applications to high-speed gasdynamic flows have been performed. Recently Weatherill [17] *et al.* have applied the KFVS scheme to unstructured grids.

In the present work the KFVS scheme, which was initially developed for perfect gases, is extended to flows with chemical and thermodynamic non-equilibrium by means of non-equilibrium kinetic theory [18]. The details of the theoretical approach are described in Chap. 6 and the resulting Euler schemes will be discussed. The behavior of the KFVS algorithm is examined for solving the Euler equations, the Navier-Stokes equations, and flows with both finite-rate-chemistry and vibrational relaxation. The results are compared with some of the more well-known upwind schemes in use today.

1.2.2 Multi-Dimensional Kinetic Fluctuation Splitting

To effectively compute the reacting flowfields around hypersonic vehicles as well as within high speed inlets and combustors, solvers must be capable of accurately resolving very complex fluid-dynamic phenomena, in addition to modeling the thermo-chemical rate processes. For instance, the flow inside an inlet is highly three-dimensional and possibly turbulent depending on the flight Reynolds number. The flowfield is characterized by complex shock-expansion-wave interactions as well

as strong shock-boundary-layer interactions that may result in regions of separated flow [19]. Inside the combustor the flow dynamics are further complicated by the injection of fuel, the fuel-air mixing process, and the combustion process [20,21]. To obtain accurate numerical simulations for flows of this type, solvers must be capable of calculating highly resolved shock waves, shear and contact discontinuities, flame fronts, mixing layers and boundary layers. Unfortunately, the current generation of Euler and Navier-Stokes solvers are limited by their inability to accurately resolve these fluid-dynamic phenomena when they are oriented oblique to the computational grid. This problem arises in central-difference codes because of the inability to properly tune the numerical dissipation. In upwind codes this problem occurs because current upwind technology is essentially one-dimensional in nature and must be implemented in a dimensionally-split approach for calculations in two and three spatial dimensions (this is the case for all the upwind schemes mentioned earlier, including the KFVS scheme). Treating the flowfield in a dimensionally-split manner yields grid-dependent schemes which require excessive numbers of grid points (and associated very high computational costs) to accurately resolve the critical flow features. This problem is magnified for calculations involving chemical and thermal non-equilibrium since additional rate equations must be solved in a coupled fashion, and the species densities and non-equilibrium internal energies must be stored at each grid point. Advanced upwind solvers must incorporate truly multi-dimensional ideas based on more realistic physical models so that accurate numerical simulations may be carried out with as few grid points as possible.

One approach towards the development of upwind solvers with multi-dimensional behavior involves rotated or *multi-directional* [22] Riemann solvers. These schemes require the choice of a dominant upwinding direction and a local Riemann solution with left and right states that are functions of the upwinding angle. Efforts

along these lines include the work of Davis [23], Levy [24] *et al.* and Dadone and Grossman [25]. Solvers of this type have succeeded in calculating shocks oblique to the grid with nearly the same resolution as shocks which are aligned with the grid. However, for three-dimensional flows with complex fluid phenomena, the task of choosing only one pertinent upwinding direction will be a formidable one. While these schemes represent a marked improvement over directionally-split schemes they are by no means the final answer, and still leave the CFD community in need of truly multi-dimensional ideas. Other approaches to putting more multi-dimensional information into Riemann solvers involve the multi-dimensional flux function approach of Rumsey [26] *et al.* and Parpia and Michalek [27].

Recent progress in genuinely multi-dimensional upwind Euler solvers [28–32] has been centered around the generalization of Roe's one-dimensional scheme. The basic concepts underlying the extension of Roe's scheme for two and three dimensions have been put forth in Struijs [32] *et al.* Three basic steps are described. Step one requires an eigenvector decomposition of the divergence of the flux vector which is written (as in Roe's one-dimensional scheme) as the sum of terms of the form (eigenvector)×(wavespeed)×(wavestrength). This process is not uniquely determined as in one space dimension and several decompositions have been introduced which *recognize* and select relevant simple wave patterns. Step two is to obtain the discretized counterpart of the previous wave decomposition based on a conservative linearization procedure. In Ref. [32] this step is carried out for triangular cells in two dimensions and tetrahedra in three dimensions. At this point the discretized wave structure (orientation and corresponding advection speeds) is known in terms of the dependent variables at the cell vertices and each of these simple waves is governed by the linear scalar advection equation. Step three advances the solution in time in an explicit manner utilizing multi-dimensional fluctuation splitting

schemes for the scalar advection equation, whereby decomposed portions of the flux balance are distributed to the vertices of the computational cell. As a result, the numerical behavior of the system is governed completely by the characteristics of these scalar distribution schemes. Struijs *et al.* have considered two scalar advection schemes for triangular cells. The first scheme, called the N-scheme, is the optimal (allows the maximum time step and has the most narrow stencil) linear scheme satisfying positivity; it is at most first-order accurate in space. The second scheme is a nonlinear variant of the N-scheme, termed the NN-scheme, and is both positive and second order in space. Positivity is an important characteristic since it prohibits the occurrence of new extrema and allows these schemes to maintain monotone profiles across discontinuities without the need for limiters. Positivity also imposes stability on the explicit scheme. Preliminary results using these concepts [32,33] have shown improvements in shock capturing compared to standard solvers. Although these schemes have great potential, more work is needed in the wave modeling stage [32,34].

The objective of this work is to develop a genuinely multi-dimensional upwind Euler solver [35]. Here, the same kinetic-theory considerations as used in the development of the KFVS scheme will be implemented, and the schemes will utilize a cell-vertex finite-volume approach with residual distribution strategies to send portions of the decomposed flux residual (at the Euler level) to the cell verticies depending on the propagation of information at the kinetic level. The first step will be to apply the multi-dimensional linear advection schemes described in Ref. [32] (the N-scheme and the NN-scheme) at the Boltzmann level. The resulting Euler schemes will be obtained as moments of the fluctuations in the Maxwellian velocity distribution function. This development is significantly more complicated than standard (dimensionally-split) kinetic schemes in that the Boltzmann discretization

will depend upon the direction of the molecular velocities which must be accounted for in the limits of integration in velocity space. The details of the theoretical approach are described in Chap. 7 and the resulting Euler schemes will be discussed. It is important to note that an explicit wave decomposition model is not required for the development of Euler schemes with this approach.

The multi-dimensional Euler solvers presented in this work consider only frozen mixtures of thermally perfect gases that are in thermal equilibrium. The extension to flows in chemical and thermal non-equilibrium is feasible, but will not be presented here. However, the benefits realized by the sharp resolution of flow-field structures will be even more pronounced for cases with chemical and thermal non-equilibrium because they are very sensitive to the resolution of discontinuities, particularly contact surfaces

1.3 Hypersonic Shock Structure

In this portion of the work, methods are considered for obtaining accurate gas dynamic simulations in the rarefied continuum transition regime. Within this regime the continuum assumption still applies, but the decreased molecular collision frequency causes bow shock waves to become thick when compared to the shock stand-off distance. The interior of a shock wave is characterized by strong gradients and large departures from translational and rotational equilibrium, and the resulting rotational/translational energy exchange causes the peak temperature and peak radiation intensity to occur inside the shock wave itself. For these reasons, it is no longer valid to treat the shock wave as a discontinuous jump and it becomes necessary to actually compute *through* the shock wave [36,37]. The altitude limits for this regime are discussed in Ref. [36] and depend on the vehicle size and speed.

The fundamental problem associated with calculating in this regime is that the

Navier-Stokes equations do not contain the necessary physics to accurately predict hypersonic shock structure [36,38]. The primary reason for this is that the Navier-Stokes equations were derived from a first-order Chapman-Enskog expansion about the Maxwellian velocity distribution function, and are therefore only valid for small departures from local translational equilibrium [9]. The need for improved methods for calculating in the continuum transition regime has lead to the recent work by the research group at Stanford. These researchers have considered the use of the Burnett equations as an alternative to Navier-Stokes for this regime. The Burnett equations are derived by retaining second-order terms in the Chapman-Enskog procedure and should be valid for larger departures from translational equilibrium [9,36]. Here, the continuum formulation of the governing equations is retained, but quadratic constitutive relations for the shear stress and heat flux are introduced [39]. Fiscko and Chapman [40,41] were the first to calculate Burnett solutions for hypersonic shock waves. They implemented a time-dependent equation set and marched in time to the steady-state solution. Calculations have been performed up to Mach 50 for three types of gases; hard-sphere, argon, and Maxwellian. Earlier attempts to calculate shock structure with the Burnett equations were based on a steady-state formulation and could not obtain solutions above Mach 2 [42,43]. The Stanford group also discovered that the Burnett equations tend to become unstable as the mesh spacing is refined. This problem is now understood and has been addressed by Zong [44] *et al.* who have shown that the Burnett equations may be stabilized by adding select so called Super-Burnett terms. These terms include cubic shear stress and heat flux constitutive relations. A major drawback of the Burnett equations is their overwhelming complexity.

Equally important in the prediction of hypersonic shock structure is the ability to model rotational non-equilibrium [36,37,45,46] . Here, the rotational/translation-

al energy exchange causes the peak temperature to occur inside the shock wave, and correct modeling of this phenomena is necessary for obtaining accurate predictions of radiative heating. Wang Chang and Uhlenbeck [47] were the first to carry out first-order Chapman-Enskog theory for gases with an internal energy mode. They have shown that when the energy exchange occurs *freely* so that the rotational energy is essentially at all times in equilibrium at the translational temperature, the system yields the Navier-Stokes equations plus an additional bulk-viscosity term. For cases where the relaxation time for rotation is significant and large deviations from rotational equilibrium occur, the system yields the Navier-Stokes equations with an additional rate equation (in the form of a Landau-Teller type model) describing the relaxation of the rotational mode. The rotational collision numbers that appear in this formulation have been obtained theoretically by Parker [48] and Lordi and Mates [49]. To the authors knowledge, no one has carried out second-order Chapman-Enskog theory for an internal energy mode, however, it is generally assumed that the same treatment of rotational energy is valid in conjunction with the Burnett equations [45]. Although the assumptions used to derive the Landau-Teller model are probably violated in hypersonic flows [46,47], good shock profiles have been obtained up to Mach 11 by adjusting the parameters for the rotational collision number as suggested in Ref. [46].

In the present work, both the Navier-Stokes equations and the Burnett equations are used to model one-dimensional shock wave structure in argon and diatomic nitrogen. Rotational non-equilibrium is modeled using either a Landau-Teller relaxation model or a bulk-viscosity model that has been derived from the theory of Goldstein [50]. This work is described in Chap. 8 and parallels the research of the Stanford group with my primary contributions being related to the bulk-viscosity model and the use of upwind schemes.

1.4 Overview

The subject matter of this work has been organized in the following manner. Chaps. 2 - 5 are of a general descriptive nature and set the stage for the detailed analysis to follow. These chapters do not represent new contributions. In Chap. 2 the thermally perfect gas and continuum assumptions are described. A general description of chemical reactions and internal energy modes is given and the concept of non-equilibrium processes in gas dynamics is introduced. Also, the framework for the general thermal and chemical models will be addressed. In Chap. 3 the necessary kinetic theory for mixtures in chemical and thermal non-equilibrium is presented. Here the velocity distribution function and the Boltzmann equation are introduced and the governing equations for mixtures of thermally perfect gases in chemical and thermal non-equilibrium are derived via moments of the Boltzmann equation. Finally, the governing equations are extended to generalized coordinates and the more general integral form is given. A simplified quasi-one-dimensional equation set is also presented. In Chap. 4 the chemical and thermal source term modeling is considered. Here, a simple high temperature air-chemistry model and a hydrogen-air combustion model are introduced along with Landau-Teller models for both vibrational/translational and rotational/translational energy exchanges. In Chap. 5 the viscous modeling is addressed. Here, Chapman-Enskog theory is described and the results are presented for the shear-stress tensor, the heat-flux vector, and the diffusion velocity. Simplified curve fits and semi-emperical mixture rules are presented as well. The bulk-viscosity model and the Burnett equations for one space dimension are also described in this chapter. Chaps. 6 - 8 contain the new contributions of this work. In the beginning of Chap. 6 a general introduction to *traditional* upwind techniques is presented. Flux-vector splitting and flux-difference

splitting methods are described in conjunction with a cell-centered finite-volume approach and the MUSCL formulation. The Euler-Implicit time integration method is also described. In Sec. 6.4 the new kinetic flux-vector splitting method is developed; first for perfect gases in one space dimension following the development of Deshpande, and then for flows in chemical and thermal non-equilibrium and for general three-dimensional coordinate systems. Results for the KFVS scheme are presented and comparisons are made with standard upwind solvers. In Chap. 7 the new multi-dimensional upwind Euler solver is developed. Here, multi-dimensional fluctuation-splitting methods are initially described in conjunction with the scalar advection equation and then extended to the Euler equations using kinetic theory. Three different Euler schemes are developed. Results are presented for Cartesian meshes and comparisons are made with results from a standard dimensionally-split kinetic-based solver. Chap. 8 gives the basic modeling used for the hypersonic shock-structure calculations. Numerical issues are discussed and results are presented for shock waves in argon and diatomic nitrogen.

Chapter 2

General Thermo-Chemical Considerations

2.1 Introduction

In this chapter, the general thermo-chemical framework necessary for modeling hypersonic flowfields and supersonic/hypersonic combustion is presented. First, the thermally perfect gas and continuum assumptions are discussed, and their consequences at the macroscopic level are described. These assumptions are assumed to apply throughout this work. Next, a brief description of the chemical and internal energy modes is given and the concept of non-equilibrium processes in gas dynamics is introduced. A somewhat detailed description of translational, rotational, vibrational, and chemical non-equilibrium processes is then presented, again with emphasis on their consequences at the gas-dynamic level. Finally, the general non-equilibrium thermodynamic model and finite-rate chemistry model is stated, and several "practical" thermodynamic models are discussed for modeling vibrational and rotational non-equilibrium. Throughout this chapter emphasis is placed on a molecular description wherever possible since a clear physical picture at the microscopic level is essential to the understanding of macroscopic gas dynamics.

2.1.1 Thermally Perfect Gases

At the molecular level a gas is composed of a large number of very small individual molecules, not necessarily of the same species, that are in a state of constant motion. Each molecule travels with its own, possibly unique, molecular velocity which may be altered by external body forces, intermolecular forces, and by col-

lisions with other molecules and with any boundaries that may be present. The scope of this work is confined to gases with relatively low densities and moderate to high temperatures so that the order-of-magnitude estimates corresponding to a *thermally perfect gas* are valid. That is, the range of intermolecular forces is much smaller than the average molecular spacing which is in turn much smaller than the average distance a molecule travels between collisions. This representation of a gas implies a "straight-line trajectory through relatively empty space interrupted occasionally by abrupt collisions [9]" . Hence, the particles are *weakly interacting* and intermolecular effects are not present; except during collisions. The major consequence of thermally perfect gases is that the internal energy becomes a function of temperature *only*. Each species (denoted by s) in a mixture of thermally perfect gases has a partial pressure given by

$$p_s = \rho_s R_s T\,, \tag{2.1}$$

where ρ_s is the species density, T is the absolute temperature as defined in classical thermodynamics, and R_s is the species gas constant determined as

$$R_s = \frac{\hat{R}}{\hat{m}_s}\,, \tag{2.2}$$

Here, $\hat{R}$ is the universal gas constant and $\hat{m}_s$ is the species molecular weight. Strictly related to the thermally perfect gas assumption is the validity of Dalton's Law for obtaining the total mixture pressure from the summation of the species partial pressures. That is, for a mixture of N species

$$p = \sum_{s=1}^{N} p_s = \sum_{s=1}^{N} \rho_s R_s T = \rho \tilde{R} T\,, \tag{2.3}$$

where the mixture gas constant, $\tilde{R}$, and the mixture density ρ have been introduced and are defined as

$$\tilde{R} = \sum_{s=1}^{N} \frac{\rho_s}{\rho} R_s\,, \tag{2.4}$$

and

$$\rho = \sum_{s=1}^{N} \rho_s \,. \tag{2.5}$$

The foregoing equation of state was derived empirically, strictly for a gas in complete thermodynamic equilibrium, *i.e.*, classical thermodynamics. In Chapter 3 the same form as Eqs. (2.1) and (2.3) will be obtained using the kinetic pressure and temperature (*i.e.*, translational temperature), and will be valid in cases of translational equilibrium as well as in non-equilibrium situations. For cases of translational non-equilibrium, the situation may arise where electrons (or other extremely light particles) may exist at a kinetic temperature different from the heavy particle translational temperature. This issue is discussed in Sec. 2.2.1. For this case the equation of state becomes

$$p = \sum_{s=1}^{N} p_s = \sum_{s=1}^{N-1} \rho_s R_s T + \rho_e \tilde{R}_e T_e \,, \tag{2.6}$$

where the Nth index represents free electrons and is handled separately at the electron translational temperature, T_e. In the present work multiple translational temperatures are not considered and the equation of state, Eq. (2.3), is sufficient.

From experience, it has been confirmed that Eqs. (2.1) and (2.3) are valid for situations of chemical non-equilibrium given the instantaneous chemical composition. When chemical reactions occur the gas mixture, as a whole, does not behave as a thermally perfect gas, *i.e.*, $\tilde{R}$ is not constant. However, each chemical species in the mixture is assumed to behave separately as a thermally perfect gas so that only mixtures of thermally perfect gases are considered. Equations (2.1) and (2.3) are further assumed to be valid in the presence of thermal non-equilibrium such as vibrational or rotational non-equilibrium which are discussed in the following sections.

2.1.2 Continuum Gas Dynamics

This work is also confined to gases with densities large enough so that the the continuum assumption is valid, *i.e.*, the gas may be considered a continuous medium. In continuum gas dynamics the entire flowfield may divided into a large number of subsystems called fluid elements. Each fluid element is of infinitesimal size compared to the macroscopic scale but large enough at the microscopic level to consist of a sufficiently large number of molecules so that meaningful molecular averages may be obtained. If there is no motion of the gas at the macroscopic level then the microscopic motion is purely random with no preferred direction. Continuum gas dynamics arises when the motion of a sufficiently large number of molecules in the fluid element tends to dominate the motion of individual molecules. When this occurs the average molecular velocity for a fluid element is non-zero and gives rises to the flow velocity at the macroscopic level. The close proximity of the fluid elements in continuum gas dynamics gives rise to interactions between fluid elements that tend to dominate the motion of the individual molecules within. Hence, we may view the resulting motion, collectively, as the molecular motion of thermal translation superimposed on the average flow velocity associated with a fluid element. The macroscopic flow variables of pressure, temperature, entropy, and so on, typically associated with gas dynamics, are defined as molecular averages for a fluid element. For instance, temperature is related to the average kinetic energy of thermal molecular motion within a gas. Pressure, for a thermally perfect gas, is given by a momentum flux due to the thermal motion of molecules crossing an imaginary boundary within a gas.

2.1.3 Chemical Reactions

Typically, chemical reactions become active for high temperatures. One mea-

sure of this phenomena is the Zel'dovich number (E_a/RT, where E_a is the Arrhenius activation energy) [51]. As the temperature increases and the Zel'dovich number begins to approach unity, the number of collisions with sufficient energy to cause reactions becomes appreciable. When molecules collide with sufficient energy and proper orientation the molecular bonds may break and rearrange to produce other molecules, atoms, ions or individual electrons, giving rise to new chemical species. These are called homogeneous reactions. Reactions may also be caused by collisions with boundary surfaces as opposed to collisions with other molecules. These non-homogeneous chemical reactions are known as surface catalyst reactions. Other reactions, known as photochemical reactions, such as photoionization and photodissociation result from the interaction of radiation with an atom or a molecule. The present work is limited to the consideration of only homogeneous reactions. In particular, models for the dissociation-recombination reactions associated with high temperature air as well as hydrogen-air combustion processes will be considered.

2.1.4 Internal Energy Contributions

Each molecule may have some internal structure which is important in terms of the effect on the molecule's total energy content and hence on the total energy content of the gas. For instance, in addition to the energy associated with translational motion, a monatomic molecule may posses the internal energy due to electronic excitation. This energy includes the kinetic energy of the electrons as well as the potential energy associated with the electron orbit. Diatomic and polyatomic molecules may also have contributions due to molecular rotation and vibration included in their internal energies. The characteristic temperature for rotation for most gases is small ($2.1°K$ for O_2, $2.9°K$ for N_2, and $2.5°K$ for NO) so that fully excited rotational energy is present at ordinary temperatures. In contrast, the

characteristic temperatures for vibration are typically large ($2270°K$ for O_2, $3390°K$ for N_2, and $3370°K$ for NO) and vibrational energy is dependent on the existence of high temperatures. The species internal energy may be derived from the partition function of statistical mechanics. However, there remains some controversy as to the proper partitioning of modes into independent groups. The significance of independent modes is that they give rise to summable contributions to the internal energy. For weakly interacting particles, separation of the translational and internal modes is completely legitimate. Also, except at low temperatures, the internal energy can be broken into electronic and vibrational/rotational contributions, with good approximation. Stricly speaking, however, the vibrational and rotational modes are not independent [9]. Vibration/rotation coupling occurs because rotation creates a centrifugal field that affects vibration and likewise vibration creates variations in the molecular moment of inertia which in turn affects rotation. For this reason, some researchers suggest that the vibrational/rotational contributions must be considered in a coupled fashion [52,53]. In the present work, vibration and rotation are treated as independent modes. One other form of internal energy that is important for chemically reacting flows is the internal energy due to the presence of chemical bonds. When chemical reactions occur, bonds are broken and rearranged and significant amounts of energy may be released or absorbed. Adding the contributions due to all chemical bonds leads to the heat of formation for a molecule. The species internal energies are evaluated from a common reference state for all species in the mixture. The heats of formation (evaluated at the same reference state) are then added to the internal energies to bring each species to its own reference state.

2.2 Non-Equilibrium Processes

Intermolecular collisions are the primary mechanism for bringing a gas to a state of equilibrium. As a fluid element moves throughout the domain it encounters a continuously changing flowfield. Readjustment of the chemical and thermal modes to the changing flow conditions takes place through molecular collisions and hence requires a finite length of time. Furthermore, each of the molecular processes involved (translation, rotation, vibration, chemical, *etc.*) requires a different number of collisions to reach equilibrium, so that the characteristic time for readjustment may be significantly different for each process.

Each specific mode, say mode p for instance, may be classified based on an order-of-magnitude analysis where its characteristic time for readjustment by collisions τ_p is compared to the characteristic fluid-dynamic time τ_{fd}, *i.e.*, the time required for the fluid element to encounter significant changes in conditions. Three distinct cases may arise

$$\tau_p \gg \tau_{fd}\,,$$

$$\tau_p \ll \tau_{fd}\,, \text{ or}$$

$$\tau_p \simeq \tau_{fd}\,.$$

In the first case, τ_p is much greater than τ_{fd} and the process has essentially no time to adjust to the fluid dynamics. The process is said to be *frozen* and calculations may be carried out assuming the process variable does not change. In the second case, τ_p is negligible compared to τ_{fd}. Here, the process has virtually infinite time to adjust to fluid-dynamic changes, and maintains a state of *equilibrium*. For chemical and thermal equilibrium, the results from statistical mechanics may be utilized; at least within the limits of the previous discussion on the coupling of internal energy modes. The assumption of equilibrium adds some complexity over

the frozen case; however, only in the form of algebraic equations. Although these two situations represent limiting cases and can actually never be fully realized, they may valid working assumptions. In the third case, τ_p is of the same order as τ_{fd} so that non-equilibrium effects must be taken into account. *Chemical non-equilibrium* results from non-equilibrium in the chemical modes, while *thermal non-equilibrium* is associated with non-equilibrium in the internal energy modes. Here, the energy modes that are in non-equilibrium may be assumed to satisfy a Boltzmann distribution at the non-equilibrium temperature for that process, T_p, that is different from the translational temperature, T. Hence, non-equilibrium thermodynamics gives rise to the concept of multiple temperature flows. In reality, the non-equilibrium modes may not satisfy a Boltzmann distribution, and the difference between the non-equilibrium temperature T_p and the translational temperature T becomes simply a measure of the amount non-equilibrium energy present. Non-equilibrium simulations become much more complex since they require additional differential equations to model the rate processes. In the general case these rate equations must be solved in a fully-coupled manner with the fluid-dynamic equations. Such non-equilibrium phenomena can occur for any of the molecular processes; translation, rotation, vibration, chemical composition, and so on. Experimental studies of relaxation processes in and behind shock waves [54] show the relative order of the characteristic times (for pure gases at modest temperatures) is typically given as follows

$$\tau_{tr} < \tau_{rot} \ll \tau_{vib} < \tau_{diss} < \tau_{ion} \simeq \tau_{el} \,, \tag{2.7}$$

where τ_{tr}, τ_{rot}, τ_{vib}, τ_{diss}, τ_{ion}, and τ_{el} are the characteristic times for translation, rotation, vibration, dissociation, ionization, and electronic excitation respectively.

2.2.1 Translational Non-Equilibrium

The translational energy mode is the fastest mode and requires at most 4 or 5 collisions for adjustment to equilibrium (Maxwellian distribution) [50,55]. For this reason the translational mode is regarded as a "fast" or "active" mode. One exception occurs when considering mixtures of molecules with large disparities in the molecular weights [55]. Here, the collisional energy exchange is not efficient enough and the translational relaxation time for the lighter particle may be many times larger than for the heavy particle. This is the case for ionized plasmas where many free electrons are present. To accurately account for this phenomena, multiple translational temperatures must be defined [56,57]. These effects are not considered in this work and all species will be assumed to exist at the translational temperature of the heavy particles.

Since only several collisions are necessary to reach translational equilibrium, τ_{tr} is very short, and non-equilibrium effects become important only when τ_{fd} is small (*i.e.*, large flow gradients such as in boundary layers or shock waves). It is important to note that translational non-equilibrium is not dependent on the existence of high temperatures. If the flow gradients are small enough it may be assumed that a fluid element maintains a state of *local* translational equilibrium. The resulting motion is the superposition of the molecular motion of thermal translation (predicted by the Maxwellian velocity distribution) onto the average flow velocity associated with the fluid element. This description corresponds to a particular sub-class of gas dynamic flows known as inviscid flows where the transport phenomena of viscosity, thermal conductivity, and mass diffusion are neglected.

For large flow gradients translational non-equilibrium gives rise to the macroscopic phenomena of viscosity, thermal conductivity, and species mass diffusion.

Classically, the study of flows in translational non-equilibrium is concerned with approximate solutions to the Boltzmann equation of non-equilibrium kinetic theory. Flows with small departures from translational equilibrium are modeled using the Navier-Stokes equations which are derived as a first-order Chapman-Enskog expansion for the Boltzmann equation [9–39]. Chapman-Enskog theory has been applied to multi-component mixtures of monatomic gases [58,59]. Here, the viscous stress tensor, the heat-flux vector, and the diffusion velocities are obtained as moments of the truncated series representation for the velocity distribution function. Further calculations in terms of collision integrals (based on an accurate representation for the intermolecular potential) are required to determine the associated mixture transport properties [59]. These calculations are very mathematically involved. Application of Chapman-Enskog theory to polyatomic gases requires some mechanism to account for inelastic collisions in the treatment of collision integrals [9,47,58]. Modifications have been proposed to address this issue, but add additional complexity [58]. In general, rigorous treatment of transport phenomena using multi-component Chapman-Enskog theory is much too complicated for practical applications, and many simplifications in the form of curve fits and semi-empirical mixture rules are necessary.

The Burnett equations are obtained by retaining the second-order term in the Chapman-Enskog expansion [39]. For larger departures from translational equilibrium, such as in the interior of a shock wave, the Burnett equations are found to yield significant improvements over the Navier-Stokes equations. A major drawback of the Burnett equations is their complexity.

It is noted that throughout this work nothing is said about the complex issue of turbulence which is beyond the scope of this research. All calculations have been run at sufficiently low Reynolds numbers so that laminar flow may be assumed.

2.2.2 Rotational Non-Equilibrium

The rotational energy mode is the next fastest energy mode; it requires only several more collisions to reach equilibrium (9 collisions for N_2, 12 collisions for O_2, and 300 collisions for H_2) [50,55]. The characteristic time corresponding to rotation is accordingly short, and again non-equilibrium effects become important only when τ_{fd} is small (*i.e.*, large flow gradients). Like translation, rotational effects are not dependent on the existence of high temperatures.

Rotational non-equilibrium is caused by the lag in adjustment of the rotational mode to equilibrium at the translational temperature, T. For instance, consider a fluid element subject to an abrupt compression. Initially, the increase in energy of the fluid element (due to the work of pressure forces) is realized by an increase in energy of the "fast" translational mode. The increase in kinetic energy of the molecules results in increased values for the kinetic temperature and pressure (higher than if rotational equilibrium was maintained). After several collisions a Maxwellian velocity distribution is established. Inelastic collisions also occur whereby energy exchanges take place between the translational mode and the internal energy and chemical modes. In particular, a relaxation process occurs between the translational and rotational modes whereby some of the energy of translation is imparted to the rotational mode through collisions. This results in lowering the translational temperature and pressure. After a time on the order of τ_{rot} the rotational mode reaches an equilibrium distribution at the translational temperature. Thus, the effect of rotational non-equilibrium is to produce temperatures and pressures that are higher (for compressions) than would be realized if equilibrium distributions were maintained. The effect is opposite for expansions.

For cases where the characteristic time for rotation is sufficiently short such

that the rotational energy is at all times very near equilibrium at the translational temperature, (*i.e.*, small departures from rotational equilibrium) rotational non-equilibrium can be modeled by a bulk-viscosity term [47]. This case is termed *easy exchange*. For cases where the characteristic time for rotation is significant and large deviations from rotational equilibrium occur (termed *difficult exchange*) and rotational non-equilibrium must be modeled explicitly using a relaxation model [46,47]. For this case a separate rotational temperature, T_{rot} is considered.

As previously mentioned, rotational non-equilibrium effects become important in calculating hypersonic shocks in the continuum transition regime. Typically, for these calculations, a rotational relaxation model is used in conjunction with higher order constitutive relations that are valid for large departures from translational equilibrium (*i.e.*, the Burnett equations). In general, its seems that rotational non-equilibrium is not important in shear type phenomena such as boundary layers, however, rotational non-equilibrium effects could have important consequences in hypersonic shock-boundary-layer interactions. The present work considers rotational non-equilibrium only in the context of one-dimensional hypersonic shock structure (see Chap. 8).

Theoretical studies [60,61] in H_2 have shown that molecular rotation can also effect the coupled vibration/dissociation phenomena. During a vibrational relaxation, the rotational energy tends to relax the lower vibrational levels and serves as a temporary storage of the vibrational energy, thereby delaying the dissociation process. It has been suggested in Ref. [37] that this inherent coupling between the vibrational and rotational modes may be modeled through an energy exchange mechanism. Vibration/dissociation coupling is discussed in detail in Sec. 2.2.3.

2.2.3 Vibrational Non-Equilibrium

Collisions are not as efficient at producing vibrational energy. As a result, the vibrational modes requires many more collisions to reach equilibrium (on the order of 10^5 collisions) [9,50]. Hence, the characteristic time for vibrational relaxation is relatively long and vibrational-non-equilibrium may occur when the flow gradients are small compared to those required for translational and rotational non-equilibrium. Hence, it is possible to consider cases where vibration may be out of equilibrium while the translational and rotational modes maintain equilibrium distributions. It is also noted that vibrational non-equilibrium is dependent on higher temperatures, since the vibrational mode is not active for temperatures lower than about 1000 ^0K.

Vibrational non-equilibrium results because of the lag in adjustment of the vibrational mode to an equilibrium distribution at the translational temperature. A similar relaxation process as for rotation (as described in the previous section) occurs, however, because the characteristic relaxation time for vibration is relatively large, vibrational non-equilibrium effects become very important in modeling hypersonic flowfields and combustion problems. For significant deviations from vibrational equilibrium, a separate vibrational temperature, T_v, must be considered. The most important factor contributing to the relaxation of the vibrational energy toward an equilibrium level is the collisional exchange of vibrational and translational energy through inelastic collisions [55]. This process is usually treated by Landau-Teller theory, which was developed by considering a homogeneous system of harmonic oscillators, along with the assumption of weak interactions, *i.e.*, that collisions produce quantum jumps of only one energy state [9]. Modifications to the original Landau-Teller theory include a characteristic relaxation time that is a

function of all the vibrating species present [62] as well as corrections to account for other limitations that occur at higher temperatures [37,63,64]. It is noted that Landau-Teller theory is restricted by the assumption of the harmonic oscillator itself, since it is only strictly valid for the lower vibrational states [9].

Vibrational energy exchanges other than vibrational/translational process, described above, may occur. For example, collisions may cause intra-vibration-vibration exchanges to take place. Here, molecules of like species collide causing an increase in the vibrational energy of one molecule and a decrease in vibrational energy of the other molecule. These processes are very fast and do not change energy for the harmonic oscillator model since the energy states are equally spaced [55]. Vibration/vibration coupling also takes place between the vibrational modes of each species, if more than one vibrating species is present. Here, each species tends to transfer its vibrational energy to the other vibrating species in a process that works to drive the separate vibrational temperatures together [37,64]. This process sometimes leads to quick equilibration of the species vibrational temperatures so that only one "lumped" vibrational temperature may be considered. A vibration/vibration coupling may also result from resonance effects [60,61]. Vibration/dissociation coupling occurs because highly excited vibrational states tend to promote dissociation. This results in the "preferential" removal of vibrational energy through dissociation [64]. That is, the molecules that dissociate tend to be those in the highly excited vibrational levels. Hence, dissociation removes higher than average vibrational energy and therefore results in the reduction of the vibrational temperature. Park [65,66] has introduced a two-temperature model where an "effective temperature" ($T_a = T_v^{.5}T^{.5}$) is used to determine the dissociation rates ω_s. Vibrational energy is then preferentially removed as $\omega_s(e_{vib_s} + \alpha\Theta_{d_s})$, where e_{vib} is the average vibrational energy and Θ_{d_s} is the dissociation energy. A value of

$\alpha = .5$ has been used in Ref. [37] but appears to be too large. A more sophisticated translational-vibration-dissociation model has been developed by Candler [61] where two vibrational energy levels are considered. The lower level contains molecules below a certain cutoff value of vibrational energy and the upper level contains molecules above the cutoff. Dissociation occurs from the upper level and recombination occurs at the lower level, again with a significant portion of the dissociation energy. A similar model has been developed by Sharma [60] except that it also includes rotational effects. An electronic/Vibrational energy exchange may also take place. Theoretical experiments for air have shown a strong coupling of the electron/electronic temperature T_e with the vibrational temperature of N_2 (the coupling with other species appears to be negligibly small) [64]. For flows with high concentrations of N_2, the electron/electronic temperature T_e can be lumped with the vibrational temperature for N_2 [37,64]. It is noted that polarization effects may also be important. In the present work we consider only the simple Landau-Teller model for vibrational/translational exchanges.

2.2.4 Chemical Non-Equilibrium

Chemical processes also require many collisions to reach equilibrium (on the order of 10^5 collisions) [9], and have relatively long relaxation times. If $\tau_{chem} \ll \tau_{fd}$ the reactions have virtually infinite time to evolve so that the chemical species maintain an equilibrium composition corresponding to the Law of Mass Action from statistical mechanics (at least within the limits of the previous discussion on partitioning of internal energies). Here, interest is only in the final chemical composition and the particular reaction path taken is not of concern. Modeling flows in chemical non-equilibrium requires simulating the actual kinetic behavior of the chemical system. The study of chemical reaction rates is known as *chemical*

kinetics. This subject includes both exerimental studies as well as the development of theories to determine the relevant reaction paths, intermediate products, and appropriate reaction rates for a chemical system. Chemical kinetics is a complex science and remains in a state of development. However, detailed models are available for specific cases. In particular, the present work will implement a simple high temperature air-chemistry model as well as a hydrogen-air combustion model.

It is noted that in general chemical reaction rates are determined under controlled conditions and may not be strictly valid in conjunction with thermal non-equilibrium. One example of this is the vibration/dissociation coupling that was described in Sec. 2.2.3. Here, additional species production terms are introduced to account for dissociation from the highly excited vibrational states.

2.2.5 Final Remarks

One additional assumption, that is relevant to the general development and implementation of non-equilibrium rate constants, must be stated. That is, that the non-equilibrium processes considered are usually established for stationary closed systems, using combinations of laboratory measurements, quantum mechanics, kinetic theory and chemical kinetics. For use in fluid dynamics, it is then assumed that these results may be extended to moving fluid elements subject to continuously changing flowfields. Finally, it is noted that throughout this work the radiation effects that may occur at extremely high temperatures are neglected.

2.3 Internal Energy Model

Certain simplifications may arise if the time scales are such that certain modes may be assumed to be either frozen or in equilibrium so that their rate processes may be neglected. In this section practical models will be introduced that are capable of handling most of the cases that may occur in non-equilibrium gas dynamics.

A general representation for the species internal energy per unit mass that is suitable for modeling many problems with thermodynamic non-equilibrium is given as

$$e_s = \tilde{e}_s(T) + e_{n_s}(T_{n_s}) + e_{e_s}(T_e)\,. \tag{2.8}$$

This model was first introduced by Liu and Vinokur [67] and has been used by Grossman and Cinnella [8]. Here, $\tilde{e}_s(T)$ is the contribution due to the kinetic energy of thermal translation and internal modes that are assumed to be in equilibrium at the heavy particle translational temperature, T. The term $e_{n_s}(T_{n_s})$ is the contribution due to the internal modes that are in thermal non-equilibrium with respect to T, and are assumed to satisfy a Boltzmann distribution at the non-equilibrium temperature, T_{n_s}. Again, T_{n_s} only represents a measure of the amount of non-equilibrium energy present, and in reality the non-equilibrium energy may not satisfy a Boltzmann distribution. The portion $e_{e_s}(T_e)$ represents the contribution from the electron energy states within a particle, or from free electrons when they are present. It is assumed that free and bound electrons can interact in a uninhibited manner so that only one electron/electronic temperature, T_e, is necessary. For the general case, with N species present, each species is assumed to have equilibrium contributions, $\tilde{e}_s(T)$, and electronic contributions, $e_{e_s}(T_e)$, due to bound electrons. The first M species, where $M \leq N$, are assumed to have non-equilibrium contributions, $e_{n_s}(T_{n_s})$. If free electrons are present they are represented by the last index, N, and have only a contribution due to thermal translation at the electron/electronic temperature, T_e. Appropriate rate equations will be used to describe the energy exchange between the various modes.

Several simplifying assumptions can be made for the general model of Eq. (2.8). For instance, the electron/electronic contributions may be considered to co-exist

at either the heavy particle translational temperature, T, or the non-equilibrium temperature, T_{n_s}. In the present work the electronic energy from bound electrons is neglected and if free electrons are present their translational energy is assumed to exist at the heavy particle translational temperature, T. For these assumptions Eq. (2.8) becomes

$$e_s = \tilde{e}_s(T) + e_{n_s}(T_{n_s}) . \tag{2.9}$$

The equilibrium portion of the internal energy typically represents the thermal translation and rotational modes. This is appropriate for *easy* exchanges between the translational and rotational modes so that the rotational energy continuously maintains an equilibrium distribution at the translational temperature. The portion e_{n_s} typically represents the vibrational contribution to the internal energy, however, this term may be modified to include rotational non-equilibrium contributions or coupled rotational/vibrational contributions (if rotational and vibrational partitioning is not deemed satisfactory).

The equilibrium portion of the internal energy is generally expressed in terms of specific heats at constant volume

$$\tilde{e}_s = \int_{Tref}^{T} \tilde{c}_{v_s}(\xi) d\xi + h_{f_s} , \tag{2.10}$$

where h_{f_s} is the heat of formation for species s, and

$$\tilde{c}_{v_s} = \frac{d\tilde{e}_s}{dT} . \tag{2.11}$$

The equilibrium portion of the species enthalpy is introduced as

$$\tilde{h}_s = \tilde{e}_s + \frac{p_s}{\rho_s} , \tag{2.12}$$

and the corresponding specific heat at constant pressure is

$$\tilde{c}_{p_s} = \frac{d\tilde{h}_s}{dT} . \tag{2.13}$$

The internal energy for the mixture may be written using the standard mass-fraction averaged summation as

$$e = \sum_{i=1}^{N} \frac{\rho_s}{\rho} e_s = \tilde{e} + \sum_{i=1}^{M} \frac{\rho_s}{\rho} e_{n_s} , \tag{2.14}$$

where

$$\tilde{e} = \sum_{i=1}^{N} \frac{\rho_s}{\rho} \tilde{e}_s . \tag{2.15}$$

It is also convenient to define reduced specific heats for the mixture as

$$\tilde{c}_v = \sum_{i=1}^{N} \frac{\rho_s}{\rho} \tilde{c}_{v_s} , \tag{2.16a}$$

$$\tilde{c}_p = \sum_{i=1}^{N} \frac{\rho_s}{\rho} \tilde{c}_{p_s} , \tag{2.16b}$$

and the mixture gas constant as defined in Eq. (2.4) is related to these as follows

$$\tilde{R} = \tilde{c}_p - \tilde{c}_v . \tag{2.17}$$

As previously mentioned, the equilibrium contributions to the species internal energy may be derived from the partition function of statistical mechanics, where independent modes give rise to summable contributions to the internal energy. This derivation assumes complete thermodynamic equilibrium. For cases of translational non-equilibrium, the equilibrium contributions are assumed to have the same form but are evaluated at the translational temperature *i.e.*, they are considered in equilibrium at the translational temperature, T. The equilibrium value for translational energy is given as

$$\tilde{e}_{tr_s} = \tilde{c}_{v_{tr_s}} T , \tag{2.18a}$$

where

$$\tilde{c}_{v_{tr_s}} = \frac{3}{2} R_s . \tag{2.18b}$$

The equilibrium value for rotational energy is given as

$$\tilde{e}_{rot_s} = \tilde{c}_{v_{rot_s}} T , \tag{2.19a}$$

where

$$\tilde{c}_{v_{rot_s}} = \begin{cases} R_s, & \text{for diatomic and linear polyatomic molecules;} \\ \frac{3}{2}R_s, & \text{for non-linear polyatomic molecules.} \end{cases} \tag{2.19b}$$

The equilibrium values for the vibrational energy and the corresponding specific heat at constant volume are given as [9,68]

$$\tilde{e}_{vib_s} = \sum_{i=1}^{N_{\Theta,s}} \frac{R_s \Theta_{vib_{s,i}}}{e^{\Theta_{vib_{s,i}}/T} - 1}, \tag{2.20a}$$

and

$$\tilde{c}_{v_{vib_s}} = \sum_{i=1}^{N_{\Theta,s}} R_s \left(\frac{\Theta_{vib_{s,i}}}{T}\right)^2 \frac{e^{\Theta_{vib_{s,i}}/T}}{(e^{\Theta_{vib_{s,i}}/T} - 1)^2}, \tag{2.20b}$$

where $N_{\Theta,s}$ is the number of characteristic vibrational temperatures $\Theta_{vib_{s,i}}$ for species s.

Several variations of Eq. (2.9) will be used throughout this work and are described below. The *perfect gas model* corresponds to gases where the temperature is low enough that vibrational energy is not present. The internal energy consists of the translational energy and a rotational contribution in equilibrium at the translational temperature.

$$e_s = \tilde{e}_{tr_s}(T) + \tilde{e}_{rot_s}(T). \tag{2.21}$$

The *vibrational equilibrium model* corresponds to temperatures where the vibrational mode is excited but flow gradients are small enough so that vibration is assumed to be in equilibrium at the translational temperature

$$e_s = \tilde{e}_{tr_s}(T) + \tilde{e}_{rot_s}(T) + \tilde{e}_{vib_s}(T). \tag{2.22}$$

The *vibrational non-equilibrium model* is used for cases where non-equilibrium vibrational effects are important

$$e_s = \tilde{e}_{tr_s}(T) + \tilde{e}_{rot_s}(T) + e_{vib_s}(T_{vib}). \tag{2.23}$$

The *rotational non-equilibrium model* is used for the hypersonic shock structure cases. Here, the vibrational energy is frozen within the shock and is therefore neglected

$$e_s = \tilde{e}_{tr_s}(T) + e_{rot_s}(T_{rot})\,. \tag{2.24}$$

2.4 Chemical Model

A general representation for a chemical system of N species where J reactions may occur is given as

$$\nu'_{1,j}X_1 + \nu'_{2,j}X_2 + ... + \nu'_{N,j}X_N \rightleftharpoons \nu''_{1,j}X_1 + \nu''_{2,j}X_2 + ... + \nu''_{N,j}X_N$$
$$j = 1, 2, ..., J\,, \tag{2.25}$$

where $\nu'_{s,j}$ and $\nu''_{s,j}$ are the stoichiometric coefficients of the reactants and products of species X_s in the jth reaction, respectively. The rate of production of species s, denoted ω_s, is given as

$$\omega_s \equiv \frac{d\rho_s}{dt} = \hat{m}_s \sum_{j=1}^{J} (\nu''_{s,j} - \nu'_{s,j}) \left[k_{f,j} \prod_{l=1}^{N} (\frac{\rho_l}{\hat{m}_l})^{\nu'_{i,j}} - k_{b,j} \prod_{l=1}^{N} (\frac{\rho_l}{\hat{m}_l})^{\nu''_{i,j}} \right]$$
$$s = 1, 2, ..., N\,, \tag{2.26}$$

where $k_{f,j}$ and $k_{b,j}$ are the forward and backward reaction rates and are assumed to be functions of the translational temperature. For conditions of chemical equilibrium the species concentrations are governed by the Law of Mass Action

$$K_{e,j}(T) = \frac{\prod_{l=1}^{N} (\rho_l/\hat{m}_l)^{\nu''_{i,j}}}{\prod_{l=1}^{N} (\rho_l/\hat{m}_l)^{\nu'_{i,j}}} \qquad j = 1, 2, ..., J\,, \tag{2.27}$$

where $K_{e,j}$ is the equilibrium constant. For conditions of chemical equilibrium Eq. (2.26), Eq. (2.27) and the fact that $\omega_s = 0$ may be combined to give the relation

$$K_{e,j} = \frac{K_{f,j}}{K_{b,j}}\,. \tag{2.28}$$

Using Eq. (2.27), an alternate form for Eq. (2.25) is obtained as

$$\omega_s \equiv \frac{d\rho_s}{dt} = \hat{m}_s \sum_{j=1}^{J} (\nu''_{s,j} - \nu'_{s,j}) k_{f,j} \left[\prod_{l=1}^{N} (\frac{\rho_l}{\hat{m}_l})^{\nu'_{l,j}} - \frac{1}{k_{e,j}} \prod_{l=1}^{N} (\frac{\rho_l}{\hat{m}_l})^{\nu''_{l,j}} \right]$$

$$s = 1, 2, ..., N, \quad (2.29)$$

The limiting case of frozen chemistry corresponds to zero species production terms, *i.e.*, $k_{f,j} \to 0$. For this case the species mass fractions remain unchanged, assuming no diffusion occurs. The limiting case of chemical equilibrium may be modeled by allowing the forward reaction rate $k_{f,j} \to \infty$. For this case the term inside the brackets in Eq. (2.29) will approach zero since an equilibrium concentration is maintained.

The equilibrium constants $K_{e,j}$ can be obtained theoretically from statistical mechanics for a given thermodynamic model. However, experimental curve fits tend to be more reliable than theoretically determined formulas based on partition functions, since they may include certain assumptions or approximations. Furthermore, the theoretical approach becomes ill-defined in the presence of thermal non-equilibrium.

Chapter 3

Governing Equations

3.1 Introduction

In this chapter, the mathematical foundation necessary for the study of flows in chemical and thermal non-equilibrium is presented. First, in Sec. 3.2, the essentials of non-equilibrium kinetic theory for gas mixtures are discussed. Here, the velocity distribution function is introduced, and the average flow variables, including the species velocities, the mass-averaged mixture velocity, the species diffusion velocities, as well as the kinetic pressure and temperature, are defined as moments of the velocity distribution function. Also, the Boltzmann equation for non-equilibrium kinetic theory is stated in differential form and its limitations are discussed. In Sec. 3.3 the general macroscopic conservation equations that govern the motion of gas mixtures in chemical and thermal non-equilibrium are derived from a molecular analysis as moments of the Boltzmann equation. The final vector form of the governing equations for Cartesian coordinates is given along with the necessary closure relations and simplification to the Euler equations for local translational equilibrium is described. Finally, the governing equations are extended to generalized coordinates and the more general integral form is discussed. The simplified quasi-one-dimensional equation set is also presented.

3.2 Non-Equilibrium Kinetic Theory for Gas Mixtures

Kinetic theory provides a statistical means of describing the translational motion of the individual molecules in a gas. In particular, kinetic theory defines a

velocity distribution function that gives the probability that a molecule will have a specific molecular velocity. For gas mixtures, each species (denoted by s) will have a velocity distribution function f_s that is a function of the particle velocity vector $\bar{c}$, the position vector $\bar{x}$, and time t. The probability that a particle of species s will have velocity components within the range c_1, c_2, c_3 and $c_1 + dc_1$, $c_2 + dc_2$, $c_3 + dc_3$ is given as $f_s(\bar{c}, \bar{x}, t)\, dc_1 dc_2 dc_3$.

The velocity distribution function provides a means for obtaining statistical averages at the kinetic level that give rise to the macroscopic flow variables of temperature, pressure, viscosity, *etc.*, for each fluid element. In general, if $\psi = \psi(\bar{c})$ is any quantity (characteristic of a molecule) that is a function of the molecular velocity components, then the mean value of ψ for species s at a given time and spatial location is given as the following moment of the velocity distribution function and denoted by brackets as follows

$$\int_{-\infty}^{\infty}\int_{-\infty}^{\infty}\int_{-\infty}^{\infty} f_s(\bar{c}, \bar{x}, t)\, \psi(\bar{c})\, dc_1 dc_2 dc_3 = < \psi >_s (\bar{x}, t)\,. \tag{3.1}$$

For example, the component of the species mean velocity in the i-direction is obtained by letting $\psi = c_i$ in Eq. (3.1). The result is written as

$$(u_i)_s = < c_i >_s \ . \tag{3.2}$$

Using Eq. (3.2), the mass-averaged mixture velocity components are defined as

$$\rho u_i = \sum_{s=1}^{N} \rho_s (u_i)_s \,, \tag{3.3}$$

where N represents the total number of species present. It is also convenient to define a thermal velocity $\bar{c}'$ with respect to the mass-averaged mixture velocity $\bar{u}$ where components are given by

$$c_i = u_i + c_i' \,. \tag{3.4}$$

Averaging Eq. (3.4) over velocity space yields

$$< c_i >_s = u_i + < c_i' >_s , \tag{3.5a}$$

which may be rewritten using Eq. (3.2) as

$$(u_i)_s = u_i + (V_i)_s . \tag{3.5b}$$

Here, $(V_i)_s$ are the species diffusion velocity components defined by

$$(V_i)_s \equiv < c_i' >_s . \tag{3.5c}$$

Combining Eq. (3.3) with Eq. (3.5b) yields the following relationship

$$\sum_{s=1}^{N} \rho_s (V_i)_s \equiv 0 . \tag{3.6}$$

Kinetic theory defines a "kinetic" pressure based on the mean thermal motion of the gas. The kinetic pressure for species s is given by

$$p_s = \frac{1}{3} \rho_s < c_i' c_i' >_s . \tag{3.7}$$

This relation is strictly valid *only* for thermally prefect gases (*i.e.*, negligible intermolecular forces) and is based solely on the thermal momentum flux through an imaginary surface element within the gas. The kinetic definition of pressure is valid for equilibrium as well as non-equilibrium situations. Application of Dalton's law, Eq. (2.3), results in the mixture kinetic pressure

$$p = \sum_{s=1}^{N} p_s = \sum_{s=1}^{N} \frac{1}{3} \rho_s < c_i' c_i' >_s . \tag{3.8}$$

In Eqs. (3.7) and (3.8), and throughout the paper, the tensor notation of summation of repeated indices is implied.

The kinetic energy of thermal translation per unit mass for a molecule is given by

$$\epsilon_{tr} = \frac{1}{2} (c_i' c_i') . \tag{3.9}$$

The mean thermal translational energy per unit mass for species s is obtained by averaging over all the molecules of species s,

$$e_{tr_s} = < \epsilon_{tr} >_s = \frac{1}{2} < c_i' c_i' >_s , \tag{3.10}$$

and the mixture value is obtained by considering contributions from all species using the mass-fraction averaged mixture law as follows

$$e_{tr} = \sum_{s=1}^{N} \frac{\rho_s}{\rho} e_{tr_s} = \sum_{s=1}^{N} \frac{\rho_s}{\rho} \frac{1}{2} < c_i' c_i' >_s . \tag{3.11}$$

For the case of local translational equilibrium, the thermal motion of the gas is governed by the Maxwellian velocity distribution function. For this case, each species in the gas will maintain a Maxwellian distribution at the mixture temperature T and the species diffusion velocities will reduce identically to zero so that $(u_i)_s \equiv u_i$. The species Maxwellian velocity distribution function, denoted f_{0_s}, is given by

$$f_{0_s}(\bar{c}, \bar{x}, t) = \left(\frac{\beta_s}{\pi}\right)^{3/2} exp\{-\beta_s[(c_1 - u_1)^2 + (c_2 - u_2)^2 + (c_3 - u_3)^2]\} , \tag{3.12a}$$

where

$$\beta_s = \frac{m_s}{2kT} = \frac{1}{2R_s T} . \tag{3.12b}$$

Here, k is Boltzmann's constant, m_s is the mass for a molecule of species s, and T is the absolute temperature as defined in classical equilibrium thermodynamics. Moments with respect to the Maxellian distribution function are represented by brackets as $<>^0$. If translational equilibrium is assumed, the previous results from kinetic theory can be evaluated as moments of the Maxwellian velocity distribution function. For a local Maxwellian distribution the species kinetic pressure, given by Eq. (3.7) becomes

$$p_s = \frac{1}{3} \rho_s < c_i' c_i' >_s^0 , \tag{3.13}$$

where

$$< c_i'c_i' >_s^0 = \int_{-\infty}^{\infty}\int_{-\infty}^{\infty}\int_{-\infty}^{\infty} c_i'c_i' f_{0_s}\, dc_1 dc_2 dc_3 = 3R_sT\,. \tag{3.14}$$

Combining Eqs. (3.13) and (3.14) yields the result for a thermally perfect gas as given in Eq. (2.1). Hence, for the case of local translational equilibrium the species kinetic pressure reduces identically to the result from classical equilibrium thermodynamics. Evaluating Eqs. (3.10) and (3.11) for a Maxwellian distribution yields

$$e_{tr_s} = \frac{1}{2} < c_i'c_i' >_s^0 = \frac{3}{2}R_sT\,, \tag{3.15}$$

and

$$e_{tr} = \sum_{s=1}^{N} \frac{\rho_s}{\rho}\frac{1}{2} < c_i'c_i' >_s^0 = \frac{3}{2}\tilde{R}T\,, \tag{3.16}$$

respectively. Here, the average kinetic energy of thermal motion has been related to the absolute temperature as defined in classical thermodynamics.

In non-equilibrium kinetic theory it is common to define a species translational temperature T_s, based on average thermal kinetic energy following the form of Eq. (3.15)

$$\frac{3}{2}R_sT_s = \frac{1}{2} < c_i'c_i' >_s\,. \tag{3.17}$$

The translational temperature agrees with the thermodynamic temperature for translational equilibrium and is also valid in regions of translational non-equilibrium. Combining Eq. (3.17) with the species kinetic pressure, Eq. (3.7), yields

$$p_s = \rho_s R_s T_s\,. \tag{3.18}$$

For the present work it is assumed that each species in the mixture exists at the same translational temperature so that $T_s \equiv T$. This assumption is rigorously limited to small departures from translational equilibrium and to mixtures without large disparities in species molecular mass [9]. Equation (3.18) now reduces to

the relation for a thermally perfect gas, Eq. (2.1). Thus, by using the definition of the translational temperature, the thermally perfect gas relation (strictly valid for equilibrium conditions) may be used in cases of translational equilibrium and non-equilibrium alike.

The Boltzmann equation is the basic governing equation at the kinetic level and is derived from the conservation of molecules with molecular velocities differing only slightly from the velocity vector $\bar{c}$ (molecules of class $\bar{c}$). The resulting equation is the partial differential equation that governs the rate of change, with respect to position and time, of the velocity distribution function. It is written here for species s as follows

$$\frac{\partial}{\partial t}(n_s f_s) + c_i \frac{\partial}{\partial x_i}(n_s f_s) + \frac{\partial}{\partial c_i}\{(X_i)_s n_s f_s\} = \sum_r \{\frac{\partial}{\partial t}(n_s f_s)\}_{coll_{r-s}}, \tag{3.19}$$

where n_s is the number density for species s and $(X_i)_s$ is the external force per unit mass acting on a particle of species s. The term on the right-hand side represents the collision integral and is the rate of production of molecules of class $\bar{c}$ per unit volume due to collisions. Here r is a "dummy" index that denotes any species of the mixture. The summation over r then includes $s-s$ collisions as well as collisions between species s and all other species.

In the development of the Boltzmann equation certain restrictions have been implied. First, the Boltzmann equation is valid only for thermally perfect gases or mixtures of thermally perfect gases since the effect of intermolecular forces is considered only during collisions (*i.e.*, only in the evaluation of collision integrals). As a result, intermolecular forces will not explicitly appear in the development of the conservation equations (Sec. 3.3). Moreover, the restriction to thermally perfect gases insures that the molecular spacing is large enough so that only binary collisions must be accounted for in the evaluation of collision integrals. It is also

assumed that the distribution function does not vary appreciably over the distance corresponding to the range of intermolecular forces or a time comparable to the duration of a collision. This is important for a valid representation of the collision integral in terms of the distribution function. One final assumption states that there is no correlation of the velocities of two molecules in a collision (molecular chaos) [9].

It is noted that only the minimum amount of non-equilibrium kinetic theory has been presented here. A detailed treatment may be found in Hirschfelder, Curtiss, and Bird [58].

3.3 Governing Equations of Gas Dynamics

The equation of transfer for species s is obtained by multiplying the corresponding Boltzmann equation by any function $\psi = \psi(\bar{c})$ of the molecular velocity components and integrating over velocity space. These so called moments of the Boltzmann equation are written as

$$\int_{-\infty}^{\infty}\int_{-\infty}^{\infty}\int_{-\infty}^{\infty}\psi\Big[\frac{\partial}{\partial t}(n_s f_s) + c_i\frac{\partial}{\partial x_i}(n_s f_s) + \frac{\partial}{\partial c_i}\{(X_i)_s n_s f_s\} - \sum_r\{\frac{\partial}{\partial t}(n_s f_s)\}_{coll_{r-s}}\Big]dc_1 dc_2 dc_3 = 0\,. \qquad (3.20)$$

This equation may be simplified by interchanging the order of integration and differentiation and making use of the fact that $\bar{c}$, $\bar{x}$, and t are all independent variables. The body force term may be simplified using integration by parts as in Vincenti and Kruger [9]. The resulting equation of transfer is given as

$$\frac{\partial}{\partial t}(n_s < \psi >_s) + \frac{\partial}{\partial x_i}(n_s < c_i\psi >_s) - n_s < X_i\frac{\partial \psi}{\partial c_i} >_s = \sum_r\{\frac{\partial}{\partial t}(n_s < \psi >_s)\}_{coll_{r-s}}\,. \qquad (3.21)$$

The species conservation equations are obtained by taking ψ to be the elements of the moment function vector Ψ which represent the molecular mass, momentum,

non-equilibrium internal energy and total energy

$$\Psi = \begin{pmatrix} m_s \\ m_s c_k \\ m_s \epsilon_n \\ m_s \epsilon_0 \end{pmatrix} , \tag{3.22}$$

where

$$\epsilon_0 = \frac{c_k c_k}{2} + \epsilon' , \tag{3.23a}$$

and ϵ' represents the internal energy per unit mass (not including the energy of thermal translation) which may have an equilibrium portion $\tilde{\epsilon}'$ as well as non-equilibrium portion ϵ_n as follows

$$\epsilon' = \tilde{\epsilon}'(T) + \epsilon_n(T_n) . \tag{3.23b}$$

This is consistent with Eq. (2.9). The term on the right-hand side of Eq. (3.21) which results from moments of the collision integral represents the collisional rate of change of ψ per unit volume. Global conservation equations for the mixture can be obtained by direct summation over all the species equations. Many simplifications occur as a result of cancellation of interaction terms which result from the physical fact that collisions can produce no change in the total mass, momentum, and energy of the system as a whole (*i.e.*, they are collisional invariants). A similar development of the governing equations is given by Lee [69].

The species continuity equation is obtained when $\psi = m_s$, the mass of a particle of species s. Here, the terms inside parentheses on the left-hand side of the equation of transfer, Eq. (3.21), become

$$n_s < m_s >_s = \rho_s , \tag{3.24a}$$

$$\begin{aligned} n_s < m_s c_i >_s &= \rho_s < u_i + c_i' >_s \\ &= \rho_s [u_i + (V_i)_s] , \end{aligned} \tag{3.24b}$$

where Eqs. (3.4) and (3.5c) have been utilized. The body force term reduces identically to zero as follows

$$n_s < X_i \frac{\partial m_s}{\partial c_i} >_s = 0 , \tag{3.24c}$$

and the production term on the right-hand side of the equation of transfer becomes

$$\sum_r \{ \frac{\partial}{\partial t} (n_s < m_s >_s) \}_{coll_{r-s}} = \omega_s , \tag{3.24d}$$

where ω_s is the chemical source term representing the production of species s due to chemical reactions given in Eq. (2.29). Substituting Eqs. (3.24a)-(3.24d) into the equation of transfer yields the species continuity equation

$$\frac{\partial \rho_s}{\partial t} + \frac{\partial}{\partial x_i} [\rho_s u_i] + \frac{\partial}{\partial x_i} [\rho_s (V_i)_s] = \omega_s , \tag{3.25a}$$

or in vector notation

$$\frac{\partial \rho_s}{\partial t} + \bar{\nabla} \cdot [\rho_s \bar{\mathbf{u}}] + \bar{\nabla} \cdot [\rho_s \bar{\mathbf{V}}_s] = \omega_s . \tag{3.25b}$$

The mixture continuity equation is obtained by simply adding the species contributions. Using the definition of the mixture density, Eq. (2.5), along with Eq. (3.6), and the fact that the chemical interaction terms among species must sum to zero, that is

$$\sum_{s=1}^{N} \omega_s \equiv 0 , \tag{3.26}$$

the following form is obtained

$$\frac{\partial \rho}{\partial t} + \frac{\partial}{\partial x_i} [\rho u_i] = 0 . \tag{3.27a}$$

In vector notation Eq. (3.27a) is written as

$$\frac{\partial \rho}{\partial t} + \bar{\nabla} \cdot [\rho \bar{\mathbf{u}}] = 0 . \tag{3.27b}$$

Similarly, the species momentum equation for the k-direction is obtained by letting $\psi = m_s c_k$. In this case the terms in the equation of transfer become

$$n_s < m_s c_k >_s = \rho_s (u_k)_s \,, \tag{3.28a}$$

$$\begin{aligned} n_s < m_s c_i c_k >_s &= \rho_s < [u_i + c_i'][u_k + c_k'] >_s \\ &= \rho_s u_i u_k + \rho_s u_i (V_k)_s + \rho_s (V_i)_s u_k + \rho_s < c_i' c_k' >_s \,, \end{aligned} \tag{3.28b}$$

where again Eqs. (3.4) and (3.5c) have been used. The term $\rho_s < c_i' c_k' >_s$ appearing in Eq. (3.28b) is identified with an element of the species stress tensor $(\sigma_{ik})_s$, and may be broken into contributions due to the species shear stress $(\tau_{ik})_s$, and the species kinetic pressure, defined in Eq. (3.7), as follows

$$(\sigma_{ik})_s = -\rho_s < c_i' c_k' >_s = (\tau_{ik})_s - p_s \, \delta_{ik} \,, \tag{3.28c}$$

where the term $\delta_{ik} = 1$ if $i = k$, otherwise $\delta_{ik} = 0$. The body force term becomes

$$n_s < X_i \frac{\partial}{\partial c_i} (m_s c_k) >_s = \rho_s < X_k >_s \,, \tag{3.28d}$$

and the term on the right-hand side now represents the production of momentum for species s in the k-direction due to collisions

$$\sum_r \left\{ \frac{\partial}{\partial t} (n_s < m_s c_k >_s) \right\}_{coll_{r-s}} = (F_k)_{s_E} + (F_k)_{s_I} \,. \tag{3.28e}$$

Here $(F_k)_{s_E}$ and $(F_k)_{s_I}$ represent the elastic and inelastic interaction forces in the k-direction acting on species s. The final result for the species momentum equation in the k-direction is given as

$$\begin{aligned} &\frac{\partial}{\partial t} [\rho_s (u_k)_s] + \frac{\partial}{\partial x_i} [\rho_s u_i u_k + p_s \delta_{ik}] + \frac{\partial}{\partial x_i} [\rho_s u_i (V_k)_s] + \frac{\partial}{\partial x_i} [\rho_s (V_i)_s u_k] \\ &\qquad - \frac{\partial}{\partial x_i} (\tau_{ik})_s = \rho_s < X_k >_s + (F_k)_{s_E} + (F_k)_{s_I} \,. \end{aligned} \tag{3.29}$$

The mixture momentum equation in the k-direction is obtained by summing the species momentum equations. The species shear stresses sum to the mixture value

as follows

$$\sum_{s=1}^{N}(\tau_{ik})_s = \tau_{ik}\,, \tag{3.30a}$$

the elastic and inelastic interaction terms sum identically to zero

$$\sum_{s=1}^{N}(F_k)_{s_E} = \sum_{s=1}^{N}(F_k)_{s_I} = 0\,, \tag{3.30b}$$

and using Daltons Law, Eq.(2.3), along with Eqs. (3.3), (3.6), and the definition of mixture density, Eq. (2.5), yields

$$\frac{\partial}{\partial t}[\rho u_k] + \frac{\partial}{\partial x_i}[\rho u_i u_k + p\delta_{ik}] - \frac{\partial}{\partial x_i}[\tau_{ik}] = \sum_{s=1}^{N}\rho_s < X_k >_s\,. \tag{3.31a}$$

In vector notation the mixture momentum equation becomes

$$\frac{\partial}{\partial t}[\rho\bar{\mathbf{u}}] + \bar{\nabla}\cdot[\rho\bar{\mathbf{u}}\bar{\mathbf{u}} + p\bar{\mathbf{I}}] - \bar{\nabla}\cdot\bar{\mathbf{T}} = \sum_{s=1}^{N}\rho_s < \bar{\mathbf{X}} >_s\,, \tag{3.31b}$$

where $\bar{\mathbf{I}}$ is the unit dyadic

$$\bar{\mathbf{I}} = \hat{\mathbf{i}}\hat{\mathbf{i}} + \hat{\mathbf{j}}\hat{\mathbf{j}} + \hat{\mathbf{k}}\hat{\mathbf{k}}\,, \tag{3.32}$$

and $\bar{\mathbf{T}}$ is the stress tensor

$$\begin{aligned}\bar{\mathbf{T}} = {} & \tau_{11}\hat{\mathbf{i}}\hat{\mathbf{i}} + \tau_{12}\hat{\mathbf{i}}\hat{\mathbf{j}} + \tau_{13}\hat{\mathbf{i}}\hat{\mathbf{k}} \\ & \tau_{21}\hat{\mathbf{j}}\hat{\mathbf{i}} + \tau_{22}\hat{\mathbf{j}}\hat{\mathbf{j}} + \tau_{23}\hat{\mathbf{j}}\hat{\mathbf{k}} \\ & \tau_{31}\hat{\mathbf{k}}\hat{\mathbf{i}} + \tau_{32}\hat{\mathbf{k}}\hat{\mathbf{j}} + \tau_{33}\hat{\mathbf{k}}\hat{\mathbf{k}}\,.\end{aligned} \tag{3.33}$$

The species energy equation is recovered when $\psi = m_s\epsilon_0$. Using Eq. (3.4) along with Eq. (3.23a), ψ may be rewritten as

$$\psi = m_s\left[\frac{1}{2}u_k u_k + u_k c_k{}' + \epsilon\right]\,, \tag{3.34}$$

where the internal energy per unit mass ϵ now includes the energy of translational thermal motion and is given by

$$\epsilon = \tilde{\epsilon}(T) + \epsilon_n(T_n)\,. \tag{3.35}$$

The terms in the equation of transfer are given by

$$n_s < m_s[\frac{1}{2}u_k u_k + u_k c_k{}' + \epsilon] >_s = \rho_s(\frac{1}{2}u_k u_k + e_s) + \rho_s u_k (V_k)_s$$

$$= \rho_s e_{0_s} + \rho_s u_k (V_k)_s \,, \tag{3.36a}$$

where $< \epsilon >_s = e_s$ and $e_{0_s} = u_k u_k/2 + e_s$ is the species total energy,

$$n_s < m_s[\frac{1}{2}c_i u_k u_k + c_i u_k c_k{}' + c_i \epsilon] >_s = \rho_s u_i [e_{0_s} + u_k (V_k)_s] + \frac{1}{2}\rho_s (V_i)_s u_k u_k$$

$$+ \rho_s u_k < c_i{}' c_k{}' >_s + \rho_s < c_i{}' \epsilon >_s \,, \tag{3.36b}$$

where again elements of the species stress tensor appear, as defined in Eq. (3.28c), and the last term in Eq. (3.36b) is identified with the component of the species heat-flux vector in the i-direction $(q_i)_s$, given as

$$(q_i)_s = \rho_s < c_i{}' \epsilon >_s \,. \tag{3.36c}$$

The body force term becomes

$$n_s < X_i \frac{\partial}{\partial c_i}[m_s(\frac{c_k c_k}{2} + \epsilon')] >_s = \rho_s < X_k c_k >_s \,, \tag{3.36d}$$

and the production term on the right-hand side becomes

$$\sum_r \{\frac{\partial}{\partial t}(n_s < m_s \epsilon_0 >_s)\}_{coll_{r-s}} = \dot{Q}_{s_E} + \dot{Q}_{s_I} \,, \tag{3.36e}$$

where, $\dot{Q}_{s_E}$ and $\dot{Q}_{s_I}$ represent the power generated per unit volume by elastic and inelastic interaction forces. The final result for the species energy equation is

$$\frac{\partial}{\partial t}[\rho_s e_{0_s}] + \frac{\partial}{\partial t}[\rho_s u_k (V_k)_s] + \frac{\partial}{\partial x_i}[\rho_s u_i e_{0_s} + u_k p_s \delta_{ik}]$$

$$+ \frac{\partial}{\partial x_i}[\rho_s u_i u_k (V_k)_s + \frac{1}{2}\rho_s (V_i)_s u_k u_k] - \frac{\partial}{\partial x_i}[u_k (\tau_{ik})_s] + \frac{\partial}{\partial x_i}(q_i)_s$$

$$= \rho_s < X_k c_k >_s + \dot{Q}_{s_E} + \dot{Q}_{s_I} \,, \tag{3.37}$$

Again, the mixture energy equation is obtained by summing the species contributions, where the mixture total energy is given by

$$\rho_s e_0 = \sum_{s=1}^{N} \rho_s e_{0_s} \,, \tag{3.38a}$$

the elastic and inelastic power terms sum identically to zero

$$\sum_{s=1}^{N} \dot{Q}_{s_E} = \sum_{s=1}^{N} \dot{Q}_{s_I} = 0 \,, \tag{3.38b}$$

and the species heat fluxes sum to the mixture value as

$$\sum_{s=1}^{N} (q_i)_s = q_i \,, \tag{3.38c}$$

along with Eqs. (3.30a), (3.6), and (2.3) yield

$$\frac{\partial}{\partial t}[\rho e_0] + \frac{\partial}{\partial x_i}[\rho e_0 u_i + u_k p \delta_{ik}] - \frac{\partial}{\partial x_i}[u_k \tau_{ik}] + \frac{\partial}{\partial x_i} q_i = \sum_{s=1}^{N} \rho_s < X_k c_k >_s \,. \tag{3.39a}$$

The vector form becomes

$$\frac{\partial}{\partial t}[\rho e_0] + \bar{\nabla} \cdot [\rho e_0 \bar{\mathbf{u}} + \bar{\mathbf{u}} \cdot p\bar{\mathbf{I}}] - \bar{\nabla} \cdot [\bar{\mathbf{T}} \cdot \bar{\mathbf{u}}] + \bar{\nabla} \cdot \bar{\mathbf{q}} = \sum_{s=1}^{N} \rho_s < \bar{\mathbf{X}} \cdot \bar{\mathbf{c}} >_s \,. \tag{3.39b}$$

The first divergence term in Eqs. (3.39a) and (3.39b) can be rewritten in terms of total enthalpy, $h_0 = e_0 + p/\rho$, and an alternate form of the total energy equation becomes

$$\frac{\partial}{\partial t}[\rho e_0] + \frac{\partial}{\partial x_i}[\rho u_i h_0] - \frac{\partial}{\partial x_i}[u_k \tau_{ik}] + \frac{\partial}{\partial x_i} q_i = \sum_{s=1}^{N} \rho_s < X_k c_k >_s \,, \tag{3.40a}$$

or in vector form

$$\frac{\partial}{\partial t}[\rho e_0] + \bar{\nabla} \cdot [\rho \bar{\mathbf{u}} h_0] - \bar{\nabla} \cdot [\bar{\mathbf{T}} \cdot \bar{\mathbf{u}}] + \bar{\nabla} \cdot \bar{\mathbf{q}} = \sum_{s=1}^{N} \rho_s < \bar{\mathbf{X}} \cdot \bar{\mathbf{c}} >_s \,. \tag{3.40b}$$

In order to complete the mathematical formulation, M rate equations must be included for the species non-equilibrium internal energy contributions. These equations are obtained when $\psi = m_s \epsilon_n$, the non-equilibrium contribution to the internal energy for a particle of species s. Here, the terms inside parentheses on the left-hand side of the equation of transfer, Eq. (3.21), become

$$n_s < m_s \epsilon_n >_s = \rho_s e_{n_s} \,, \tag{3.41a}$$

$$n_s < m_s c_i \epsilon_n >_s = \rho_s < [u_i + c_i{}'] \epsilon_n >_s = \rho_s e_{n_s} u_i + \rho_s < c_i{}' \epsilon_n >_s \,, \tag{3.41b}$$

where Eq. (3.4) has been utilized. The last term in Eq. (3.41b) is identified with the i-component of the non-equilibrium heat-flux vector for species s, $(q_i)_{n_s}$,

$$(q_i)_{n_s} = \rho_s < c_i' \epsilon_n >_s \ . \tag{3.41c}$$

The body force term reduces identically to zero as follows

$$n_s < X_i \frac{\partial(m_s \epsilon_n)}{\partial c_i} >_s = 0 \, , \tag{3.41d}$$

and the term on the right-hand-side of the equation of transfer becomes

$$\sum_r \{ \frac{\partial}{\partial t} (n_s < m_s \epsilon_n >_s) \}_{coll_{r-s}} = \dot{Q}_{n_{s_E}} + \dot{Q}_{n_{s_I}} \, , \tag{3.41e}$$

where $\dot{Q}_{n_{s_E}}$ and $\dot{Q}_{n_{s_I}}$ represent the non-equilibrium portion of the power generated per unit volume through interaction forces. Two basic physical phenomena can contribute to these production terms. The first is the creation or destruction of the non-equilibrium internal energy mode through chemical reactions, denoted by $\dot{\rho}_s e_{n_s}$. The second contribution is due to the various energy exchange phenomena between the internal energy modes, given by $\rho_s \dot{e_{n_s}}$. Hence, the combined effects of the elastic and inelastic non-equilibrium power production may be written as follows

$$\dot{Q}_{n_{s_E}} + \dot{Q}_{n_{s_I}} = \dot{\rho}_s e_{n_s} + \rho_s \dot{e_{n_s}} \, , \tag{3.41f}$$

Substituting Eqs. (3.41a)-(3.41f) into the equation of transfer we obtain the species non-equilibrium energy equation

$$\frac{\partial}{\partial t}[\rho_s e_{n_s}] + \frac{\partial}{\partial x_i}[\rho_s e_{n_s} u_i] + \frac{\partial}{\partial x_i}[(q_i)_{n_s}] = \dot{\rho}_s e_{n_s} + \rho_s \dot{e_{n_s}} \, , \tag{3.42a}$$

or in vector notation

$$\frac{\partial}{\partial t}[\rho_s e_{n_s}] + \bar{\nabla} \cdot [\rho_s e_{n_s} \bar{\mathbf{u}}] + \bar{\nabla} \cdot \bar{\mathbf{q}}_{n_s} = \dot{\rho}_s e_{n_s} + \rho_s \dot{e_{n_s}} \, . \tag{3.42b}$$

In summary, the governing partial differential equations for mixtures of thermally perfect gases out of chemical and thermal equilibrium have been developed from the Boltzmann equations using non-equilibrium kinetic theory. They are written below for a Cartesian Coordinate system as

$$\frac{\partial \mathbf{Q}}{\partial t} + \bar{\nabla} \cdot (\bar{\mathbf{S}} - \bar{\mathbf{S}}_v) = \mathbf{W} \,. \tag{3.43a}$$

where

$$\bar{\mathbf{S}} - \bar{\mathbf{S}}_v = (\mathbf{F} - \mathbf{F}_v)\hat{\mathbf{i}}_1 + (\mathbf{G} - \mathbf{G}_v)\hat{\mathbf{i}}_2 + (\mathbf{H} - \mathbf{H}_v)\hat{\mathbf{i}}_3 \,. \tag{3.43b}$$

The conserved variable vector $\mathbf{Q}$ and the chemical and thermal source term vector $\mathbf{W}$, are given as

$$\mathbf{Q} = \begin{pmatrix} \rho_1 \\ \rho_2 \\ \vdots \\ \rho_N \\ \rho u_1 \\ \rho u_2 \\ \rho u_3 \\ \rho_1 e_{n_1} \\ \vdots \\ \rho_M e_{n_M} \\ \rho e_0 \end{pmatrix} , \mathbf{W} = \begin{pmatrix} \omega_1 \\ \omega_2 \\ \vdots \\ \omega_N \\ \sum_s \rho_s < X_1 >_s \\ \sum_s \rho_s < X_2 >_s \\ \sum_s \rho_s < X_3 >_s \\ \rho_1 \dot{e}_{n_1} + \dot{\rho}_1 e_{n_1} \\ \vdots \\ \rho_M \dot{e}_{n_M} + \dot{\rho}_M e_{n_M} \\ \sum_s \rho_s < \bar{\mathbf{X}} \cdot \bar{\mathbf{c}} >_s \end{pmatrix} , \tag{3.44a,b}$$

and the inviscid flux vectors $\mathbf{F}$, $\mathbf{G}$, and $\mathbf{H}$ are

$$\mathbf{F} = \begin{pmatrix} \rho_1 u_1 \\ \rho_2 u_1 \\ \vdots \\ \rho_N u_1 \\ \rho {u_1}^2 + p \\ \rho u_1 u_2 \\ \rho u_1 u_3 \\ \rho_1 e_{n_1} u_1 \\ \vdots \\ \rho_M e_{n_M} u_1 \\ \rho u_1 h_0 \end{pmatrix} , \mathbf{G} = \begin{pmatrix} \rho_1 u_2 \\ \rho_2 u_2 \\ \vdots \\ \rho_N u_2 \\ \rho u_2 u_1 \\ \rho {u_2}^2 + p \\ \rho u_2 u_3 \\ \rho_1 e_{n_1} u_2 \\ \vdots \\ \rho_M e_{n_M} u_2 \\ \rho u_2 h_0 \end{pmatrix} , \mathbf{H} = \begin{pmatrix} \rho_1 u_3 \\ \rho_2 u_3 \\ \vdots \\ \rho_N u_3 \\ \rho u_3 u_1 \\ \rho u_3 u_2 \\ \rho {u_3}^2 + p \\ \rho_1 e_{n_1} u_3 \\ \vdots \\ \rho_M e_{n_M} u_3 \\ \rho u_3 h_0 \end{pmatrix} . \tag{3.45a,b,c}$$

The viscous flux vectors $\mathbf{F}_v$, $\mathbf{G}_v$, and $\mathbf{H}_v$ are

$$\mathbf{F}_v = \begin{pmatrix} -\rho_1(V_1)_1 \\ -\rho_2(V_1)_2 \\ \vdots \\ -\rho_N(V_1)_N \\ \tau_{11} \\ \tau_{12} \\ \tau_{13} \\ -(q_1)_{n_1} \\ \vdots \\ -(q_1)_{n_M} \\ -q_1 + \tau_{1i}u_i \end{pmatrix}, \mathbf{G}_v = \begin{pmatrix} -\rho_1(V_2)_1 \\ -\rho_2(V_2)_2 \\ \vdots \\ -\rho_N(V_2)_N \\ \tau_{21} \\ \tau_{22} \\ \tau_{23} \\ -(q_2)_{n_1} \\ \vdots \\ -(q_2)_{n_M} \\ -q_2 + \tau_{2i}u_i \end{pmatrix}, \mathbf{H}_v = \begin{pmatrix} -\rho_1(V_3)_1 \\ -\rho_2(V_3)_2 \\ \vdots \\ -\rho_N(V_3)_N \\ \tau_{31} \\ \tau_{32} \\ \tau_{33} \\ -(q_3)_{n_1} \\ \vdots \\ -(q_3)_{n_M} \\ -q_3 + \tau_{3i}u_i \end{pmatrix}. \qquad (3.46a, b, c)$$

The relations necessary to close inviscid system of equations have appeared previously, however, they are listed again here for completeness. The closure relations are

$$\rho = \sum_{s=1}^{N} \rho_s \,, \qquad (3.47)$$

$$p = \sum_{s=1}^{N} p_s = \sum_{s=1}^{N} \rho_s R_s T = \rho \tilde{R} T \,, \qquad (3.48)$$

$$e_0 = \frac{u_k u_k}{2} + e \,, \qquad (3.49)$$

$$h_0 = e_0 + \frac{p}{\rho} \,, \qquad (3.50)$$

and

$$e = \sum_{s=1}^{N} \frac{\rho_s}{\rho} \Big[\int_{Tref}^{T} \tilde{c}_{v_s}(\xi) d\xi + h_{f_s} \Big] + \sum_{s=1}^{M} \frac{\rho_s}{\rho} e_{n_s} \,, \qquad (3.51)$$

The relationship between pressure, Eq. (3.48), and internal energy, Eq. (3.51), is obtained implicitly through the temperature for a given conserved variable vector $\mathbf{Q}$.

The viscous flux vectors contain elements of the viscous shear-stress tensor, the heat-flux vector, and the diffusion velocity. These terms are the direct result of translational non-equilibrium and are defined as moments of the velocity distribution function. The necessary viscous closure relations have appeared previously

and are listed below for completeness. They are

$$\tau_{ik} = \sum_{s=1}^{N} (\tau_{ik})_s \,, \tag{3.52a}$$

$$(\sigma_{ik})_s = -\rho_s < c_i' c_k' >_s = (\tau_{ik})_s - p_s \, \delta_{ik} \,, \tag{3.52b}$$

$$q_i = \sum_{s=1}^{N} (q_i)_s \,, \tag{3.53a}$$

$$(q_i)_s = \rho_s < c_i' \epsilon >_s \,. \tag{3.53b}$$

$$(q_i)_{n_s} = \rho_s < c_i' \epsilon_n >_s \,, \tag{3.54}$$

and

$$(V_i)_s = < c_i' >_s \,. \tag{3.55}$$

The rigorous evaluation of these terms requires a solution of the Boltzmann equation for the velocity distribution function, f. The Boltzmann equation is difficult to solve for the general case and for the most part approximate methods are required for modeling these terms. This issue is considered in Chap. 5. For the assumption of local translational equilibrium, *i.e.*, $f = f_0$, the moments in Eqs. (3.52a)-(3.55) reduce identically to zero. For this case the viscous fluxes are zero and the governing equations reduce to the Euler equations for inviscid non-heat-conducting flows. In general, the Euler equations may be obtained as moments of the Boltzmann equation with a locally Maxwellian velocity distribution. This connection provides a means of obtaining upwind Euler schemes as moments of discretized Boltzmann schemes with a locally Maxwellian velocity distribution. This will be the topic of Chaps. 6 and 7.

3.3.1 Transformation to Generalized Coordinates

The governing differential equations have been developed for a Cartesian Coordinate system. For calculations over complex geometries it is common practice to

transform them from physical (x_1, x_2, x_3) space to a uniformly spaced computational grid (ξ, η, ζ) [70]. Mathematically the transformation is given as

$$\xi = \xi(x_1, x_2, x_3)$$

$$\eta = \eta(x_1, x_2, x_3)$$

$$\zeta = \zeta(x_1, x_2, x_3)\,, \tag{3.56}$$

where ξ,η,ζ represent a structured curvilinear coordinate system. Using the chain rule of partial differentiation for the space derivatives, the governing equations, Eq. (3.43a), may be rewritten in the (ξ, η, ζ) coordinate system as

$$\frac{1}{J}\frac{\partial \mathbf{Q}}{\partial t} + \frac{\partial}{\partial \xi}(\tilde{\mathbf{F}} - \tilde{\mathbf{F}}_v) + \frac{\partial}{\partial \eta}(\tilde{\mathbf{G}} - \tilde{\mathbf{G}}_v) + \frac{\partial}{\partial \zeta}(\tilde{\mathbf{H}} - \tilde{\mathbf{H}}_v) = \frac{1}{J}\mathbf{W}\,, \tag{3.57}$$

where

$$\tilde{\mathbf{F}} - \tilde{\mathbf{F}}_v = \frac{|\,\bar{\nabla}\xi\,|}{J}\bar{\nabla}\tilde{\xi}\cdot(\bar{\mathbf{S}} - \bar{\mathbf{S}}_v)\,, \tag{3.58a}$$

$$\tilde{\mathbf{G}} - \tilde{\mathbf{G}}_v = \frac{|\,\bar{\nabla}\eta\,|}{J}\bar{\nabla}\tilde{\eta}\cdot(\bar{\mathbf{S}} - \bar{\mathbf{S}}_v)\,, \tag{3.58b}$$

$$\tilde{\mathbf{H}} - \tilde{\mathbf{H}}_v = \frac{|\,\bar{\nabla}\zeta\,|}{J}\bar{\nabla}\tilde{\zeta}\cdot(\bar{\mathbf{S}} - \bar{\mathbf{S}}_v)\,, \tag{3.58c}$$

and J is the Jacobian of the transformation

$$J = \frac{\partial(\xi, \eta, \zeta)}{\partial(x_1, x_2, x_3)} = \mathrm{Det}\begin{pmatrix} \xi_{x_1} & \xi_{x_2} & \xi_{x_3} \\ \eta_{x_1} & \eta_{x_2} & \eta_{x_3} \\ \zeta_{x_1} & \zeta_{x_2} & \zeta_{x_3} \end{pmatrix}. \tag{3.59}$$

The vectors $\bar{\nabla}\tilde{\xi}$,$\bar{\nabla}\tilde{\eta}$,$\bar{\nabla}\tilde{\zeta}$, are the unit vectors normal to the transformed coordinate surfaces and are defined by

$$\bar{\nabla}\tilde{k} = \frac{\bar{\nabla}k}{|\,\bar{\nabla}k\,|} = \tilde{k}_{x_1}\mathbf{i}_1 + \tilde{k}_{x_2}\mathbf{i}_2 + \tilde{k}_{x_3}\mathbf{i}_3\,, \tag{3.60}$$

for $k = \xi,\ \eta,\ \zeta$ respectively. The contravariant velocity components in these directions are given as

$$\tilde{u}_1 = \bar{\mathbf{u}}\cdot\bar{\nabla}\tilde{\xi}\,, \tag{3.61a}$$

$$\tilde{u}_2 = \bar{\mathbf{u}}\cdot\bar{\nabla}\tilde{\eta}\,, \tag{3.61b}$$

$$\tilde{u}_3 = \bar{\mathbf{u}}\cdot\bar{\nabla}\tilde{\zeta}\,. \tag{3.61c}$$

For modeling the viscous, heat flux, and diffusion terms in Chap. 5, space derivatives with respect to x_1, x_2, and x_3, must be expanded according to the chain rule as

$$\frac{\partial(\cdot)}{\partial x_i} = \mid \bar{\nabla}\xi \mid \tilde{\xi}_{x_i}\frac{\partial(\cdot)}{\partial \xi} + \mid \bar{\nabla}\eta \mid \tilde{\eta}_{x_i}\frac{\partial(\cdot)}{\partial \eta} + \mid \bar{\nabla}\zeta \mid \tilde{\zeta}_{x_i}\frac{\partial(\cdot)}{\partial \zeta} \qquad i = 1,2,3\,. \tag{3.62}$$

In this Chapter, the governing differential equations appear in conservative form. The conservative form is important since it leads to numerical schemes that are consistent discretizations of the conservation law. That is, schemes in which internal fluxes cancel hence conserving total mass, momentum, and energy (*i.e.*, the "telescoping" property). This condition is necessary in order for the numerical scheme to obtain the correct jump relations through a discontinuity. It is noted, however, that the differential formulation is not strictly valid in the presence of discontinuities such as shock waves or slip lines because derivatives become ill-defined. Conservative finite-difference techniques, however, may be used to capture shocks since the discretized differential equations behave like the more general integral formulation of the governing equations for *weak* solutions [71]. The integral form will be considered in the following section.

3.3.2 Integral Form

The derivation of the governing equations could have proceeded from the more general integral form of the Boltzmann equation, where the conservation of molecules of velocity class $\bar{c}$ is written in terms of volume and surface integrals as

$$\begin{aligned}\frac{\partial}{\partial t}\iiint_{\delta V} n_s f_s dV + \oint_{\delta S} (\bar{c}\cdot\hat{n}) n_s f_s dS + \iiint_{\delta V}\frac{\partial}{\partial c_i}\{(X_i)_s n_s f_s\}dV \\ = \iiint_{\delta V}\sum_r \{\frac{\partial}{\partial t}(n_s f_s)\}_{coll_{r-s}} dV\,,\end{aligned} \tag{3.63}$$

where δV is an arbitrary volume bounded by the surface δS and $\hat{n}$ is an outward pointing unit normal vector. Moments lead to the following integral form of the

equation of transfer

$$\frac{\partial}{\partial t}\iiint_{\delta V} n_s < \psi >_s dV + \oint_{\delta S} n_s < \psi \bar{\mathbf{c}} >_s \cdot \hat{\mathbf{n}} dS - \iiint_{\delta V} n_s < X_i \frac{\partial \psi}{\partial c_i} >_s dV$$
$$= \iiint_{\delta V} \sum_r \{\frac{\partial}{\partial t}(n_s < \psi >_s)\}_{coll_{r-s}} dV \,. \tag{3.64}$$

Evaluating Eq. (3.64) for the elements of the moment function vector Ψ, Eq. (3.22), yields the integral form of the governing equations

$$\frac{\partial}{\partial t}\iiint_{\delta V} \mathbf{Q} dV + \oint_{\delta S} (\bar{\mathbf{S}} - \bar{\mathbf{S}}_v) \cdot \hat{\mathbf{n}} dS = \iiint_{\delta V} \mathbf{W} dV \,, \tag{3.65}$$

where $\bar{\mathbf{S}}$ is defined in Eq. (3.43b). The integral form of the governing equations is equivalent to the differential form in regions of smooth flow and is also valid across discontinuities where it reduces to the Rankine-Hugoniot jump conditions in the limit of a vanishing control volume. The integral form will be particularly useful when considering finite-volume discretization techniques. This is discussed in Chap. 6.

3.3.3 Quasi-One-Dimensional Approximation

In certain instances, the important features of complex flowfields may be determined while neglecting two and three-dimensional effects. This is typically accomplished by integrating the governing equations over two space dimensions, so that only one-dimensional effects in the remaining space dimension must be resolved [72]. Common applications of this procedure has been to nozzle and combustor analysis where the area is a smoothly varying function of only one space variable. The governing equations for this case may be written in the appropriate area-averaged variables, where $A = A(x_1)$, as follows

$$\frac{\partial \mathbf{Q}}{\partial t} + \frac{\partial}{\partial x_1}(\mathbf{F} - \mathbf{F}_v) = \mathbf{W} + \mathbf{W}_A \,. \tag{3.66}$$

where the conserved variable vector $\mathbf{Q}$, the chemical and thermal source term vector $\mathbf{W}$ and the area source term $\mathbf{W}_A$ are given as

$$\mathbf{Q} = \begin{pmatrix} \rho_1 \\ \rho_2 \\ \vdots \\ \rho_N \\ \rho u_1 \\ \rho_1 e_{n_1} \\ \vdots \\ \rho_M e_{n_M} \\ \rho e_0 \end{pmatrix}, \mathbf{W} = \begin{pmatrix} \omega_1 \\ \omega_2 \\ \vdots \\ \omega_N \\ \sum_s \rho_s < X_1 >_s \\ \rho_1 \dot{e}_{n_1} + \dot{\rho}_1 e_{n_1} \\ \vdots \\ \rho_M \dot{e}_{n_M} + \dot{\rho}_M e_{n_M} \\ \sum_s \rho_s < \bar{\mathbf{X}} \cdot \bar{\mathbf{c}} >_s \end{pmatrix}, \mathbf{W}_A = -\frac{u_1}{A}\frac{dA}{dx_1} \begin{pmatrix} \rho_1 \\ \rho_2 \\ \vdots \\ \rho_N \\ \rho u_1 \\ \rho_1 e_{n_1} \\ \vdots \\ \rho_M e_{n_M} \\ \rho h_0 \end{pmatrix}. \qquad (3.67a, b, c)$$

The inviscid and viscous flux vectors, $\mathbf{F}$ and $\mathbf{F}_v$ are given as

$$\mathbf{F} = \begin{pmatrix} \rho_1 u_1 \\ \rho_2 u_1 \\ \vdots \\ \rho_N u_1 \\ \rho {u_1}^2 + p \\ \rho_1 e_{n_1} u_1 \\ \vdots \\ \rho_M e_{n_M} u_1 \\ \rho u_1 h_0 \end{pmatrix}, \mathbf{F}_v = \begin{pmatrix} -\rho_1 (V_1)_1 \\ -\rho_2 (V_1)_2 \\ \vdots \\ -\rho_N (V_1)_N \\ \tau_{11} \\ -(q_1)_{n_1} \\ \vdots \\ -(q_1)_{n_M} \\ -q_1 + \tau_{11} u_1 \end{pmatrix}, \qquad (3.68a, b)$$

where only the viscous terms in the x_1 direction have been included. It is noted that $\mathbf{F}_v$ is not appropriate for modeling wall viscous effects since only variations in the streamwise direction are considered. In general, these wall viscous effects cannot be easily evaluated for the quasi-one-dimensional approach and typically only inviscid calculations are performed. For the normal shock calculations in Chap. 5, Eq. (3.66) will be used without the area source term. For these calculations the streamwise viscous flux vector $\mathbf{F}_v$ becomes important and must be modeled correctly to accurately predict the shock-wave structure.

Chapter 4

Modeling of the Source Terms

4.1 Introduction

The high temperatures and large flow gradients brought on either by combustion processes or by high speeds of flight result in finite-rate chemical and energy exchange phenomena. Flows in chemical and thermal non-equilibrium require additional rate equations for species and non-equilibrium internal energy production that must be solved in conjunction with the gas-dynamic equations. The species mass conservation equations, Eqs. (3.25a) and (3.25b), contain chemical source terms ω_s that must be modeled. Likewise, the species non-equilibrium energy equations, Eqs. (3.42a) and (3.42b), contain the chemical source terms as well as non-equilibrium internal energy source terms $\rho\dot{e}_{n_s}$ (due to various energy exchange phenomena) that also require modeling.

4.2 Chemical Source Terms

The general framework for the chemical system of N species and J reactions was established in Sec. 2.4, and the species production rates ω_s were given in terms of the forward reaction rates $K_{f,j}$ and the equilibrium constants $K_{e,j}$ in Eq. (2.29). In this work two specific chemistry models are considered; a simple high temperature air chemistry model and a hydrogen-air combustion model.

4.2.1 Simple Air Chemistry Model

The simple air chemistry model considers five species N_2, O_2, NO, N, and O,

and five basic reactions

$$N_2 + M \rightleftharpoons 2N + M$$

$$O_2 + M \rightleftharpoons 2O + M$$

$$NO + M \rightleftharpoons N + O + M$$

$$N_2 + O \rightleftharpoons NO + N$$

$$NO + O \rightleftharpoons O_2 + N\,, \tag{4.1}$$

where M is a catalytic particle and may be any of the species present. The first three basic reactions listed above represent dissociation-recombination processes and account for 15 separate reactions. The last two reactions are rearrangement or "shuffle" reactions. This model is adequate for gas-dynamic simulations up to about 8000 ^0K, however, it is noted that the ionization of NO occurs at about 5000 ^0K and must be modeled if electromagnetic considerations are important. The forward reaction rates are given in Kang and Dunn [73] and are fit according to the general Arrhenius Law form [9]

$$K_{f,j} = c_{f,j} T^{\eta_{f,j}} e^{-\epsilon_{f,j}/T} \qquad j = 1, 2, ..., J\,. \tag{4.2}$$

The equilibrium constants are taken from Vincenti and Kruger [9] and are modeled according to

$$K_{c,j} = c_{c,j} T^{\eta_{c,j}} e^{-\epsilon_{c,j}/T} \qquad j = 1, 2, ..., J\,, \tag{4.3}$$

where the coefficients have been obtained to give the best fit of the partition function results. The temperature T in these equations is taken to be the translational temperature.

4.2.2 Hydrogen-Air Combustion Model

The hydrogen-air combustion model used in this work considers seven species, N_2, O_2, H_2, OH, H_2O, O, and H, and seven reactions

$$
\begin{aligned}
O_2 + H_2 &\rightleftharpoons OH + OH \\
O_2 + H &\rightleftharpoons OH + O \\
H_2 + OH &\rightleftharpoons H_2O + H \\
H_2 + O &\rightleftharpoons OH + H \\
OH + OH &\rightleftharpoons H_2O + O \\
OH + H + N_2 &\rightleftharpoons H_2O + N_2 \\
H + H + N_2 &\rightleftharpoons H_2 + N_2 \,,
\end{aligned}
\tag{4.4}
$$

The forward reaction rates follow the same form as Eq. (4.2) and the constants are given in Drummond, Rogers and Hussaini [20]. The equilibrium constants are determined as

$$
K_{e,j} = \left(\frac{f_c}{\hat{R}T}\right)^{\Delta\hat{\eta}_j} e^{-\Delta g_j^0/\hat{R}T} \,, \tag{4.5}
$$

where $\Delta\hat{\eta}_j$ represents the net change in moles in going from reactants to products for the jth reaction

$$
\Delta\hat{\eta}_j = \sum_{s=1}^{N} (\nu''_{s,j} - \nu'_{s,j}) \,, \tag{4.6}
$$

and Δg_j^0 is the change in Gibbs free energy at constant pressure

$$
\Delta g_j^0 = \sum_{s=1}^{N} (\nu''_{s,j} - \nu'_{s,j}) g_s^0 \,. \tag{4.7}
$$

The Gibbs free energy is obtained from the "new" LeRC curve fits as

$$
\begin{aligned}
\frac{g_s^0}{\hat{R}} = &-\frac{a_{1,s}}{2T} + a_{2,s}(1 + lnT) + a_{3,s}T(1 - lnT) - a_{4,s}\frac{T^2}{2} \\
&- a_{5,s}\frac{T^3}{6} - a_{6,s}\frac{T^4}{12} - a_{7,s}\frac{T^5}{20} + a_{9,s} - a_{10,s}T \,.
\end{aligned}
\tag{4.8}
$$

4.3 Thermal Source Terms

For temperatures greater than several thousand degrees K the vibrational modes become active and vibrational non-equilibrium must be considered along with the chemistry [64]. Vibrational effects tend to be important because of the relatively large characteristic relaxation time associated with the vibrational mode. Comparisons of numerical data with experimental results suggest the importance of modeling these vibrational effects properly [74].

Rotational non-equilibrium effects become important in modeling hypersonic shock structure in the continuum transition regime where shock thicknesses are no longer negligible. Here, the energy exchange between the rotational and translational modes causes the peak temperature to occur within the shock wave. Correct modeling of this energy exchange phenomena is tantamount for obtaining accurate predictions for radiative heating [36].

In this work vibrational/translational energy exchanges will be modeled using Landau-Teller theory in conjunction with the vibrational non-equilibrium model given in Eq. (2.23). A similar Landau-Teller relaxation model will be used with the rotational non-equilibrium model given in Eq. (2.24) for rotational/translational energy exchanges.

4.3.1 Vibrational Non-Equilibrium Model

The collisional exchange of vibrational and translational energy through inelastic collisions is usually treated by considering a system of harmonic oscillators [9]. The assumption of weak interactions, *i.e.*, collisions produce quantum jumps of only one energy state, leads to the Landau-Teller model for vibrational relaxation [9]. No attempt has been made to take into account the inhomogeneity of the fluid element, due to the presence of other species, and the preferential removal of vibra-

tional energy through dissociation is not considered. The Landau-Teller relaxation model is given as

$$\rho_s \dot{e}_{vib_s} = \rho_s \frac{e_{vib_s}{}^*(T) - e_{vib_s}}{\tau_s} \qquad s = 1, 2, ..., M, \tag{4.9}$$

where $e_{vib}{}^*$ is the equilibrium vibrational energy, given in Eq. (2.20a), at the translational temperature T, and τ is the relaxation time given by Millikan and White [75]

$$\tau_s = \frac{1.013\text{x}10^5}{p} e^{[A_s(T^{-1/3} - 0.015B_s^{1/4}) - 18.42]}, \tag{4.10}$$

where

$$A_s = 1.16\text{x}10^{-3} B_s^{1/2} \theta_{vib_s}{}^{4/3}, \tag{4.11}$$

and

$$B_s = \frac{\hat{m}_s \hat{m}_s}{\hat{m}_s + \hat{m}_s} = \frac{\hat{m}_s}{2}, \tag{4.12}$$

where θ_{vib_s} is the characteristic vibrational temperature [9].

The Landau-Teller model has been developed under relatively restrictive assumptions that are not necessarily valid for hypersonic flows [46]. More sophisticated models have been proposed that allow quantum jumps of more than one energy state [37,63,64] as well as the preferential removal of highly excited vibrational states through dissociation [60–65]. Only simple Landau-Teller theory is used in the present work in an attempt to capture only some of the physics involved.

4.3.1 Rotational Non-Equilibrium Model

For cases where the relaxation time for rotation is significant and large deviations from rotational equilibrium occur (termed *difficult exchange*) an additional equation describing the relaxation of rotational energy is necessary. Again a Landau-Teller type model is used [46,47]

$$\rho_s \dot{e}_{rot_s} = \rho_s \frac{e_{rot_s}{}^*(T) - e_{rot_s}}{Z_{r_s} \tau_c} \qquad s = 1, 2, ..., M. \tag{4.13}$$

Here, $\hat{e}_{rot}$ is the equilibrium rotational energy at the translational temperature given by Eq. (2.19a). The value Z_r is known as the rotational collision number and the functional form is given as [46]

$$Z_r = Z_r^{\infty} / \left[1. + \frac{\pi^{3/2}}{2} (\frac{T^*}{T})^{1/2} + (\frac{\pi^2}{4} + \pi)(\frac{T^*}{T}) \right] . \tag{4.14}$$

The mean collision time τ_c is taken as that for a hard sphere molecule, following the work of Ref. [46]

$$\tau_c = \frac{\pi \mu}{4p} . \tag{4.15}$$

The effect of more realistic gases enters through the viscosity μ.

Although the assumptions used to derive the Landau-Teller model are probably violated for hypersonic flows, good shock profiles for diatomic nitrogen have been obtained for very high Mach numbers by adjusting the parameters Z_r^{∞} and T^* as suggested in Ref. [46].

Chapter 5

Modeling of Viscous Terms

5.1 Introduction

In Chap. 3 a molecular analysis was used to obtain the general macroscopic conservation equations that govern the motion of gas mixtures in chemical and thermal non-equilibrium. These equations along with the appropriate equations of state (relating p, T, and e) are not sufficient to close the system of equations. Additional moments of the velocity distribution function that represent components of the stress tensor σ_{ik}, the heat-flux vector q_i, the species non-equilibrium heat-flux vectors $(q_i)_{n_s}$, and the species diffusion velocities $(V_i)_s$, must be resolved. These moments are defined by Eqs. (3.52a)-(3.55) and correspond to the molecular transport of momentum, energy, and chemical species respectively. They are a direct result of translational non-equilibrium and therefore depend on the collisional processes between molecules [9].

Rigorous evaluation of these moments requires a solution of the Boltzmann equations, Eq. (3.19), for the velocity distribution function f. Unfortunately this equation is difficult to solve for the general case, largely because of the nonlinear nature of the collision integral, and approximate methods are required [9]. One such method, the Chapman-Enskog (C-E) expansion [39], is an expansion of the velocity distribution function about the Maxwellian distribution for local translational equilibrium

$$f = f_o(1 + \xi\phi_1 + \xi^2\phi_2 + \dots\ ), \tag{5.1}$$

where ξ is the Kudsen number given by

$$\xi = \lambda / L \,, \tag{5.2}$$

and λ represents the molecular mean free path and L is a characteristic length. The Knudsen number gives a measure of the degree of departure from local translational equilibrium [9]. The zeroth-order solution ($\xi \to 0$) corresponds to local translational equilibrium and the governing equations reduce to the Euler equations for inviscid non-heat-conducting flows. The constitutive relations corresponding to the Navier-Stokes equations are obtained by retaining first-order terms in ξ. For this reason the Navier-Stokes equations are valid only for small departures from local translational equilibrium. By substituting the truncated form of Eq. (5.1) into the Boltzmann equation an expression for ϕ_1 may be obtained in terms of Sonine polynomials as in Vincenti and Kruger [9]. The form of the shear-stress tensor, heat-flux vectors, and diffusion velocities may now be obtained as moments with respect to the truncated series representation for f, *i.e.*, $f = f_o(1+\xi\phi_1)$. To determine the associated transport properties (*i.e.*, the coefficients of viscosity, thermal conductivity, diffusion, *etc.*) further "collision integrals" must be evaluated based on an accurate representation of the intermolecular force field [9,51,58]. Typically, a spherically symmetric, conservative force field is assumed and is given in terms of an intermolecular potential $V(r)$, where r is the distance between the molecular centers for a binary collision [9,51]. The intermolecular force is then given as

$$F(r) = -\frac{dV}{dr} \,. \tag{5.3}$$

Results have been obtained for the simple hard-sphere potential as well as for an inverse-radius potential given as

$$V = \frac{\kappa}{r^{\eta}} \,. \tag{5.4a}$$

The intermolecular force for this case is

$$F = \eta \frac{\kappa}{r^{\eta+1}}\,, \tag{5.4b}$$

and the parameters κ and η can be adjusted to fit experimental data. The most successful potential has been the Lennard-Jones potential [68] that models both repulsion and attraction

$$V = 4\beta_{ew}\left[\left(\frac{r_0}{r}\right)^{12} - \left(\frac{r_0}{r}\right)^{6}\right]. \tag{5.5}$$

Here, r_0 is the distance where V is zero, and again two parameters are available for adjustment to experimental data. It is noted that the use of conservative force fields implies that all collisions are elastic. This is certainly not always the case for polyatomic molecules since inelastic collisions may occur whereby energy is exchanged between the translational and internal degrees of freedom. Hence, intermolecular potentials are strictly valid *only* for monatomic molecules. Methods have been developed to account for inelastic collisions within C-E theory, however, they are very mathematically involved [58]. Except for very near or within shock waves, elastic collisions tend to dominate inelastic ones, and potential fields have been used to successfully predict coefficients of viscosity and diffusion for polyatomic molecules [51]. Thermal conductivities for polyatomic molecules are not accurately predicted using monatomic theory [9].

Chapman-Enskog theory has been successfully applied to mixtures of monatomic gases, however, again the results are extremely involved and expensive to carry out computationally [58,59]. Typically curve fits or single-component C-E theory are used in conjunction with semi-empirical mixture rules. Second-order C-E theory leads to the Burnett equations which are valid for larger departures from local translational equilibrium [39]. Here, the same continuum form of the governing equations is maintained and only new higher-order constitutive relations are intro-

duced.

In the following Sections some of the results of C-E theory will presented and the simplifications, in terms of curve fits and semi-empirical rules, that are necessary for efficient yet meaningful calculations, will be described.

5.2 Navier-Stokes Equations

5.2.1 Shear Stress Tensor

First-order C-E theory for a single monatomic gas predicts a viscous shear stress tensor with elements given by [9]

$$\tau_{ik} = \mu(\frac{\partial u_i}{\partial x_k} + \frac{\partial u_k}{\partial x_i} - \frac{2}{3}\frac{\partial u_j}{\partial x_j}\delta_{ik}) . \tag{5.6}$$

Single-component C-E theory has been used to obtain very accurate formulas for the species coefficient of viscosity μ_s for monatomic gases [51,58]. The results are in terms of collision integrals which have been tabulated versus non-dimensional temperature for various intermolecular potentials [39,58,76]. Alternatively, species viscosities may be determined using curve fits and semi-empirical laws. This procedure reduces the CPU time otherwise necessary for the analytical expressions. In the present work both the Blottner curve fits and an extended Sutherland type law are used. The Blottner curve fits [77] are given in the form

$$\mu_s = e^{[(A_s lnT + B_s)lnT + C_s]} , \tag{5.7}$$

where A_s, B_s, and C_s are chosen to best fit experimental data. The Sutherland law is given as

$$\mu_s = T^{3/2}\frac{E_s}{T + F_s} , \tag{5.8}$$

where again E_s and F_s are determined to best fit experimental data. Values for E_s and F_s have been tabulated Refs. [76,78].

Application of C-E theory to multi-component mixtures of monatomic gases has been carried out but leads to very severe mathematical problems [58,59]. The same form as Eq. (5.6) is obtained, however calculations for the mixture viscosity μ involves determinants of matrices of collision integrals. Typically, single-component C-E theory or curve fits are used to determine the species viscosities and the mixture viscosity is obtained using semi-empirical mixture rules. In the present work the mixture viscosity is determined from the species viscosities using Wilke's law [79] which was developed from kinetic theory and several simplifying assumptions. The result is

$$\mu = \sum_{s=1}^{N} \frac{\chi_s \mu_s}{\sum_l^N \chi_l \phi_{sl}}, \tag{5.9a}$$

where

$$\phi_{sl} = \frac{1}{\sqrt{8}}(1 + \frac{\hat{m}_s}{\hat{m}_l})^{-1/2}[1 + \sqrt{\frac{\mu_s}{\mu_l}}(\frac{\hat{m}_l}{\hat{m}_s})^{1/4}]^2, \tag{5.9b}$$

and χ_s is the mole fraction for species s.

First-Order C-E theory for polyatomic gases predicts a viscous shear stress tensor with elements given as follows

$$\tau_{ik} = \mu(\frac{\partial u_i}{\partial x_k} + \frac{\partial u_k}{\partial x_i} - \frac{2}{3}\frac{\partial u_j}{\partial x_j}\delta_{ik}) + \mu_b \frac{\partial u_j}{\partial x_j}\delta_{ik}. \tag{5.10}$$

where μ_b is known as the bulk viscosity. Wang Chang and Uhlenbeck [47] were the first to carry out the C-E procedure allowing for inelastic collisions. Treatment of the viscosity μ using a multi-component C-E theory that allows for internal degrees of freedom would be extremely complex. Typically, the mixture viscosity is determined using the methods previously discussed (*i.e.*, single component C-E theory or curve fits used in conjunction with mixture rules). Although reasonable species viscosities for polyatomic gases have been obtained using monatomic C-E theory, curve fits based on experimental data should represent a more consistent

formulation, however, even these may become ill-defined in the presence of large amounts of thermal non-equilibrium.

The bulk-viscosity term is associated with the redistribution of energy between the translational and internal degrees of freedom [51]. Physically, it represents the resistance of the fluid to transfer its translational energy to the internal modes and vice-versa. It is important to note that the bulk viscosity is strictly valid only for small relaxation times (*i.e.*, easy energy exchange) so that the internal modes can be assumed "essentially" in equilibrium at the translational temperature T. For this reason the bulk-viscosity formulation is not suitable for modeling vibrational relaxation and generally an explicit vibrational non-equilibrium model is necessary. Usually the bulk viscosity is associated with rotational non-equilibrium when small departures from rotational equilibrium are present. For larger departures from equilibrium, *e.g.*, the interior of a shock wave, the bulk viscosity should be taken as zero and an explicit rotational non-equilibrium model must be used. It is important to note that bulk-viscosity effects tend to be important only in compressions or expansions since the bulk viscosity is multiplied by the divergence of the velocity in Eq. (5.10).

5.2.1.1 Bulk-Viscosity Model

A simple bulk-viscosity model for rotational non-equilibrium may be derived based on the theory put forth by Goldstein [50]. The derivation is carried out for a single-component gas (for simplicity) where the energy exchange between the translational and rotational modes occurs freely (*i.e.*, τ_{rot} is sufficiently small). The stress tensor components given by (3.28c) become

$$\begin{aligned}\sigma_{ik} &= -\rho < c_i' c_k' >= \tau_{ik} - \tilde{p}\,\delta_{ik} \\ &= \mu\left(\frac{\partial u_i}{\partial x_k} + \frac{\partial u_k}{\partial x_i} - \frac{2}{3}\frac{\partial u_j}{\partial x_j}\delta_{ik}\right) + \mu_b \frac{\partial u_j}{\partial x_j}\delta_{ik} - \tilde{p}\delta_{ik}\,, \end{aligned} \tag{5.11}$$

where Eq. (5.10) has been used. Here, $\tilde{p}$ represents the pressure corresponding to the rotational mode in equilibrium at the translational temperature T. The trace of the stress tensor (*i.e.*, $\sigma_{ii}/3$) is related to the kinetic pressure p, defined in Eq. (3.7), as follows

$$-\frac{\sigma_{ii}}{3} = p = \tilde{p} - \mu_b \frac{\partial u_j}{\partial x_j}. \tag{5.12}$$

It is noted that the kinetic pressure is valid for non-equilibrium situations. The pressures in Eq. (5.12) may be related to mean translational energies using Eq. (3.10) and gives

$$\frac{2}{3}\rho e_{tr} = \frac{2}{3}\rho \tilde{e}_{tr} - \mu_b \frac{\partial u_j}{\partial x_j}, \tag{5.13}$$

where again $\tilde{e}_{tr}$ is the translational energy corresponding to the rotational mode in equilibrium at the translational temperature. It now becomes apparent that the bulk viscosity is a relaxation phenomenon resulting from the lag in adjustment to equilibrium of the rotational mode. For example, when a gas is compressed there will be a net increase in the internal energy e. Initially, this increase will will be realized entirely by the translational mode (fast mode) resulting in higher kinetic energies and hence higher kinetic temperatures and pressures. At this time a relaxation process begins whereby some of the kinetic energy of thermal translation is imparted to the rotational mode through inelastic collisions. This process works to lower the kinetic pressure and temperature, and after some time on the order of τ_{rot} the rotational mode reaches an equilibrium distribution at the translational temperature T. Thus, the effect of rotational non-equilibrium is to produce kinetic pressures and temperatures that are higher (for compressions) than would be realized if the rotational mode maintained an equilibrium distribution at T. The effect is just the opposite for expansions. This process is consistent with Eqs. (5.12) and (5.13) since for a compression $\partial u_j/\partial x_j < 0$ and a correction term proportional to μ_b

is added to the kinetic pressure. Again, the opposite is true for expansions.

An expression for the bulk viscosity may be developed by considering a small fluid element of volume δV that is undergoing an expansion or compression [50]. It is assumed that the gas has an initial internal energy denoted by e^1. For the case where the internal energy consists of only the rotational and translational modes in equilibrium at the translational temperature T, the energies are partitioned as $\tilde{e}^1_{tr} = 3/5e^1$ and $\tilde{e}^1_{rot} = 2/5e^1$. If only the work done by pressure forces is taken into account the change in internal energy in a short time t^* is given as

$$\Delta e = -\frac{p}{\rho}\frac{\partial u_j}{\partial x_j}t^*\,, \tag{5.14}$$

and assuming that equilibrium distributions are maintained the during the change in energy, the translational and rotational energies at the new state ($\tilde{e}^2_{tr}$ and $\tilde{e}^2_{rot}$ respectively) are given by

$$\tilde{e}^2_{tr} = \frac{3}{5}e^1 + \frac{3}{5}\Delta e\,, \tag{5.15a}$$

and

$$\tilde{e}^2_{rot} = \frac{2}{5}e^1 + \frac{2}{5}\Delta e\,. \tag{5.15b}$$

However, when there is a lag in the rotational mode the entire change in energy should initially go into the translational mode and the actual change in translational energy is given by

$$\begin{aligned} e^2_{tr} &= \frac{3}{5}e^1 + \frac{3}{5}\Delta e + \frac{2}{5}\Delta e \\ &= \tilde{e}^2_{tr} + \frac{2}{5}\Delta e\,, \end{aligned} \tag{5.16}$$

leading to the relation

$$e_{tr} = \tilde{e}_{tr} - \frac{2}{5}\frac{p}{\rho}\frac{\partial u_j}{\partial x_j}t^*\,. \tag{5.17}$$

In comparison with Eq. (5.13) it follows that

$$\mu_B = \frac{4}{15} p t^* . \tag{5.18}$$

Goldstein [50] has shown that t^* is approximately the relaxation time for rotation τ_r and is taken as

$$t^* = \tau_r = Z_r \tau_c . \tag{5.19}$$

The relaxation time may be calculated using Eqs. (4.14) and (4.15). In the present work adjusted parameters for Z_r^∞ and T^* are used, as suggested in Ref. [46].

The bulk-viscosity model will be used in Chap. 8 for the hypersonic shock structure calculations (where it is not strictly valid) where it will be compared with the rotational non-equilibrium model described in Sec. 4.3.1 . For all other calculations the bulk viscosity is neglected.

5.2.2 Diffusion Velocities

Multi-component C-E theory for monatomic gases gives the diffusion velocity components $(V_i)_s$ implicitly as a driving force for the concentration gradients as follows [51]

$$\begin{aligned} \frac{\partial \chi_s}{\partial x_i} = & \sum_{l=1}^{N} \frac{\chi_s \chi_l}{D_{sl}} [(V_i)_l - (V_i)_s] + (\frac{\rho_s}{\rho} - \chi_s) \frac{1}{p} \frac{\partial p}{\partial x_i} \\ & + \frac{\rho}{p} \sum_{l=1}^{N} \frac{\rho_s}{\rho} \frac{\rho_l}{\rho} [(X_i)_s - (X_i)_l] \\ & + \sum_{l=1}^{N} \frac{\chi_s \chi_l}{\rho D_{sl}} [\frac{D_{T_l}}{\rho_l/\rho} - \frac{D_{T_s}}{\rho_s/\rho}] \frac{1}{T} \frac{\partial T}{\partial x_i} \qquad s = 1, 2, ..., N , \end{aligned} \tag{5.20}$$

where χ_s are the species mole fractions, D_{sl} are the binary diffusion coefficients, $(X_i)_s$ are the body force components as introduced in Eq. (3.19), and D_{T_s} are the thermal diffusion coefficients. The contributions to the concentration gradients on the right-hand side of Eq. (5.20) are due to molecular diffusion, pressure gradients, body forces, and to thermal diffusion (the Soret effect) respectively. The binary

diffusion terms have been rigorously determined for multi-component mixtures of monatomic gases using C-E theory [58,59], but again the formulation is extremely complex and in terms determinants of matrices. Using this theoretical approach D_{sl} is effectively determined while considering collisions between all species present. The usual simplification is to approximate D_{sl} with results for binary mixtures and neglect the presence of other species. Effectively, a binary mixture is considered for each species pairing in the original multi-component system. C-E theory for binary mixtures gives [39,58]

$$D_{sl} = .001858\left[\frac{\hat{m}_s + \hat{m}_l}{\hat{m}_s \hat{m}_l}\right]^{1/2} \frac{T^{3/2}}{p\, d_{sl}^2 \Omega_D}\,. \tag{5.21}$$

Here, Ω_D is the diffusion collision integral and can be approximated by

$$\Omega_D = T^{*-0.145} + (T^* + 0.5)^{-2}\,, \tag{5.22}$$

where $T^* = T/T_{\epsilon_{sl}}$. Values for the effective temperature T_ϵ and the effective collision diameter d_{sl} are taken as averages of the separate species properties [78]

$$d_{sl} = \frac{1}{2}(d_s + d_l)\,, \tag{5.23a}$$

and

$$T_{\epsilon_{sl}} = (T_{\epsilon_s} T_{\epsilon_l})^{1/2}\,. \tag{5.23b}$$

This procedure has been used by Drummond, Rogers, and Hussaini [20].

The thermal diffusion coefficients are also predicted by C-E theory but are typically very small and may be neglected in the calculation of $(V_i)_s$ as suggested in Ref. [80]. At this point, a system of N equations given by Eq. (5.20) may be solved implicitly for each component of the species diffusion velocities. It is noted that this system is not linearly independent and one of the equations must be replaced by the constraint

$$\sum_{s=1}^{N} \rho_s (V_i)_s \equiv 0\,, \tag{5.24}$$

as given in Eq. (3.6).

To avoid solving the system given in Eq. (5.20) further approximations may be considered. If the pressure diffusion terms, the body forces, and the thermal diffusion terms are negligible the system reduces to the Stefan-Maxwell equation [51]

$$\frac{\partial \chi_s}{\partial x_i} = \sum_{l=1}^{N} \frac{\chi_s \chi_l}{D_{sl}} [(V_i)_l - (V_i)_s] \qquad s = 1, 2, ..., N, \tag{5.25}$$

If it is further assumed the mixture behaves like a binary mixture, writing the two Stefan-Maxwell equations yields Fick's law of diffusion given by

$$\rho_s (V_i)_s = -\rho D_s \frac{\partial}{\partial x_i} \left(\frac{\rho_s}{\rho}\right) \qquad s = 1, 2, ..., N. \tag{5.26}$$

Again Eq. (5.24) must be satisfied and the diffusion coefficients cannot be fixed independently of one another. In the present work Fick's law has been used and the diffusion coefficients are obtained using a constant Lewis number Le

$$D_s = D = \frac{Lek}{\rho \tilde{c}_p} \qquad s = 1, 2, ..., N. \tag{5.27}$$

This model satisfies Eq. (5.24) trivially.

Rigorous treatment of diffusion that allows for internal degree of freedom is extremely complex. For most problems, reasonable results are obtained using monatomic theory [9].

5.2.2 Heat-Flux Vector

First-order C-E theory for a single monatomic gas predicts a heat flux vector with components given as

$$q_i = -k \frac{\partial T}{\partial x_i}. \tag{5.28}$$

Again, single-component C-E theory has been used to predict the species coefficient of thermal conductivity k_s for a monatomic gas [51]. The result of this analysis is

$$k_s = \frac{5}{2} \mu_s \tilde{c}_{v_s}, \tag{5.29}$$

where $\tilde{c}_{v_s} = 3/2R_s$ for a monatomic gas.

For multi-component mixtures of monatomic gases C-E theory predicts a heat flux vector as follows [51]

$$q_i = -k\frac{\partial T}{\partial x_i} + \sum_{s=1}^{N} \rho_s h_s (V_i)_s + \sum_{s=1}^{N}\sum_{l=1}^{N} \frac{\chi_l D_{T_s}}{\hat{m}_s D_{sl}}[(V_i)_s - (V_i)_l]\,. \tag{5.30}$$

The terms on the right-hand side represent the thermal conduction, the transport of enthalpy through species diffusion, and the Dufour effect, where heat is transferred proportionally to differences in diffusion velocities $(V_i)_s$. The Dufour effect is generally a second-order effect and is typically ignored. Mixture values for thermal conductivity have been rigorously treated using multi-component C-E theory for monatomic gases, again this is very mathematically involved [58].

For polyatomic molecules, the transport of internal energy must be accounted for in addition to the transport of translational energy. A rigorous treatment of of thermal conduction including internal degrees of freedom has not been successfully carried out [51,81]. Equation (5.30) may be extended to flows with thermal non-equilibrium by adding similar contributions from the non-equilibrium temperatures as follows

$$q_i = -k\frac{\partial T}{\partial x_i} - \sum_{s=1}^{M} k_{n_s}\frac{\partial T_{n_s}}{\partial x_i} + \sum_{s=1}^{N} \rho_s h_s (V_i)_s + \sum_{s=1}^{N}\sum_{l=1}^{N} \frac{\chi_l D_{T_s}}{\hat{m}_s D_{sl}}[(V_i)_s - (V_i)_l]\,. \tag{5.31}$$

In the present work the thermal diffusion terms have been neglected. Reasonable values for species thermal conductivities may be obtained from Euken's relation which is a generalization of Eq. (5.29) that includes internal energy contributions as follows

$$k_s = k_{tr_s} + k_{int_s}\,, \tag{5.32a}$$

where

$$k_{tr_s} = \frac{5}{2}\mu_s \tilde{c}_{v_{tr_s}}\,, \tag{5.32b}$$

and

$$k_{int_s} = \mu_s(\tilde{c}_{v_s} - \tilde{c}_{v_{tr_s}})\,. \tag{5.32c}$$

The final result becomes

$$k_s = \mu_s(\frac{3}{2}\tilde{c}_{v_{tr_s}} + \tilde{c}_{v_s})\,, \tag{5.32d}$$

where $\tilde{c}_{v_s}$ represents the contribution of the specific heat at constant volume at the translational temperature. The species thermal conductivities may also be obtained from a Sutherland type curve fit given as

$$k_s = T^{3/2}\frac{E'_s}{T + F'_s}\,, \tag{5.33}$$

where again E'_s and F'_s are determined to best fit experimental data. Values for these constants have been tabulated in Refs. [76,78]. Both Euken and Sutherland models have been used in the present work. Mixture values for the thermal conductivity may be obtained by using a Wilke's type rule as follows

$$k = \sum_{s=1}^{N}\frac{\chi_s k_s}{\sum_l^N \chi_l \phi_{sl}}\,, \tag{5.34a}$$

where

$$\phi_{sl} = \frac{1}{\sqrt{8}}(1 + \frac{\hat{m}_s}{\hat{m}_l})^{-1/2}[1 + \sqrt{\frac{\mu_s}{\mu_l}}(\frac{\hat{m}_l}{\hat{m}_s})^{1/4}]^2\,. \tag{5.34b}$$

Similar mixture rules are found in Refs. [20,51,81]. A very simplified approach for obtaining the mixture thermal conductivity is to assume a constant Prandtl number Pr. For this case the individual species conductivities need not be considered, and the result is given as

$$k = \frac{\mu\tilde{c}_p}{Pr}\,. \tag{5.35}$$

The non-equilibrium thermal conductivities k_{n_s} are treated by using a Euken type relation

$$k_{n_s} = \mu_s c_{v_{n_s}}\,, \tag{5.36}$$

where $c_{v_{n_s}}$ is approximated using the fully-excited value. For vibrational energy, the fully excited values are $c_{v_{vib_s}} = R_s$ for diatomic molecules and $c_{v_{vib_s}} = 3R_s$ for H_2O. The fully-excited values for rotation are given in Eq. (2.19b).

5.3 Burnett Equations

When second-order terms in ξ are retained C-E theory leads to the Burnett equations [39]. These equations should be more accurate for flows with large deviations from translational equilibrium and will allow meaningful calculations in the continuum transition regime. The Burnett equations have the same continuum formulation as Navier-Stokes, however additional higher order constitutive relations are introduced. The shear stress and heat flux terms for the Burnett equations are presented here for one spatial dimension. They have been derived for the special case of an inverse-radius intermolecular potential, Eq. (5.4a), and are given as

$$\tau_{11} = \tau_1' + \tau_2' , \tag{5.37a}$$

and

$$q_1 = q_1' + q_2' , \tag{5.37b}$$

where τ_1' and q_1' are the Navier-Stokes contributions given as [39,82]

$$\tau_1' = \frac{4}{3}\mu\frac{\partial u_1}{\partial x_1} , \tag{5.38a}$$

and

$$q_1' = -k\frac{\partial T}{\partial x_1} , \tag{5.38b}$$

and τ_2' and q_2' are the additional Burnett terms given as

$$\begin{aligned}\tau_2' = -\frac{\mu^2}{p}\Bigg[&(\frac{2}{3}\omega_1 - \frac{14}{9}\omega_2 + \frac{2}{9}\omega_6)(\frac{\partial u_1}{\partial x_1})^2 - \frac{2}{3}\omega_2\frac{RT}{\rho}\frac{\partial^2 u}{\partial x_1^2} + \frac{2}{3}\omega_2\frac{RT}{\rho^2}(\frac{\partial \rho}{\partial x_1})^2 \\ &- \frac{2}{3}(\omega_2 - \omega_4)\frac{R}{\rho}\frac{\partial \rho}{\partial x_1}\frac{\partial T}{\partial x_1} + \frac{2}{3}(\omega_4 + \omega_5)\frac{R}{T}(\frac{\partial T}{\partial x_1})^2 - \frac{2}{3}(\omega_2 - \omega_3)R\frac{\partial^2 T}{\partial x_1^2}\Bigg] ,\end{aligned} \tag{5.39a}$$

$$q_2' = \frac{\mu^2}{\rho}\left[(\theta_1 + \frac{8}{3}\theta_2 + \frac{2}{3}\theta_3 + \frac{2}{3}\theta_5)\frac{1}{T}\frac{\partial u_1}{\partial x_1}\frac{\partial T}{\partial x_1} + \frac{2}{3}(\theta_2 + \theta_4)\frac{\partial^2 u_1}{\partial x_1^2} + \frac{2}{3}\theta_3\frac{1}{\rho}\frac{\partial u_1}{\partial x_1}\frac{\partial \rho}{\partial x_1}\right], \qquad (5.39b)$$

and the ω_i's and θ_i's are constants determined from Chapman-Enskog theory and depend on the constant η in the inverse power model. Values for ω_i and θ_i have been determined in Ref. [82] for both hard-sphere ($\eta = \infty$) and Maxwellian molecules ($\eta = 5$). One drawback of the Burnett equations, other than their complexity, is that numerical solutions tend to become unstable as mesh spacing is refined. This problem has been addressed by Zong *et al.* [44] who found that the Burnett equations could be stabilized by adding select terms from the third-order so-called "Super-Burnett" equations. As a result, the Burnett equations are solved in the augmented form

$$\tau_{11} = \tau_1' + \tau_2' + \tau_3', \qquad (5.40a)$$

and

$$q_1 = q_1' + q_2' + q_3', \qquad (5.40b)$$

where the higher-order Super Burnett terms [83,84] are

$$\tau_3' = -\frac{\mu^3}{p^2}(\frac{2}{9}RT\frac{\partial^3 u_1}{\partial x_1^3}), \qquad (5.41a)$$

and

$$q_3' = \frac{\mu^3}{p\rho}(\frac{11}{16}R\frac{\partial^3 T}{\partial x_1^3} - \frac{5}{8}\frac{RT}{\rho}\frac{\partial^3 \rho}{\partial x_1^3}). \qquad (5.41b)$$

These Burnett terms will be used for the hypersonic shock structure calculations in Chap. 8.

Chapter 6

Upwind Flux-Vector Splitting Methods

6.1 Introduction

The development of upwind discretization techniques has had a substantial impact on the numerical calculation of both the Euler and Navier-Stokes equations. These algorithms tend to be highly accurate and robust for a wide range of problems, and are known for their excellent shock capturing ability. Although upwind-based algorithms require more arithmetic operations (and hence increased computational times) than central-difference approaches, the differences in CPU time per iteration are typically offset by improved rates of convergence and an overall more general approach without the need for user adjustable parameters [70].

All upwind methods, in some fashion or another, attempt to "recognize" the direction of propagation of information within the flowfield (in accordance with characteristic theory) and exploit this knowledge using biased differencing procedures. These methods include flux-vector splitting techniques, flux-difference splitting techniques, as well as the fluctuation-splitting methods that will be presented in Chap. 7. In the flux-vector splitting approach, the inviscid flux vector in one space dimension is split into two parts, $\mathbf{F}^+$ and $\mathbf{F}^-$, based on information propagating upstream and downstream respectively. In the flux-difference splitting procedure, the one-dimensional flux-vector is not split but is reconstructed from left and right states using the jumps corresponding to an approximate linearised

Riemann solver. Extensions of these schemes to multiple dimensions is carried out using a dimension-by-dimension analysis whereby separate one-dimensional problems are considered.

Several of the more popular upwind algorithms are those due to Steger and Warming [3], Van Leer [4], and to Roe [5]. All of these upwind algorithms utilize the characteristic theory corresponding to hyperbolic systems of conservation laws (the Euler equations). In Sec. 6.4 a new kinetic flux-vector splitting (KFVS) procedure is presented whereby the flux vector is split based on the propagation of information at the kinetic level. Here, the relevant characteristic theory reduces to that of the homogeneous scalar advection equation and the link between the Boltzmann equation and the Euler equations is exploited leading to upwind Euler schemes obtained as moments of upwind Boltzmann schemes with a locally Maxwellian velocity distribution.

In order to perform numerical computations, the governing equations must first be discretized, thereby reducing the system of partial differential equations to a set of algebraic equations. In this chapter finite-volume discretization techniques are considered. Here, the domain of interest is partitioned into a large number of very small, but finite, control volumes and discrete approximations are obtained by direct application of the integral conservation laws [70]. Spatial accuracy is related to the truncation error of difference operators and is therefore linked to the mesh spacing. Since the finite-volume approach is based on the discretization of the integral form of the governing equations the basic quantities of mass, momentum, and energy will be conserved at the discrete level. This conservation property is fundamental for numerical schemes and allows for the correct treatment of discontinuities [71]. Another advantage of this method is that it lends itself directly to unstructured meshes with various shaped control volumes and allows for a natural

treatment of boundary conditions. Considerable flexibility may also be obtained by changing the rules for selecting the support stencil used to reconstruct data at the cell interfaces [70,85]. In Sec. 6.2 the cell-centered finite-volume method will be described as applied to a structured curvilinear coordinate system. It should be mentioned, however, that the finite volume viewpoint tends to lead to one-dimensional approaches where fluxes are determined in a dimensionally-split manner. In Chap. 7 the finite-volume method is used in conjunction with a cell-vertex scheme and residual distribution strategies. This procedure is more compatible with the development of truly multi-dimensional upwind schemes.

Solutions are advanced to the steady state using Euler Implicit time integration. The implicit formulation is important from a stability viewpoint since it allows larger time steps and thus faster convergence to the steady state [70]. Furthermore, for reacting flows with widely varying time scales, implicit treatment of the source terms is necessary to alleviate the numerical stiffness problem [86,87,88]. The Euler Implicit scheme is only first-order accurate in time and is not sufficient for problems where temporal accuracy is of concern. For time accurate calculations higher-order schemes such as the implicit Runge-Kutta scheme developed by Ianelli and Baker [89] must be used. In Sec. 6.3 the Euler Implicit method will be described in conjunction with the standard spatially-split approximate factorization scheme that is used for two-dimensional calculations [70].

6.2 Cell-Centered Finite-Volume Discretization

In this section, the finite-volume formulation is applied to the structured curvilinear coordinate system (ξ, η, ζ) defined by the transformation in Eq. (3.56). For this case a computational cell is bounded by two ξ =constant faces, two η =constant faces, and to ζ =constant faces and the indices i, j, k will be used to indicate the

coordinate directions for ξ, η, ζ respectively. It is noted that each cell face is shared by two adjacent cells or is part of the external boundary. This is important for the conservative "telescoping" property since when summing surface integrals, contributions from internal surfaces appear twice but with opposite signs, and will cancel one another. Application of the integral form of the governing equations, Eq. (3.65), to the computational cell described above yields

$$\frac{\partial \langle\langle \mathbf{Q} \rangle\rangle}{\partial t}\,\delta V + \oint_{\delta S} (\bar{\mathbf{S}} - \bar{\mathbf{S}}_v)\cdot \hat{\mathbf{n}} dS = \langle\langle \mathbf{W} \rangle\rangle\,\delta V\,, \tag{6.1}$$

where the average variables $\langle\langle \mathbf{Q} \rangle\rangle$, $\langle\langle \mathbf{W} \rangle\rangle$ have been introduced as

$$\langle\langle \mathbf{Q} \rangle\rangle = \frac{1}{\delta V}\iiint_{\delta V} \mathbf{Q}\,dV\,, \tag{6.2a}$$

$$\langle\langle \mathbf{W} \rangle\rangle = \frac{1}{\delta V}\iiint_{\delta V} \mathbf{W}\,dV\,. \tag{6.2b}$$

The surface integral term may be evaluated as the summation over the six cell faces $i \pm 1/2$, $j \pm 1/2$, $k \pm 1/2$, and the following semi-discrete result is obtained

$$\begin{aligned}\frac{\partial \langle\langle \mathbf{Q} \rangle\rangle}{\partial t}\,\delta V &+ \langle\langle (\bar{\mathbf{S}} - \bar{\mathbf{S}}_v)\cdot \hat{\mathbf{n}} \rangle\rangle_{i+1/2}\delta S_{i+1/2} + \langle\langle (\bar{\mathbf{S}} - \bar{\mathbf{S}}_v)\cdot \hat{\mathbf{n}} \rangle\rangle_{i-1/2}\delta S_{i-1/2} \\ &+ \langle\langle (\bar{\mathbf{S}} - \bar{\mathbf{S}}_v)\cdot \hat{\mathbf{n}} \rangle\rangle_{j+1/2}\delta S_{j+1/2} + \langle\langle (\bar{\mathbf{S}} - \bar{\mathbf{S}}_v)\cdot \hat{\mathbf{n}} \rangle\rangle_{j-1/2}\delta S_{j-1/2} \\ &+ \langle\langle (\bar{\mathbf{S}} - \bar{\mathbf{S}}_v)\cdot \hat{\mathbf{n}} \rangle\rangle_{k+1/2}\delta S_{k+1/2} + \langle\langle (\bar{\mathbf{S}} - \bar{\mathbf{S}}_v)\cdot \hat{\mathbf{n}} \rangle\rangle_{k-1/2}\delta S_{k-1/2} = \langle\langle \mathbf{W} \rangle\rangle\,\delta V\,,\end{aligned} \tag{6.3}$$

where area-averaged variables have been introduced and are defined for a generic variable ϑ as

$$\langle\langle \vartheta \rangle\rangle_{i+1/2} = \frac{1}{\delta S_{i+1/2}}\iint_{\delta S_{i+1/2}} \vartheta\,dS\,. \tag{6.4}$$

The unit normal vectors $\hat{\mathbf{n}}$ are defined as

$$\hat{\mathbf{n}}_{i\pm 1/2} = \pm\bar{\nabla}\tilde{\xi}\,, \tag{6.5a}$$

$$\hat{\mathbf{n}}_{j\pm 1/2} = \pm\bar{\nabla}\tilde{\eta}\,, \tag{6.5b}$$

$$\hat{\mathbf{n}}_{k\pm 1/2} = \pm\bar{\nabla}\tilde{\zeta}\,. \tag{6.5c}$$

At this point it is useful to consider a semi-discrete differential formulation using Eq. (3.57), whereby comparison with Eq. (6.3) leads to a geometrical interpretation of the metric terms. That is, that $1/J$ can be associated with the cell volume δV and the terms $\mid \bar{\nabla}\xi \mid /J$, $\mid \bar{\nabla}\eta \mid /J$, and $\mid \bar{\nabla}\zeta \mid /J$ can be associated with the cell face area in the ξ, η, ζ directions respectively [70]. Incorporating the metric terminology and dropping the average notation yields

$$\frac{1}{J}\frac{\partial \mathbf{Q}}{\partial t} + \delta_\xi(\tilde{\mathbf{F}} - \tilde{\mathbf{F}}_v) + \delta_\eta(\tilde{\mathbf{G}} - \tilde{\mathbf{G}}_v) + \delta_\zeta(\tilde{\mathbf{H}} - \tilde{\mathbf{H}}_v) = \frac{1}{J}\mathbf{W}\,, \tag{6.6}$$

where the difference operators are defined as $\delta_\xi(\cdot) = (\cdot)_{i+1/2} - (\cdot)_{i-1/2}$ and the flux terms are defined in Eqs. (3.58a) - (3.58c). This differential notation will be used throughout to denote the finite-volume approach.

Various methods are available for generating pointwise values at a cell face using cell average data from surrounding cells. The $\phi - \kappa$ approach is based on a one-dimensional reconstruction using known cell averages and a polynomial basis set. This approach gives a one-parameter family of reconstruction polynomials evaluated at the cell face. Values for the left state on the $i+1/2$ cell face are given as

$$\varphi^-_{i+1/2} = \varphi_i + \frac{\phi}{4}\Big[(1+\kappa)\Delta + (1-\kappa)\nabla\Big]\varphi_i\,, \tag{6.7a}$$

for a generic cell-average variable φ. The value for the right state on the $i+1/2$ face is

$$\varphi^+_{i+1/2} = \varphi_{i+1} - \frac{\phi}{4}\Big[(1+\kappa)\nabla + (1-\kappa)\Delta\Big]\varphi_{i+1}\,. \tag{6.7b}$$

Here, Δ, ∇ are forward and backward difference operators and ϕ is an on/off switch for higher-order interpolation. A value of $\kappa = -1$ yields a fully upwind linear reconstruction that is second-order accurate on uniform grids. An upwind-biased quadratic reconstruction is obtained for $\kappa = 1/3$ and is third-order accurate on uniform grids [70]. Interpolation may be carried out using conserved variables, however

primitive variables or characteristic variables tend to be more robust for hypersonic flows. In the present work primitive variables are used. The inviscid fluxes at the interfaces are obtained using the standard MUSCL formulation [70] whereby

$$\tilde{\mathbf{F}} = \tilde{\mathbf{F}}(q^+, q^-)\,, \tag{6.8a}$$

$$\tilde{\mathbf{G}} = \tilde{\mathbf{G}}(q^+, q^-)\,, \tag{6.8b}$$

$$\tilde{\mathbf{H}} = \tilde{\mathbf{H}}(q^+, q^-)\,, \tag{6.8c}$$

The formulation given by Eqs. (6.7a)-(6.8c) represents a linear scheme (*i.e.*, all coefficients in the update are constant) that is linearity preserving (LP) for the higher-order interpolations. That is, the scheme preserves the exact steady state solution whenever this is a linear function of space. The major drawback of schemes of this type is that they lack the crutial property of positivity (P) (*i.e.*, all coefficients in the update are positive) by extension of Gudonov's theorem, and cannot maintain monotone profiles across discontinuities [32]. To remedy this problem limiters are used that reduce the scheme to first-order accuracy in regions of large flow gradients. In this work both the Van Albeda and MIN-MOD limiters are used [70]. To combine the properties of (P) and (LP) nonlinear schemes such as the TVD schemes must be used [85].

The viscous terms are determined using second-order accurate central differences and averages.

6.3 Euler-Implicit Time Integration

For a large number of flow problems only the steady-state results are desired. These calculations are performed by advancing the flow variables through a sequence of time steps until convergence to the steady state is reached. Here, temporal accuracy is of no concern and typically the Euler-Implicit method is used

[70]. As previously mentioned, the implicit formulation is important in terms of efficiency in reaching the steady-state, and is necessary for alleviating the numerical stiffness problem associated with reacting flows [86,87,88]. The Euler-Implicit scheme is obtained by discretizing the system of governing equations about time level $n+1$

$$\frac{1}{J}\left(\frac{\partial \mathbf{Q}}{\partial t}\right)^{n+1} + R(\mathbf{Q}^{n+1}) = 0\,, \tag{6.9a}$$

where

$$R(\mathbf{Q}^{n+1}) = \delta_\xi(\tilde{\mathbf{F}} - \tilde{\mathbf{F}}_v) + \delta_\eta(\tilde{\mathbf{G}} - \tilde{\mathbf{G}}_v) + \delta_\zeta(\tilde{\mathbf{H}} - \tilde{\mathbf{H}}_v) - \frac{1}{J}\mathbf{W}\,. \tag{6.9b}$$

Equation (6.9a) represents a set on coupled non-linear algebraic equations. Realizing that

$$\left(\frac{\partial \mathbf{Q}}{\partial t}\right)^{n+1} = \left(\frac{\partial \mathbf{Q}}{\partial \mathbf{q}}\right)^{n}\frac{\Delta \mathbf{q}}{\Delta t} + O(\Delta t)\,, \tag{6.10a}$$

where $\Delta \mathbf{q} = \mathbf{q}^{n+1} - \mathbf{q}^n$, and linearizing as follows

$$R(\mathbf{Q}^{n+1}) = R(\mathbf{q}^n) + \left(\frac{\partial R}{\partial \mathbf{q}}\right)^{n}\Delta \mathbf{q} + O(\Delta \mathbf{q}^2)\,, \tag{6.10b}$$

yields the the Euler-Implicit scheme in terms of primitive variables as

$$\left[\frac{1}{J}\frac{\partial \mathbf{Q}}{\partial \mathbf{q}}\frac{\mathbf{I}}{\Delta t} + \frac{\partial}{\partial \mathbf{q}}R(\mathbf{q}^n)\right]\Delta \mathbf{q} = -R(\mathbf{q}^n)\,. \tag{6.11}$$

The formulation in terms of primitive variables eliminates the need to iterate for temperature, as was formerly the case with the simple vibrational equilibrium model, Eq. (2.20a), and represents a more consistent formulation since interpolation to cell interfaces is performed in terms of primitive variables. The term $(\partial R/\partial \mathbf{q})\Delta \mathbf{q}$ is interpreted as

$$\frac{\partial R}{\partial \mathbf{q}}\Delta \mathbf{q} = \delta_\xi\left(\frac{\partial}{\partial \mathbf{q}}(\tilde{\mathbf{F}} - \tilde{\mathbf{F}}_v)\Delta \mathbf{q}\right) + \delta_\eta\left(\frac{\partial}{\partial \mathbf{q}}(\tilde{\mathbf{G}} - \tilde{\mathbf{G}}_v)\Delta \mathbf{q}\right) + \delta_\zeta\left(\frac{\partial}{\partial \mathbf{q}}(\tilde{\mathbf{H}} - \tilde{\mathbf{H}}_v)\Delta \mathbf{q}\right) - \frac{1}{J}\frac{\partial \mathbf{W}}{\partial \mathbf{q}}\,. \tag{6.12}$$

The final form may be written as

$$\left[\frac{1}{J}\frac{\partial \mathbf{Q}}{\partial \mathbf{q}}\frac{\mathbf{I}}{\Delta t} + \delta_\xi\left(\tilde{\mathbf{A}} - \tilde{\mathbf{A}}_v\right) + \delta_\eta\left(\tilde{\mathbf{B}} - \tilde{\mathbf{B}}_v\right) + \delta_\zeta\left(\tilde{\mathbf{C}} - \tilde{\mathbf{C}}_v\right) - \frac{1}{J}\frac{\partial \mathbf{W}}{\partial \mathbf{q}}\right]\Delta\mathbf{q} = -R(\mathbf{q}^n)\,, \qquad (6.13)$$

where the inviscid flux Jacobians $\tilde{\mathbf{A}}$, $\tilde{\mathbf{B}}$, $\tilde{\mathbf{C}}$, and viscous flux Jacobians $\tilde{\mathbf{A}}_v$, $\tilde{\mathbf{B}}_v$, $\tilde{\mathbf{C}}_v$ have been introduced. Equation (6.13) represents a banded block (N+M+4)×(N+M+4) matrix equation, with the band width being dependent on the choice of the spatial discretization and on the grid size. Typically, the spatial dependence of the inviscid flux Jacobians is handled in a first-order manner as

$$\begin{aligned}\left(\frac{\partial \tilde{\mathbf{F}}}{\partial \mathbf{q}}\Delta\mathbf{q}\right)_{i+1/2} &= \left(\tilde{\mathbf{A}}\Delta\mathbf{q}\right)_{i+1/2} \\ &= \left(\tilde{\mathbf{A}}^+\Delta\mathbf{q}^-\right)_{i+1/2} + \left(\tilde{\mathbf{A}}^-\Delta\mathbf{q}^+\right)_{i+1/2} \\ &= \left(\tilde{\mathbf{A}}^+\Delta\mathbf{q}^-\right)_i + \left(\tilde{\mathbf{A}}^-\Delta\mathbf{q}^+\right)_{i+1}\,. \end{aligned} \qquad (6.14)$$

The viscous Jacobians can be written in a similar form if only the thin-layer Jacobians are considered in each direction

$$\begin{aligned}\left(\frac{\partial \tilde{\mathbf{F}}_v}{\partial \mathbf{q}}\Delta\mathbf{q}\right)_{i+1/2} &= \left(\tilde{\mathbf{A}}_v\Delta\mathbf{q}\right)_{i+1/2} \\ &= \left(\tilde{\mathbf{A}}_v^+\Delta\mathbf{q}^-\right)_i + \left(\tilde{\mathbf{A}}_v^-\Delta\mathbf{q}^+\right)_{i+1}\,. \end{aligned} \qquad (6.15)$$

The source term vector Jacobian has been determined analytically [8] and is implemented in complete form. The inviscid flux Jacobian for the Van Leer flux-vector splitting scheme has been derived analytically and is used in conjunction with the KFVS scheme. Also, the thin-layer Jacobian has been treated analytically.

Two-dimensional calculations have been carried out using the standard spatially-split approximate-factorization (AF) scheme whereby the problem is solved approximately as two one-dimensional problems

$$\left[M + \delta_\xi\left(\tilde{\mathbf{A}} - \tilde{\mathbf{A}}_v\right)\right]\Delta\mathbf{q}' = -R^n\,, \qquad (6.16a)$$

$$\left[M + \delta_\eta\left(\tilde{\mathbf{B}} - \tilde{\mathbf{B}}_v\right)\right]\Delta\mathbf{q} = M\Delta\mathbf{q}'\,, \qquad (6.16b)$$

where

$$M = \frac{1}{J}\frac{\partial \mathbf{Q}}{\partial \mathbf{q}}\frac{\mathbf{I}}{\Delta t} - \frac{1}{J}\frac{\partial \mathbf{W}}{\partial \mathbf{q}}\,. \tag{6.16c}$$

This procedure requires the solution of two block tri-diagonal systems. In the present work a block LU-decomposition is used with forward and backward substitutions. The AF scheme has the advantage of being highly vectorizable, however, convergence rates tend to be time-dependent [70].

6.4 Kinetic Flux-Vector Splitting (KFVS)

In this section, the development of the KFVS method is presented. Initially, in Sec. 6.4.1.1, the KFVS scheme is derived for perfect gases in one space dimension following the development of Deshpande [12,11]. The extension to flows in chemical and thermal non-equilibrium follows directly from non-equilibrium kinetic theory [18], and is presented for one space dimension in Sec. 6.4.1.2. Finally, the general scheme is extended to a generalized three-dimensional coordinate system [18].

6.4.1 KFVS in One-Dimension

6.4.1.1 Perfect Gas

The KFVS scheme originates from the Boltzmann equation of non-equilibrium kinetic theory. The Boltzmann equation for a single species gas in local translational equilibrium and subject to zero body forces reduces to the homogeneous scalar advection equation in terms of the Maxwellian velocity distribution function

$$\frac{\partial}{\partial t}(nf_0) + c_i\frac{\partial}{\partial x_i}(nf_0) = 0\,. \tag{6.17}$$

The collision integral for this case is identically zero since the number of molecules in each velocity class must be constant. The development of the KFVS scheme

is carried out by first discretizing the Boltzmann equation in an upwind fashion [11,12,13]. Here, the one-dimensional Boltzmann equation is written in semi-discrete form using an upwind Courant-Isaacson-Rees (CIR) type procedure as

$$\frac{\partial}{\partial t}(nf_0)_i + \frac{c_1 + \mid c_1 \mid}{2} \cdot \frac{(nf_0)_i - (nf_0)_{i-1}}{\Delta x_1} + \frac{c_1 - \mid c_1 \mid}{2} \cdot \frac{(nf_0)_{i+1} - (nf_0)_i}{\Delta x_1} = 0 . \qquad (6.18)$$

Taking moments of the discretized Boltzmann scheme with elements of the moment function vector, Eq. (3.22), except for a single species and zero non-equilibrium internal energy contributions, yields the upwind Euler scheme

$$\left(\frac{\partial \mathbf{Q}}{\partial t}\right)_i + \frac{\mathbf{F}_i^{+} - \mathbf{F}_{i-1}^{+}}{\Delta x_1} + \frac{\mathbf{F}_{i+1}^{-} - \mathbf{F}_i^{-}}{\Delta x_1} = 0 , \qquad (6.19a)$$

where the split flux vector $\mathbf{F}^{\pm}$ and the conserved variable vector $\mathbf{Q}$ are given as

$$\mathbf{F}^{\pm} = \rho < \frac{c_1 \pm \mid c_1 \mid}{2} \begin{pmatrix} 1 \\ c_1 \\ \epsilon_0 \end{pmatrix} >^0 , \qquad (6.19b)$$

$$\mathbf{Q} = \begin{pmatrix} \rho \\ \rho u_1 \\ \rho e_0 \end{pmatrix} . \qquad (6.19c)$$

Here $\mathbf{F}^{+}$ and $\mathbf{F}^{-}$ are the portions of the moments over the positive and negative halves of velocity space respectively. Utilizing this fact, the positive split flux for the continuity equation, denoted F_1^{+}, may be evaluated as

$$F_1^{+} = \rho \int_{-\infty}^{\infty}\int_{-\infty}^{\infty}\int_{0}^{\infty} c_1 f_0 \, dc_1 dc_2 dc_3 = \rho(\frac{\beta}{\pi})^{3/2} I_1 I_2 I_3 , \qquad (6.20a)$$

where

$$I_1 = \int_0^{\infty} c_1 e^{-\beta(c_1 - u_1)^2} dc_1 , \qquad (6.20b)$$

$$I_2 = \int_{-\infty}^{\infty} e^{-\beta(c_2 - u_2)^2} dc_2 , \qquad (6.20c)$$

$$I_3 = \int_{-\infty}^{\infty} e^{-\beta(c_3 - u_3)^2} dc_3 , \qquad (6.20d)$$

and $\beta = 1/2RT$. Evaluating these integrals along with the definition of the error function

$$erf(x) = \frac{2}{\sqrt{\pi}} \int_0^x e^{-t^2} dt , \qquad (6.21)$$

the positive split flux for the continuity equation becomes

$$F_1^+ = \frac{1}{2}\rho u_1 \left[1 + erf(\sqrt{\beta}u_1) \right] + \frac{\rho}{2\sqrt{\beta\pi}} e^{-\beta {u_1}^2} . \tag{6.22}$$

The split fluxes for the momentum and energy equations are obtained in a similar manner and the final results written in terms of the error function are listed below

$$F_1^\pm = \frac{1}{2}\rho u_1 \left[1 \pm erf(\sqrt{\beta}u_1) \right] \pm \frac{\rho}{2\sqrt{\beta\pi}} e^{-\beta {u_1}^2} , \tag{6.23a}$$

$$F_2^\pm = \frac{1}{2}(\rho {u_1}^2 + p) \left[1 \pm erf(\sqrt{\beta}u_1) \right] \pm \frac{\rho u_1}{2\sqrt{\beta\pi}} e^{-\beta {u_1}^2} , \tag{6.23b}$$

$$F_3^\pm = \frac{1}{2}(\rho u_1 h_0) \left[1 \pm erf(\sqrt{\beta}u_1) \right] \pm (\rho h_0 - \frac{1}{2}p) \frac{1}{2\sqrt{\beta\pi}} e^{-\beta {u_1}^2} . \tag{6.23c}$$

Alternatively, the KFVS scheme could have been derived by starting with the finite-volume discretization

$$\frac{1}{J}\frac{\partial}{\partial t}(nf_0) + \delta_\xi (c_1 nf_0) = 0 . \tag{6.24}$$

The flux at the interface $i + 1/2$, for example, can now be split into two portions based on the sign of the molecular velocity

$$(c_1 nf_0)_{i+1/2} = \frac{c_1 + \mid c_1 \mid}{2}(nf_0)^-_{i+1/2} + \frac{c_1 - \mid c_1 \mid}{2}(nf_0)^+_{i+1/2} . \tag{6.25}$$

Taking moments yields

$$\mathbf{F}_{i+1/2} = \mathbf{F}^+_{i+1/2} + \mathbf{F}^-_{i+1/2} . \tag{6.26}$$

The first-order scheme is recovered when $(nf_0)^-_{i+1/2} = (nf_0)_i$ and $(nf_0)^+_{i+1/2} = (nf_0)_{i+1}$.

6.4.1.2 Chemical and Thermal Non-Equilibrium

For flows with chemical and thermal non-equilibrium the KFVS scheme originates from the species Boltzmann equation for a gas in local translational equilibrium and subject to zero body forces [18]

$$\frac{\partial}{\partial t}(n_s f_{0_s}) + c_i \frac{\partial}{\partial x_i}(n_s f_{0_s}) = \sum_r \left\{ \frac{\partial}{\partial t}(n_s f_{0_s}) \right\}_{coll_{r-s}} . \tag{6.27}$$

Now the collision integral term must be retained, even though each species maintains a Maxwellian distribution. This is because the number of molecules in each velocity class may change as a result of inelastic collisions that give rise to species and non-equilibrium internal energy production terms. The development proceeds in a manner similar to the perfect gas case except now each species Boltzmann equation must be discretized using an upwind CIR procedure [18]

$$\frac{\partial}{\partial t}(n_s f_{0_s})_i + \frac{c_{1+} \mid c_1 \mid}{2} \cdot \frac{(n_s f_{0_s})_i - (n_s f_{0_s})_{i-1}}{\Delta x_1} + \frac{c_{1-} \mid c_1 \mid}{2} \cdot \frac{(n_s f_{0_s})_{i+1} - (n_s f_{0_s})_i}{\Delta x_1} = \sum_r \{ \frac{\partial}{\partial t}(n_s f_{0_s}) \}_{coll_{r-s}} . \tag{6.28}$$

Taking moments of the discretized species Boltzmann scheme using elements of Eq. (3.22) and summing the species momentum contributions and the species total energy contributions yields the upwind Euler scheme

$$\left(\frac{\partial \mathbf{Q}}{\partial t}\right)_i + \frac{\mathbf{F}_i{}^+ - \mathbf{F}_{i-1}{}^+}{\Delta x_1} + \frac{\mathbf{F}_{i+1}{}^- - \mathbf{F}_i{}^-}{\Delta x_1} = \mathbf{W}_i \quad , \tag{6.29a}$$

where the components of the split flux vector $\mathbf{F}^{\pm}$ are given as the following moments of the distribution function

$$F_s^{\pm} = \rho_s < \frac{c_{1\pm} \mid c_1 \mid}{2} >_s^0 , \qquad s = 1, ..., N , \tag{6.29b}$$

$$F_{N+1}^{\pm} = \sum_{s=1}^{N} \rho_s < \frac{c_{1\pm} \mid c_1 \mid}{2} \cdot c_1 >_s^0 , \tag{6.29c}$$

$$F_{N+1+s}^{\pm} = \rho_s e_{n_s} < \frac{c_{1\pm} \mid c_1 \mid}{2} >_s^0 , \qquad s = 1, ..., M , \tag{6.29d}$$

$$F_{N+M+2}^{\pm} = \sum_{s=1}^{N} \rho_s < \frac{c_{1\pm} \mid c_1 \mid}{2} \cdot \epsilon_0 >_s^0 , \tag{6.29e}$$

and the conserved variable vector $\mathbf{Q}$ and the chemical and thermal source term

vector $\mathbf{W}$, are given as

$$\mathbf{Q} = \begin{pmatrix} \rho_1 \\ \rho_2 \\ \vdots \\ \rho_N \\ \rho u_1 \\ \rho_1 e_{n1} \\ \vdots \\ \rho_M e_{nM} \\ \rho e_0 \end{pmatrix}, \quad \mathbf{W} = \begin{pmatrix} \dot{\omega}_1 \\ \dot{\omega}_2 \\ \vdots \\ \dot{\omega}_N \\ 0 \\ \rho_1 \dot{e}_{n1} + \dot{\rho}_1 e_{n1} \\ \vdots \\ \rho_M \dot{e}_{nM} + \dot{\rho}_M e_{nM} \\ 0 \end{pmatrix}. \tag{6.30a,b}$$

The split fluxes, after evaluation, may again be written in terms of the error function and are given in Ref. [18]. They are listed below as

$$F_s^{\pm} = \frac{1}{2}\rho_s u_1 \left[1 \pm erf(\sqrt{\beta_s} u_1) \right] \pm \frac{\rho_s}{2\sqrt{\beta_s \pi}} e^{-\beta_s {u_1}^2}, \quad s = 1, ..., N, \tag{6.31a}$$

$$F_{N+1}^{\pm} = \sum_{s=1}^{N} \left\{ \frac{1}{2}(\rho_s {u_1}^2 + p_s) \left[1 \pm erf(\sqrt{\beta_s} u_1) \right] \pm \frac{\rho_s u_1}{2\sqrt{\beta_s \pi}} e^{-\beta_s {u_1}^2} \right\}, \tag{6.31b}$$

$$F_{N+1+s}^{\pm} = \frac{1}{2}\rho_s e_{ns} u_1 \left[1 \pm erf(\sqrt{\beta_s} u_1) \right] \pm \frac{\rho_s e_{ns}}{2\sqrt{\beta_s \pi}} e^{-\beta_s {u_1}^2}, \quad s = 1, ..., M, \tag{6.31c}$$

$$F_{N+M+2}^{\pm} = \sum_{s=1}^{N} \left\{ \frac{1}{2}\rho_s u_1 h_{0s} \left[1 \pm erf(\sqrt{\beta_s} u_1) \right] \pm (\rho_s h_{0s} - \frac{1}{2} p_s) \frac{1}{2\sqrt{\beta_s \pi}} e^{-\beta_s {u_1}^2} \right\}, \tag{6.31d}$$

where $\beta_s = 1/2R_sT$.

6.4.2 KFVS in Generalized Coordinates

For cell-centered finite-volume schemes it is simplest to start with the species Boltzmann equation expressed in conservative integral form, Eq. (3.63). The assumption of local translational equilibrium and negligible body forces reduces the species Boltzmann equation to

$$\frac{\partial}{\partial t} \iiint_{\delta V} n_s f_{0s} dV + \oint_{\delta S} (\bar{c} \cdot \hat{\mathbf{n}}) n_s f_{0s} dS = \iiint_{\delta V} \sum_r \left\{ \frac{\partial}{\partial t}(n_s f_{0s}) \right\}_{coll_{r-s}} dV. \tag{6.32}$$

By applying the finite-volume methodology as developed in Sec. 6.2, the Boltzmann equation may be discretized as follows

$$\frac{1}{J}\frac{\partial}{\partial t}(n_s f_{0s}) + \delta_\xi \left[\frac{|\bar{\nabla}\xi|}{J} \bar{\nabla}\tilde{\xi} \cdot (\bar{c} n_s f_{0s}) \right]$$

$$+\delta_\eta\left[\frac{|\bar{\nabla}\eta|}{J}\bar{\nabla}\tilde{\eta}\cdot(\bar{c}n_sf_{0_s})\right]$$
$$+\delta_\zeta\left[\frac{|\bar{\nabla}\zeta|}{J}\bar{\nabla}\tilde{\zeta}\cdot(\bar{c}n_sf_{0_s})\right]=\frac{1}{J}\sum_r\{\frac{\partial}{\partial t}(n_sf_{0_s})\}_{coll_{r-s}}. \tag{6.33}$$

Introducing the contravariant molecular velocity components $\tilde{c}_1$, $\tilde{c}_2$, $\tilde{c}_3$, defined by

$$\tilde{c}_1=\bar{c}\cdot\bar{\nabla}\tilde{\xi}, \tag{6.34a}$$

$$\tilde{c}_2=\bar{c}\cdot\bar{\nabla}\tilde{\eta}, \tag{6.34b}$$

$$\tilde{c}_3=\bar{c}\cdot\bar{\nabla}\tilde{\zeta}, \tag{6.34c}$$

Eq. (6.33) may be rewritten as

$$\frac{1}{J}\frac{\partial}{\partial t}(n_sf_{0_s})+\delta_\xi(\frac{|\bar{\nabla}\xi|}{J}\tilde{c}_1n_sf_{0_s})$$
$$+\delta_\eta(\frac{|\bar{\nabla}\eta|}{J}\tilde{c}_2n_sf_{0_s})$$
$$+\delta_\zeta(\frac{|\bar{\nabla}\zeta|}{J}\tilde{c}_3n_sf_{0_s})=\frac{1}{J}\sum_r\{\frac{\partial}{\partial t}(n_sf_{0_s})\}_{coll_{r-s}}. \tag{6.35}$$

The flux at an interface may now be split into two parts based on the sign of the contravariant molecular velocity component. For instance, consider the $i+1/2$ face

$$(\frac{|\bar{\nabla}\xi|}{J}\tilde{c}_1n_sf_{0_s})_{i+1/2}=\frac{|\bar{\nabla}\xi|}{J}_{i+1/2}\left[\frac{\tilde{c}_1+|\tilde{c}_1|}{2}(n_sf_{0_s})^-_{i+1/2}+\frac{\tilde{c}_1-|\tilde{c}_1|}{2}(n_sf_{0_s})^+_{i+1/2}\right]. \tag{6.36}$$

Taking moments yields the finite-volume KFVS scheme

$$\frac{1}{J}\frac{\partial\mathbf{Q}}{\partial t}+\delta_\xi(\tilde{\mathbf{F}}^++\tilde{\mathbf{F}}^-)+\delta_\eta(\tilde{\mathbf{G}}^++\tilde{\mathbf{G}}^-)+\delta_\zeta(\tilde{\mathbf{H}}^++\tilde{\mathbf{H}}^-)=\frac{1}{J}\mathbf{W}, \tag{6.37a}$$

where

$$\tilde{F}^\pm_s=\frac{|\bar{\nabla}\xi|}{J}\rho_s<\frac{\tilde{c}_1\pm|\tilde{c}_1|}{2}>^0_s \qquad s=1,...,N, \tag{6.37b}$$

$$\tilde{F}^\pm_{N+1}=\frac{|\bar{\nabla}\xi|}{J}\sum_{s=1}^N\rho_s<\frac{\tilde{c}_1\pm|\tilde{c}_1|}{2}\cdot c_1>^0_s, \tag{6.37c}$$

$$\tilde{F}^\pm_{N+2}=\frac{|\bar{\nabla}\xi|}{J}\sum_{s=1}^N\rho_s<\frac{\tilde{c}_1\pm|\tilde{c}_1|}{2}\cdot c_2>^0_s, \tag{6.37d}$$

$$\tilde{F}^{\pm}_{N+3} = \frac{|\bar{\nabla}\xi|}{J}\sum_{s=1}^{N}\rho_s < \frac{\tilde{c}_1 \pm |\tilde{c}_1|}{2}\cdot c_3 >^0_s , \tag{6.37e}$$

$$\tilde{F}^{\pm}_{N+3+s} = \frac{|\bar{\nabla}\xi|}{J}\rho_s e_{n_s} < \frac{\tilde{c}_1 \pm |\tilde{c}_1|}{2} >^0_s \qquad s = 1, ..., M , \tag{6.37f}$$

$$\tilde{F}^{\pm}_{N+M+4} = \frac{|\bar{\nabla}\xi|}{J}\sum_{s=1}^{N}\rho_s < \frac{\tilde{c}_1 \pm |\tilde{c}_1|}{2}\cdot \epsilon_0 >^0_s . \tag{6.37g}$$

The fluxes for $\tilde{\mathbf{G}}^{\pm}$ can be obtained by substituting η and $\tilde{c}_2$ for ξ and $\tilde{c}_1$ respectively. Likewise, $\tilde{\mathbf{H}}^{\pm}$ can be obtained by substituting ζ and $\tilde{c}_3$.

At this point it is helpful to consider a Maxwellian distribution function in the transformed coordinate system normal to the cell face. Evaluating the moments represented by Eqs. (6.37b) - (6.37g) gives the following split flux terms:

$$\tilde{F}^{\pm}_{s} = \frac{|\bar{\nabla}\xi|}{J}\left\{\frac{1}{2}\rho_s\tilde{u}_1\left[\,1 \pm erf(\sqrt{\beta_s}\tilde{u}_1)\right] \pm \frac{\rho_s}{2\sqrt{\beta_s\pi}}e^{-\beta_s\tilde{u}_1^2}\right\} \quad s = 1, ..., N , \tag{6.38a}$$

$$\tilde{F}^{\pm}_{N+1} = \frac{|\bar{\nabla}\xi|}{J}\sum_{s=1}^{N}\left\{\frac{1}{2}(\rho_s\tilde{u}_1u_1 + p_s\tilde{\xi}_{x_1})\left[\,1 \pm erf(\sqrt{\beta_s}\tilde{u}_1)\right] \pm \frac{\rho_s u_1}{2\sqrt{\beta_s\pi}}e^{-\beta_s\tilde{u}_1^2}\right\}, \tag{6.38b}$$

$$\tilde{F}^{\pm}_{N+2} = \frac{|\bar{\nabla}\xi|}{J}\sum_{s=1}^{N}\left\{\frac{1}{2}(\rho_s\tilde{u}_1u_2 + p_s\tilde{\xi}_{x_2})\left[\,1 \pm erf(\sqrt{\beta_s}\tilde{u}_1)\right] \pm \frac{\rho_s u_2}{2\sqrt{\beta_s\pi}}e^{-\beta_s\tilde{u}_1^2}\right\}, \tag{6.38c}$$

$$\tilde{F}^{\pm}_{N+3} = \frac{|\bar{\nabla}\xi|}{J}\sum_{s=1}^{N}\left\{\frac{1}{2}(\rho_s\tilde{u}_1u_3 + p_s\tilde{\xi}_{x_3})\left[\,1 \pm erf(\sqrt{\beta_s}\tilde{u}_1)\right] \pm \frac{\rho_s u_2}{2\sqrt{\beta_s\pi}}e^{-\beta_s\tilde{u}_1^2}\right\}, \tag{6.38d}$$

$$\tilde{F}^{\pm}_{N+3+s} = \frac{|\bar{\nabla}\xi|}{J}\left\{\frac{1}{2}\rho_s e_{n_s}\tilde{u}_1\left[\,1 \pm erf(\sqrt{\beta_s}\tilde{u}_1)\right] \pm \frac{\rho_s e_{n_s}}{2\sqrt{\beta_s\pi}}e^{-\beta_s\tilde{u}_1^2}\right\} \quad s = 1, ..., M , \tag{6.38e}$$

$$\tilde{F}^{\pm}_{N+M+4} = \frac{|\bar{\nabla}\xi|}{J}\sum_{s=1}^{N}\left\{\frac{1}{2}\rho_s\tilde{u}_1h_{0_s}\left[\,1 \pm erf(\sqrt{\beta_s}\tilde{u}_1)\right]\right.$$
$$\left. \pm (\rho_s h_{0_s} - \frac{1}{2}p_s)\frac{1}{2\sqrt{\beta_s\pi}}e^{-\beta_s\tilde{u}_1^2}\right\}. \tag{6.38f}$$

The fluxes for $\tilde{\mathbf{G}}^{\pm}$ can be obtained by substituting η and $\tilde{u}_2$ for ξ and $\tilde{u}_1$ respectively. Likewise, $\tilde{\mathbf{H}}^{\pm}$ can be obtained by substituting ζ and $\tilde{u}_3$.

6.5 Results

Computational results are presented for a series of test cases:

1. quasi-one-dimensional inviscid simulations of air treated as a perfect gas.
2. quasi-one-dimensional inviscid simulations of air in chemical non-equilibrium.

3. two-dimensional inviscid simulations of a perfect gas in a supersonic channel.
4. two-dimensional inviscid simulations of air in chemical non-equilibrium in a supersonic channel.
5. viscous simulation of a perfect gas around a cone.
6. two-dimensional viscous simulation over a wedge with shock-induced combustion/detonation of premixed hydrogen-air
7. two-dimensional inviscid simulations of the transonic flow over a bump in a channel and an NACA 0012 airfoil.

Comparisons are made between the KFVS results and those of the Van Leer flux-vector splitting and Roe flux-differencing schemes. The calculations were performed using a two-dimensional/axi-symmetric finite-volume Navier-Stokes code for chemical and thermal non-equilibrium that was developed by the present author for research purposes. In all cases MUSCL-type ($\phi - \kappa$) differencing is used in conjunction with either the Van Albeda or MIN-MOD limiters, *e.g.,* see Walters and Thomas [70].

The first case considered is a quasi-one-dimensional calculation of perfect air through a supersonic channel. The geometry for the channel is that of a rapidly expanding nozzle with an area ratio of $4:1$ over a length of 2 meters. The area distribution is given according to the formula

$$A = \frac{\pi}{16}[1 + sin(\frac{\pi x}{2L})]^2 \qquad 0 \leq x \geq L \quad , \tag{1}$$

where $L = 2m$. The inlet conditions for this case are $M_1 = 1.58$, $T_1 = 4000\,^0K$, $V_1 = 2000\,m/s$, $\rho_1 = 0.086756\,Kg/m^3$, and the back pressure is fixed at $p_b = 1.50 \times 10^5\,N/m^2$, a value such that a normal shock exists within the channel. The calculation is carried out with 51 equally spaced grid points. Figures 6.1a and 6.1b show the pressure and temperature distributions respectively for both KFVS and Roe first-

order solutions. Both solutions are nearly identical except near the shock where the KFVS splitting appears to smear the shock slightly more than the Roe scheme. Fig. 6.2a shows the temperature distribution for a locally third-order ($\kappa = 1/3$) calculation with the MIN-MOD limiter while Fig. 6.2b shows the same calculation with the Van Albeda limiter. In both cases the solutions are nearly identical, even through the shock region, except that the smaller dissipation associated with the MIN-MOD limiter results in a numerical overshoot just behind the shock with the KFVS splitting as seen in Fig. 6.2a.

The second case is a quasi-one-dimensional calculation of reacting air through the same supersonic channel. Here, the inflow Mach number is 1.5 and again the back pressure is fixed at a value of $p_b = 1.50 \times 10^5\, N/m^2$, so that normal shock stands in the duct. The air chemistry model is that due to Kang and Dunn [73] and consists of 5 species N_2, O_2, NO, N, O and 17 reactions as described in Sec. 4.2.1. The inlet conditions are $V_1 = 2000 m/s$, $T_1 = 4000\,^0K$ and initial species densities in kg/m^3 of 0.0642 for N_2, 0.00369 for O_2, 0.00485 for NO, 6.60×10^{-5} for N and 0.0139 for O. Figure 6.3a shows the temperature distributions for third-order KFVS and Roe solutions using the MIN-MOD limiter and 51 grid points. Again the KFVS and Roe schemes produce nearly identical results. The same calculation with 101 grid points shown in Fig. 6.3b exhibits a nearly exact comparison between the two schemes. It is noted that both schemes perform equally well in capturing the physical reaction zone just behind the shock. Here, the rapid decrease in temperature is caused by the endothermic nature of the dissociation reactions. Additional grid points would be necessary to adequately resolve this region. Figures 6.4a and 6.4b show the O_2 mass fraction distributions for 51 and 101 grid point calculations respectively. Both calculations show excellent agreement between the two schemes.

Case 3 is the inviscid, two-dimensional calculation of perfect air through a su-

personic inlet. The inlet geometry consisted of a 10 degree compression followed by a 10 degree expansion and is symmetric with respect to the centerline. At the inflow boundary all conditions were held fixed at $M_1 = 5$, $p_1 = 66760.0 N/m^2$ and $T_1 = 3573K$. The outflow boundary is always supersonic and a first-order extrapolation boundary condition was used. On the lower surface, wall tangency was enforced along with imposing that the wall enthalpy, entropy, and pressure are equal to that at the first point off the wall. Symmetry conditions were used on the centerline. Second-order fully upwind MUSCL differencing ($\kappa = -1$), was used in the axial direction and third-order upwind biased MUSCL differencing was used in the normal direction. A catastrophic limiter was also used. Figures 6.5a and 6.5b show the non-dimensional pressure and temperature distributions respectively along the lower wall ramp for Roe, Van Leer and KFVS solutions on a 51×51 grid. The pressure distributions for all three schemes are nearly identical and agree very well with the exact solution, except that each scheme exhibits a slight numerical overshoot in the post-shock region. The temperature distributions do not agree as well with the exact solution. For this case the Roe scheme over-predicts the temperature behind the shock as well as the temperature past the expansion. The KFVS and Van Leer flux-vector splittings produce results that are very similar to one another and also over-predict the temperature past the shock and expansion, but to a lesser degree than the Roe results. It is noted that the Roe solution produces relatively constant values of temperature behind the shock and expansion waves while the Van Leer and KFVS schemes result in slightly varying temperatures in these regions. In this regard, the Roe solution represents a more physical solution. Figures 6.6a and 6.6b show the non-dimensional pressure and temperature distributions for a solution with 101 axial grid points and 51 normal grid points. Again, the pressure distributions for the three schemes are essentially identical and compare well with the exact solution.

It is noted that the numerical overshoot for this case is slightly larger than for the 51×51 case. Comparing the 101×51 temperature distribution with the 51×51 case, the Roe solution agrees better with the exact solution and is closer to the Van Leer and KFVS solutions, however, all three schemes still over-predict the temperature. Again, the KFVS and Van Leer solutions are nearly identical.

Case 4 is the $M_1 = 5$ inviscid, two-dimensional calculation of reacting air through the same supersonic inlet. The air chemistry model is the same as that used in case 2. The inlet conditions are $V_1 = 6095\, m/s$, $T_1 = 3573\,^0K$ and initial species densities in kg/m^3 of 0.0651 for N_2, 0.00860 for O_2, 0.00556 for NO, 1.22×10^{-5} for N and 0.00900 for O. Figures 6.7a and 6.7b show the non-dimensional pressure and temperature distributions respectively on the lower wall ramp for the KFVS, Roe and Van Leer schemes on the 101×51 grid. The pressure distributions for the three schemes are nearly identical except in the post-shock region where each scheme exhibits a numerical overshoot. Here, the KFVS overshoot is slightly less than that of the Van Leer scheme and slightly larger than the overshoot produced by the Roe scheme. The temperature distributions produced by the three schemes are also very similar. Here, the Roe solution exhibits the largest post-shock oscillation while again the KFVS and Van Leer schemes produce nearly identical results. The Roe scheme produces a higher value of temperature past the expansion compared to the two flux-vector splitting schemes. The flux-split results for this case with equilibrium chemistry are found in Ref. [90].

Case 5 is a viscous perfect air calculation over a 10 degree cone at zero angle-of-attack. Here, the assumption of conical flow reduces the problem to a one-dimensional calculation in the radial direction from the cone. The parameters for this case are $M_1 = 7.95$, $Re = 0.42 \times 10^6$, and $Pr = 0.72$. Also, a no-slip, adiabatic-wall boundary condition is used. The results of this case allow a study of the interfer-

ence of numerical dissipation of the flux-vector splitting scheme with the modeling of physical dissipation. Because of the adiabatic-wall condition the scheme must provide the proper wall temperature of about 11.73. Figure 6.8a shows the dimensionless temperature profiles T/T_1 as a function of $\theta - \theta_c$ for a first order calculation with 51 grid points. The Roe solution for this case represents an essentially grid converged solution and produces a wall temperature that is very close to 11.73 while the KFVS and Van Leer solutions considerably thicken the boundary layer and leave significant over-prediction of the wall temperature. Also, the shock location for the KFVS and Van Leer schemes is further removed from the wall and is slightly thicker compared to the Roe solution. Figure 6.8b shows a the temperature profiles for a second order calculation with $\kappa = -1$ again for 51 grid points. Here, the KFVS and Van Leer solutions are greatly improved, while no further improvement is realized by the Roe scheme solution. The KFVS and Van Leer solutions are again very similar to each other and are now in much better agreement with the Roe solution. It is noted that the flux-vector splitting schemes require an additional grid point to capture the shock and now slightly underpredict wall temperature. The Roe and Van Leer solutions for this case agree with those in Ref. [91].

Case 6 is the two-dimensional viscous simulation of Mach 5 flow over a 20^0 wedge in premixed hydrogen-air. The premixed fuel/oxidizer mixture is taken as stoichiometric, (*i.e.*, $2H_2 + O_2 + 3.76N_2$). The conditions at the inflow are $T_1 = 800\,^0K$ and $p_1 = 101325\,N/m^2$. The calculations were carried out on a 51×61 grid with a stretching factor of $\beta = 1.02$. Calculations were performed using the locally third-order accurate upwind biased MUSCL differencing scheme ($\kappa = 1/3$) with the MIN-MOD limiter. Extrapolation boundary conditions were used at the outflow boundaries and a no-slip adiabatic wall boundary condition was imposed on the wedge surface. The chemistry model for this case is the 7 species, 7 reaction hydrogen-air

combustion model of Drummond, Rogers, and Hussaini [20] that was described in Sec. 4.4.2. The individual species viscosities were determined from Sutherland's law, and the mixture viscosity was obtained from the species values and Wilke's law. The mixture thermal conductivity and diffusivities were obtained using the mixture viscosity and specifying constant Prandtl and Schmidt numbers of .72 and .22 respectively. Singh, Carpenter and Kumar [92] have performed a detailed numerical of this problem for the purpose of studying the structural stability of the oblique detonation wave. In their work no unstable temporal modes were isolated, and it was concluded that for engineering purposes the oblique detonation wave is a stable phenomena for sufficient levels of overdrive [92]. It is the objective of the present work to perform a detailed flowfield analysis using the KFVS scheme that includes viscous effects and finite-rate-chemistry at hypersonic speeds. No attempt is made to address the stability issue.

Figures 6.9a and 6.9b shows the temperature and water mass fraction contours respectively for the KFVS scheme. From the temperature contours, the shock wave and boundary layer are clearly visible. As the flow passes through the shock the increased temperature is sufficient to ignite the mixture, however, because of the finite characteristic time for the chemistry and the high flow velocities, the reactions occur only after a fluid element has traveled a significant distance past the shock (*i.e.*, the induction distance). This causes a separation between the shock and the flame front called the induction zone. The flame front is also apparent from the temperature contours, and shows up as an increase in temperature behind the shock due to the exothermic nature of the hydrogen-air combustion. The temperature inside the boundary layer is very high because of viscous effects as well as combustion and is about twice the peak temperature in the inviscid region. The water contours show the flame front initially located in the boundary layer

and later curving up behind the shock wave and nearly becoming parallel to it. Because of the very high temperatures in the boundary layer dissociation occurs resulting in a decrease in the water mass fraction very near the wall. Figure 6.10a shows non-dimensional temperature profiles along $j = 1$, $j = 11$, $j = 21$, and $j = 41$ grid lines. Considering the $j = 41$ grid line, located in the inviscid region, one sees the abrupt increase in temperature behind the shock and the relatively constant temperature through the induction zone. A further increase in temperature is then observed due to the combustion processes. The $j = 1$ grid line shows the relatively high temperatures in the boundary layer as compared to the inviscid portion of the flow. Figure 6.10b shows water mass fraction profiles along the same j=constant grid lines. Along the $j = 21$ and $j = 41$ grid lines one sees the rapid production of water through the flame front and then the relatively slow adjustment to the equilibrium value. The slightly lower values of water mass fraction seen along grid lines $j = 1$ and $j = 11$ are a result of dissociation. Essentially identical results have been obtained using the Van Leer flux-vector splitting scheme and these results agree with those obtained from the CFD code GASP [93]. The results presented here show the same trends as predicted by Singh, Carpenter and Kumar [92], however, the shock wave shown in Fig. 6.9a does not exhibit the same upward curvature as predicted in their study.

Case 7 includes inviscid perfect gas simulations with the KFVS scheme. First is the Mach .85 inviscid flow through a channel with a bump on the lower wall. Riemann boundary conditions are used at the inflow and outflow boundaries and flow tangency was enforced at the wall along with imposing that the wall enthalpy, entropy, and pressure are equal to that at the first point off the wall. Figure 6.11a shows pressure contours for a KFVS solution on grid with 61 grid points in the axial direction and 31 grid points in the normal direction. Next, the supercritical

flow around a NACA 0012 airfoil at $M_\infty = .8$ and zero angle-of-attack has been considered. Again Riemann boundary conditions are used at the farfield and the usual inviscid wall boundary conditions are imposed on the airfoil surface. Figure 6.11b shows pressure contours for a KFVS solution 145×33 C-grid. Both cases exhibit qualitatively correct solutions with crisp shock waves.

6.6 Conclusions

A new kinetic flux-vector splitting scheme has been developed for flows in chemical and thermal non-equilibrium. The Euler scheme has been derived by taking moments of a discretized Boltzmann scheme with a flux-split, locally Maxwellian velocity distribution. This method differs from existing flux-splitting schemes in that the fluxes are split at the kinetic level based on particle velocity and then averaged over velocity space whereas traditional schemes use a splitting based on the eigenvalues of the flux Jacobian at the Euler level.

The KFVS scheme has been compared with the flux-vector scheme of Van Leer and the flux-difference splitting scheme of Roe for a series of test cases. In all cases the KFVS scheme compares very closely with the Van Leer scheme, showing excellent shock capturing properties. However, in the quasi-one-dimensional results the KFVS scheme appears to smear the shock slightly more than the Roe scheme for a first-order calculation. Higher-order calculations agree much better. The Roe solution on the cone exhibits much better grid convergence and is much more accurate in the boundary layer than either the KFVS or Van Leer scheme. The results show that even though the KFVS scheme may be expressed as a Riemann solver at the kinetic level its behavior at the Euler level is more similar to the the existing flux-vector splitting algorithms than to the flux-difference scheme of Roe.

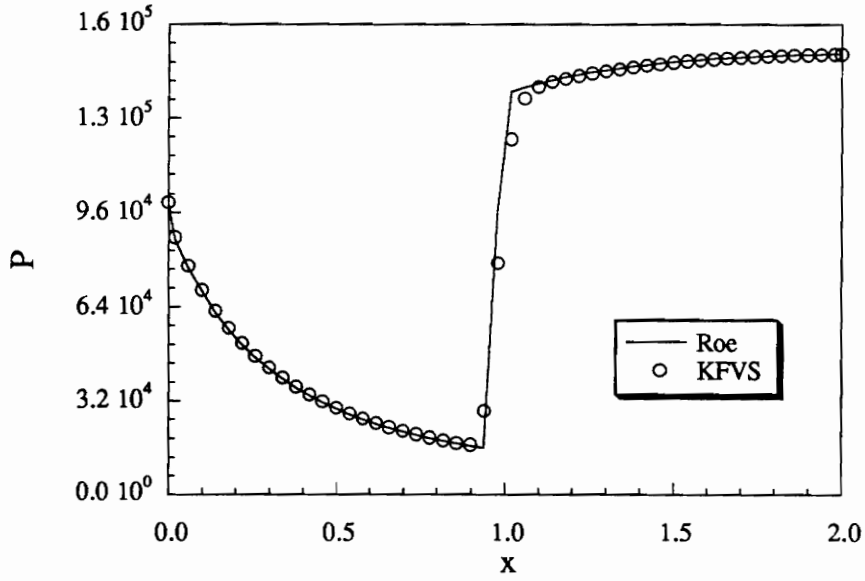

6.1a – Pressure distribution

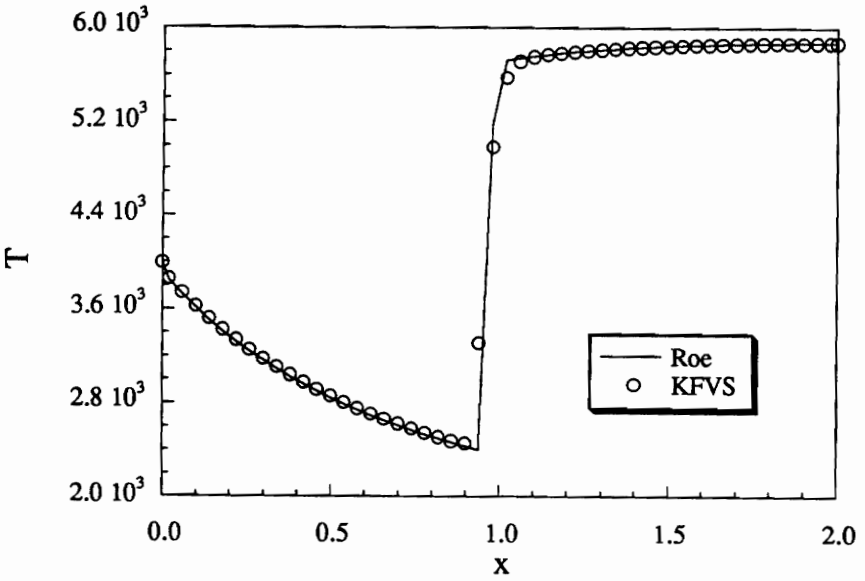

6.1b – Temperature distribution

Fig. 6.1 – Supersonic channel with perfect air, 51 grid points, 1st-order

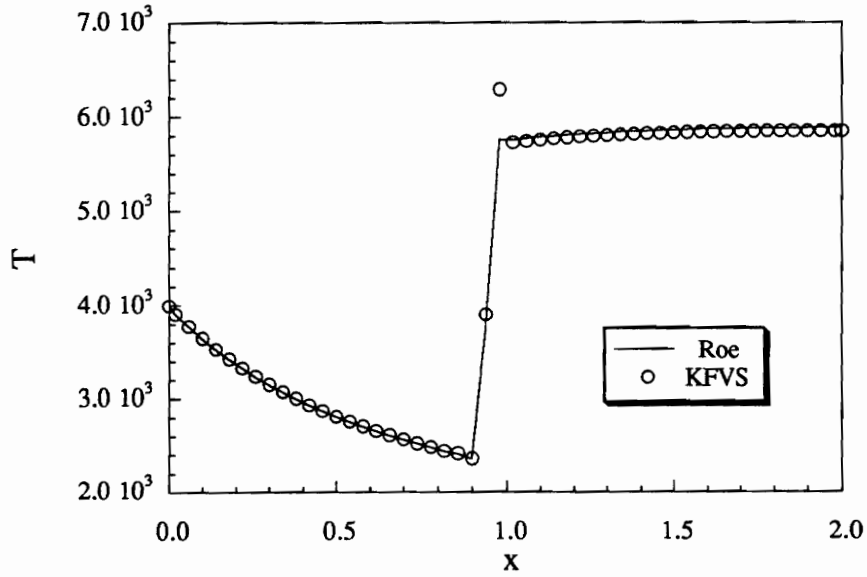

6.2a – Temperature distribution, MIN-MOD limiter

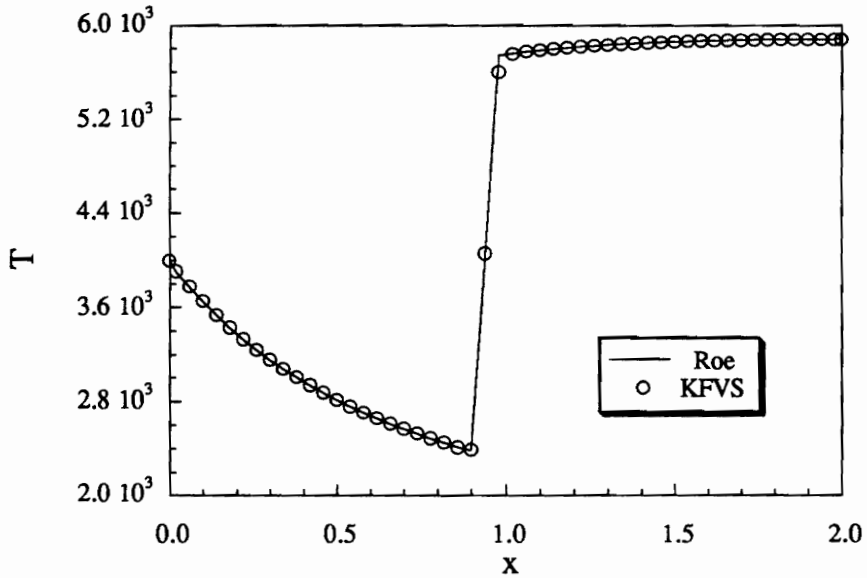

6.2b – Temperature distribution, Van Albeda limiter

Fig. 6.2 – Supersonic channel with perfect air, 51 grid points, 3rd-order

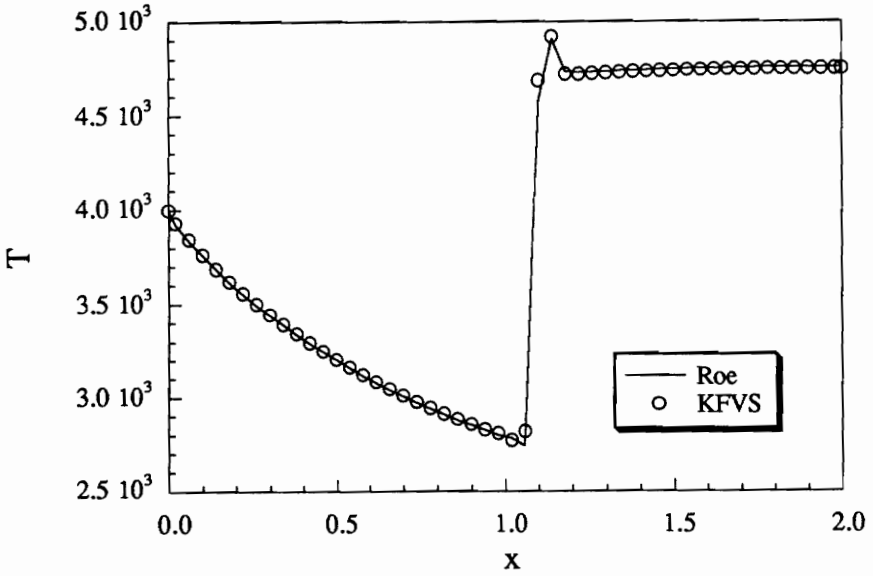

6.3a – Temperature distribution, 51 grid points

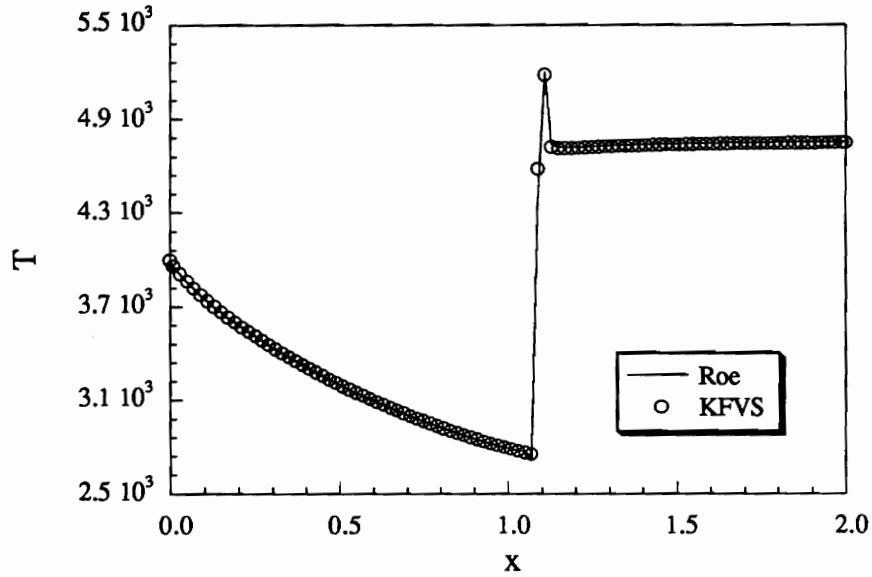

6.3b – Temperature distribution, 101 grid points

Fig. 6.3 – Supersonic channel with air chemistry, 3rd-order, Min-Mod limiter

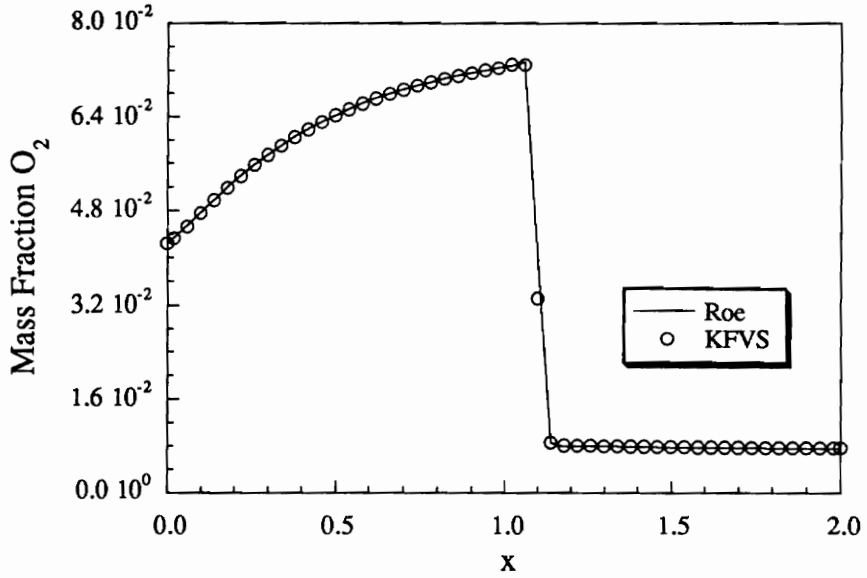

6.4a – O_2 mass fraction distribution, 51 grid points

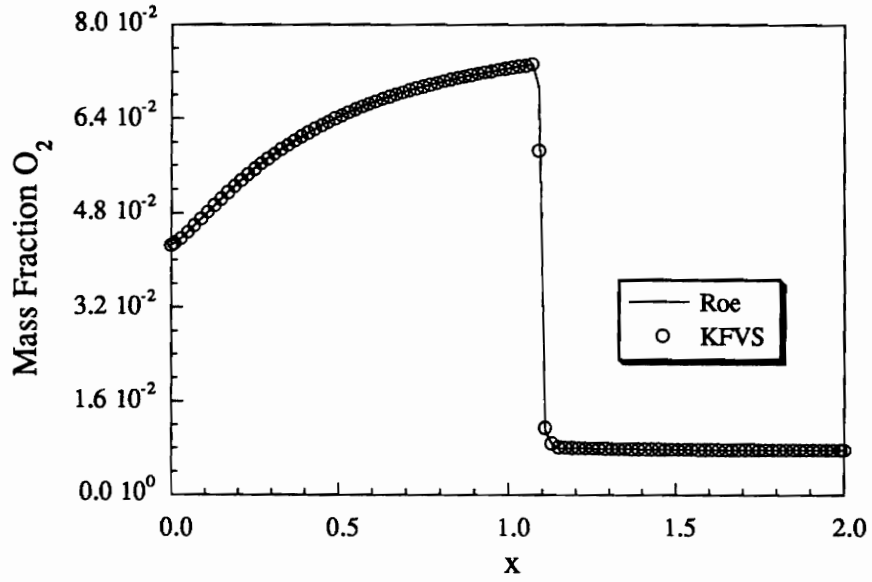

6.4b – O_2 mass fraction distribution, 101 grid points

Fig. 6.4 – Supersonic channel with air chemistry, 3rd-order, Min-Mod limiter

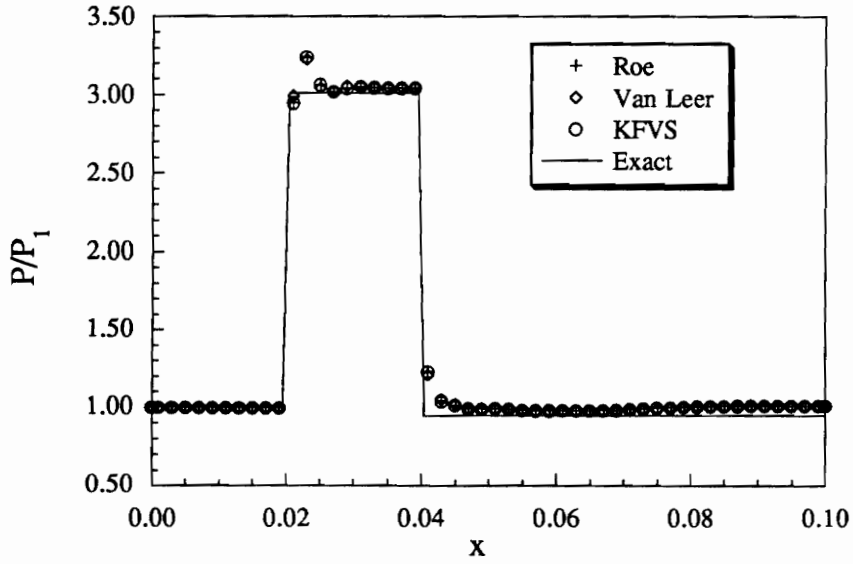

6.5a – Normalized pressure distribution

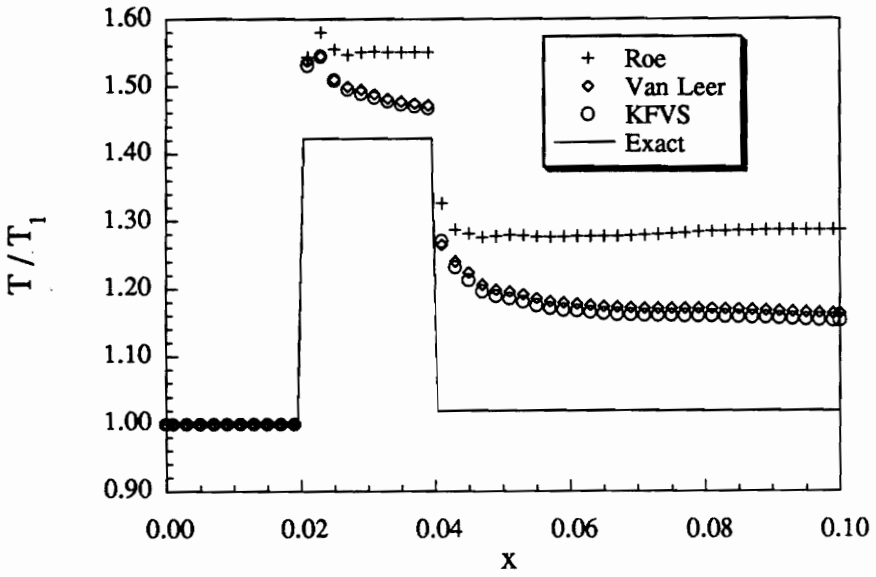

6.5b – Normalized temperature distribution

Fig. 6.5 – 10^0 ramp with perfect air, 2nd-order, 51 grid points

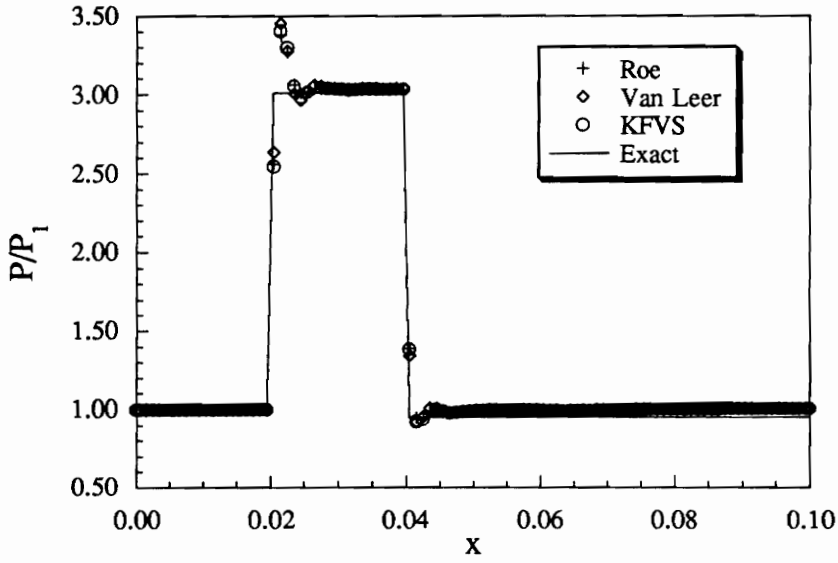

6.6a – Normalized pressure distribution

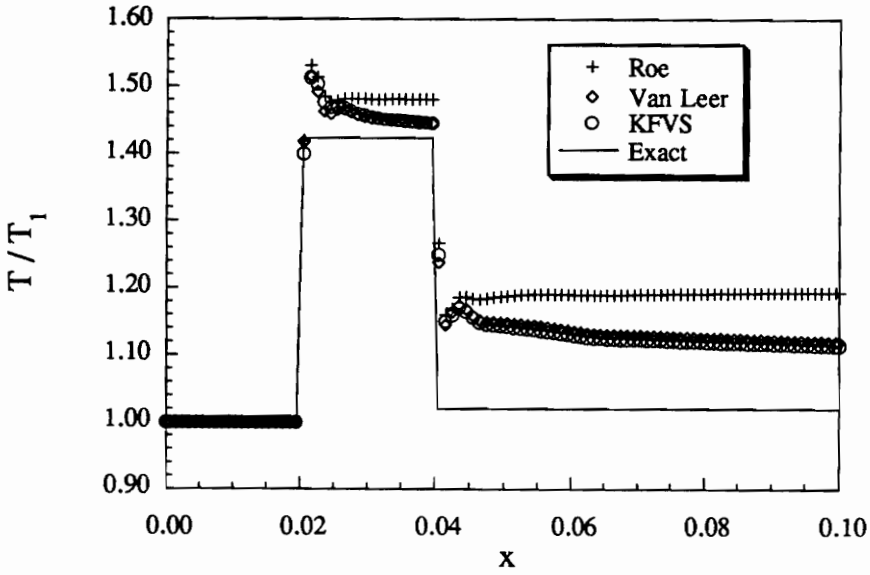

6.6b – Normalized temperature distribution

Fig. 6.6 – 10^0 ramp with perfect air, 2nd-order, 101 grid points

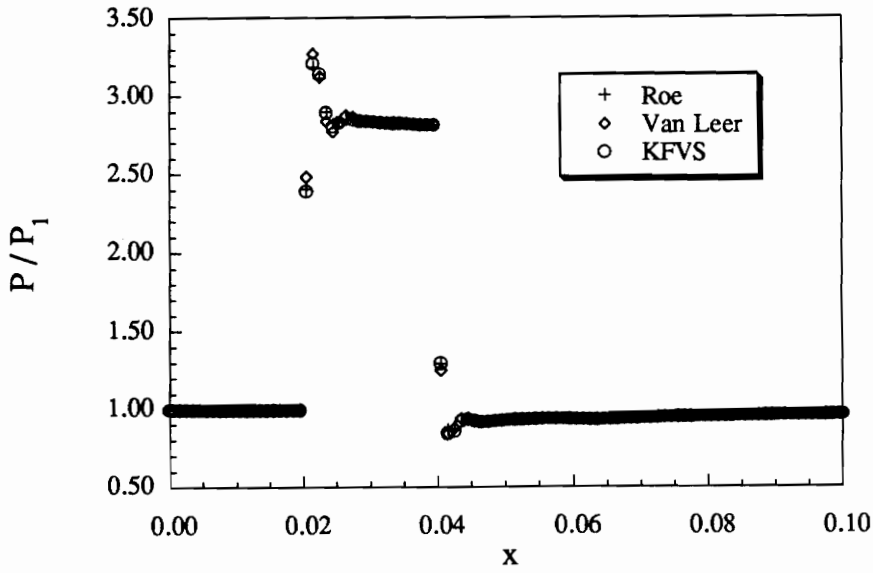

6.7a – Normalized pressure distribution

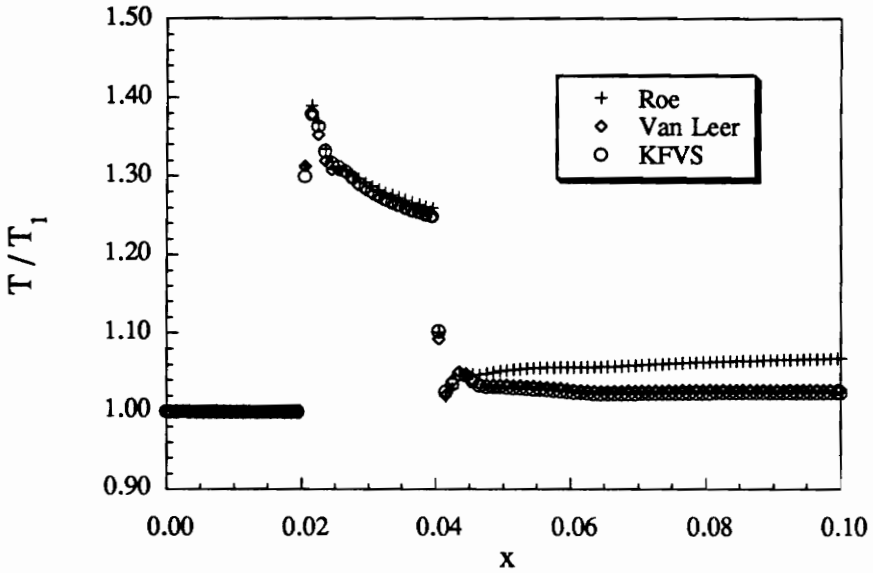

6.7b – Normalized temperature distribution

Fig. 6.7 – 10^0 ramp with air chemistry, 2nd-order, 101 grid points

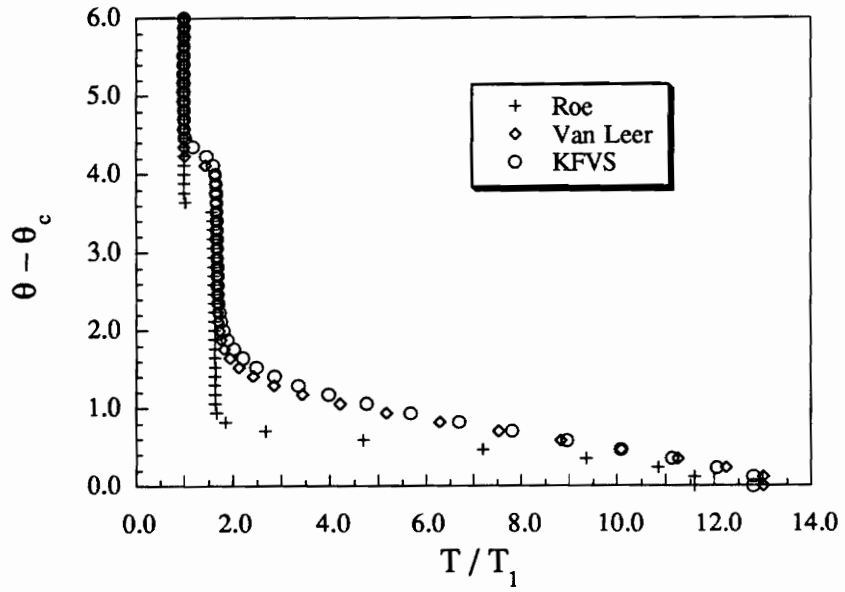

6.8a – Normalized temperature distribution, 1st-order

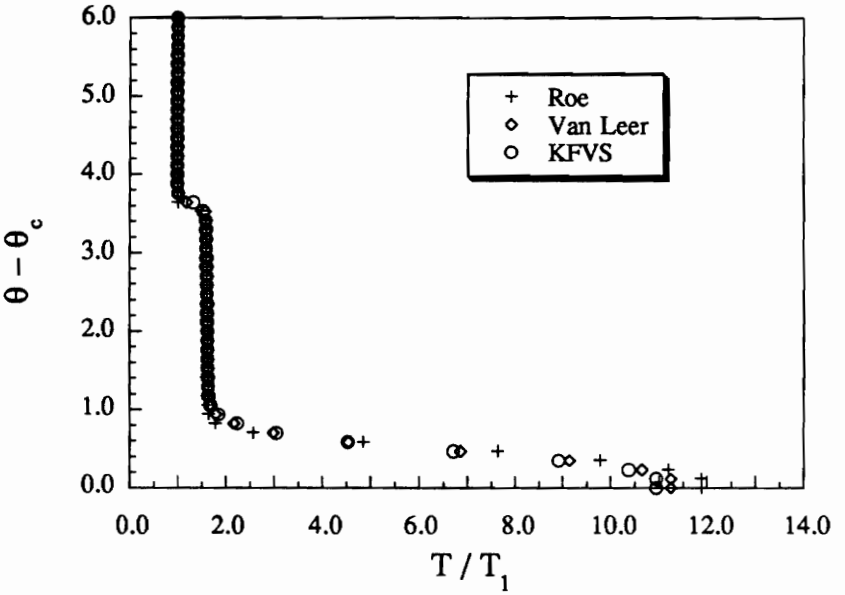

6.8b – Normalized temperature distribution, 2nd-order

Fig. 6.8 – Mach 7.95, 10^0 cone with perfect air, 51 grid points

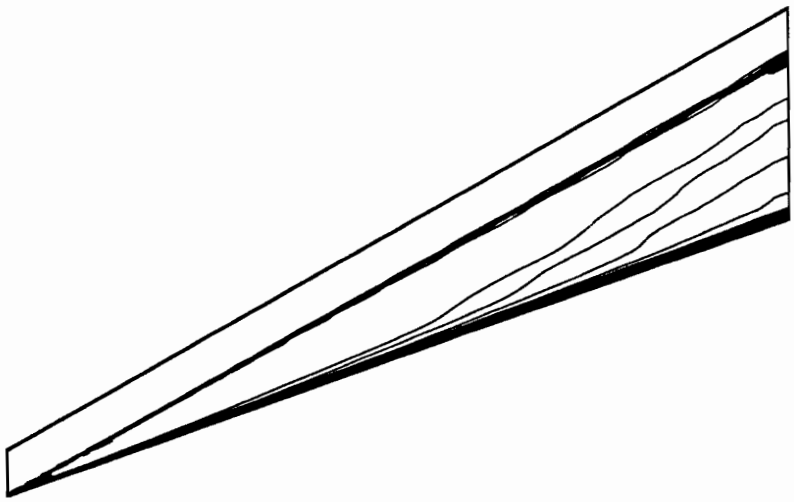

6.9a – Temperature Contours

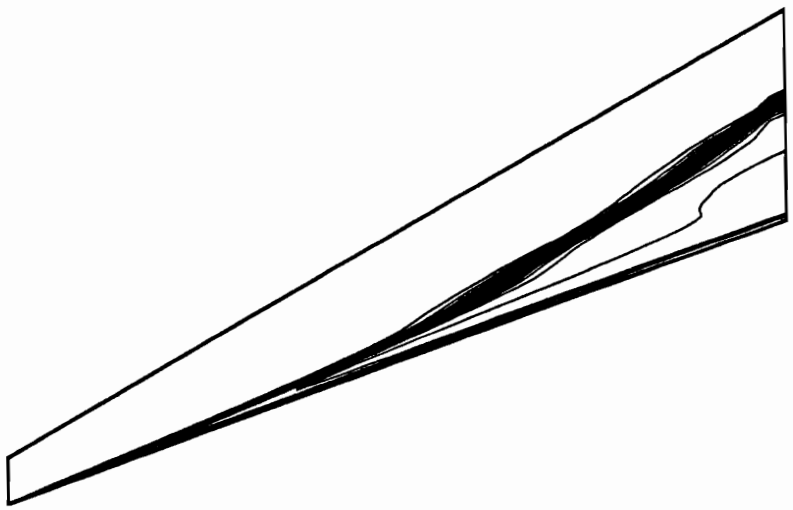

6.9b – H_2O mass fraction Contours

Fig. 6.9 – Mach 5, 20^0 wedge with hydrogen-air chemistry

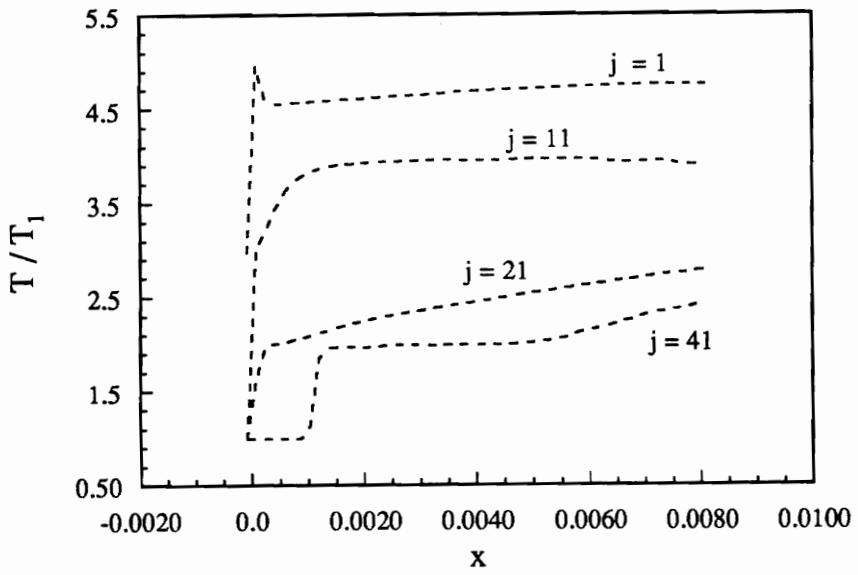

6.10a – Normalized temperature along various j=const. grid lines

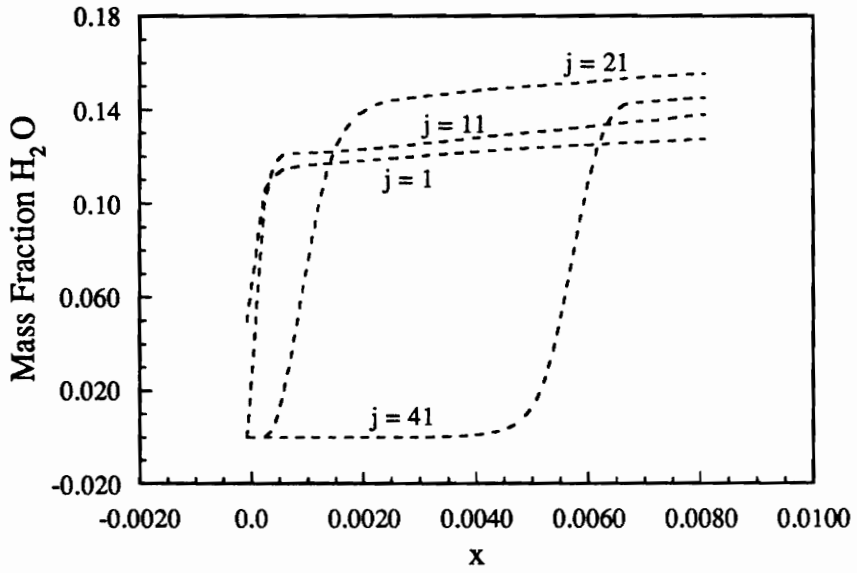

6.10b – H_2O mass fraction along various j=const. grid lines

Fig. 6.10 – Mach 5, 20^0 wedge with hydrogen-air chemistry

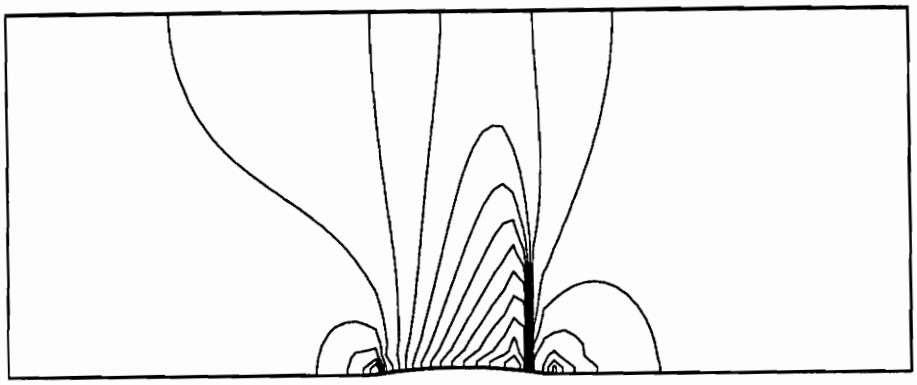

6.11a – Mach 0.85 flow over bump in channel, 61×31 grid

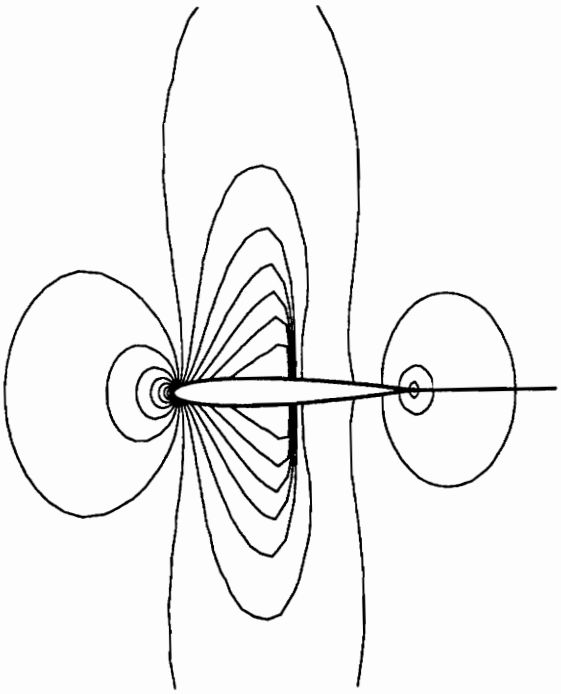

6.11b – Mach 0.80 flow around NACA 0012 airfoil, 145×33 grid

Fig. 6.11 – Pressure contours for transonic flow cases

Chapter 7

Multi-Dimensional Fluctuation-Splitting Methods

7.1 Introduction

The present state of the art for upwind Euler solvers in multiple dimensions involves using current one-dimensional upwind technology in a directionally-split approach. Treating the flowfield in this directionally-split manner yields grid dependent schemes that have limited regard to the physical features of the flow and results in poor resolution of shock and shear waves when they are oriented oblique to the computational grid. Consequently, excessive numbers of grid points and associated large amounts of computational time and memory are required to accurately resolve the important flow features. This problem is magnified for calculations involving chemical and thermal non-equilibrium since additions rate equations must be solved in a coupled fashion, and the species densities and non-equilibrium energies must be stored at each grid point. Advanced upwind solvers should incorporate truly multi-dimensional ideas based on more realistic physical models so that accurate numerical simulations may be carried out using as few grid points as possible.

The most promising work toward the development of genuinely multidimensional upwind Euler solvers [28–32] has been centered around the generalization of Roe's one-dimensional scheme. The basic concepts underlying the extension of Roe's scheme for two and three dimensions have been outlined in Struijs [32] *et al.* Here, a discrete wave structure is determined based on an eigenvector decomposition of the divergence of the flux vector and a conservative linearization procedure

for triangles and tetrahedra. This step is not uniquely determined as in the one-dimensional case, and several wave recognition models have been proposed. At this stage, the orientation and advection speed is known for each discrete wave in terms of the unknowns at the cell vertices, and each simple wave is governed by a separate linear scalar advection equation. The solution is now advanced in time in an explicit manner using multi-dimensional fluctuation-splitting schemes for the scalar advection equation, whereby decomposed portions of the flux balance are distributed to the vertices of the computational cell. As a result, the numerical behavior of the system is governed completely by the characteristics of these scalar distribution schemes. In Ref. [32] two scalar advection schemes for triangular cells have been considered. The first scheme, called the N-scheme, is the optimal (allows the maximum time step and has the most narrow stencil) linear scheme satisfying positivity. It is at most first-order accurate in space. The second scheme is a non-linear variant of the N-scheme, termed the NN-scheme, and is both positive and second order in space. Positivity is an important characteristic since it prohibits the occurrence of new extrema and allows these schemes to maintain monotone profiles across discontinuities without the need for limiters. Positivity also imposes stability on the explicit scheme. Preliminary results using these concepts [32,33] have shown improvements in shock capturing compared to standard solvers. Although these schemes have great potential, more work is needed in the wave modeling stage [32,34].

In this chapter a multi-dimensional upwind Euler solver is presented that has been developed from the Boltzmann equation for the kinetic theory of gases. The scheme uses a cell-vertex finite-volume approach along with residual distribution strategies to send portions of the decomposed flux residual (at the Euler level) to the vertices of the cells depending on the orientation and advection speed of

waves at the kinetic level. The present work has largely been motivated by the work of the aforementioned researchers and would not have been possible without their contributions. Of particular significance is the development of the multi-dimensional schemes for the scalar advection equation.

As shown in Sec. 6.4.1.1, the Boltzmann equation for a single species gas in local translational equilibrium and subject to zero body forces reduces to the homogeneous scalar advection equation in terms of the Maxwellian velocity distribution function (see Eq. (6.17)). Hence, for this case, the multi-dimensional fluctuation-splitting schemes for the advection equation (*i.e.*, the N-scheme and the NN-scheme) may be used to discretize the Boltzmann equation. This is essentially the same procedure as used to develop the KFVS scheme, except now a multi-dimensional discretization is used as opposed to a dimensionally-split discretization in the direction normal to a cell face. When the fluctuation-splitting schemes are applied to the Boltzmann equation they send appropriate fluctuations of the Maxwellian velocity distribution function to each of the cell vertices, and the resulting Euler schemes are obtained as moments of these fluctuations. The development is significantly more complicated than standard dimensionally-split kinetic schemes in that the Boltzmann discretization now depends upon the direction of the molecular velocities which must be accounted for in the limits of integration in velocity space. The details of the theoretical approach are described in the following sections and the resulting Euler schemes will be presented. It is important to note that an explicit wave decomposition model is not required for the development of Euler schemes with this approach.

The Euler solvers presented in this chapter have been developed by applying the N-scheme to triangulated Cartesian grids in two space dimensions. As a result, the schemes will only be first-order accurate in space. The extension to the NN-scheme,

for higher-order spatial accuracy, appears to be much more complex because of the non-linear nature of this scheme. More work will be necessary in this area before algorithms of this type reach a useful level.

7.2 Scalar Advection Schemes

In this section the basic framework for the fluctuation-splitting schemes is presented as applied to the Boltzmann equation. The development shown here closely follows that of Struijs *et al.* in Ref. [32]. As previously mentioned, when considering flows in local translational equilibrium with negligible body forces (*i.e.*, Euler flows) the Boltzmann equation reduces to the homogeneous scalar advection equation in terms of the Maxwellian velocity distribution function. For this case the integral form of the Boltzmann equation for an arbitrary volume δV with surface area δS, and inward pointing unit normal vector $\hat{\mathbf{n}}$ is given by

$$\frac{\partial}{\partial t}\iiint_{\delta V} nf_0 dV = \oint_{\delta S} (\bar{\mathbf{c}}\cdot\hat{\mathbf{n}}) nf_0 dS\,. \tag{7.1}$$

Using a finite-volume approach, the integral form given in Eq. (7.1) is applied to an arbitrary triangular cell T in two space dimensions as shown in Fig. 7.1. For a piecewise linear representation of nf_0 the flux residual on the right-hand side of Eq. (7.1), denoted ϕ_T, becomes

$$\phi_T = \frac{1}{2}[(nf_0)_1 + (nf_0)_2]\bar{\mathbf{c}}\cdot\bar{\mathbf{n}}_3 + \frac{1}{2}[(nf_0)_2 + (nf_0)_3]\bar{\mathbf{c}}\cdot\bar{\mathbf{n}}_1 + \frac{1}{2}[(nf_0)_3 + (nf_0)_1]\bar{\mathbf{c}}\cdot\bar{\mathbf{n}}_2\,. \tag{7.2}$$

Here, the $\bar{\mathbf{n}}_i$'s represent normal vectors that have been scaled with the corresponding edge length E_i such that

$$\bar{\mathbf{n}}_i = \hat{\mathbf{n}}_i E_i \qquad i = 1,2,3\,. \tag{7.3}$$

It is noted that when $\bar{\mathbf{c}}\cdot\bar{\mathbf{n}}_i$ is positive then flow enters the triangle through side E_i and so on. Alternate forms for the flux residual may be obtained by making use of

the fact that for any triangle

$$\bar{\mathbf{n}}_1 + \bar{\mathbf{n}}_2 + \bar{\mathbf{n}}_3 = \bar{\mathbf{0}}\,. \tag{7.4}$$

The alternative forms that will be useful are

$$\phi_T = -\frac{1}{2}\sum_{i=1}^{3}(nf_0)_i \bar{\mathbf{c}}\cdot\bar{\mathbf{n}}_i\,, \tag{7.5}$$

and

$$\phi_T = -\frac{\bar{\mathbf{c}}\cdot\bar{\mathbf{n}}_1}{2}[(nf_0)_1 - (nf_0)_3] - \frac{\bar{\mathbf{c}}\cdot\bar{\mathbf{n}}_2}{2}[(nf_0)_2 - (nf_0)_3]\,, \tag{7.6a}$$

$$= -\frac{\bar{\mathbf{c}}\cdot\bar{\mathbf{n}}_2}{2}[(nf_0)_2 - (nf_0)_1] - \frac{\bar{\mathbf{c}}\cdot\bar{\mathbf{n}}_3}{2}[(nf_0)_3 - (nf_0)_1]\,, \tag{7.6b}$$

$$= -\frac{\bar{\mathbf{c}}\cdot\bar{\mathbf{n}}_3}{2}[(nf_0)_3 - (nf_0)_2] - \frac{\bar{\mathbf{c}}\cdot\bar{\mathbf{n}}_1}{2}[(nf_0)_1 - (nf_0)_2]\,. \tag{7.6c}$$

In the present analysis, schemes are considered where a given triangle can send contributions *only* to its own vertices. This feature leads to compact schemes where a meshpoint receives updates only from triangles that have this point as a vertex. The general distribution scheme for each triangle is carried out as the following updates for each vertex

$$(nf_0)_i^{\,n+1} = (nf_0)_i^{\,n} + \frac{\alpha_i{}^T}{S_i}\Delta t\,\phi_T \qquad i = 1,2,3\,, \tag{7.7}$$

where S_i is the median dual cell (1/3 the area of all triangles having i as a vertex) and the α_i's are the upwinding parameters which depend on the wave speed (*i.e.*, the molecular velocity) and its orientation with respect to the cell geometry. The scheme is consistent providing

$$\sum_{i=1}^{3}\alpha_i{}^T = 1\,. \tag{7.8}$$

The global scheme is obtained by summing the contributions from all triangles T meeting at vertex i

$$(nf_0)_i^{\,n+1} = (nf_0)_i^{\,n} + \frac{\Delta t}{S_i}\sum_T \alpha_i{}^T\,\phi_T\,. \tag{7.9}$$

Different fluctuation-splitting schemes may be obtained depending on how the upwind parameters α_i are determined. In the following two subsections the N-scheme and the NN-scheme are described. Complete details are presented for the N-scheme while the NN-scheme is only discussed. The details for the NN-scheme are not included here and may found in Ref. 32.

7.2.1 N-Scheme

The N-scheme distinguishes between triangles with one or two inflow sides as illustrated in Fig. 7.2. For example, consider the triangle in Fig. 7.2a with one inflow side E_3 such that $\bar{c}\cdot\bar{n}_3 > 0$, $\bar{c}\cdot\bar{n}_1 < 0$, and $\bar{c}\cdot\bar{n}_2 < 0$. Here, the entire fluctuation is sent to the downstream node 3 such that $\alpha_1 = \alpha_2 = 0$, and $\alpha_3 = 1$, giving

$$(nf_0)_3^{n+1} = (nf_0)_3^{n} - \frac{\Delta t}{S_3}\left\{-\frac{\bar{c}\cdot\bar{n}_1}{2}[(nf_0)_1 - (nf_0)_3] + \frac{\bar{c}\cdot\bar{n}_2}{2}[(nf_0)_2 - (nf_0)_3]\right\}, \tag{7.10}$$

where Eq. (7.6a) has been utilized. Since $\bar{c}\cdot\bar{n}_1$ and $\bar{c}\cdot\bar{n}_2$ are negative, the update is locally positive for

$$\Delta t \le \frac{2S_3}{\bar{c}\cdot\bar{n}_3}. \tag{7.11}$$

This update is also linearity preserving. That is, for an exact linear solution the updating vanishes and second-order spatial accuracy can be obtained on uniform Cartesian grids. A triangle with two inflow sides E_1 and E_2 such that $\bar{c}\cdot\bar{n}_1 > 0$, $\bar{c}\cdot\bar{n}_2 > 0$, and $\bar{c}\cdot\bar{n}_3 < 0$ is shown in Fig. 7.2b. Here, no portion of the fluctuation is sent to node 3 and the following updates have been shown to be optimal [32]

$$(nf_0)_1^{n+1} = (nf_0)_1^{n} - \frac{\Delta t}{S_1}\left\{-\frac{\bar{c}\cdot\bar{n}_1}{2}[(nf_0)_1 - (nf_0)_3]\right\}, \tag{7.12a}$$

$$(nf_0)_2^{n+1} = (nf_0)_2^{n} - \frac{\Delta t}{S_2}\left\{-\frac{\bar{c}\cdot\bar{n}_2}{2}[(nf_0)_2 - (nf_0)_3]\right\}. \tag{7.12b}$$

Again, Eq. (7.6a) has been utilized, and the portions sent to nodes 1 and 2 are based on velocity components along E_1 and E_2 respectively. This updating is locally

positive for

$$\Delta t \leq \min \left[\frac{2S_1}{\bar{c} \cdot \bar{n}_1}, \frac{2S_2}{\bar{c} \cdot \bar{n}_2}\right]. \tag{7.13}$$

It may be shown that individually the two updates given by Eqs. (7.12a) and (7.12b) do not vanish for a linear solution, and will send updates that will destroy an exact linear solution. As a result, the N-scheme is not linearity preserving and is only first-order accurate in space. It has been shown in general, that linear schemes cannot be both positive and linearity preserving. This is a generalization of Gudonov's theorem that states the incompatibility between monotone preserving and second-order accuracy for linear schemes. In comparison, the upwind schemes described in Chap. 6 are linear and linearity preserving but lack the property of positivity. As a result, these schemes produce less numerical diffusion as compared to linear and positive schemes, but cannot preserve monotone profiles through discontinuities.

When applying the N-scheme to Cartesian grids, the choice of the diagonal for the Cartesian triangulation becomes an important factor. This issue is discussed in Ref. [32]. For instance, when the convection velocity $\bar{c}$ is oriented such that its projection onto the diagonal maximized, as shown in Fig. 7.3a, the N-scheme becomes the optimal most compact linear positive scheme on a Cartesian mesh. This scheme is known as the streamlined upwind scheme of Rice and Schnipke [94]. When the projection of $\bar{c}$ onto the diagonal approaches a minimum, as shown in Fig. 7.3b, the N-scheme reduces to the more dissipative dimensionally-split first-order upwind scheme. Hence, the orientation of the diagonal will play a large role in determining the quality of numerical solutions on Cartesian meshes. As a result, Euler schemes will be developed for both diagonal orientations and an adaptive strategy will be considered, where the appropriate diagonal is chosen based on the

orientation of the convection velocity.

7.2.2 NN-Scheme

The NN-scheme is a non-linear variant of the N-scheme, and will have the properties of positivity as well as linearity preservation. For triangles with only one inflow side no modification to the N-scheme is necessary, since the updating given by Eq. (7.10) is already linearity preserving. For triangles with two inflow sides, the updates in Eqs. (7.12a) and (7.12b) are not linearity preserving and alternate forms must be considered. This problem may be remedied by replacing $\bar{c}$ with the gradient dependent convection velocity given by

$$\bar{c}_g = (\bar{c} \cdot \bar{g})\, \bar{g}\,, \tag{7.14a}$$

where

$$\bar{g} = \frac{\bar{\nabla} f_0}{|\, \bar{\nabla} f_0 \,|}\,. \tag{7.14b}$$

This does not change the residual since it may be shown that

$$\bar{c}_g \cdot \bar{\nabla} f_0 = \bar{c} \cdot \bar{\nabla} f_0\,. \tag{7.15}$$

Further details of the NN-scheme are presented in Ref. [32].

7.3 Kinetic-Based Euler Schemes

Multi-dimensional Kinetic Fluctuation-Splitting (MKFS) schemes have been developed for the Euler equations by applying the N-scheme to structured uniform Cartesian grids [35]. Three different multi-dimensional schemes have been considered based on the different Cartesian triangulations as shown in Fig. 7.4. The first scheme, denoted the NDD scheme, is derived for the triangulation shown in Fig. 7.4a with the diagonal going downward to the right. The second scheme is derived for the triangulation shown in Fig. 7.4b with the diagonal going upward

to the right, and is called as the NDU scheme. Finally, a diagonal-adaptive scheme is presented where the diagonal is chosen to be either up or down based on the orientation of the molecular velocity. This scheme is denoted the NDA scheme.

7.3.1 MKFS-NDD Scheme

The MKFS-NDD scheme is based on a triangulation with the diagonal pointed down to the right. The global and local numbering systems are shown in Fig. 7.4a. Fluctuations in nf_0 are determined locally by applying the N-scheme, for a given molecular velocity, to both triangles separately. These values are then summed together to obtain the appropriate fluctuations for the rectangular cell at the global level. As previously mentioned, it is necessary for the N-scheme to recognize which sides of the triangle are inflow sides. For an arbitrary triangle six distinct cases can occur depending on the wave orientation and the cell geometry. For example, the triangle below the diagonal in Fig. 7.4a (composed of vertices 1,2,3) may have only one inflow side (either 1, 2 or 3), or combinations of two inflow sides (1 and 2, 1 and 3, or 2 and 3) depending on the direction of the molecular velocity and the spacings in the x_1 and x_2 directions (Δx_1 and Δx_2). For this simple geometry, it is easy to show that each of the six possible cases corresponds to a distinct portion of velocity space, and the resulting velocity-space decomposition is shown in Fig. 7.5a. The dashed line in Fig. 7.5a represents the spatial orientation of the diagonal and the inflow sides for each case are denoted in parentheses. The fluctuations for each velocity subspace are now determined using the N-scheme with Eq. (7.10) used for triangles with one inflow side and Eqs. (7.12a) and (7.12b) used for triangles with two inflow sides. The global fluctuations are listed below.

The fluctuations for Case 1, denoted $\Delta(nf_0)^{(1)}$, are given as

$$\Delta(nf_0)_{i,j}{}^{(1)} = -\frac{\Delta t}{S_{i,j}}\Big\{\frac{c_2\Delta x_1}{2}[(nf_0)_{i,j+1} - (nf_0)_{i,j}] + \frac{c_1\Delta x_2}{2}[(nf_0)_{i+1,j} - (nf_0)_{i,j}]\Big\}, \tag{7.16a}$$

$$\Delta(nf_0)_{i+1,j}{}^{(1)} = \frac{\Delta t}{S_{i+1,j}}\Big\{\frac{c_2\Delta x_1}{2}[(nf_0)_{i+1,j} - (nf_0)_{i+1,j+1}]\Big\}, \tag{7.16b}$$

$$\Delta(nf_0)_{i,j+1}{}^{(1)} = \frac{\Delta t}{S_{i,j+1}}\Big\{\frac{c_1\Delta x_2}{2}[(nf_0)_{i,j+1} - (nf_0)_{i+1,j+1}]\Big\}. \tag{7.16c}$$

It is noted that for Case 1 no fluctuation is sent to node $(i+1, j+1)$. Similarly, fluctuations for Case 2 are given by

$$\Delta(nf_0)_{i,j+1}{}^{(2)} = -\frac{\Delta t}{S_{i,j+1}}\Big\{-(\frac{c_1\Delta x_2 + c_2\Delta x_1}{2})[(nf_0)_{i,j} - (nf_0)_{i,j+1}] + c_1\Delta x_2[(nf_0)_{i+1,j} - (nf_0)_{i,j+1}]\Big\}, \tag{7.17a}$$

$$\Delta(nf_0)_{i+1,j+1}{}^{(2)} = -\frac{\Delta t}{S_{i+1,j+1}}\Big\{(\frac{c_1\Delta x_2 + c_2\Delta x_1}{2})[(nf_0)_{i+1,j+1} - (nf_0)_{i+1,j}]\Big\}. \tag{7.17b}$$

For Case 2 no contribution is sent to nodes (i, j) and $(i+1, j)$. The fluctuations for the other four cases are of similar form and are listed below

$$\Delta(nf_0)_{i+1,j}{}^{(3)} = -\frac{\Delta t}{S_{i+1,j}}\Big\{-(\frac{c_1\Delta x_2 + c_2\Delta x_1}{2})[(nf_0)_{i,j} - (nf_0)_{i+1,j}] + c_2\Delta x_1[(nf_0)_{i,j+1} - (nf_0)_{i+1,j}]\Big\}, \tag{7.18a}$$

$$\Delta(nf_0)_{i+1,j+1}{}^{(3)} = -\frac{\Delta t}{S_{i+1,j+1}}\Big\{(\frac{c_1\Delta x_2 + c_2\Delta x_1}{2})[(nf_0)_{i+1,j+1} - (nf_0)_{i,j+1}]\Big\}, \tag{7.18b}$$

$$\Delta(nf_0)_{i,j+1}{}^{(4)} = -\frac{\Delta t}{S_{i,j+1}}\Big\{-(\frac{c_1\Delta x_2 + c_2\Delta x_1}{2})[(nf_0)_{i+1,j+1} - (nf_0)_{j,i+1}] - c_2\Delta x_1[(nf_0)_{i+1,j} - (nf_0)_{i,j+1}]\Big\}, \tag{7.19a}$$

$$\Delta(nf_0)_{i,j}{}^{(4)} = \frac{\Delta t}{S_{i,j}}\Big\{(\frac{c_1\Delta x_2 + c_2\Delta x_1}{2})[(nf_0)_{i,j} - (nf_0)_{i+1,j}]\Big\}, \tag{7.19b}$$

$$\Delta(nf_0)_{i+1,j}{}^{(5)} = -\frac{\Delta t}{S_{i+1,j}}\Big\{(\frac{c_1\Delta x_2 + c_2\Delta x_1}{2})[(nf_0)_{i+1,j+1} - (nf_0)_{i+1,j}] - c_1\Delta x_2[(nf_0)_{i,j+1} - (nf_0)_{i+1,j}]\Big\}, \tag{7.20a}$$

$$\Delta(nf_0)_{i,j}{}^{(5)} = \frac{\Delta t}{S_{i,j}}\Big\{(\frac{c_1\Delta x_2 + c_2\Delta x_1}{2})[(nf_0)_{i,j} - (nf_0)_{i,j+1}]\Big\}, \tag{7.20b}$$

and

$$\Delta(nf_0)_{i+1,j+1}{}^{(6)} = -\frac{\Delta t}{S_{i+1,j+1}}\Big\{-\frac{c_2\Delta x_1}{2}[(nf_0)_{i+1,j} - (nf_0)_{i+1,j+1}] - \frac{c_1\Delta x_2}{2}[(nf_0)_{i,j+1} - (nf_0)_{i+1,j+1}]\Big\}, \tag{7.21a}$$

$$\Delta(nf_0)_{i+1,j}{}^{(6)} = -\frac{\Delta t}{S_{i+1,j}}\Big\{\frac{c_1\Delta x_2}{2}[(nf_0)_{i+1,j} - (nf_0)_{i,j}]\Big\}, \tag{7.21b}$$

$$\Delta(nf_0)_{i,j+1}{}^{(6)} = -\frac{\Delta t}{S_{i,j+1}}\Big\{\frac{c_2\Delta x_1}{2}[(nf_0)_{i,j+1} - (nf_0)_{i,j}]\Big\}. \tag{7.21c}$$

The criteria for global stability/positivity for the Cartesian scheme is given by

$$\Big(\frac{|\,c_1\,|}{\Delta x_1} + \frac{|\,c_2\,|}{\Delta x_2}\Big)\Delta t \le 1\,. \tag{7.22}$$

At the Euler level the total fluctuation in the conserved-variable vector, $\mathbf{Q}$, is given by moments of the fluctuations in the Maxwellian velocity distribution function

$$\Delta\mathbf{Q} = \int_{-\infty}^{\infty}\int_{-\infty}^{\infty}\int_{-\infty}^{\infty}\mathbf{\Psi}\Delta(nf_0)dc_1dc_2dc_3\,, \tag{7.23a}$$

where $\mathbf{\Psi}$ is the moment function vector given in Eq. (3.22). The integration over the entire velocity space can be broken into the integration over the six discrete velocity subspaces shown in Fig. 7.5a

$$\begin{aligned}\Delta\mathbf{Q} = \int_{-\infty}^{\infty}\Big\{&\int_{-\infty}^{0}\int_{-\infty}^{0}\mathbf{\Psi}\Delta(nf_0)^{(1)}dc_2dc_1 + \int_{-\infty}^{0}\int_{-c_1\alpha}^{\infty}\mathbf{\Psi}\Delta(nf_0)^{(2)}dc_2dc_1 \\ &+ \int_{0}^{\infty}\int_{-c_1\alpha}^{0}\mathbf{\Psi}\Delta(nf_0)^{(3)}dc_2dc_1 + \int_{-\infty}^{0}\int_{0}^{-c_1\alpha}\mathbf{\Psi}\Delta(nf_0)^{(4)}dc_2dc_1 \\ &+ \int_{0}^{\infty}\int_{-\infty}^{-c_1\alpha}\mathbf{\Psi}\Delta(nf_0)^{(5)}dc_2dc_1 + \int_{0}^{\infty}\int_{0}^{\infty}\mathbf{\Psi}\Delta(nf_0)^{(6)}dc_2dc_1\Big\}\,dc_3\end{aligned}\,, \tag{7.23b}$$

where α is the cell aspect ratio given by

$$\alpha = \frac{\Delta x_2}{\Delta x_1}\,. \tag{7.24}$$

The distribution scheme at the Euler level may now be determined as moments of the distribution scheme at the kinetic level and not all subspaces will contribute

to each node. For example, the fluctuation in $\mathbf{Q}$ at node (i,j), denoted $\Delta\mathbf{Q}_{i,j}$, has contributions from integration over velocity subspaces 1, 4, and 5 given by

$$\Delta\mathbf{Q}_{i,j} = \Delta\mathbf{Q}_{i,j}{}^{(1)} + \Delta\mathbf{Q}_{i,j}{}^{(4)} + \Delta\mathbf{Q}_{i,j}{}^{(5)}. \tag{7.25}$$

The fluctuation resulting from integration over velocity subspace 1, $\Delta\mathbf{Q}_{i,j}{}^{(1)}$, may be determined by substituting the fluctuation formula for $\Delta(nf_0)_{i,j}{}^{(1)}$, given by Eq. (7.16a), into the first integral of (7.23b)

$$\Delta\mathbf{Q}_{i,j}{}^{(1)} = \int_{-\infty}^{\infty}\int_{-\infty}^{0}\int_{-\infty}^{0} -\frac{\Psi\Delta t}{S_{i,j}}\Big\{\frac{c_2\Delta x_1}{2}[(nf_0)_{i,j+1} - (nf_0)_{i,j}] + \frac{c_1\Delta x_2}{2}[(nf_0)_{i+1,j} - (nf_0)_{i,j}]\Big\}dc_2dc_1dc_3\,. \tag{7.26a}$$

This fluctuation may be rewritten in terms of the moments $\mathbf{I}_D^1$ and $\mathbf{I}_D^2$ as

$$\Delta\mathbf{Q}_{i,j}{}^{(1)} = \frac{\Delta t\Delta x_2}{2S_{i,j}}(\mathbf{I}_{Di,j}^1 - \mathbf{I}_{Di+1,j}^1) + \frac{\Delta t\Delta x_1}{2S_{i,j}}(\mathbf{I}_{Di,j}^2 - \mathbf{I}_{Di,j+1}^2)\,, \tag{7.26b}$$

where

$$\mathbf{I}_D^1 = \int_{-\infty}^{\infty}\int_{-\infty}^{0}\int_{-\infty}^{0}\Psi c_1 nf_0 dc_2dc_1dc_3\,, \quad \mathbf{I}_D^2 = \int_{-\infty}^{\infty}\int_{-\infty}^{0}\int_{-\infty}^{0}\Psi c_2 nf_0 dc_2dc_1dc_3\,, \tag{7.27a,b}$$

and the subscript D denotes the downward-diagonal scheme. The fluctuations for $\Delta\mathbf{Q}_{i,j}{}^{(4)}$, and $\Delta\mathbf{Q}_{i,j}{}^{(5)}$ are determined in a similar manner by substituting Eq. (7.19b) and Eq. (7.20b) into the fourth and fifth integrals respectively in Eq. (7.23b). The fluctuation in $\mathbf{Q}$ at the other three nodes $\Delta\mathbf{Q}_{i+1,j}$,$\Delta\mathbf{Q}_{i,j+1}$,and $\Delta\mathbf{Q}_{i+1,j+1}$ have contributions given by

$$\Delta\mathbf{Q}_{i+1,j} = \Delta\mathbf{Q}_{i+1,j}{}^{(1)} + \Delta\mathbf{Q}_{i+1,j}{}^{(3)} + \Delta\mathbf{Q}_{i+1,j}{}^{(5)} + \Delta\mathbf{Q}_{i+1,j}{}^{(6)}\,, \tag{7.28a}$$

$$\Delta\mathbf{Q}_{i,j+1} = \Delta\mathbf{Q}_{i,j+1}{}^{(1)} + \Delta\mathbf{Q}_{i,j+1}{}^{(2)} + \Delta\mathbf{Q}_{i,j+1}{}^{(4)} + \Delta\mathbf{Q}_{i,j+1}{}^{(6)}\,, \tag{7.28b}$$

$$\Delta\mathbf{Q}_{i+1,j+1} = \Delta\mathbf{Q}_{i+1,j+1}{}^{(2)} + \Delta\mathbf{Q}_{i+1,j+1}{}^{(3)} + \Delta\mathbf{Q}_{i+1,j+1}{}^{(6)}\,. \tag{7.28c}$$

and are determined in the same fashion. The complete Euler scheme is given as

$$\Delta\mathbf{Q}_{i,j} = \frac{\Delta t\Delta x_2}{2S_{i,j}}[\mathbf{I}_{Di,j}^1 - \mathbf{I}_{Di+1,j}^1 + \mathbf{I}_{Di,j}^3 - \mathbf{I}_{Di+1,j}^3 + \mathbf{I}_{Di,j}^5 - \mathbf{I}_{Di,j+1}^5] + \frac{\Delta t\Delta x_1}{2S_{i,j}}[\mathbf{I}_{Di,j}^2 - \mathbf{I}_{Di,j+1}^2 + \mathbf{I}_{Di,j}^4 - \mathbf{I}_{Di+1,j}^4 + \mathbf{I}_{Di,j}^6 - \mathbf{I}_{Di,j+1}^6]\,, \tag{7.29a}$$

$$\Delta \mathbf{Q}_{i+1,j} = \frac{\Delta t \Delta x_2}{2S_{i+1,j}} \left[\mathbf{I}^7_{Di,j} - \mathbf{I}^7_{Di+1,j} - \mathbf{I}^5_{Di+1,j+1} + 2\mathbf{I}^5_{Di,j+1} - \mathbf{I}^5_{Di+1,j} - \mathbf{I}^9_{Di+1,j} + \mathbf{I}^9_{Di,j} \right]$$
$$+ \frac{\Delta t \Delta x_1}{2S_{i+1,j}} \left[\mathbf{I}^2_{Di+1,j} - \mathbf{I}^2_{Di+1,j+1} + \mathbf{I}^8_{Di,j} - 2\mathbf{I}^8_{Di,j+1} + \mathbf{I}^8_{Di+1,j} - \mathbf{I}^6_{Di+1,j+1} + \mathbf{I}^6_{Di+1,j} \right], \tag{7.29b}$$

$$\Delta \mathbf{Q}_{i,j+1} = \frac{\Delta t \Delta x_2}{2S_{i,j+1}} \left[\mathbf{I}^1_{Di,j+1} - \mathbf{I}^1_{Di+1,j+1} + \mathbf{I}^{11}_{D\,i,j} - 2\mathbf{I}^{11}_{D\,i+1,j} + \mathbf{I}^{11}_{D\,i,j+1} - \mathbf{I}^3_{Di+1,j+1} + \mathbf{I}^3_{Di,j+1} \right]$$
$$+ \frac{\Delta t \Delta x_1}{2S_{i,j+1}} \left[\mathbf{I}^{12}_{D\,i,j} - \mathbf{I}^{12}_{D\,i,j+1} - \mathbf{I}^4_{Di+1,j+1} + 2\mathbf{I}^4_{Di+1,j} - \mathbf{I}^4_{Di,j+1} - \mathbf{I}^{10}_{D\,i,j+1} + \mathbf{I}^{10}_{D\,i,j} \right], \tag{7.29c}$$

and

$$\Delta \mathbf{Q}_{i+1,j+1} = \frac{\Delta t \Delta x_2}{2S_{i+1,j+1}} \left[\mathbf{I}^{11}_{D\,i+1,j} - \mathbf{I}^{11}_{D\,i+1,j+1} - \mathbf{I}^7_{Di+1,j+1} + \mathbf{I}^7_{Di,j+1} + \mathbf{I}^9_{Di,j+1} - \mathbf{I}^9_{Di+1,j+1} \right]$$
$$+ \frac{\Delta t \Delta x_1}{2S_{i+1,j+1}} \left[\mathbf{I}^{12}_{D\,i+1,j} - \mathbf{I}^{12}_{D\,i+1,j+1} - \mathbf{I}^8_{Di+1,j+1} + \mathbf{I}^8_{Di,j+1} + \mathbf{I}^{10}_{D\,i+1,j} - \mathbf{I}^{10}_{D\,i+1,j+1} \right], \tag{7.29d}$$

where the moments $\mathbf{I}^1_D$ and $\mathbf{I}^2_D$ have been defined in Eqs. (7.27a,b) and

$$\mathbf{I}^3_D = \int_{-\infty}^{\infty}\int_{-\infty}^{0}\int_{0}^{-c_1\alpha} \Psi c_1 n f_0 dc_2 dc_1 dc_3\,, \quad \mathbf{I}^4_D = \int_{-\infty}^{\infty}\int_{-\infty}^{0}\int_{0}^{-c_1\alpha} \Psi c_2 n f_0 dc_2 dc_1 dc_3\,, \tag{7.30a,b}$$

$$\mathbf{I}^5_D = \int_{-\infty}^{\infty}\int_{0}^{\infty}\int_{-\infty}^{-c_1\alpha} \Psi c_1 n f_0 dc_2 dc_1 dc_3\,, \quad \mathbf{I}^6_D = \int_{-\infty}^{\infty}\int_{0}^{\infty}\int_{-\infty}^{-c_1\alpha} \Psi c_2 n f_0 dc_2 dc_1 dc_3\,, \tag{7.31a,b}$$

$$\mathbf{I}^7_D = \int_{-\infty}^{\infty}\int_{0}^{\infty}\int_{-c_1\alpha}^{0} \Psi c_1 n f_0 dc_2 dc_1 dc_3\,, \quad \mathbf{I}^8_D = \int_{-\infty}^{\infty}\int_{0}^{\infty}\int_{-c_1\alpha}^{0} \Psi c_2 n f_0 dc_2 dc_1 dc_3\,, \tag{7.32a,b}$$

$$\mathbf{I}^9_D = \int_{-\infty}^{\infty}\int_{0}^{\infty}\int_{0}^{\infty} \Psi c_1 n f_0 dc_2 dc_1 dc_3\,, \quad \mathbf{I}^{10}_D = \int_{-\infty}^{\infty}\int_{0}^{\infty}\int_{0}^{\infty} \Psi c_2 n f_0 dc_2 dc_1 dc_3\,, \tag{7.33a,b}$$

and

$$\mathbf{I}^{11}_D = \int_{-\infty}^{\infty}\int_{-\infty}^{0}\int_{-c_1\alpha}^{\infty} \Psi c_1 n f_0 dc_2 dc_1 dc_3\,, \quad \mathbf{I}^{12}_D = \int_{-\infty}^{\infty}\int_{-\infty}^{0}\int_{-c_1\alpha}^{\infty} \Psi c_2 n f_0 dc_2 dc_1 dc_3\,. \tag{7.34a,b}$$

Hence, the final Euler scheme is a residual distribution scheme where fluctuations are determined based on moments evaluated at the cell vertices. Each of the 12 integrals that appear in this formulation represent vectors and must be evaluated

for each element of Ψ, yielding a total of 48 integrals for two space dimensions. These integrals are included in Appendix A in Secs. A.1.1 - A.1.4. It is noted that one portion of the integration could not be performed analytically, and a Gauss-Laguerre quadrature was used to approximate this integral. This procedure is discussed in Sec. A.1.5 in Appendix A. The results showed very little sensitivity to the accuracy of this integral.

7.3.2 MKFS-NDU Scheme

The NDU-scheme is based on a triangulation with the diagonal going up and to the right. The global and local numbering systems are shown in Fig. 7.4b. This scheme is derived in exactly the same manner as the NDD scheme and has a velocity space decomposition as shown in Fig. 7.5b. For brevity, only the final results are presented. The Euler fluctuations are

$$\begin{aligned}\Delta\mathbf{Q}_{i,j} = &\frac{\Delta t\Delta x_2}{2S_{i,j}}\left[\mathbf{I}^1_{U\,i,j} - \mathbf{I}^1_{U\,i+1,j} + \mathbf{I}^9_{U\,i,j+1} - 2\mathbf{I}^9_{U\,i+1,j+1} + \mathbf{I}^9_{U\,i,j} + \mathbf{I}^{11}_{U\,i,j} - \mathbf{I}^{11}_{U\,i+1,j}\right] \\ &+ \frac{\Delta t\Delta x_1}{2S_{i,j}}\left[\mathbf{I}^{10}_{U\,i,j} - \mathbf{I}^{10}_{U\,i,j+1} + \mathbf{I}^{12}_{U\,i+1,j} - 2\mathbf{I}^{12}_{U\,i+1,j+1} + \mathbf{I}^{12}_{U\,i,j} + \mathbf{I}^8_{U\,i,j} - \mathbf{I}^8_{U\,i,j+1}\right],\end{aligned} \tag{7.35a}$$

$$\begin{aligned}\Delta\mathbf{Q}_{i+1,j} = &\frac{\Delta t\Delta x_2}{2S_{i+1,j}}\left[\mathbf{I}^9_{U\,i+1,j+1} - \mathbf{I}^9_{U\,i+1,j} + \mathbf{I}^5_{U\,i,j} - \mathbf{I}^5_{U\,i+1,j} + \mathbf{I}^7_{U\,i,j} - \mathbf{I}^7_{U\,i+1,j}\right] \\ &+ \frac{\Delta t\Delta x_1}{2S_{i+1,j}}\left[\mathbf{I}^{10}_{U\,i+1,j} - \mathbf{I}^{10}_{U\,i+1,j+1} + \mathbf{I}^6_{U\,i+1,j} - \mathbf{I}^6_{U\,i,j} + \mathbf{I}^8_{U\,i+1,j} - \mathbf{I}^8_{U\,i+1,j+1}\right],\end{aligned} \tag{7.35b}$$

$$\begin{aligned}\Delta\mathbf{Q}_{i,j+1} = &\frac{\Delta t\Delta x_2}{2S_{i,j+1}}\left[\mathbf{I}^1_{U\,i,j+1} - \mathbf{I}^1_{U\,i+1,j+1} + \mathbf{I}^{11}_{U\,i,j+1} - \mathbf{I}^{11}_{U\,i+1,j+1} + \mathbf{I}^3_{U\,i,j+1} - \mathbf{I}^3_{U\,i,j}\right] \\ &+ \frac{\Delta t\Delta x_1}{2S_{i,j+1}}\left[\mathbf{I}^2_{U\,i,j} - \mathbf{I}^2_{U\,i,j+1} + \mathbf{I}^{12}_{U\,i+1,j+1} - \mathbf{I}^{12}_{U\,i,j+1} + \mathbf{I}^4_{U\,i,j} - \mathbf{I}^4_{U\,i,j+1}\right],\end{aligned} \tag{7.35c}$$

and

$$\Delta \mathbf{Q}_{i+1,j+1} = \frac{\Delta t \Delta x_2}{2S_{i+1,j+1}} \left[\mathbf{I}^5_{U_{i+1,j}} - \mathbf{I}^5_{U_{i+1,j+1}} - \mathbf{I}^3_{U_{i+1,j+1}} + 2\mathbf{I}^3_{U_{i,j+1}} + \mathbf{I}^3_{U_{i,j+1}} + \mathbf{I}^7_{U_{i,j+1}} - \mathbf{I}^7_{U_{i+1,j+1}} \right]$$
$$+ \frac{\Delta t \Delta x_1}{2S_{i+1,j+1}} \left[\mathbf{I}^2_{U_{i+1,j}} - \mathbf{I}^2_{U_{i+1,j+1}} - \mathbf{I}^6_{U_{i+1,j+1}} + 2\mathbf{I}^6_{U_{i,j}} - \mathbf{I}^6_{U_{i,j+1}} + \mathbf{I}^4_{U_{i+1,j}} - \mathbf{I}^4_{U_{i+1,j+1}} \right] . \tag{7.35d}$$

The moments $\mathbf{I}_U$ that appear in this formulation can be related to the moments $\mathbf{I}_D$ in the previous section through a change in variables. These relations are given in Sec. A.2 in Appendix A.

7.3.3 MKFS-NDA Scheme

When applying the N-scheme to Cartesian triangulations the choice of the diagonal becomes an important factor, and solutions will become severely degraded if the "wrong" diagonal is used. Therefore, it is not surprising that the Euler schemes developed in the previous two sections will also produce results that exhibit a similar "diagonal dependence". This behavior has been confirmed by numerical tests using the NDD and and NDU schemes, and the results of these calculations will be presented in the following section. To eliminate the diagonal dependence of the N-scheme, an adaptive strategy is considered where the appropriate diagonal is chosen based on the location in velocity space. The orientation of the diagonal varies for each of the four velocity space quadrants as shown diagrammatically below:

$$\nearrow \text{ if } \begin{cases} c_1 > 0, \ c_2 > 0, \ \text{or} \\ c_1 < 0, \ c_2 < 0, \end{cases}$$

and

$$\searrow \text{ if } \begin{cases} c_1 < 0, \ c_2 > 0, \ \text{or} \\ c_1 > 0, \ c_2 < 0. \end{cases}$$

This diagonal-splitting method is illustrated in Fig. 7.6a where the appropriate diagonal is shown for each of the four velocity space quadrants. The fluctuations

are now determined based on the choice for the diagonal and the resulting scheme has contributions from both the NDD scheme and the NDU scheme. The resulting velocity space decomposition is shown in Fig. 7.6b, and the Euler fluctuations are given as

$$\begin{aligned}\Delta\mathbf{Q}_{i,j} = &\frac{\Delta t\Delta x_2}{2S_{i,j}}\left[\mathbf{I}^3_{Di,j} - \mathbf{I}^3_{Di+1,j} + \mathbf{I}^5_{Di,j} - \mathbf{I}^5_{Di,j+1}\right]\\ &+\frac{\Delta t\Delta x_1}{2S_{i,j}}\left[\mathbf{I}^4_{Di,j} - \mathbf{I}^4_{Di+1,j} + \mathbf{I}^6_{Di,j} - \mathbf{I}^6_{Di,j+1}\right]\\ &+\frac{\Delta t\Delta x_2}{2S_{i,j}}\left[\mathbf{I}^9_{Ui,j+1} - 2\mathbf{I}^9_{Ui+1,j+1} + \mathbf{I}^9_{Ui,j} + \mathbf{I}^{11}_{U\,i,j} - \mathbf{I}^{11}_{U\,i+1,j}\right]\\ &+\frac{\Delta t\Delta x_1}{2S_{i,j}}\left[\mathbf{I}^{10}_{U\,i,j} - \mathbf{I}^{10}_{U\,i,j+1} + \mathbf{I}^{12}_{U\,i+1,j} - 2\mathbf{I}^{12}_{U\,i+1,j+1} + \mathbf{I}^{12}_{U\,i,j}\right], \qquad (7.36a)\end{aligned}$$

$$\begin{aligned}\Delta\mathbf{Q}_{i+1,j} = &\frac{\Delta t\Delta x_2}{2S_{i+1,j}}\left[\mathbf{I}^7_{Di,j} - \mathbf{I}^7_{Di+1,j} - \mathbf{I}^5_{Di+1,j+1} + 2\mathbf{I}^5_{Di,j+1} - \mathbf{I}^5_{Di+1,j}\right]\\ &+\frac{\Delta t\Delta x_1}{2S_{i+1,j}}\left[\mathbf{I}^8_{Di,j} - 2\mathbf{I}^8_{Di,j+1} + \mathbf{I}^8_{Di+1,j} - \mathbf{I}^6_{Di+1,j+1} + \mathbf{I}^6_{Di+1,j}\right]\\ &+\frac{\Delta t\Delta x_2}{2S_{i+1,j}}\left[\mathbf{I}^9_{Ui+1,j+1} - \mathbf{I}^9_{Ui+1,j} + \mathbf{I}^5_{Ui,j} - \mathbf{I}^5_{Ui+1,j}\right]\\ &+\frac{\Delta t\Delta x_1}{2S_{i+1,j}}\left[\mathbf{I}^{10}_{U\,i+1,j} - \mathbf{I}^{10}_{U\,i+1,j+1} + \mathbf{I}^6_{Ui+1,j} - \mathbf{I}^6_{Ui,j}\right], \qquad (7.36b)\end{aligned}$$

$$\begin{aligned}\Delta\mathbf{Q}_{i,j+1} = &\frac{\Delta t\Delta x_2}{2S_{i,j+1}}\left[\mathbf{I}^{11}_{D\,i,j} - 2\mathbf{I}^{11}_{D\,i+1,j} + \mathbf{I}^{11}_{D\,i,j+1} - \mathbf{I}^3_{Di+1,j+1} + \mathbf{I}^3_{Di,j+1}\right]\\ &+\frac{\Delta t\Delta x_1}{2S_{i,j+1}}\left[\mathbf{I}^{12}_{D\,i,j} - \mathbf{I}^{12}_{D\,i,j+1} - \mathbf{I}^4_{Di+1,j+1} + 2\mathbf{I}^4_{Di+1,j} - \mathbf{I}^4_{Di,j+1}\right]\\ &+\frac{\Delta t\Delta x_2}{2S_{i,j+1}}\left[\mathbf{I}^{11}_{U\,i,j+1} - \mathbf{I}^{11}_{U\,i+1,j+1} + \mathbf{I}^3_{Ui,j+1} - \mathbf{I}^3_{Ui,j}\right]\\ &+\frac{\Delta t\Delta x_1}{2S_{i,j+1}}\left[\mathbf{I}^{12}_{U\,i+1,j+1} - \mathbf{I}^{12}_{U\,i,j+1} + \mathbf{I}^4_{Ui,j} - \mathbf{I}^4_{Ui,j+1}\right], \qquad (7.36c)\end{aligned}$$

and

$$\begin{aligned}\Delta\mathbf{Q}_{i+1,j+1} = &\frac{\Delta t\Delta x_2}{2S_{i+1,j+1}}\left[\mathbf{I}^{11}_{D\,i+1,j} - \mathbf{I}^{11}_{D\,i+1,j+1} - \mathbf{I}^7_{Di+1,j+1} + \mathbf{I}^7_{Di,j+1}\right]\\ &+\frac{\Delta t\Delta x_1}{2S_{i+1,j+1}}\left[\mathbf{I}^{12}_{D\,i+1,j} - \mathbf{I}^{12}_{D\,i+1,j+1} - \mathbf{I}^8_{Di+1,j+1} + \mathbf{I}^8_{Di,j+1}\right]\\ &+\frac{\Delta t\Delta x_2}{2S_{i+1,j+1}}\left[\mathbf{I}^5_{Ui,j+1} - \mathbf{I}^5_{Ui+1,j+1} - \mathbf{I}^3_{Ui+1,j+1} + 2\mathbf{I}^3_{Ui,j} + \mathbf{I}^3_{Ui+1,j}\right]\\ &+\frac{\Delta t\Delta x_1}{2S_{i+1,j+1}}\left[2\mathbf{I}^6_{Ui,j} - \mathbf{I}^6_{Ui+1,j+1} - \mathbf{I}^6_{Ui,j+1} + \mathbf{I}^4_{Ui+1,j} - \mathbf{I}^4_{Ui+1,j+1}\right]. \qquad (7.36d)\end{aligned}$$

It is important to note that the diagonal switching appears only at the kinetic level and no explicit logic for this feature is necessary in the Euler scheme. A similar adaptive procedure for the extended Roe-type schemes has not yet been developed, since no clear procedure is available to ensure conservation. At the present date, the extended Roe-type solvers are conservative only if the same diagonal is taken for all waves in the decomposition [32].

7.3.4 CIR-Scheme

A similar kinetic scheme has been developed using the same type cell-vertex residual-distribution approach except with fluctuations based on the dimensionally-split CIR scheme. The fluctuations for this scheme are not included here, however, results obtained with this scheme will be used for comparison purposes. This scheme is essentially identical to the KFVS scheme on Cartesian meshes.

7.4 Results

The first case considered is the 29 degree shock reflection off a flat plate with a Mach 2.9 freestream. The grid was 2.75 length units long and 1.0 length unit high and calculations were obtained on a uniformly spaced 61×33 mesh. The boundary conditions at the inflow were fixed so that the oblique shock was located at a height of 0.75 length units. Inviscid wall boundary conditions were imposed on the lower wall and extrapolation boundary conditions were used at the outflow and upper boundaries. All calculations presented are first-order accurate in space. Density contours are plotted in Figs. 7.7a and 7.7b for the MKFS-CIR scheme and the MKFS-NDD scheme respectively. The results from the CIR scheme are typical of a first-order dimensionally-split scheme and exhibit excessive smearing of the shock wave. The NDD scheme produces a significantly sharper inflow shock as compared to the CIR inflow shock, however, the reflected shock tends to thicken

considerably and represents no improvement over the CIR reflected shock. This is a direct consequence of the diagonal dependence of the N-scheme. The NDD scheme provides a much improved solution when the shock is aligned with the diagonal, but reduces to the more dissipative CIR scheme when the shock is oriented perpendicular to the diagonal. Figures 7.8a and 7.8b show density contours again for the MKFS-CIR scheme and now for the MKFS-NDU scheme respectively. The NDU scheme produces an inflow shock that is identical to the CIR solution, however now the reflected shock tends to become sharper as compared to the CIR solution. This is again consistent with the diagonal dependence of the N-scheme. Figures 7.9a and 7.9b show density contours for the MKFS-CIR scheme and now for the MKFS-NDA scheme respectively. The NDA scheme produces very sharp inflow and reflected shocks and captures both shocks in half the grid points that are necessary for the CIR solution. The slight thickening of the reflected shock near the wall is due to the one-dimensional nature of the wall boundary conditions. These results confirm that the adaptive NDA scheme has effectively eliminated the diagonal dependence of the N-scheme that was apparent in the NDD and NDU schemes. Figures 7.10, 7.11 and 7.12 show results for normalized density, pressure and temperature distributions along the $j = 12$ grid line respectively for the CIR scheme, the multi-dimensional NDA scheme and the exact solution. All three plots show significant improvement of the multi-dimensional NDA scheme results over the dimensionally-split CIR results. The results produced by the multi-dimensional NDA scheme show much sharper shock profiles and agree much better with the exact solution. The multi-dimensional scheme also captures the peak values of density and pressure behind the reflected shock while the CIR scheme slightly underpredicts these values.

The second case is the same Mach 2.9, 29 degree reflected shock, but on a 121×61

mesh. Density contours for this case are shown in Figs. 7.13a and 7.13b for the MKFS-CIR scheme and the MKFS-NDA scheme respectively. Again it is noted that both schemes are first-order accurate in space. The multi-dimensional NDA scheme produces highly resolved inflow and reflected shocks that are again much sharper than the corresponding CIR results. Moreover, it is noted that the multi-dimensional NDA scheme produces results on the 61×33 grid (Fig 7.9b) that are as good as the CIR results on the 121×61 grid shown in Fig. 7.13a.

The next case is a 45 degree shear discontinuity separating Mach 2.9 and Mach 2.4 flows. Calculations are performed on a 33×33 uniform grid with a length and height of 1.0. Density contours for this case are shown in Figs. 7.14a and 7.14b for the MKFS-CIR scheme and the MKFS-NDA scheme respectively. Again, the multi-dimensional NDA scheme captures the shear wave in approximately half the grid points necessary for the CIR scheme. One undesirable feature of both schemes is that the shear wave thicknesses tend to increase in the direction of propagation.

The last case is the uniform Mach 3 flow in a channel with a backward facing step as presented in Woodward and Colella [95]. The computational grid is 1.0 length unit tall and 3.0 length units long and the step is located on the lower wall at 0.6 length units from the left-hand side and is 0.2 length units tall. The left boundary is fixed at the inflow conditions and the outflow boundary is always supersonic and extrapolation boundary conditions are used. Inviscid wall boundary conditions are used along the lower wall and step and on the upper wall. The calculations are carried out on uniform Cartesian grid with dimensions of 241×81 and solutions are presented for the non-dimensionalized time of 4. All cases are run at a CFL number of 1. Figures 7.15a and 7.15b show the density contours for the MKFS-CIR scheme and the MKFS-NDA scheme respectively.

In general, the shock waves produced by the multi-dimensional NDA scheme

tend to be noticeably sharper than those predicted by the CIR scheme, especially for downstream reflected shocks. The multi-dimensional scheme also produces a thinner bow shock wave in the region near the mach stem where the shock is aligned oblique to the grid. Also, in comparison with the CIR results, the results produced by the multi-dimensional NDA scheme are in much better agreement with the contours presented in Ref. [95]. The CIR scheme predicts a mach stem at the upper wall that is too short, while the multi-dimensional scheme produces a mach stem that is approximately 0.2 length units long and agrees fairly well with the results in Ref. [95]. The multi-dimensional scheme also appears correctly locate the weak contact discontinuity caused by the Mach reflection of the bow shock at the upper wall. However, the contact discontinuity shown here is not nearly as resolved as those shown in Ref. [95] for higher-order accurate schemes.

7.5 Conclusions

A multi-dimensional kinetic fluctuation-splitting scheme has been developed for the Euler equations. The scheme is based on an N-scheme discretization of the Boltzmann equation at the kinetic level for triangulated Cartesian meshes with a diagonal-adaptive strategy. The resulting Euler scheme is a cell-vertex fluctuation-splitting scheme where fluctuations in the conserved variable vector $\mathbf{Q}$ are obtained as moments of the fluctuations in the Maxwellian velocity distribution function at the kinetic level. Encouraging preliminary results have been obtained for perfect gases on Cartesian meshes with first-order spatial accuracy. Results for a simple oblique shock reflection and shear wave show that the MKFS-NDA scheme effectively eliminates the diagonal dependence of the N-scheme and produces discontinuities that are much sharper than those produced by the dimensionally-split CIR scheme. The test case of Woodward and Colella represents a relatively complicated

flowfield with complex shock intersections and reflections, contact discontinuities, expansions, and significant regions of subsonic flow. Again, the multi-dimensional scheme produces superior results as compared to the CIR scheme, and produces results that are in general agreement with those in Ref. [95]. Overall, the results for MKFS-NDA scheme show that the methodology presented in this chapter represents an improvement to the well established dimensionally-split upwind schemes.

The extension of the present scheme to general two-dimensional structured or unstructered grids should not be difficult. However, the extension to general three-dimensional grids would involve integrations over three-dimensional regions in velocity space. The extension to the NN-scheme, for higher-order spatial accuracy, appears to be very complex because of the non-linear nature of this scheme. More work remains to be done in these areas before algorithms of this type could be considered at a production level. The schemes presented here are very complex and inefficient. We have followed this line of research with the hope of gaining some insight into multi-dimensional Riemann solvers. The schemes presented here may give some additional understanding of appropriate multi-dimensional wave decompositions for the Euler equations and may also lead to considerations of multi-dimensional boundary conditions. Finally, it is noted that it may be possible to develop similar upwind schemes that include viscous effects by using the Boltzmann equation with some some model for the collision integral. Initial work along these lines has been carried out by Prendergast and Xu [96] who have used a Bhatnagar-Gross-Krook model of the Boltzmann equation.

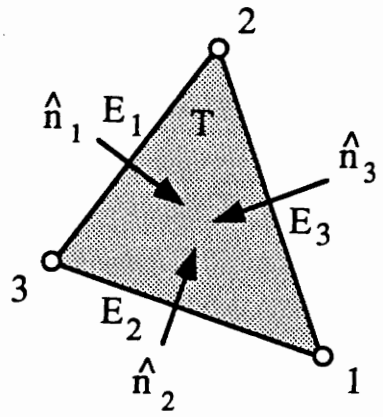

Fig. 7.1 – Triangular grid notation

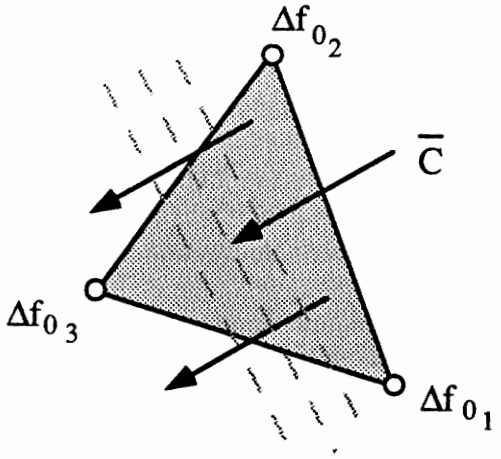

7.2a – One inflow side triangle

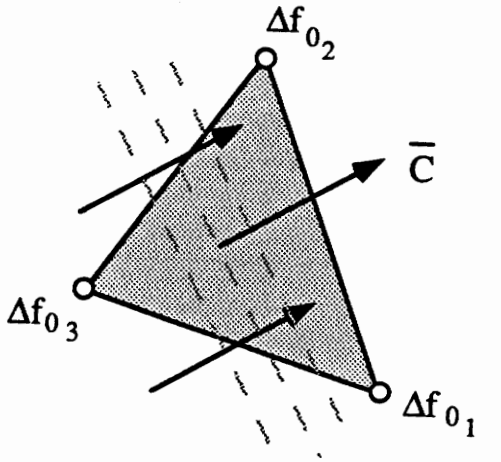

7.2b – Two inflow side triangle

Fig. 7.2 – One and two inflow side triangles

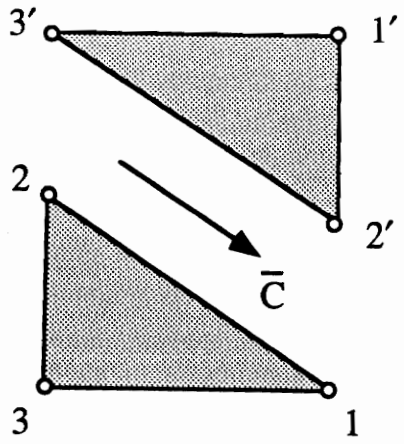

7.3a – Convection velocity aligned with diagonal

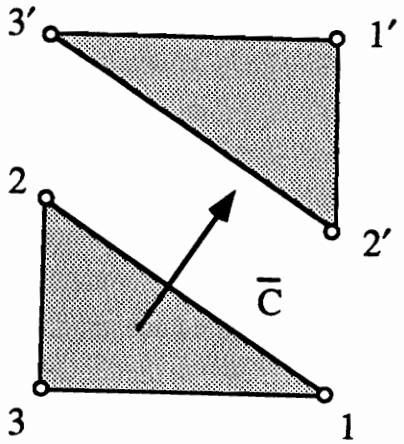

7.3b – Convection velocity perpendicular to diagonal

Fig. 7.3 – Diagonal dependence of N-scheme

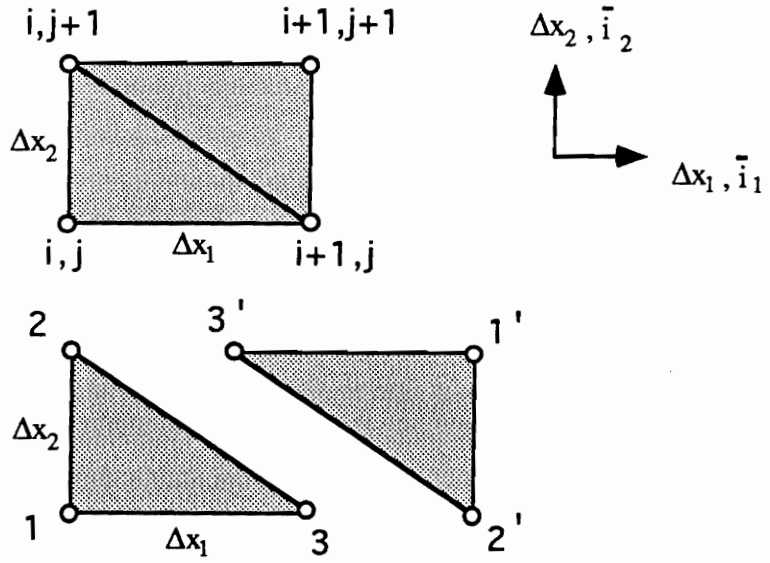

7.4a – Diagonal down (NDD) scheme

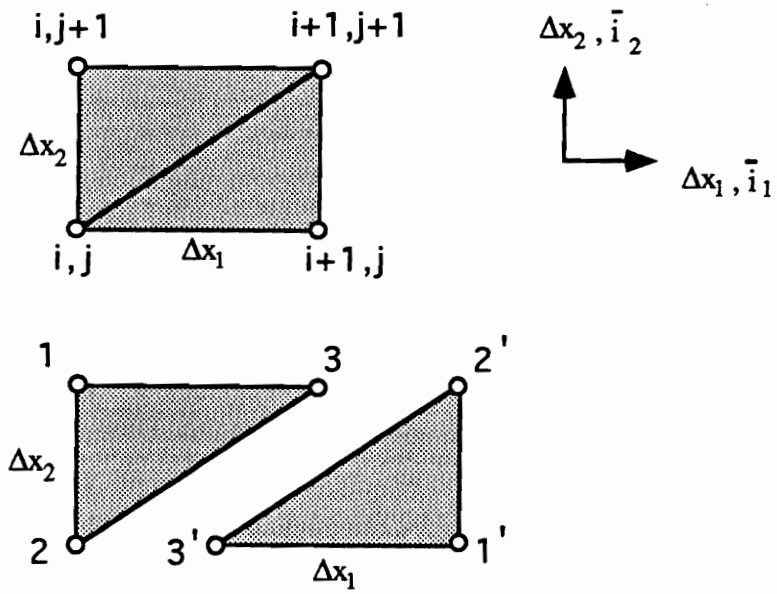

7.4b – Diagonal up (NDU) scheme

Fig. 7.4 – Global and local numbering for Cartesian triangulation

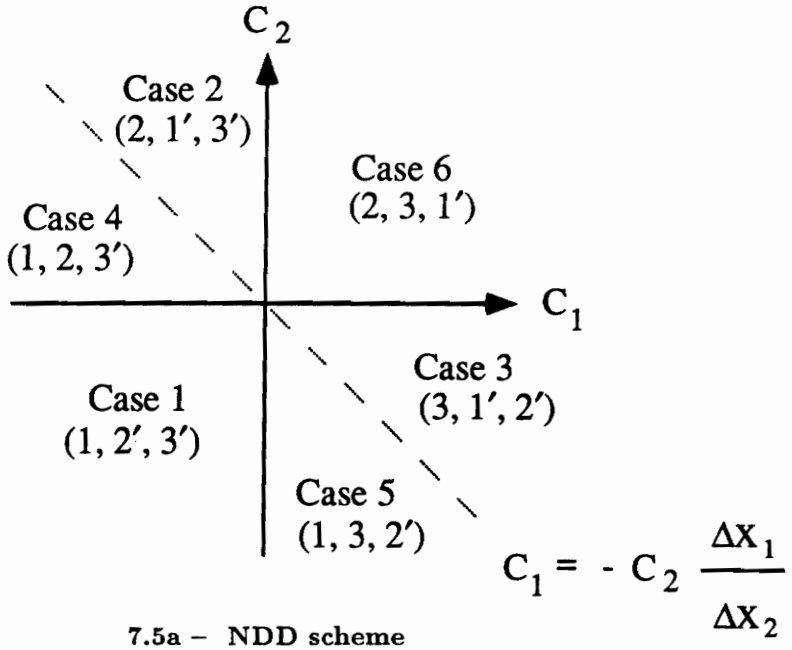

7.5a – NDD scheme

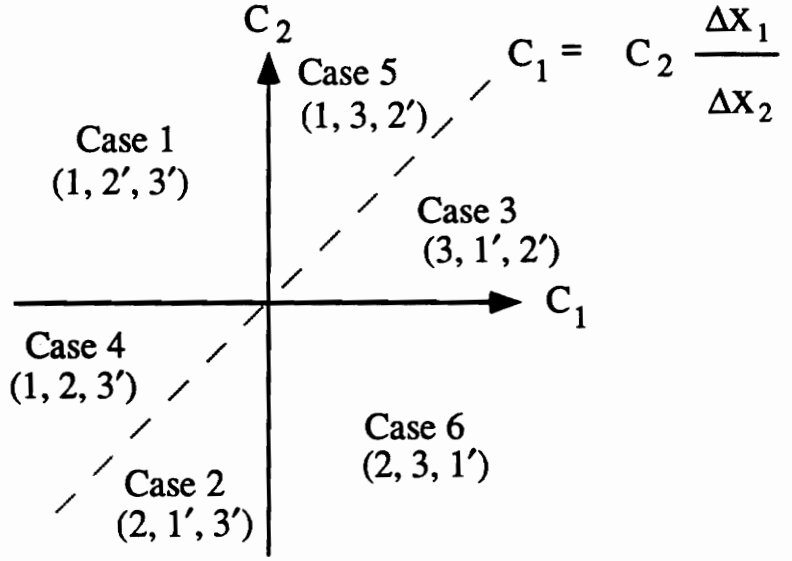

7.5b – NDU scheme

Fig. 7.5 – Velocity space decomposition with inflow sides in ( )

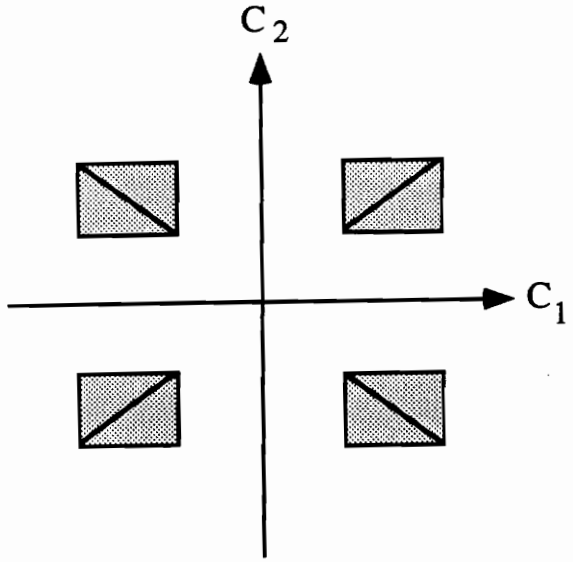

7.6a – Diagonal splitting

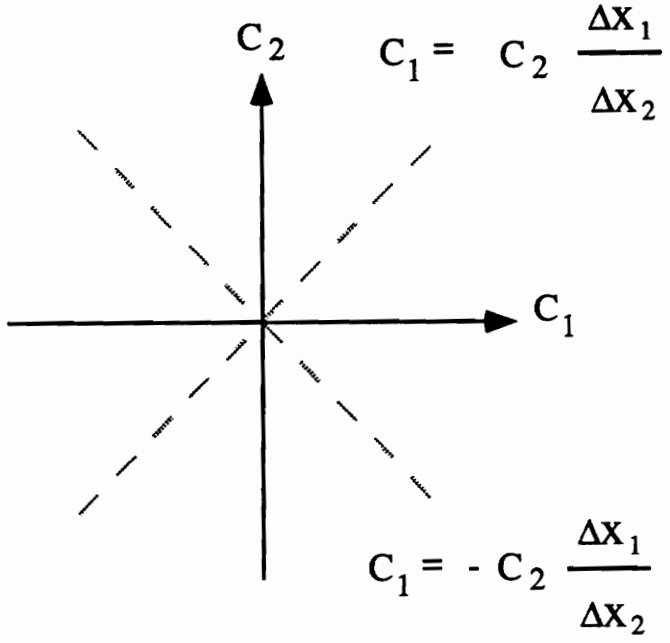

7.6b – Velocity space decomposition

Fig. 7.6 – Diagonal adaptive (NDA) scheme

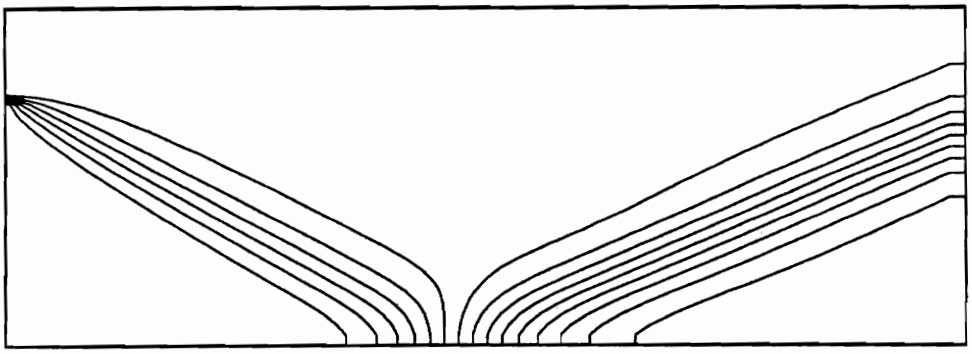

7.7a – MKFS-CIR scheme

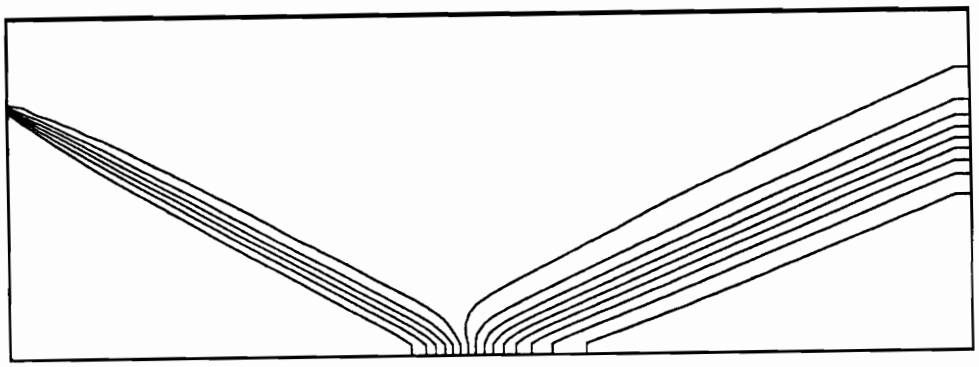

7.7b – MKFS-NDD scheme

Fig. 7.7 – Density contours, 29^0 shock reflection, 61×33 grid

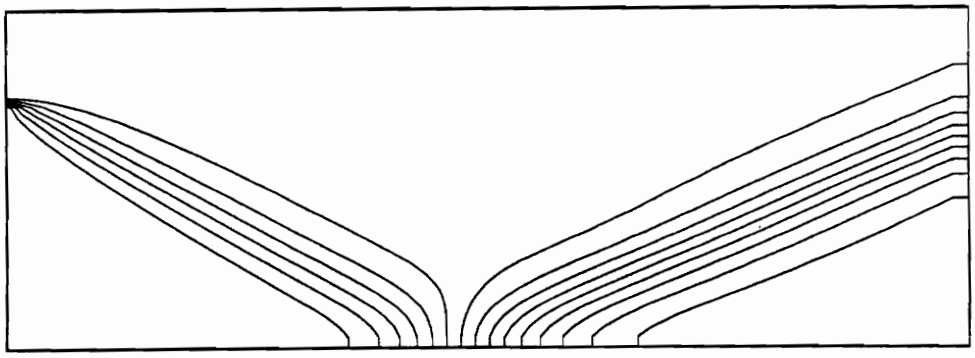

7.8a – MKFS-CIR scheme

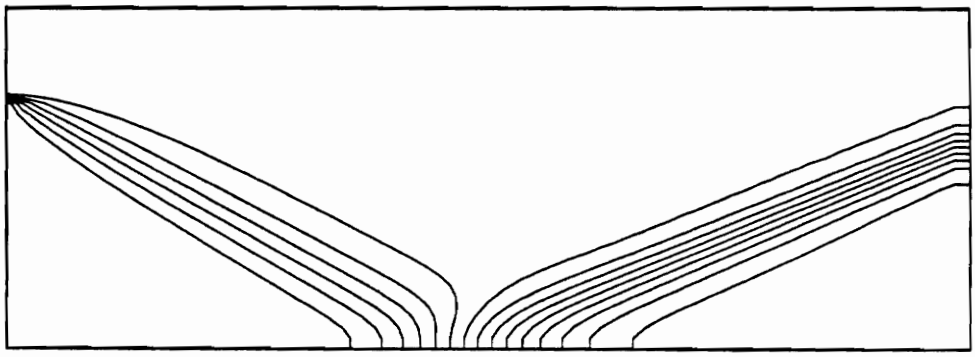

7.8b – MKFS-NDU scheme

Fig. 7.8 – Density contours, 29^0 shock reflection, 61×33 grid

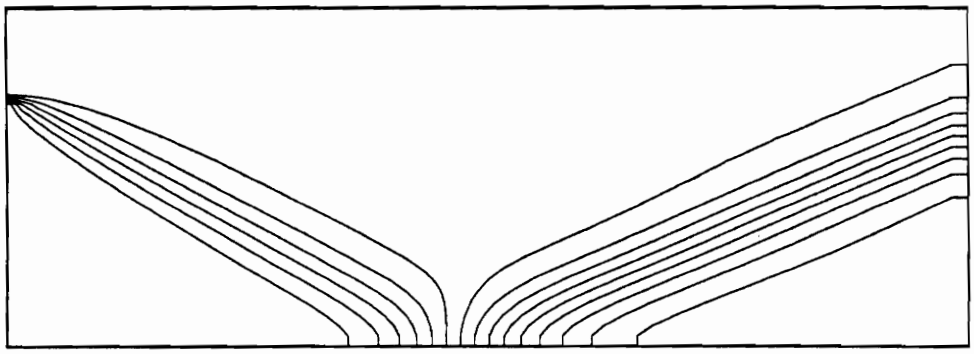

7.9a – MKFS-CIR scheme

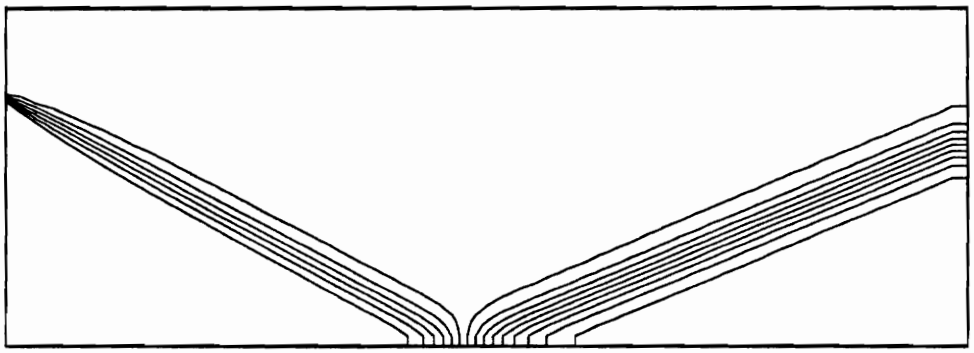

7.9b – MKFS-NDA scheme

Fig. 7.9 – Density contours, 29^0 shock reflection, 61×33 grid

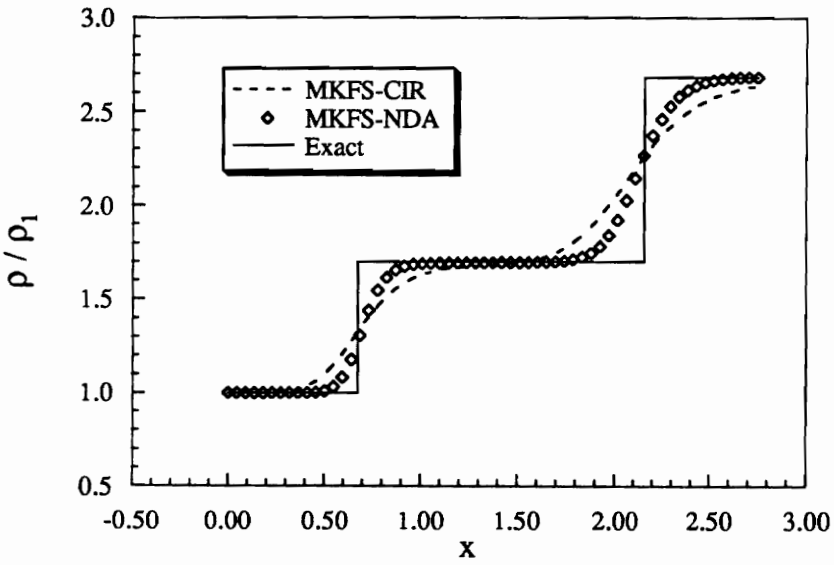

Fig. 7.10 – Normalized density along j=12 grid line, 29^0 shock reflection

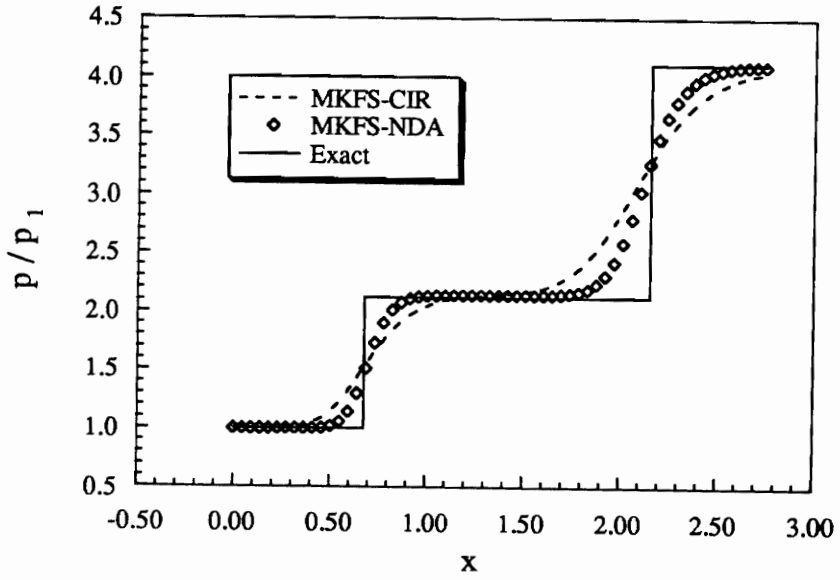

Fig. 7.11 – Normalized pressure along j=12 grid line, 29^0 shock reflection

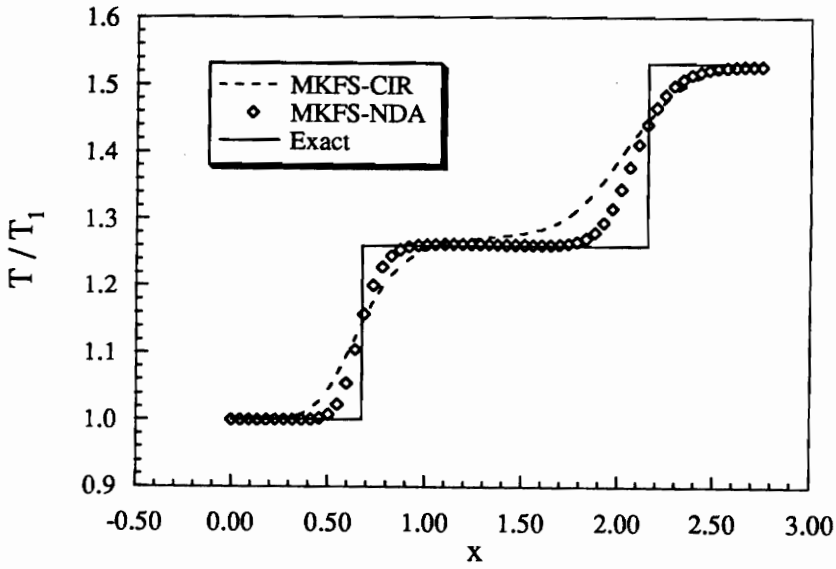

Fig. 7.12 – Normalized temperature along j=12 grid line, 29^0 shock reflection

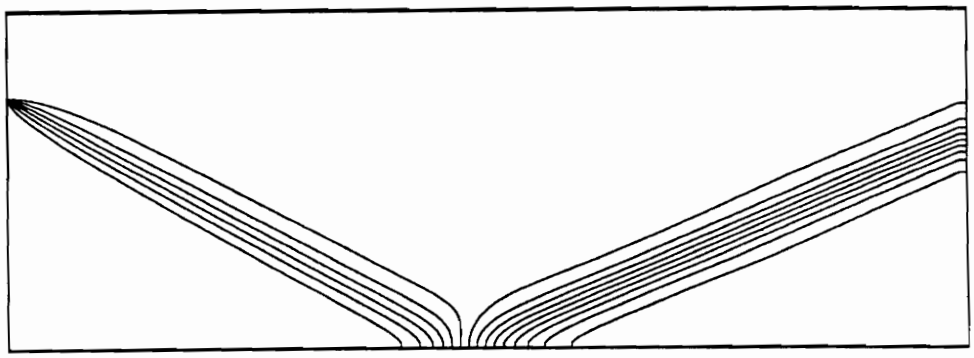

7.13a – MKFS-CIR scheme

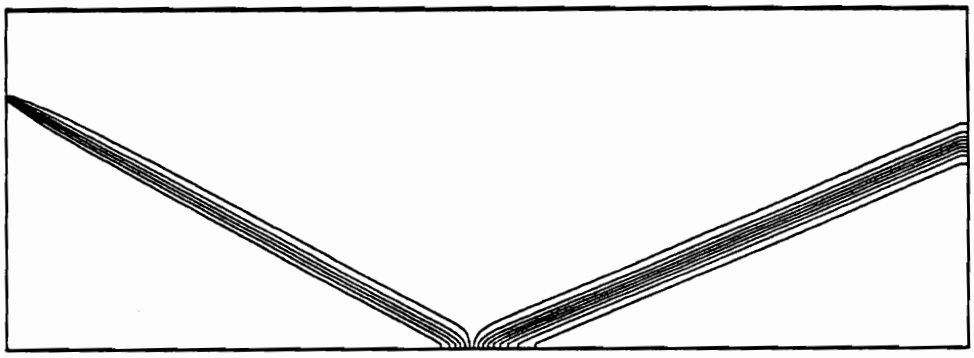

7.13b – MKFS-NDA scheme

Fig. 7.13 – Density contours, 29^0 shock reflection, 121×61 grid

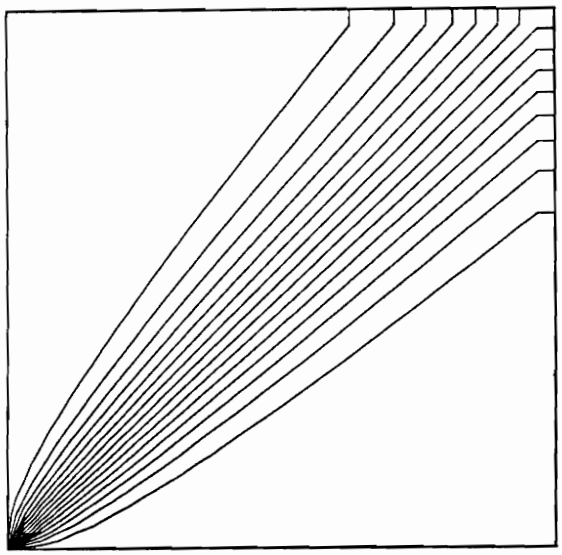

7.14a – MKFS-CIR scheme

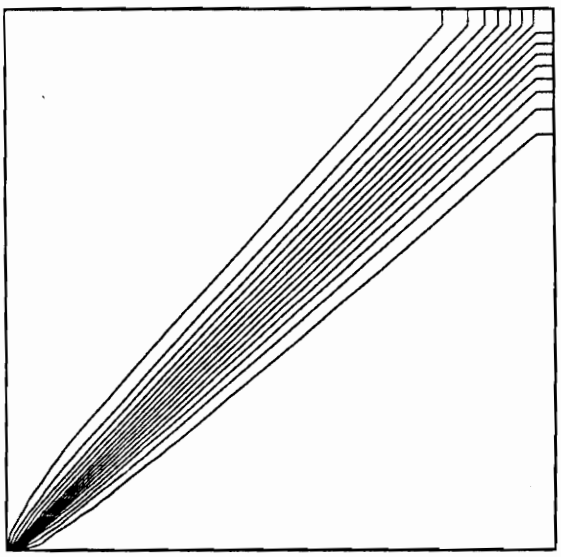

7.14b – MKFS-NDA scheme

Fig. 7.14 – Density contours, 45^0 shear discontinuity, 33×33 grid

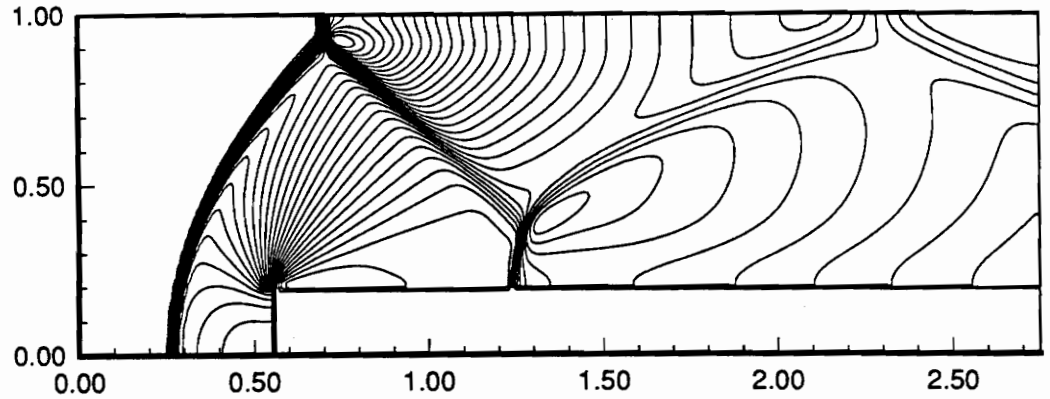

7.15a – MKFS-CIR scheme

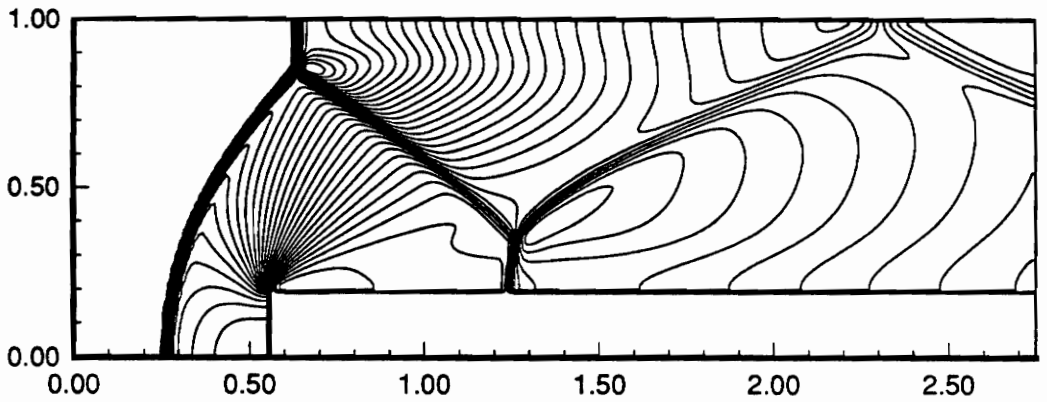

7.15b – MKFS-NDA scheme

Fig. 7.15 – Density contours, Mach 3 step, 241×81 grid

Chapter 8

Hypersonic Shock Structure

8.1 Introduction

Molecular collisions are the primary mechanism for the redistribution of energy within a shock wave. For rarefied flows at higher altitudes the molecular mean free path λ increases and shock waves tend to become thicker. There exists an altitude regime in the atmosphere that is within the continuum domain, but wherein the conventional Navier-Stokes equations cease to be accurate. Within this regime the thickness of the bow shock wave is no longer negligible when compared to the shock stand-off distance and the peak radiation intensity occurs within the shock wave structure itself [36,37]. For this reason it is no longer valid to treat the shock wave as a discontinuous jump and it becomes necessary to compute through the shock wave itself. The altitude limits for this so called continuum transition regime depend on vehicle size and speed. In Ref. [36], Chapman gives a plot that shows the altitude where the hypersonic shock wave thickness becomes 10 percent of the shock-detachment distance. The plot is a function of nose radius, and for altitudes above those shown, "thick" shock waves must be considered. To give an illustrative example, the critical altitude for a missle with a nose radius of 50 centimeters is approximately 60 kilometers. For altitudes greater than this, thick shock waves must be considered. A more exact measure of this phenomena is the Knudsen number Kn, given in Eq. 5.2, where the characteristic length L is typically taken as the nose radius. For $Kn << 1$. the flow belongs to the continuum regime and can

accurately be described by the Navier-Stokes equations, except in the negligibly thin region within the bow shock wave. For $Kn \simeq 0.1$ the flow begins to depart from the continuum regime and enters the transition regime, however, when $Kn \leq 0.1$ the difference between Navier-Stokes and Burnett calculations is small. For $Kn >> .1$, large deviations from translational equilibrium occur, and the differences between Navier-Stokes and Burnett results can be significant. Here, it is necessary to use the Burnett equations to obtain realistic profiles of flow variables throughout the hypersonic shock wave structure. In the present work both Navier-Stokes and Burnett calculations will be made; first for the case of a monatomic gas and then for the case of a diatomic gas where rotational energy must be included. Results are presented for one-dimensional normal shock calculations with argon and nitrogen. These results have previously appeared in Ref. [97].

8.2 Basic Modeling

These shock-structure calculations are carried out for a single-component monatomic or diatomic gas in one space dimension. The governing equations for this case are given in Eq. (3.66) without the area source term vector $\mathbf{W}_A$. Because the chemical and vibrational modes are frozen through the shock both the chemical source terms and the vibrational contribution to the internal energy will be neglected. Any non-equilibrium contribution to the internal energy will be due to the rotational mode. The body force terms that appear in Eq. (3.66) are also neglected.

8.2.1 Monatomic Gases

For monatomic gases rotational energy is not present and only translational non-equilibrium must be considered. To obtain accurate shock profiles the constitutive relations, τ_{11} and q_1, that appear in the governing equations must be capable

of modeling the large amounts of translational non-equilibrium within the shock. Both the Navier-Stokes and Burnett equations have been used and the corresponding shear stress and heat-flux terms, τ_{11} and q_1, are given in Sec. 5.3. It is expected that the Burnett equations will produce more realistic shock profiles since they are valid for larger departures from translational equilibrium.

8.2.2 Diatomic Gases

For diatomic gases both the translational and rotational modes must be considered. In addition to accurate constitutive relations, some mechanism must be included to allow for the translational/rotational energy exchange processes. Six different models have been considered. They include either the Navier-Stokes or Burnett equations in conjunction with:

1. the rotational equilibrium model in Eq. (2.21), or
2. rotational equilibrium with the bulk-viscosity model of Eq. (5.18), or
3. the rotational non-equilibrium model of Eq. (4.13).

The rotational non-equilibrium model should produce the best profiles since it is capable of modeling large departures from rotational equilibrium. The bulk-viscosity model assumes that rotational equilibrium is maintained, but corrects for rotational non-equilibrium through the bulk-viscosity term. This model is not strictly valid for large departures from rotational equilibrium.

8.3 Numerical Issues

The inviscid fluxes were discretized using an upwind Steger-Warming type flux-vector splitting algorithm. A general splitting for flows in chemical and thermal non-equilibrium is presented by Grossman and Cinnella in Ref. [8]. An Euler-implicit time integration method, as described in Sec. 6.3, was used to march in time to the steady-state solution. Both the Navier-Stokes and Burnett viscous

fluxes are treated implicitly in a method similar to that of Ref. [41]. Here, the coefficients in front of the derivative terms are frozen during the linearization. The source terms resulting from non-equilibrium rotation are also handled implicitly. A locally third-order, upwind biased MUSCL extrapolation ($\kappa = 1/3$) is used for the inviscid fluxes and no limiting was necessary for any of the calculations presented. It is noted that Navier-Stokes calculations require a block tri-diagonal inversion at each time step while Burnett calculations require a block penta-diagonal inversion at each time step.

Each solution was obtained on a grid consisting of 150 equally spaced mesh points. The initial condition was composed of three segments, a constant region initialized at the inflow conditions, an initial guess at the shock profile that blended between the inflow conditions and the conditions behind the normal shock, and finally a constant region at the conditions behind a normal shock, set according to the Rankine-Hugoniot jump conditions. Characteristic boundary conditions were used at the outflow with the pressure at the exit set to that behind the normal shock.

In all the calculations presented the following expression is used as a reference length for shock structure

$$\lambda_1 = \frac{16\mu_1}{5\rho_1(2\pi RT_1)^{0.5}} . \tag{8.1}$$

This is the mean free path that would exist upstream of the shock if the gas were composed of hard elastic spheres. Also, for all calculations the coefficients in the Burnett equations are those corresponding to a hard sphere gas *i.e.*, $\eta = \infty$ and $\omega = .5$ in the inverse potential model. The viscosity law used for all cases corresponds to the inverse potential model and is given as

$$\mu = \mu_0(\frac{T}{T_0})^{(\frac{1}{2}+\frac{2}{\eta-1})} = \mu_0(\frac{T}{T_0})^{\omega} , \tag{8.2}$$

where $\omega = .72$ is used for better agreement with experiment [40,41]. In nitrogen calculations where the rotational non-equilibrium model is incorporated the constants $Z_r^\infty = 18.$ and $T^* = 91.5K$ are used [45].

Density and temperature profiles are presented in a normalized fashion where

$$\rho_n = \frac{\rho - \rho_2}{\rho_2 - \rho_1}\,, \tag{8.3a}$$

and

$$T_n = \frac{T - T_2}{T_2 - T_1}\,. \tag{8.3b}$$

8.4 Results

Results for argon shocks at Mach 20 and 35 are shown in Figs. 8.1 and 8.2. Here, normalized temperature and density profiles are presented for Navier-Stokes and Burnett calculations as well as a Direct Simulation Monte Carlo solution (DSMC) as shown in Refs. [40,41]. It is assumed that for these conditions the DSMC solution is essentially the correct solution. The density profiles predicted by the Burnett solution compare well with the DSMC results in both the Mach 20 an 35 cases. The Navier-Stokes density profiles are slightly thinner compared to the DSMC results. In the case of temperature profiles, the Burnett solution represents a significant improvement over the Navier-Stokes solution, yielding profiles that are much closer to the DSMC results. Overall, the inclusion of Burnett terms yields a significant improvement over Navier-Stokes for both temperature and density profiles. The results shown here compare well with the shock calculations from Refs. [40,41].

Results for diatomic nitrogen at Mach 11 are shown in Figs. 8.3 and 8.4. Fig. 8.3 shows calculations with the Navier-Stokes equations with rotational equilibrium, the Navier-Stokes equations with rotational non-equilibrium, and the Navier-Stokes equations with bulk viscosity, as well as the DSMC result from Ref. [45]. Again,

the DSMC solution is assumed to be essentially the correct solution. Here, the Navier-Stokes calculation with rotational equilibrium produces density profiles that are much too thin. Navier-Stokes calculations with bulk viscosity and rotational non-equilibrium produce density profiles that agree much better with the DSMC calculation. In the case of temperature thicknesses, the Navier-Stokes calculation with bulk viscosity represents only a slight improvement over Navier-Stokes calculations with rotational equilibrium. Neither of these calculations predicted an increase in temperature within the shock, and both produced profiles that were much too thin. The calculation with rotational non-equilibrium does a relatively good job of capturing the peak temperature in the shock, however, the temperature profile is still too thin. Ref. [45] did not present Navier-Stokes results for this case.

Figure 8.4 shows calculations with the Burnett equations with rotational equilibrium, the Burnett equations with rotational non-equilibrium, and the Burnett equations with bulk viscosity, as well as the DSMC calculation from Ref. [45]. The Burnett calculation with rotational equilibrium produces density profiles that are better than Navier-Stokes with rotational equilibrium, but that are still too thin. Burnett calculations with bulk viscosity produce density profiles that compare very close to the DSMC calculation, and appear to be slightly better than the calculation with rotational non-equilibrium. In the case of temperature profiles, the Burnett calculation with bulk viscosity represents a slight improvement over Burnett alone. Again, neither of these calculations predicted an increase in temperature within the shock, however, they did produced profiles that were thicker than those predicted by Navier-Stokes. The calculation with rotational non-equilibrium very closely predicts the value and location of the peak temperature in the shock and produces a profile with very nearly the correct thickness. The Burnett calculation with rotational non-equilibrium most closely matches the DSMC results. Our results for

this case agree with the results from Ref. [45].

Figs. 8.5 and 8.6 show similar results for a Mach 6 shock in nitrogen. These calculations agree well with the results from Ref. [46].

8.3 Conclusions

One-dimensional hypersonic shock wave structures in argon and nitrogen have been computed using both the Navier-Stokes and Burnett equations. For all cases tested, the Burnett equations represented a significant improvement over the Navier-Stokes equations. Rotational non-equilibrium has been modeled using a bulk-viscosity term as well as a rotational non-equilibrium model. The bulk-viscosity model used in conjunction with the Burnett equations yields density profiles that have the correct thickness, however, no mechanism is present to predict the peak temperature that occurs within the shock. It is expected that the bulk viscosity results would be more appropriate for cases with smaller amounts of rotational non-equilibrium. Navier-Stokes calculations with the rotational non-equilibrium model can predict the value and location of the peak temperature in the shock, but suffer from inaccurate shock thicknesses. The Burnett equations with the rotational non-equilibrium model represented the best combination for predicting shock structure. The results presented in this chapter very closely match those presented by the research group at Stanford.

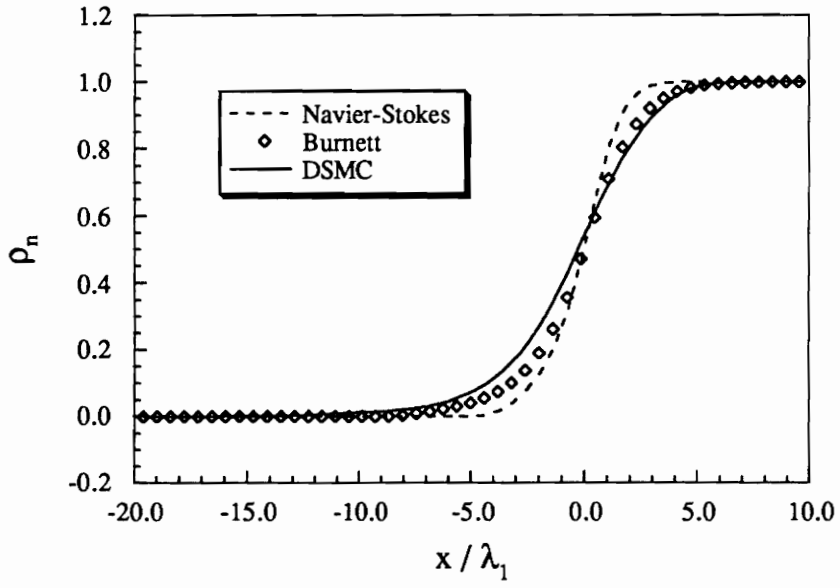

8.1a – Density profiles

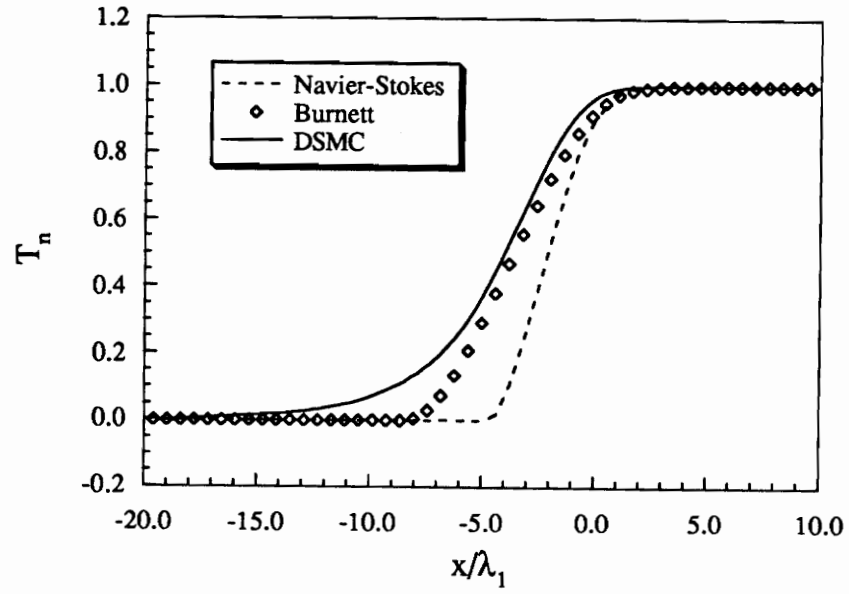

8.1b – Temperature profiles

Fig. 8.1 – Mach 20 Shock in argon

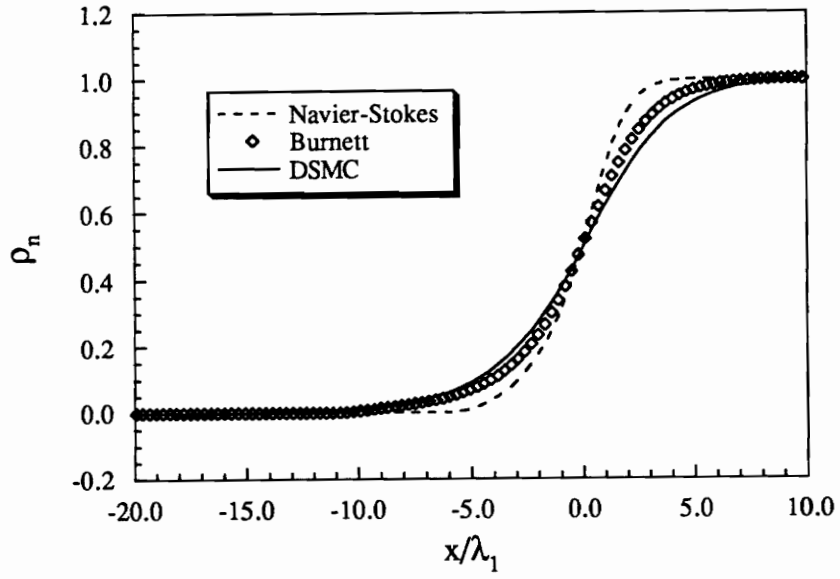

8.2a – Density profiles

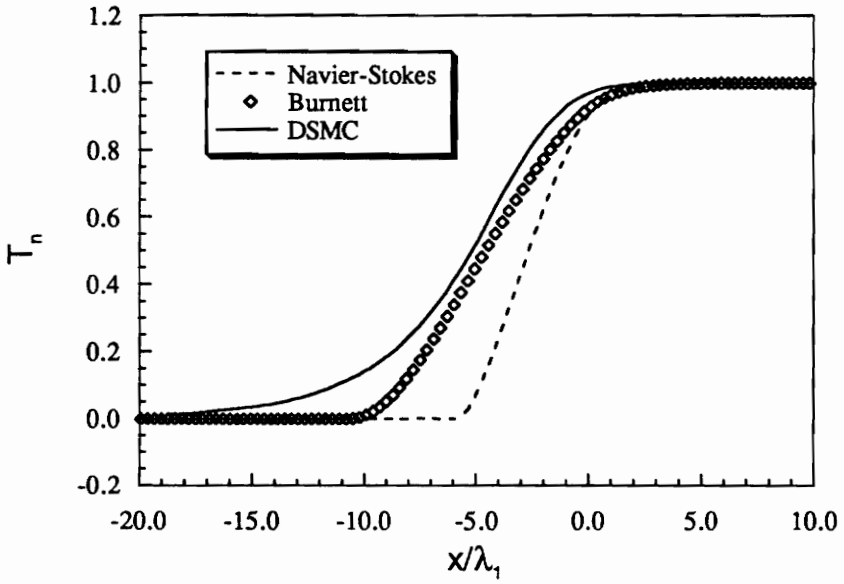

8.2b – Temperature profiles

Fig. 8.2 – Mach 35 Shock in argon

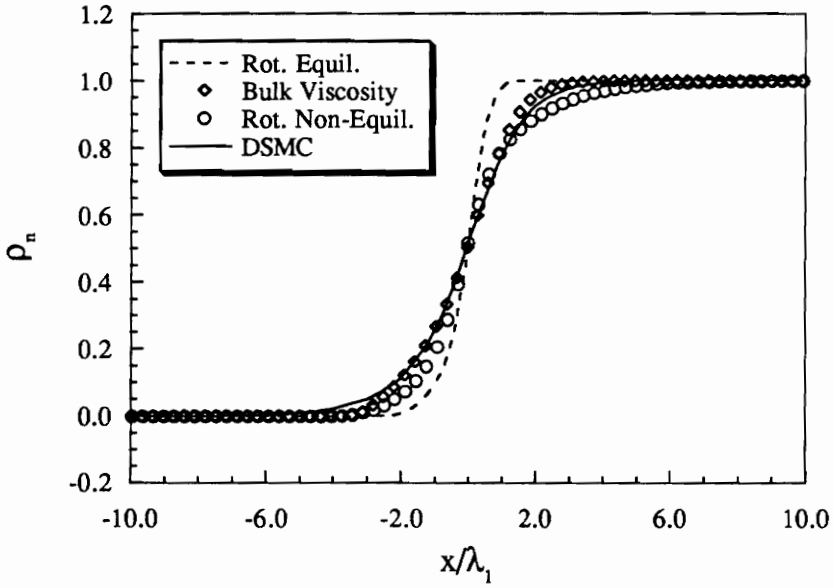

8.3a – Density profiles

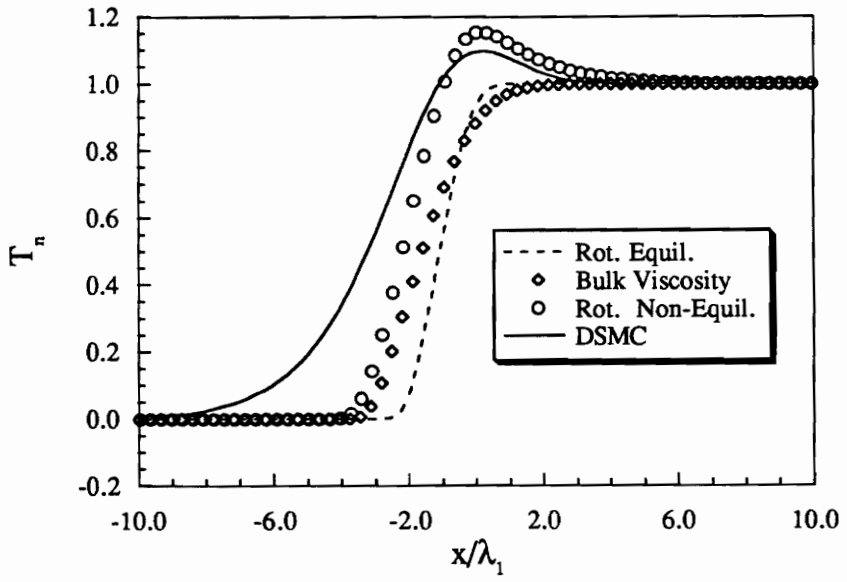

8.3b – Temperature profiles

Fig. 8.3 – Navier-Stokes profiles for a Mach 11 Shock in nitrogen

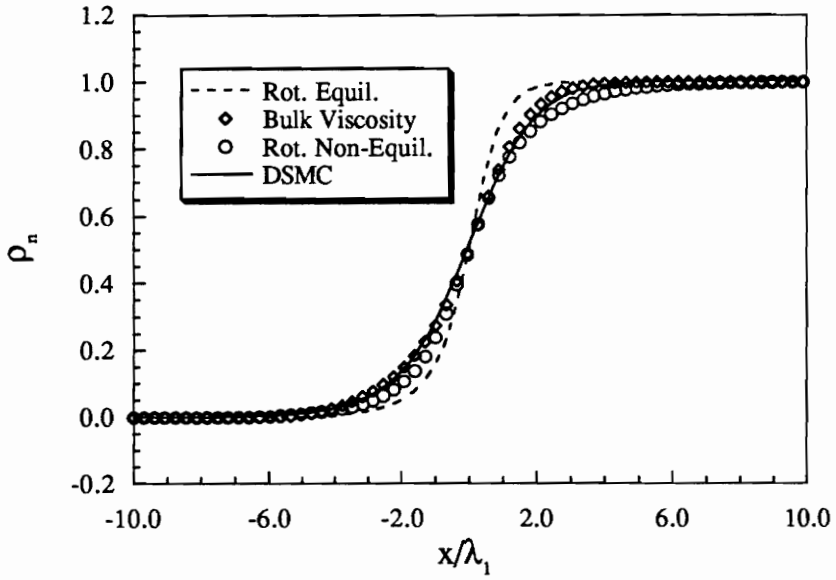

8.4a – Density profiles

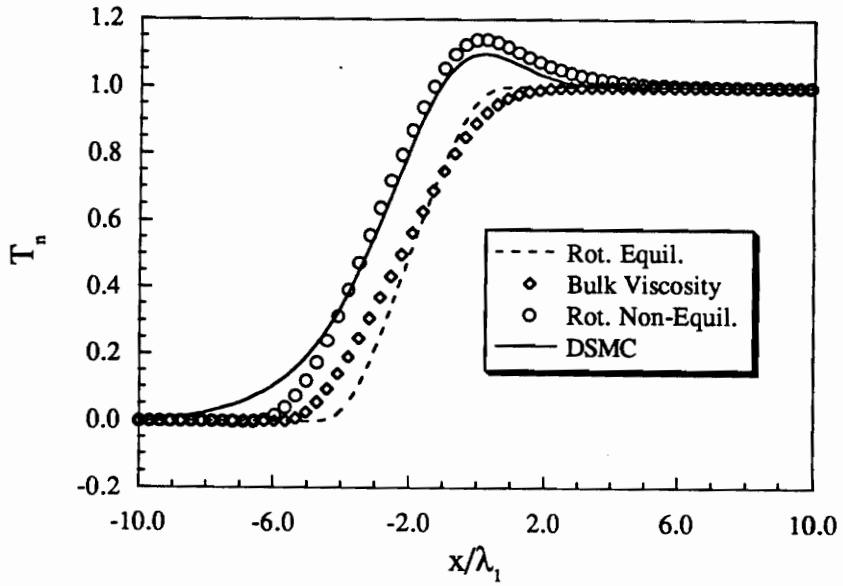

8.4b – Temperature profiles

Fig. 8.4 – Burnett profiles for a Mach 11 Shock in nitrogen

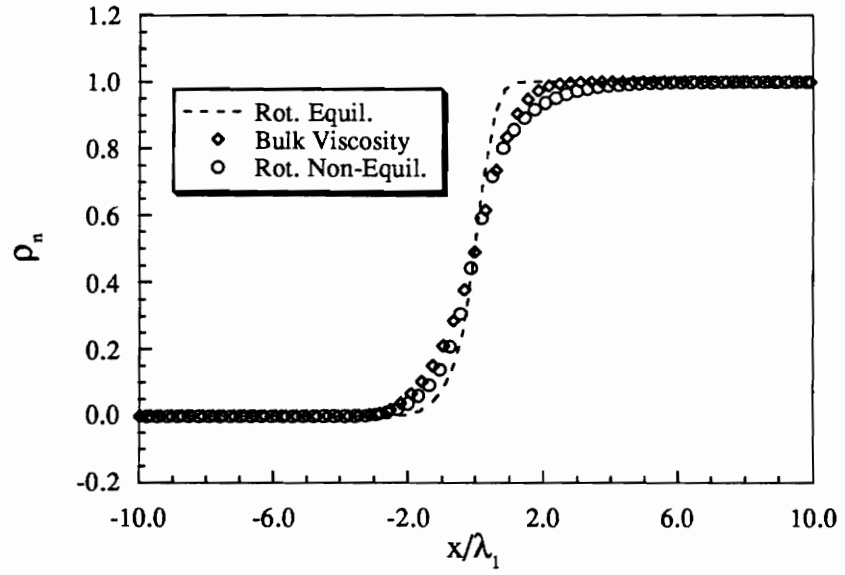

8.5a – Density profiles

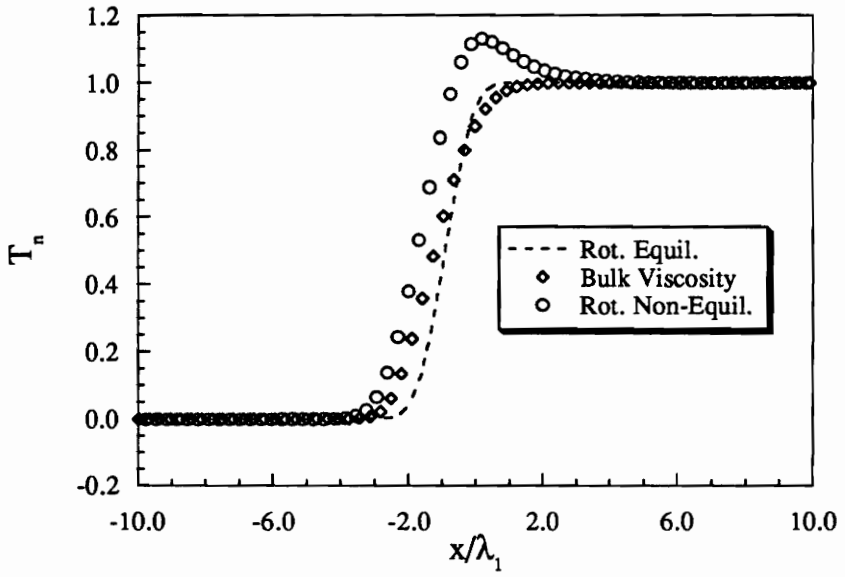

8.5b – Temperature profiles

Fig. 8.5 – Navier-Stokes profiles for a Mach 6 Shock in nitrogen

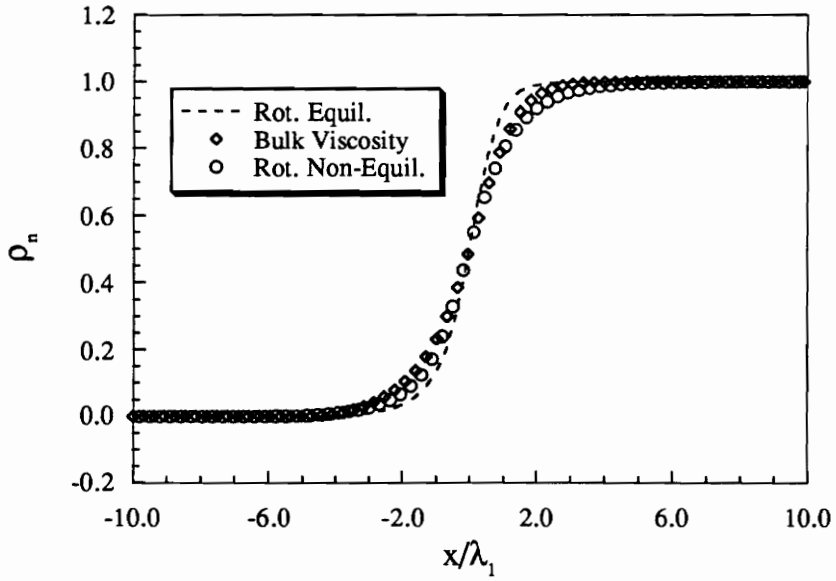

8.6a – Density profiles

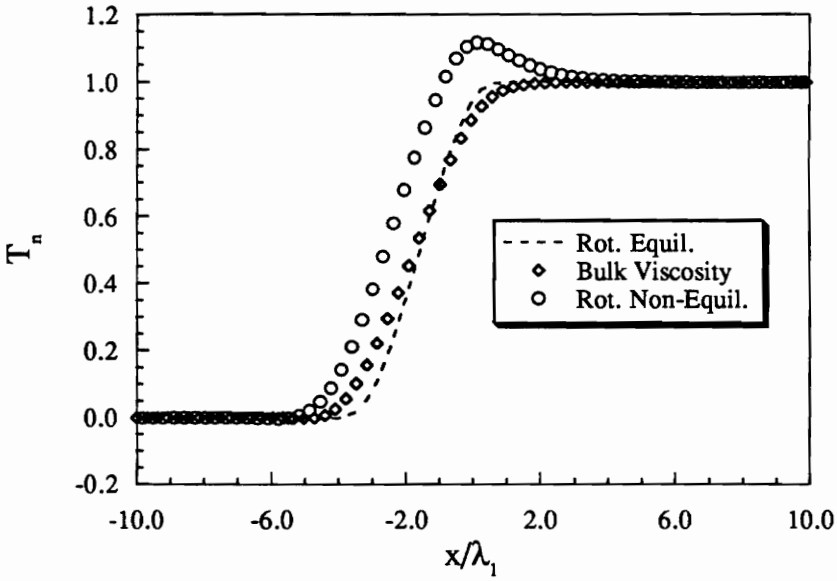

8.6b – Temperature profiles

Fig. 8.6 – Burnett profiles for a Mach 6 Shock in nitrogen

Chapter 9

Summary

9.1 Kinetic Flux-Vector Splitting

A kinetic flux-vector splitting scheme has been developed for flows in chemical and thermal non-equilibrium. The Euler scheme has been derived by taking moments of a discretized Boltzmann scheme with a flux-split, locally Maxwellian velocity distribution. This method differs from existing flux-splitting schemes in that the fluxes are split at the kinetic level based on particle velocity and then averaged over velocity space whereas traditional schemes use a splitting based on the eigenvalues of the flux Jacobian at the Euler level.

The KFVS scheme has been compared with the flux-vector scheme of Van Leer and the flux-difference splitting scheme of Roe for a series of test cases. In all cases the KFVS scheme compares very closely with the Van Leer scheme, showing excellent shock capturing properties. However, in the quasi-one-dimensional results the KFVS scheme appears to smear the shock slightly more than the Roe scheme for a first-order calculation. Higher-order calculations seem to agree much better. The Roe solution on the cone exhibits much better grid convergence and is much more accurate in the boundary layer either the KFVS or van Leer scheme. The results show that even though the KFVS scheme is a Riemann solver at the kinetic level its behavior at the Euler level is more similar to the the existing flux-vector splitting algorithms than to the flux-difference scheme of Roe.

9.2 Multi-Dimensional Kinetic Fluctuation Splitting

A multi-dimensional kinetic fluctuation-splitting scheme has been developed for the Euler equations. The scheme is based on an N-scheme discretization of the Boltzmann equation at the kinetic level for triangulated Cartesian meshes with a diagonal-adaptive strategy. The resulting Euler scheme is a cell-vertex fluctuation-splitting scheme where fluctuations in the conserved variable vector $\mathbf{Q}$ are obtained as moments of the fluctuations in the Maxwellian velocity distribution function at the kinetic level. Encouraging preliminary results have been obtained for perfect gases on Cartesian meshes with first-order spatial accuracy. Results for a simple oblique shock reflection and shear wave show that the MKFS-NDA scheme effectively eliminates the diagonal dependence of the N-scheme and produces discontinuities that are much sharper than those produced by the dimensionally-split CIR scheme. The test case of Woodward and Colella represents a relatively complicated flowfield with complex shock intersections and reflections, contact discontinuities, expansions, and significant regions of subsonic flow. Again, the multi-dimensional scheme produces superior results as compared to the CIR scheme, and produces results that are in general agreement with those in Ref. [95]. Overall, the results for MKFS-NDA scheme show that the methodology presented in this chapter represents an improvement to the well established dimensionally-split upwind schemes.

The extension of the present scheme to general two-dimensional structured or unstructered grids should not be difficult. However, the extension to general three-dimensional grids would involve integrations over three-dimensional regions in velocity space. The extension to the NN-scheme, for higher-order spatial accuracy, appears to be very complex because of the non-linear nature of this scheme. More work remains to be done in these areas before algorithms of this type could be

considered at a production level. The schemes presented here are very complex and inefficient. We have followed this line of research with the hope of gaining some insight into multi-dimensional Riemann solvers. The schemes presented here may give some additional understanding of appropriate multi-dimensional wave decompositions for the Euler equations and may also lead to considerations of multi-dimensional boundary conditions.

9.3 Hypersonic Shock Structure

One-dimensional hypersonic shock wave structures in argon and nitrogen have been computed using both the Navier-Stokes and Burnett equations. For all cases tested, the Burnett equations represented a significant improvement over the Navier-Stokes equations. Rotational non-equilibrium has been modeled using a bulk viscosity term as well as a rotational non-equilibrium model. The bulk viscosity model used in conjunction with the Burnett equations yields density profiles that have the correct thickness, however, no mechanism is present to predict the peak temperature that occurs within the shock. It is expected that the bulk viscosity results would be more appropriate for cases with smaller amounts of rotational non-equilibrium. Navier-Stokes calculations with the rotational non-equilibrium model can predict the value and location of the peak temperature in the shock, but suffer from inaccurate shock thicknesses. The Burnett equations with the rotational non-equilibrium model represented the best combination for predicting shock structure. The results presented in this chapter very closely match those presented by the research group at Stanford.

REFERENCES

[1] Harten, A., Lax, P. and Van Leer, B., "On Upstream Differencing and Godunov-Type Schemes for Hyperbolic Conservation Laws", *SIAM Rev.*, **25**, No.1, 1983, pp. 35–62.

[2] Roe, P. L., "Characteristic-Based Schemes for the Euler Equations", *Ann. Rev. Fluid Mech.*, **18**, 1986, pp. 337–365.

[3] Steger, J. L. and Warming, R. F., "Flux Vector Splitting of the Inviscid Gasdynamics Equations with Application to Finite-Difference Methods", *J. of Computational Physics*, **40**, 1981.

[4] Van Leer, B., "Flux-Vector Splitting for the Euler Equations", in *Lecture Notes in Physics*, **170**, ISBN 0-387-11948-5, Springer-Verlag, 1982.

[5] Roe, P. L., "Approximate Riemann Solvers, Parameter Vectors, and Difference Schemes", *J. of Computational Physics*, **43**, 1981.

[6] Grossman, B. and Walters, R. W., "Flux-Split Algorithms for the Multi-Dimensional Euler Equations with Real Gases", *Computers and Fluids* **17**, No. 1, pp. 99–112, 1989.

[7] Grossman, B. and Walters, R. W., "Analysis of Flux-Split Algorithms for Euler's Equations with Real Gases", *AIAA Journal*, **27**, No. 5, pp. 99–112, 1989.

[8] Grossman, B. and Cinnella, P., "Flux-Split Algorithms for Flows with Non-equilibrium Chemistry and Vibrational Relaxation," *J. Comput. Phys.* **88**, No. 1, pp. 131–168, 1990.

[9] Vincenti, W. G. and Kruger, C. J., Jr., *Introduction to Physical Gas Dynamics*, John Wiley and Sons, Inc., New York, 1965.

[10] Deshpande, S. M., "On the Maxwellian Distribution, Symmetric Form, and Entropy Conservation for the Euler Equations", NASA TP–2583, 1986.

[11] Deshpande, S. M., "Kinetic Theory Based New Upwind Methods For Inviscid Compressible Flows", AIAA Paper No. 86-0275, 1986.

[12] Deshpande, S. M. and Mandal, J. C., "Kinetic Flux Vector Splitting (KFVS) for the Euler Equations", Fluid Mech. Rept. 87–FM–2, Dept. of Aerospace Eng., Indian Institute of Science, Bangalore, India, 1987.

[13] Mandal, J. C. and Deshpande, S. M., "Higher Order Accurate Kinetic Flux Vector Splitting Method for Euler Equations", *Proceedings of the 2nd Int. Conf. on Nonlinear Hyperbolic Problems*, Aachen, Germany, Mar. 1988, *Notes on Numerical Fluid Mechanics*, Vieweg, Vol. 24, 1989, pp. 384–392.

[14] Elizarova, T. G. and Chetverushkin, B. N., "Kinetic Algorithms for Calculating Gas Dynamic Flows", *U.S.S.R. Comput. Maths. Math. Phys.*, **25**, No. 5, 1985, pp. 164–169.

[15] Elizarova, T. G., "A Class of Kinetically Compatible Difference Schemes for Gas Dynamics", *U.S.S.R. Comput. Maths. Math. Phys.*, **27**, No. 6, 1985, pp. 98–101.

[16] Elizarova, T. G. and Chetverushkin, B. N., "Kinetical Consistent Finite-Difference Gasdynamic Schemes", *Proceedings of the 3th International Symposium on Computational Fluid Dynamics*, Nagoya, Japan, 1989, pp. 493–498.

[17] Weatherill, N. P., Mathur, J. S., Natakusumah, D. K. and Marchant, M. J., "An Upwind Kinetic Flux Vector Splitting Method on General Mesh Topologies", *Proceedings of the 4th International Symposium on Computational Fluid Dynamics*, Davis CA, Sept. 1991, pp. 1192–1197.

[18] Eppard, W. M. and Grossman, B., "An Upwind, Kinetic Flux-Vector Splitting Method for Flows in Chemical and Thermal Non-Equilibrium", AIAA Paper No. 93–0894, 1993.

[19] Kumar, A., "Numerical Analysis of the Scramjet-Inlet Flow Field by Using Two-Dimensional Navier-Stokes Equations", NASA TP–1940, 1981.

[20] Drummond, J. P., Rogers, R. C. and Hussaini, M. Y., " A Detailed Numerical Model of a Supersonic Reacting Mixing Layer", AIAA Paper No. 86–1427, 1986.

[21] Carpenter, M. H., "Three-Dimensional Computations of Cross-Flow Injection and Combustion in a Supersonic Flow", AIAA Paper No. 89–1870.

[22] Van Leer, B., "Progress in Multidimensional Upwinding", *Proceedings of the Thirteenth International Conference on Numerical Methods in Fluid Mechanics*, Rome, July 1992, *Lecture Notes in Physics*, **414**, Springer-Verlag, pp. 1–26.

[23] Davis, S. F., "A Rotationally-Biased Upwind Difference Scheme for the Euler Equations", *J. Computat. Phys.*, **56**, 1984, pp. 65–92.

[24] Levy, D. W., Powell, K. G. and Van Leer, B., "An Implementation of a Grid-Independent Upwind Scheme for the Euler Equations", AIAA 89–1931–CP, June 1989.

[25] Dadone, A. and Grossman, B., "A Rotated Upwind Scheme for the Euler Equations", Paper 91–0635, January 1991, also "Characteristic-Based, Rotated Upwind Scheme for the Euler Equations", *AIAA Journal*, **30**, No. 10, 1992, pp. 2219–2226.

[26] Rumsey, C. L., Van Leer, B. and Roe, P. L., "Effect of a Multi-dimensional Flux Function on the Monotonicity of Euler and Navier-Stokes Computations", AIAA 91–1530–CP, June 1991.

[27] Parpia, I. and Michalek, D., "A Shock Capturing Method for Multidimensional Flow", AIAA 90–3016–CP, June 1990.

[28] Roe, P. L., "Discrete Models for the Numerical Analysis of Time-Dependent Multidimensional Gas Dynamics", *J. Computat. Phys.*, **63**, 1986, pp. 458–476.

[29] Hirsch, C. and Lacor, C., "Upwind Algorithms Based on a Diagonalization of the Multidimensional Euler Equations", AIAA Paper No. 89–1958, June 1989.

[30] Powell, K. G. and Van Leer, B., "A Genuine Multi-Dimensional Upwind Cell-Vertex Scheme for the Euler Equations", AIAA Paper No. 89–0095, Jan. 1989.

[31] Roe, P. L., Deconinck, H. and Struijs, R., "Recent Progress in Multidimensional Upwinding", *Proceedings of the Twelfth International Conference on Numerical Methods in Fluid Mechanics*, July 1990, *Lecture Notes in Physics*, **371** Springer-Verlag, pp. 273–277.

[32] Struijs, R., Deconinck, H., De Palma, P., Roe, P. L. and Powell, K. G., "Progress on Multidimensional Upwind Euler Solvers for Unstructured Grids", AIAA 91–1550–CP, June 1991.

[33] Catalano, L. A.,, De Palma, P. and Pascazio, G., "A Multi-Dimensional Solution Adaptive Multigrid Solver for the Euler Equations", *Proceedings of the Thirteenth International Conference on Numerical Methods in Fluid Mechanics*, Rome, July 1992, *Lecture Notes in Physics*, **414**, Springer-Verlag, pp. 90–94.

[34] Roe, P. L. and Beard, L., "An Improved Wave Model for Multidimensional Upwinding of the Euler Equations", *Proceedings of the Thirteenth International Conference on Numerical Methods in Fluid Mechanics*, Rome, July 1992, *Lecture Notes in Physics*, **414**, Springer-Verlag, pp. 135–139.

[35] Eppard, W. M. and Grossman, B., "A Multi-Dimensional Kinetic-Based Upwind Solver for the Euler Equations", *Proceedings of the 11th AIAA Computational Fluid Dynamics Conference*, Orlando FL, July 5-9, 1993 (to appear).

[36] Chapman, D. R., Fiscko, K. A. and Lumpkin, F. E., "Fundamental Problem in Computing Radiating Flow Fields with Thick Shock Waves", *SPIE Proceedings on Sensing, Discrimination, and Signal Processing, and, Superconducting Materials and Instrumentation* **879**, pp. 106–112, 1988.

[37] Moreau, S., Chapman, D. R. and MacCormack, R. W., "Effect of Rotational Relaxation and Approximate Burnett Terms on Hypersonic Flow-Field Radiation at High Altitudes", AIAA Paper No. 91–1702.

[38] Alsmeyer, H., "Density Profiles in Argon and Nitrogen Shock Waves Measured by the Absorbtion of an Electron Beam", *J.of Fluid Mechanics*, **74**, Part 3, pp. 497–513, 1976.

[39] Chapman, S. and Cowling, T. G., *The Mathematical Theory of Non-Uniform Gases*, Cambridge Univ. Press, London, 1970.

[40] Fiscko, K. A. and Chapman, D. R., "Comparison of Burnett, Super-Burnett and Monte Carlo Solutions for Hypersonic Shock Structure", *Proceedings of the 16th International Symposium of Rarefied Gas Dynamics*, ed. E. P. Muntz, D. P. Weaver and D. H. Campbell, *Progress in Aeronautics and Astronautics*, **118**, p. 374, 1988.

[41] Fiscko, K. A. and Chapman, D. R., "Hypersonic Shock Structure with Burnett Terms in the Viscous Stress and Heat Flux", AIAA Paper No. 88–2733, June, 1988.

[42] Talbot, L., and Sherman, F. S., "Structure of Weak Shock Waves in a Monatomic Gas", *NASA Memorandum* 12–14–58W, 1959.

[43] Gilbarg, D. and Paolucci, D., "The Strucure of Shock Waves in the Continuum Theory of Fluids", *J.of Rational Mechanical Analysis*, **2**, p. 617, 1953.

[44] Zong, X., MacCormack, R. W. and Chapman, D. R., "Stabilization of the Burnett Equations and Application to High-Altitude Hypersonic Flows", AIAA Paper No. 91–0770, January, 1991.

[45] Lumpkin III, F. E., "Accuracy of the Burnett Equations for Hypersonic Real Gas Flows", AIAA Paper No. 91–0771, January, 1991.

[46] Lumpkin, F. E., III and Chapman, D. R., "A New Rotational Model For Use in Hypersonic Computational Fluid Mechanics", AIAA Paper No. 89–1737.

[47] Wang Chang, C. S. and Uhlenbeck G. E., "Transport Phenomena in Polyatomic Gases", *CM–681, Engineering Research Institute, University of Michigan*, 1951.

[48] Parker, J. G., "Rotational and Vibrational Relaxation in Diatomic Gases," *Physics of Fluids* **2**, p. 449, 1959.

[49] Lordi, J. A. and R. E. Mates, "Rotational Relaxation in Nonpolar Diatomic Gases", *Physics of Fluids* **13**, p. 291, 1970.

[50] Goldstein, S. "The Navier-Stokes Equations and the Bulk Viscosity of Simple Gases", *J. of Mathematical and Physical Sciences*, **6**, pp. 225–261, 1972.

[51] Bruno, C.,"Real Gas Effects",*Hypersonics* **1**, eds. J. J. Bertin, R. Glowinski, J. Periaux, ISBN 0–8176–3420–7, Birkauser Boston, 1989.

[52] Liu, Y. and Vinokur, M., "Upwind Algorithms for General Thermo-Chemical Nonequilibrium Flows", AIAA Paper No. 89–0201, 1989.

[53] Jaffe, R. L., "The Calculation of High Temperature Equilibrium and Nonequilbrium Specific Heat Data for N_2, O_2, and NO", AIAA Paper No. 87–1633, 1987.

[54] Stupenchenko, Y. V., *et al.*, *Relaxation in Shock Waves*, Springer-Verlag, New York, Inc., 1967.

[55] Christensen, W. H., " Fundamentals of Nonequilibrium Gasdynamics", *AIAA Professional Series*, "Nonequilibrium Gasdynamics", Buffalo, N.Y., June 10-11, 1989.

[56] Cinnella, P. and Grossman, B., "Upwind Techniques for Flows with Multiple Translational Temperatures", AIAA Paper No. 90-1660, 1990.

[57] Grossman, B., Cinnella, P. and Eppard, W. M., "New Developments Pertaining to Algorithms for Non-Equilibrium Hypersonic Flows", *Computational Fluid Dynamics J.*, **1**, No. 2, July 1992, pp. 175–186.

[58] Hirschfelder, J. O. Curtiss, C. F. and Bird, R. B., *Molecular Theory of Gases and Liquids*, Library of Congress CCN 54–7621, John Wiley and Sons, 1954.

[59] Curtiss, C. F. and Hirschfelder, J. O., "Transport Properties Multicomponent Gas Mixtures", *J. of Computational Physics*, **17**, No. 6, pp. 550–555, 1949.

[60] Sharma, S. P. and Schwenke, D. W., "The Rate Parameters for Coupled Rotation-Vibration-Dissociation phenomena in H_2", AIAA Paper No. 89–1738, 1989.

[61] Candler, G. V., "Translation-Vibration-Dissociation Coupling in Nonequilibrium Hypersonic Flows", AIAA Paper No. 89–1739, 1989.

[62] Candler, G. V. and MacCormack, R. W., " The Computation of Hypersonic Ionized Flows in Chemical and Thermal Nonequilibrium", AIAA Paper No. 88-0511, 1988.

[63] Park, C., "Calculation of Nonequilibrium Radiation in the Flight Regimes of Aeroassisted Orbital Transfer Vehicles",*Thermal Design of Aeroassisted Orbital Transfer Vehicles*, ed. H. F. Nelson, *Progress in Aeronautics and Astronautics*, **96**, pp. 395–418, 1985.

[64] Candler, G. V., Park, C. and Diewert G. S., " Numerical Techniques and Application",*AIAA Professional Series*, "Nonequilibrium Gasdynamics", Buffalo, N.Y., June 10-11, 1989.

[65] Park, C., "Two-Temperature Interpretation of Dissociation Rate Data for N_2 and O_2", AIAA Paper No. 88–0458, 1988.

[66] Park, C., "A Review of Reaction Rates in High Temperature Air", AIAA Paper No. 89–1740, 1989.

[67] Liu, Y. and Vinokur, M., "Nonequilibrium Flow Computations: I. An Analysis of Numerical Formulations of Conservation Laws",NASA CR 177489, 1988.

[68] Strehlow, R. A., *Combustion Fundamentals*, McGraw-Hill, New York, 1984.

[69] Lee, J.-H.,"Basic Governing Equations for the Flight Regimes of Aeroassisted Orbital Transfer Vehicles", *Progress in Astronautics and Aeronautics*, **96**, 1985.

[70] Walters, R. W. and Thomas, J .L., "Advances in Upwind Relaxation Methods", *Chapter 4, State-of-the-Art Surveys of Computational Mechanics*, ed. A. K. Noor, ASME Publication, 1988.

[71] Lax, P. D., "Weak Solutions of the Nonlinear Hyperbolic Equations and their Computation", *Communications in Pure and Applied Mathematics*, **7**, 1954.

[72] Anderson, J. D., *Modern Compressible Flow with Historical Perspective*, ISBN 0–07–001654–2, McGraw-Hill, 1982.

[73] Kang, S.-W. and Dunn, M. G.,"Theoretical and Measured Electron-Density Distributions for the RAM Vehicle at High Altitudes", AIAA Paper No. 72–689, 1972.

[74] Candler, G.,"On the Computation of Shock Shapes in Nonequilibrium Hypersonic Flows", AIAA Paper No. 89–0312, 1989.

[75] Millikan, R. C. and White, D. R., "Systematics of Vibrational Relaxation", *The J. of Chemical Physics* **39**, No. 12, 1963.

[76] Svehla, R. A., "Estimated Viscosities and Thermal Conductivities of Gases at High Temperature", NASA Tech. Rep. TR R–132.

[77] Blottner, F. G., Johnson, M. and Ellis, M., "Chemically Reacting Viscous Flow Program for Multi-Component Gas Mixtures", Sandia Laboratories SC–RR–70–754, 1971.

[78] White, F. M., *Viscous Fluid Flow*, McGraw-Hill, Inc., New York, 1974.

[79] Wilke, C. R., "A Viscosity Equation for Gas Mixtures", *J. of Computational Physics*, **18**, No. 4, pp. 517–519, 1950.

[80] Williams, F. A., *Combustion Theory*, Addison-Wesley Publishing Company, Inc., Reading, Mass., 1965.

[81] Mason, E. A. and Monchick, L., "Heat Conductivity of Polyatomic and Polar Gases", *J. Comp Phys.*, **36**, p. 1622, 1962.

[82] Wang Chang, C. S. and Uhlenbeck, G. E., "On the Transport Phenomena in Rarefied Gases", *Studies in Statistical Mechanics*, **1**, No. 17, 1948.

[83] Simon, C. E., "Theory of Shock Structure in a Maxwell Gas Based on the Chapman-Enskog Development through Super-Burnett Order", Ph.D. thesis, University of Colorado, 1976.

[84] Shavaliev, M. S., "The Burnett Approximation of the Distribution Function and the Super-Burnett Contributions to the Stress Tensor and the Heat Flux", *J. of Applied Mathematics and Mechanics*, **42**, No. 4, pp. 656–702, 1978.

[85] Chakravarthy, S. R., Szema, K-Y., Goldberg, U. C., Gorski, J. J. and Osher, S., "Application of a New Class of High Accuracy TVD Schemes to the Navier-Stokes Equation", AIAA Paper No. 85–0165.

[86] Oran, E. S. and Boris, J. P., *Numerical Simulation of Reactive Flow*, ISBN 0–444–01251–6, Elsvier Science Publishing Co., 1987.

[87] Kee, R. J. and Dwyer, H. A., "Review of Stiffness and Implicit Finite-Difference Methods in Combustion Modeling", *Progress in Astronautics and Aeronautics*, **76**, 1979.

[88] Yee, H. C. and Shinn, J. L., "Semi-Implicit and Fully Implicit Shock Capturing Methods for Hyperbolic Conservation Laws with Stiff Source Terms", NASA TM 89415, 1986.

[89] Ianelli, G. S. and Baker, A. J., "A Stiffly-Stable Implicit Runge-Kutta Algorithm for CFD Applications", AIAA Paper No. 88–0416, 1988.

[90] Grossman, B., Cinnella, P. and Garrett, J. G., "A Survey of Upwind Methods for Flows with Equilibrium and Non-equilibrium Chemistry and Thermodynamics", Paper 89–1653, AIAA 24th Thermophysics Conference, June 1989.

[91] Van Leer, B., Thomas, J. L., Roe, P. L. and Newsome, R. W., "A Comparison of Numerical Flux Formulas for the Euler and Navier-Stokes Equations", *Proceedings AIAA 8th CFD Conf.*, AIAA–87–1104–CP, June 1987.

[92] Singh, D. H., Carpenter, M. H. and Kumar, A., "Numerical Simulation of Shock-Induced Combustion/Detonation in a Premixed H_2-Air Mixture Using Navier-Stokes Equations", AIAA Paper No. 91-3359.

[93] Walters, R. W., Cinnella, P., Slack, D. C. and Halt, D., "Characteristic-Based Algorithms for Flows in Thermo-Chemical Nonequilibrium", AIAA Paper No. 90-0393.

[94] Rice, J. G. and Schnipke, R., L., "A Monotone Streamline Upwind Finite Element for Convection Dominated Flows", *Comp. Meth in Appl. Mech. and Eng.*, **48**, pp. 313–327, 1985.

[95] Woodward, P., and Colella, P., "The Numerical Simulation of Two-Dimensional Fluid Flow with Strong Shocks", *J. of Computational Physics*, **54**, pp. 115–173, 1984

[96] Xu, K. and Prendergast, K. H., "Multidimensional Hydrocode from Kinetic Theory", submitted to *J. Comp. Phy.*, Jan 1993.

[97] Eppard, W. M., and Grossman, B., "Calculation of Hypersonic Shock Structure Using Flux-Split Algorithms", ICAM Report 91–07–04, Virginia Polytechnic Institute and State University, Blacksburg VA, July 1991.

Appendix A

Integrals for MKFS Schemes

A.1 Moments for MKFS-NDD Scheme

Expressions for the 48 moments that appear in the MKFS-NDD scheme (see Sec. 7.3.1) are given in Secs. A.1.1 - A.1.4. The results are written in terms of β, defined by Eq. (3.12b), the cell aspect ratio α, defined by Eq. (7.24), and the Cartesian velocity components u_1 and u_2. The error function $erf(x)$, defined in Eq. (6.21), and its complement $erfc(x)$, given by

$$erfc(x) = 1 - erf(x)\,, \tag{A.1}$$

also appear. One portion of the integration could not be performed analytically. This integral is given by

$$\Omega_{1,2} = \int_{\pm a}^{\infty} e^{-z^2} erf(\pm z\alpha + \mu) dz\,, \tag{A.2a}$$

where

$$\mu = \sqrt{\beta}(u_1\alpha + u_2)\,, \tag{A.2b}$$

and

$$a = -\sqrt{\beta}u_1\,. \tag{A.2c}$$

In Sec. A.1.5 approximate numerical methods will be presented for the evaluation of this integral.

A.1.1 ψ_1 Moments

The ψ_1 moments are determined when the first element of the moment function vector is considered, *i.e.*, $\psi_1 = m$, the molecular mass. The corresponding 12 integrals are given as

$$I_D^1(\psi_1) = \int_{-\infty}^{\infty}\int_{-\infty}^{0}\int_{-\infty}^{0} \rho c_1 f_0 dc_2 dc_1 dc_3$$
$$= \frac{\rho\sqrt{\beta}}{2\sqrt{\pi}}\Big[-\frac{1}{2\beta}e^{-\beta u_1^2} + \frac{u_1\sqrt{\pi}}{2\sqrt{\beta}} erfc(\sqrt{\beta}u_1)\Big] erfc(\sqrt{\beta}u_2)\,, \tag{A.3}$$

$$I_D^2(\psi_1) = \int_{-\infty}^{\infty}\int_{-\infty}^{0}\int_{-\infty}^{0} \rho c_2 f_0 dc_2 dc_1 dc_3$$
$$= \frac{\rho\sqrt{\beta}}{2\sqrt{\pi}}\Big[-\frac{1}{2\beta}e^{-\beta u_2^2} + \frac{u_2\sqrt{\pi}}{2\sqrt{\beta}} erfc(\sqrt{\beta}u_2)\Big] erfc(\sqrt{\beta}u_1)\,, \tag{A.4}$$

$$I_D^3(\psi_1) = \int_{-\infty}^{\infty}\int_{-\infty}^{0}\int_{0}^{-c_1\alpha} \rho c_1 f_0 dc_2 dc_1 dc_3$$
$$= \frac{\rho\sqrt{\beta}}{2\sqrt{\pi}}\Big[\frac{u_1\sqrt{\pi}}{2\sqrt{\beta}} erfc(\sqrt{\beta}u_1) erf(\sqrt{\beta}u_2)$$
$$- \frac{\alpha}{2\beta\sqrt{1+\alpha^2}} e^{\frac{-\mu^2}{1+\alpha^2}} erfc[\frac{\sqrt{\beta}(u_1-\alpha u_2)}{\sqrt{1+\alpha^2}}] - \frac{u_1}{\sqrt{\beta}}\Omega_2\Big]\,, \tag{A.5}$$

$$I_D^4(\psi_1) = \int_{-\infty}^{\infty}\int_{-\infty}^{0}\int_{0}^{-c_1\alpha} \rho c_2 f_0 dc_2 dc_1 dc_3$$
$$= \frac{\rho\sqrt{\beta}}{2\sqrt{\pi}}\Big[\frac{1}{2\beta}e^{-\beta u_2^2} erfc(\sqrt{\beta}u_1) + \frac{u_2\sqrt{\pi}}{2\sqrt{\beta}} erf(\sqrt{\beta}u_2) erfc(\sqrt{\beta}u_1)$$
$$- \frac{1}{2\beta\sqrt{1+\alpha^2}} e^{\frac{-\mu^2}{1+\alpha^2}} erfc[\frac{\sqrt{\beta}(u_1-\alpha u_2)}{\sqrt{1+\alpha^2}}] - \frac{u_2}{\sqrt{\beta}}\Omega_2\Big]\,, \tag{A.6}$$

$$I_D^5(\psi_1) = \int_{-\infty}^{\infty}\int_{0}^{\infty}\int_{-\infty}^{-c_1\alpha} \rho c_1 f_0 dc_2 dc_1 dc_3$$
$$= \frac{\rho\sqrt{\beta}}{2\sqrt{\pi}}\Big[\frac{1}{2\beta}e^{-\beta u_1^2} erfc(\sqrt{\beta}u_2) + \frac{u_1\sqrt{\pi}}{2\sqrt{\beta}} erfc(-\sqrt{\beta}u_1)$$
$$- \frac{\alpha}{2\beta\sqrt{1+\alpha^2}} e^{\frac{-\mu^2}{1+\alpha^2}} erfc[\frac{-\sqrt{\beta}(u_1-\alpha u_2)}{\sqrt{1+\alpha^2}}] - \frac{u_1}{\sqrt{\beta}}\Omega_1\Big]\,, \tag{A.7}$$

$$I_D^6(\psi_1) = \int_{-\infty}^{\infty}\int_{0}^{\infty}\int_{-\infty}^{-c_1\alpha} \rho c_2 f_0 dc_2 dc_1 dc_3$$
$$= \frac{\rho\sqrt{\beta}}{2\sqrt{\pi}}\Big[\frac{u_2\sqrt{\pi}}{2\sqrt{\beta}} erfc(-\sqrt{\beta}u_1)$$
$$- \frac{1}{2\beta\sqrt{1+\alpha^2}} e^{\frac{-\mu^2}{1+\alpha^2}} erfc[\frac{-\sqrt{\beta}(u_1-\alpha u_2)}{\sqrt{1+\alpha^2}}] - \frac{u_2}{\sqrt{\beta}}\Omega_1\Big], \qquad (A.8)$$

$$I_D^7(\psi_1) = \int_{-\infty}^{\infty}\int_{0}^{\infty}\int_{-c_1\alpha}^{0} \rho c_1 f_0 dc_2 dc_1 dc_3$$
$$= \frac{\rho\sqrt{\beta}}{2\sqrt{\pi}}\Big[\frac{-u_1\sqrt{\pi}}{2\sqrt{\beta}} erfc(-\sqrt{\beta}u_1) erf(\sqrt{\beta}u_2)$$
$$+ \frac{\alpha}{2\beta\sqrt{1+\alpha^2}} e^{\frac{-\mu^2}{1+\alpha^2}} erfc[\frac{-\sqrt{\beta}(u_1-\alpha u_2)}{\sqrt{1+\alpha^2}}] + \frac{u_1}{\sqrt{\beta}}\Omega_1\Big], \qquad (A.9)$$

$$I_D^8(\psi_1) = \int_{-\infty}^{\infty}\int_{0}^{\infty}\int_{-c_1\alpha}^{0} \rho c_2 f_0 dc_2 dc_1 dc_3$$
$$= \frac{\rho\sqrt{\beta}}{2\sqrt{\pi}}\Big[-\frac{1}{2\beta} e^{-\beta u_2{}^2} erfc(-\sqrt{\beta}u_1) - \frac{u_2\sqrt{\pi}}{2\sqrt{\beta}} erf(\sqrt{\beta}u_2) erfc(-\sqrt{\beta}u_1)$$
$$+ \frac{1}{2\beta\sqrt{1+\alpha^2}} e^{\frac{-\mu^2}{1+\alpha^2}} erfc[\frac{-\sqrt{\beta}(u_1-\alpha u_2)}{\sqrt{1+\alpha^2}}] + \frac{u_2}{\sqrt{\beta}}\Omega_1\Big], \qquad (A.10)$$

$$I_D^9(\psi_1) = \int_{-\infty}^{\infty}\int_{0}^{\infty}\int_{0}^{\infty} \rho c_1 f_0 dc_2 dc_1 dc_3$$
$$= \frac{\rho\sqrt{\beta}}{2\sqrt{\pi}}\Big[\frac{1}{2\beta} e^{-\beta u_1{}^2} + \frac{u_1\sqrt{\pi}}{2\sqrt{\beta}} erfc(-\sqrt{\beta}u_1)\Big] erfc(-\sqrt{\beta}u_2), \qquad (A.11)$$

$$I_D^{10}(\psi_1) = \int_{-\infty}^{\infty}\int_{0}^{\infty}\int_{0}^{\infty} \rho c_2 f_0 dc_2 dc_1 dc_3$$
$$= \frac{\rho\sqrt{\beta}}{2\sqrt{\pi}}\Big[\frac{1}{2\beta} e^{-\beta u_2{}^2} + \frac{u_2\sqrt{\pi}}{2\sqrt{\beta}} erfc(-\sqrt{\beta}u_2)\Big] erfc(-\sqrt{\beta}u_1), \qquad (A.12)$$

$$I_D^{11}(\psi_1) = \int_{-\infty}^{\infty}\int_{-\infty}^{0}\int_{-c_1\alpha}^{\infty} \rho c_1 f_0 dc_2 dc_1 dc_3$$
$$= \frac{\rho\sqrt{\beta}}{2\sqrt{\pi}}\Big[-\frac{1}{2\beta} e^{-\beta u_1{}^2} erfc(-\sqrt{\beta}u_2) + \frac{u_1\sqrt{\pi}}{2\sqrt{\beta}} erfc(\sqrt{\beta}u_1)$$
$$+ \frac{\alpha}{2\beta\sqrt{1+\alpha^2}} e^{\frac{-\mu^2}{1+\alpha^2}} erfc[\frac{\sqrt{\beta}(u_1-\alpha u_2)}{\sqrt{1+\alpha^2}}] + \frac{u_1}{\sqrt{\beta}}\Omega_2\Big], \qquad (A.13)$$

$$I_D^{12}(\psi_1) = \int_{-\infty}^{\infty}\int_{-\infty}^{0}\int_{-c_1\alpha}^{\infty} \rho c_2 f_0 dc_2 dc_1 dc_3$$
$$= \frac{\rho\sqrt{\beta}}{2\sqrt{\pi}}\Big[\frac{u_2\sqrt{\pi}}{2\sqrt{\beta}} erfc(\sqrt{\beta}u_1) + \frac{1}{2\beta\sqrt{1+\alpha^2}} e^{\frac{-\mu^2}{1+\alpha^2}} erfc[\frac{\sqrt{\beta}(u_1-\alpha u_2)}{\sqrt{1+\alpha^2}}]$$
$$+ \frac{u_2}{\sqrt{\beta}}\Omega_2\Big]. \qquad (A.14)$$

A.1.2 ψ_2 Moments

The ψ_2 moments are determined when the second element of the moment function vector is considered, *i.e.*, $\psi_1 = mc_1$, the molecular momentum in the x_1-direction. The corresponding 12 integrals are given as

$$I_D^1(\psi_2) = \int_{-\infty}^{\infty}\int_{-\infty}^{0}\int_{-\infty}^{0} \rho {c_1}^2 f_0 dc_2 dc_1 dc_3$$
$$= \frac{\rho\sqrt{\beta}}{2\sqrt{\pi}}\Big[-\frac{u_1}{2\beta} e^{-\beta {u_1}^2} erfc(\sqrt{\beta}u_2)$$
$$+ \frac{\sqrt{\pi}}{4\beta\sqrt{\beta}}(1+2\beta {u_1}^2) erfc(\sqrt{\beta}u_1) erfc(\sqrt{\beta}u_2)\Big], \qquad (A.15)$$

$$I_D^2(\psi_2) = \int_{-\infty}^{\infty}\int_{-\infty}^{0}\int_{-\infty}^{0} \rho c_1 c_2 f_0 dc_2 dc_1 dc_3$$
$$= \frac{\rho\beta}{\pi}\Big[\frac{1}{4\beta^2} e^{-\beta({u_1}^2+{u_2}^2)} - \frac{u_2\sqrt{\pi}}{4\beta\sqrt{\beta}} e^{-\beta {u_1}^2} erfc(\sqrt{\beta}u_2)$$
$$- \frac{u_1\sqrt{\pi}}{4\beta\sqrt{\beta}} e^{-\beta {u_2}^2} erfc(\sqrt{\beta}u_1) + \frac{u_1 u_2 \pi}{4\beta} erfc(\sqrt{\beta}u_1) erfc(\sqrt{\beta}u_2)\Big], \qquad (A.16)$$

$$I_D^3(\psi_2) = \int_{-\infty}^{\infty}\int_{-\infty}^{0}\int_{0}^{-c_1\alpha} \rho {c_1}^2 f_0 dc_2 dc_1 dc_3$$
$$= \frac{\rho\sqrt{\beta}}{2\sqrt{\pi}}\Big[\frac{\alpha}{2\beta\sqrt{\beta}\sqrt{\pi}(1+\alpha^2)} e^{-\beta({u_1}^2+{u_2}^2)}$$
$$+ \frac{\sqrt{\pi}}{4\beta\sqrt{\beta}}(1+2\beta {u_1}^2) erfc(\sqrt{\beta}u_1) erf(\sqrt{\beta}u_2)$$
$$- \frac{\alpha}{\beta(1+\alpha^2)^{3/2}}(u_1-\alpha u_2) e^{\frac{-\mu^2}{1+\alpha^2}} erfc[\frac{\sqrt{\beta}(u_1-\alpha u_2)}{\sqrt{1+\alpha^2}}]$$
$$- \frac{1}{2\beta\sqrt{\beta}}(1+2\beta {u_1}^2)\Omega_2\Big], \qquad (A.17)$$

$$
\begin{aligned}
I_D^4(\psi_2) &= \int_{-\infty}^{\infty}\int_{-\infty}^{0}\int_{0}^{-c_1\alpha} \rho c_1 c_2 f_0 dc_2 dc_1 dc_3 \\
&= \frac{\rho\beta}{\pi}\Big[-\frac{\alpha^2}{4\beta^2(1+\alpha^2)}e^{-\beta({u_1}^2+{u_2}^2)} + \frac{u_1\sqrt{\pi}}{4\beta\sqrt{\beta}}e^{-\beta{u_2}^2}erfc(\sqrt{\beta}u_1) \\
&\quad + \frac{u_1u_2\pi}{4\beta}erf(\sqrt{\beta}u_2)erfc(\sqrt{\beta}u_1) \\
&\quad - \frac{\sqrt{\pi}}{4\beta\sqrt{\beta}(1+\alpha^2)^{3/2}}(u_1+\alpha^3u_2)e^{\frac{-\mu^2}{1+\alpha^2}}erfc[\frac{\sqrt{\beta}(u_1-\alpha u_2)}{\sqrt{1+\alpha^2}}] \\
&\quad - \frac{u_1u_2\sqrt{\pi}}{2\beta}\Omega_2\Big], \qquad (A.18)
\end{aligned}
$$

$$
\begin{aligned}
I_D^5(\psi_2) &= \int_{-\infty}^{\infty}\int_{0}^{\infty}\int_{-\infty}^{-c_1\alpha} \rho {c_1}^2 f_0 dc_2 dc_1 dc_3 \\
&= \frac{\rho\sqrt{\beta}}{2\sqrt{\pi}}\Big[-\frac{\alpha}{2\beta\sqrt{\beta}\sqrt{\pi}(1+\alpha^2)}e^{-\beta({u_1}^2+{u_2}^2)} + \frac{u_1}{2\beta}e^{-\beta{u_1}^2}erfc(\sqrt{\beta}u_2) \\
&\quad + \frac{\sqrt{\pi}}{4\beta\sqrt{\beta}}(1+2\beta{u_1}^2)erfc(-\sqrt{\beta}u_1) \\
&\quad - \frac{\alpha}{\beta(1+\alpha^2)^{3/2}}(u_1-\alpha u_2)e^{\frac{-\mu^2}{1+\alpha^2}}erfc[\frac{-\sqrt{\beta}(u_1-\alpha u_2)}{\sqrt{1+\alpha^2}}] \\
&\quad - \frac{1}{2\beta\sqrt{\beta}}(1+2\beta{u_1}^2)\Omega_1\Big], \qquad (A.19)
\end{aligned}
$$

$$
\begin{aligned}
I_D^6(\psi_2) &= \int_{-\infty}^{\infty}\int_{0}^{\infty}\int_{-\infty}^{-c_1\alpha} \rho c_1 c_2 f_0 dc_2 dc_1 dc_3 \\
&= \frac{\rho\beta}{\pi}\Big[-\frac{1}{4\beta^2(1+\alpha^2)}e^{-\beta({u_1}^2+{u_2}^2)} \\
&\quad + \frac{u_2\sqrt{\pi}}{4\beta\sqrt{\beta}}e^{-\beta{u_1}^2}erfc(\sqrt{\beta}u_2) + \frac{u_1u_2\pi}{4\beta}erfc(-\sqrt{\beta}u_1) \\
&\quad - \frac{\sqrt{\pi}}{4\beta\sqrt{\beta}(1+\alpha^2)^{3/2}}(u_1+\alpha^3u_2)e^{\frac{-\mu^2}{1+\alpha^2}}erfc[\frac{-\sqrt{\beta}(u_1-\alpha u_2)}{\sqrt{1+\alpha^2}}] \\
&\quad - \frac{u_1u_2\sqrt{\pi}}{2\beta}\Omega_1\Big], \qquad (A.20)
\end{aligned}
$$

$$
\begin{aligned}
I_D^7(\psi_2) &= \int_{-\infty}^{\infty}\int_{0}^{\infty}\int_{-c_1\alpha}^{0} \rho {c_1}^2 f_0 dc_2 dc_1 dc_3 \\
&= \frac{\rho\sqrt{\beta}}{2\sqrt{\pi}}\Big[\frac{\alpha}{2\beta\sqrt{\beta}\sqrt{\pi}(1+\alpha^2)}e^{-\beta({u_1}^2+{u_2}^2)} \\
&\quad - \frac{\sqrt{\pi}}{4\beta\sqrt{\beta}}(1+2\beta{u_1}^2)erfc(-\sqrt{\beta}u_1)erf(\sqrt{\beta}u_2) \\
&\quad + \frac{\alpha}{\beta(1+\alpha^2)^{3/2}}(u_1-\alpha u_2)e^{\frac{-\mu^2}{1+\alpha^2}}erfc[\frac{-\sqrt{\beta}(u_1-\alpha u_2)}{\sqrt{1+\alpha^2}}]
\end{aligned}
$$

$$+\frac{1}{2\beta\sqrt{\beta}}(1+2\beta {u_1}^2)\Omega_1\Big], \tag{A.21}$$

$$\begin{aligned}
I_D^8(\psi_2) &= \int_{-\infty}^{\infty}\int_{0}^{\infty}\int_{-c_1\alpha}^{0}\rho c_1 c_2 f_0 dc_2 dc_1 dc_3 \\
&= \frac{\rho\beta}{\pi}\Big[-\frac{\alpha^2}{4\beta^2(1+\alpha^2)}e^{-\beta({u_1}^2+{u_2}^2)} \\
&\quad -\frac{u_1\sqrt{\pi}}{4\beta\sqrt{\beta}}e^{-\beta {u_2}^2}erfc(-\sqrt{\beta}u_1)-\frac{u_1u_2\pi}{4\beta}erf(\sqrt{\beta}u_2)erfc(-\sqrt{\beta}u_1) \\
&\quad +\frac{\sqrt{\pi}}{4\beta\sqrt{\beta}(1+\alpha^2)^{3/2}}(u_1+\alpha^3u_2)e^{\frac{-\mu^2}{1+\alpha^2}}erfc[\frac{-\sqrt{\beta}(u_1-\alpha u_2)}{\sqrt{1+\alpha^2}}] \\
&\quad +\frac{u_1u_2\sqrt{\pi}}{2\beta}\Omega_1\Big],
\end{aligned} \tag{A.22}$$

$$\begin{aligned}
I_D^9(\psi_2) &= \int_{-\infty}^{\infty}\int_{0}^{\infty}\int_{0}^{\infty}\rho {c_1}^2 f_0 dc_2 dc_1 dc_3 \\
&= \frac{\rho\sqrt{\beta}}{2\sqrt{\pi}}\Big[\frac{u_1}{2\beta}e^{-\beta {u_1}^2}erfc(-\sqrt{\beta}u_2) \\
&\quad +\frac{\sqrt{\pi}}{4\beta\sqrt{\beta}}(1+2\beta {u_1}^2)erfc(-\sqrt{\beta}u_1)erfc(-\sqrt{\beta}u_2)\Big],
\end{aligned} \tag{A.23}$$

$$\begin{aligned}
I_D^{10}(\psi_2) &= \int_{-\infty}^{\infty}\int_{0}^{\infty}\int_{0}^{\infty}\rho c_1 c_2 f_0 dc_2 dc_1 dc_3 \\
&= \frac{\rho\beta}{\pi}\Big[\frac{1}{4\beta^2}e^{-\beta({u_1}^2+{u_2}^2)}+\frac{u_2\sqrt{\pi}}{4\beta\sqrt{\beta}}e^{-\beta {u_1}^2}erfc(-\sqrt{\beta}u_2) \\
&\quad +\frac{u_1\sqrt{\pi}}{4\beta\sqrt{\beta}}e^{-\beta {u_2}^2}erfc(-\sqrt{\beta}u_1)+\frac{u_1u_2\pi}{4\beta}erfc(-\sqrt{\beta}u_1)erfc(-\sqrt{\beta}u_2)\Big],
\end{aligned} \tag{A.24}$$

$$\begin{aligned}
I_D^{11}(\psi_2) &= \int_{-\infty}^{\infty}\int_{-\infty}^{0}\int_{-c_1\alpha}^{\infty}\rho {c_1}^2 f_0 dc_2 dc_1 dc_3 \\
&= \frac{\rho\sqrt{\beta}}{2\sqrt{\pi}}\Big[-\frac{\alpha}{2\beta\sqrt{\beta}\sqrt{\pi}(1+\alpha^2)}e^{-\beta({u_1}^2+{u_2}^2)} \\
&\quad -\frac{u_1}{2\beta}e^{-\beta {u_1}^2}erfc(-\sqrt{\beta}u_2)+\frac{\sqrt{\pi}}{4\beta\sqrt{\beta}}(1+2\beta {u_1}^2)erfc(\sqrt{\beta}u_1) \\
&\quad +\frac{\alpha}{\beta(1+\alpha^2)^{3/2}}(u_1-\alpha u_2)e^{\frac{-\mu^2}{1+\alpha^2}}erfc[\frac{\sqrt{\beta}(u_1-\alpha u_2)}{\sqrt{1+\alpha^2}}] \\
&\quad +\frac{1}{2\beta\sqrt{\beta}}(1+2\beta {u_1}^2)\Omega_2\Big],
\end{aligned} \tag{A.25}$$

$$
\begin{aligned}
I_D^{12}(\psi_2) &= \int_{-\infty}^{\infty}\int_{-\infty}^{0}\int_{-c_1\alpha}^{\infty} \rho c_1 c_2 f_0 dc_2 dc_1 dc_3 \\
&= \frac{\rho\beta}{\pi}\Big[-\frac{1}{4\beta^2(1+\alpha^2)}e^{-\beta({u_1}^2+{u_2}^2)} \\
&\quad - \frac{u_2\sqrt{\pi}}{4\beta\sqrt{\beta}}e^{-\beta{u_1}^2}erfc(-\sqrt{\beta}u_2) + \frac{u_1u_2\pi}{4\beta}erfc(\sqrt{\beta}u_1) \\
&\quad + \frac{\sqrt{\pi}}{4\beta\sqrt{\beta}(1+\alpha^2)^{3/2}}(u_1+\alpha^3u_2)e^{\frac{-\mu^2}{1+\alpha^2}}erfc[\frac{\sqrt{\beta}(u_1-\alpha u_2)}{\sqrt{1+\alpha^2}}] \\
&\quad + \frac{u_1u_2\sqrt{\pi}}{2\beta}\Omega_2\Big]. \qquad (A.26)
\end{aligned}
$$

A.1.3 ψ_3 Moments

Likewise, the ψ_3 moments are determined when the third element of the moment function vector is considered, *i.e.*, $\psi_1 = mc_2$, the molecular momentum in the x_2-direction. Here, the odd numbered integrals can be directly related to the even numbered ones in the previous section. The 12 integrals are

$$
I_D^1(\psi_3) = \int_{-\infty}^{\infty}\int_{-\infty}^{0}\int_{-\infty}^{0} \rho c_1 c_2 f_0 dc_2 dc_1 dc_3 = I_D^2(\psi_2), \qquad (A.27)
$$

$$
\begin{aligned}
I_D^2(\psi_3) &= \int_{-\infty}^{\infty}\int_{-\infty}^{0}\int_{-\infty}^{0} \rho {c_2}^2 f_0 dc_2 dc_1 dc_3 \\
&= \frac{\rho\sqrt{\beta}}{2\sqrt{\pi}}\Big[-\frac{u_2}{2\beta}e^{-\beta{u_2}^2}erfc(\sqrt{\beta}u_1) \\
&\quad + \frac{\sqrt{\pi}}{4\beta\sqrt{\beta}}(1+2\beta{u_2}^2)erfc(\sqrt{\beta}u_2)erfc(\sqrt{\beta}u_1)\Big], \qquad (A.28)
\end{aligned}
$$

$$
I_D^3(\psi_3) = \int_{-\infty}^{\infty}\int_{-\infty}^{0}\int_{0}^{-c_1\alpha} \rho c_1 c_2 f_0 dc_2 dc_1 dc_3 = I_D^4(\psi_2), \qquad (A.29)
$$

$$
\begin{aligned}
I_D^4(\psi_3) &= \int_{-\infty}^{\infty}\int_{-\infty}^{0}\int_{0}^{-c_1\alpha} \rho {c_2}^2 f_0 dc_2 dc_1 dc_3 \\
&= \frac{\rho\beta}{\pi}\Big[-\frac{\alpha}{4\beta^2(1+\alpha^2)}e^{-\beta({u_1}^2+{u_2}^2)} + \frac{u_2\sqrt{\pi}}{4\beta\sqrt{\beta}}e^{-\beta{u_2}^2}erfc(\sqrt{\beta}u_1) \\
&\quad + \frac{\pi}{8\beta^2}(1+2\beta{u_2}^2)erf(\sqrt{\beta}u_2)erfc(\sqrt{\beta}u_1) \\
&\quad + \frac{\sqrt{\pi}}{4\beta\sqrt{\beta}(1+\alpha^2)^{3/2}}(\alpha u_1 - u_2 - 2\alpha^2u_2)e^{\frac{-\mu^2}{1+\alpha^2}}erfc[\frac{\sqrt{\beta}(u_1-\alpha u_2)}{\sqrt{1+\alpha^2}}]
\end{aligned}
$$

$$- \frac{\sqrt{\pi}}{4\beta^2}(1+2\beta {u_2}^2)\Omega_2\Big]\,, \tag{A.30}$$

$$I_D^5(\psi_3) = \int_{-\infty}^{\infty}\int_0^{\infty}\int_{-\infty}^{-c_1\alpha} \rho c_1 c_2 f_0 dc_2 dc_1 dc_3 = I_D^6(\psi_2)\,, \tag{A.31}$$

$$\begin{aligned} I_D^6(\psi_3) &= \int_{-\infty}^{\infty}\int_0^{\infty}\int_{-\infty}^{-c_1\alpha} \rho {c_2}^2 f_0 dc_2 dc_1 dc_3 \\ &= \frac{\rho\beta}{\pi}\Big[\frac{\alpha}{4\beta^2(1+\alpha^2)}e^{-\beta({u_1}^2+{u_2}^2)} + \frac{\pi}{8\beta^2}(1+2\beta {u_2}^2)erfc(-\sqrt{\beta}u_1) \\ &\quad + \frac{\sqrt{\pi}}{4\beta\sqrt{\beta}(1+\alpha^2)^{3/2}}(\alpha u_1 - u_2 - 2\alpha^2 u_2)e^{\frac{-\mu^2}{1+\alpha^2}}erfc[\frac{-\sqrt{\beta}(u_1-\alpha u_2)}{\sqrt{1+\alpha^2}}] \\ &\quad - \frac{\sqrt{\pi}}{4\beta^2}(1+2\beta {u_2}^2)\Omega_1\Big]\,, \end{aligned} \tag{A.32}$$

$$I_D^7(\psi_3) = \int_{-\infty}^{\infty}\int_0^{\infty}\int_{-c_1\alpha}^{0} \rho c_1 c_2 f_0 dc_2 dc_1 dc_3 = I_D^8(\psi_2)\,, \tag{A.33}$$

$$\begin{aligned} I_D^8(\psi_3) &= \int_{-\infty}^{\infty}\int_0^{\infty}\int_{-c_1\alpha}^{0} \rho {c_2}^2 f_0 dc_2 dc_1 dc_3 \\ &= \frac{\rho\beta}{\pi}\Big[-\frac{\alpha}{4\beta^2(1+\alpha^2)}e^{-\beta({u_1}^2+{u_2}^2)} - \frac{u_2\sqrt{\pi}}{4\beta\sqrt{\beta}}e^{-\beta {u_2}^2}erfc(-\sqrt{\beta}u_1) \\ &\quad - \frac{\pi}{8\beta^2}(1+2\beta {u_2}^2)erf(\sqrt{\beta}u_2)erfc(-\sqrt{\beta}u_1) \\ &\quad - \frac{\sqrt{\pi}}{4\beta\sqrt{\beta}(1+\alpha^2)^{3/2}}(\alpha u_1 - u_2 - 2\alpha^2 u_2)e^{\frac{-\mu^2}{1+\alpha^2}}erfc[\frac{-\sqrt{\beta}(u_1-\alpha u_2)}{\sqrt{1+\alpha^2}}] \\ &\quad + \frac{\sqrt{\pi}}{4\beta^2}(1+2\beta {u_2}^2)\Omega_1\Big]\,, \end{aligned} \tag{A.34}$$

$$I_D^9(\psi_3) = \int_{-\infty}^{\infty}\int_0^{\infty}\int_0^{\infty} \rho c_1 c_2 f_0 dc_2 dc_1 dc_3 = I_D^{10}(\psi_2)\,, \tag{A.35}$$

$$\begin{aligned} I_D^{10}(\psi_3) &= \int_{-\infty}^{\infty}\int_0^{\infty}\int_0^{\infty} \rho {c_2}^2 f_0 dc_2 dc_1 dc_3 \\ &= \frac{\rho\sqrt{\beta}}{2\sqrt{\pi}}\Big[\frac{u_2}{2\beta}e^{-\beta {u_2}^2}erfc(-\sqrt{\beta}u_1) \\ &\quad + \frac{\sqrt{\pi}}{4\beta\sqrt{\beta}}(1+2\beta {u_2}^2)erfc(-\sqrt{\beta}u_2)erfc(-\sqrt{\beta}u_1)\Big]\,, \end{aligned} \tag{A.36}$$

$$I_D^{11}(\psi_3) = \int_{-\infty}^{\infty}\int_{-\infty}^{0}\int_{-c_1\alpha}^{\infty} \rho c_1 c_2 f_0 dc_2 dc_1 dc_3 = I_D^{12}(\psi_2)\,, \tag{A.37}$$

$$\begin{aligned} I_D^{12}(\psi_3) &= \int_{-\infty}^{\infty}\int_{-\infty}^{0}\int_{-c_1\alpha}^{\infty} \rho {c_2}^2 f_0 dc_2 dc_1 dc_3 \\ &= \frac{\rho\beta}{\pi}\Big[\frac{\alpha}{4\beta^2(1+\alpha^2)} e^{-\beta({u_1}^2+{u_2}^2)} + \frac{\pi}{8\beta^2}(1+2\beta {u_2}^2) erfc(\sqrt{\beta}u_1) \\ &\quad - \frac{\sqrt{\pi}}{4\beta\sqrt{\beta}(1+\alpha^2)^{3/2}}(\alpha u_1 - u_2 - 2\alpha^2 u_2) e^{\frac{-\mu^2}{1+\alpha^2}} erfc[\frac{\sqrt{\beta}(u_1-\alpha u_2)}{\sqrt{1+\alpha^2}}] \\ &\quad + \frac{\sqrt{\pi}}{4\beta^2}(1+2\beta {u_2}^2)\Omega_2\Big]\,. \end{aligned} \tag{A.38}$$

A.1.4 ψ_4 Moments

The ψ_4 moments correspond to the integration with respect to the total molecular energy, the fourth element in the moment function vector. It is noted that ϵ' corresponds to internal energy per unit mass not including the thermal energy of translation as defined in Eq. (3.23b). Each of the ψ_4 integrals has contributions from the ψ_1 integrals in Sec. A.1.1. The 12 integrals are

$$\begin{aligned} I_D^1(\psi_4) &= \int_{-\infty}^{\infty}\int_{-\infty}^{0}\int_{-\infty}^{0} \rho(\frac{{c_1}^2}{2} + \frac{{c_2}^2}{2} + \frac{{c_3}^2}{2} + \epsilon') c_1 f_0 dc_2 dc_1 dc_3 \\ &= \frac{\rho\beta}{2\pi}(I_{1A} + I_{1B}) + (\frac{1}{4\beta} + e') I_D^1(\psi_1)\,, \end{aligned} \tag{A.39}$$

$$\begin{aligned} I_D^2(\psi_4) &= \int_{-\infty}^{\infty}\int_{-\infty}^{0}\int_{-\infty}^{0} \rho(\frac{{c_1}^2}{2} + \frac{{c_2}^2}{2} + \frac{{c_3}^2}{2} + \epsilon') c_2 f_0 dc_2 dc_1 dc_3 \\ &= \frac{\rho\beta}{2\pi}(I_{2A} + I_{2B}) + (\frac{1}{4\beta} + e') I_D^2(\psi_1)\,, \end{aligned} \tag{A.40}$$

$$\begin{aligned} I_D^3(\psi_4) &= \int_{-\infty}^{\infty}\int_{-\infty}^{0}\int_{0}^{-c_1\alpha} \rho(\frac{{c_1}^2}{2} + \frac{{c_2}^2}{2} + \frac{{c_3}^2}{2} + \epsilon') c_1 f_0 dc_2 dc_1 dc_3 \\ &= \frac{\rho\beta}{2\pi}(I_{3A} + I_{3B}) + (\frac{1}{4\beta} + e') I_D^3(\psi_1)\,, \end{aligned} \tag{A.41}$$

$$I_D^4(\psi_4) = \int_{-\infty}^{\infty}\int_{-\infty}^{0}\int_{0}^{-c_1\alpha} \rho(\frac{{c_1}^2}{2} + \frac{{c_2}^2}{2} + \frac{{c_3}^2}{2} + \epsilon')c_2 f_0 dc_2 dc_1 dc_3$$
$$= \frac{\rho\beta}{2\pi}(I_{4A} + I_{4B}) + (\frac{1}{4\beta} + e')I_D^4(\psi_1)\,, \qquad (A.42)$$

$$I_D^5(\psi_4) = \int_{-\infty}^{\infty}\int_{0}^{\infty}\int_{-\infty}^{-c_1\alpha} \rho(\frac{{c_1}^2}{2} + \frac{{c_2}^2}{2} + \frac{{c_3}^2}{2} + \epsilon')c_1 f_0 dc_2 dc_1 dc_3$$
$$= \frac{\rho\beta}{2\pi}(I_{5A} + I_{5B}) + (\frac{1}{4\beta} + e')I_D^5(\psi_1)\,, \qquad (A.43)$$

$$I_D^6(\psi_4) = \int_{-\infty}^{\infty}\int_{0}^{\infty}\int_{-\infty}^{-c_1\alpha} \rho(\frac{{c_1}^2}{2} + \frac{{c_2}^2}{2} + \frac{{c_3}^2}{2} + \epsilon')c_2 f_0 dc_2 dc_1 dc_3$$
$$= \frac{\rho\beta}{2\pi}(I_{6A} + I_{6B}) + (\frac{1}{4\beta} + e')I_D^6(\psi_1)\,, \qquad (A.44)$$

$$I_D^7(\psi_4) = \int_{-\infty}^{\infty}\int_{0}^{\infty}\int_{-c_1\alpha}^{0} \rho(\frac{{c_1}^2}{2} + \frac{{c_2}^2}{2} + \frac{{c_3}^2}{2} + \epsilon')c_1 f_0 dc_2 dc_1 dc_3$$
$$= \frac{\rho\beta}{2\pi}(I_{7A} + I_{7B}) + (\frac{1}{4\beta} + e')I_D^7(\psi_1)\,, \qquad (A.45)$$

$$I_D^8(\psi_4) = \int_{-\infty}^{\infty}\int_{0}^{\infty}\int_{-c_1\alpha}^{0} \rho(\frac{{c_1}^2}{2} + \frac{{c_2}^2}{2} + \frac{{c_3}^2}{2} + \epsilon')c_2 f_0 dc_2 dc_1 dc_3$$
$$= \frac{\rho\beta}{2\pi}(I_{8A} + I_{8B}) + (\frac{1}{4\beta} + e')I_D^8(\psi_1)\,, \qquad (A.46)$$

$$I_D^9(\psi_4) = \int_{-\infty}^{\infty}\int_{0}^{\infty}\int_{0}^{\infty} \rho(\frac{{c_1}^2}{2} + \frac{{c_2}^2}{2} + \frac{{c_3}^2}{2} + \epsilon')c_1 f_0 dc_2 dc_1 dc_3$$
$$= \frac{\rho\beta}{2\pi}(I_{9A} + I_{9B}) + (\frac{1}{4\beta} + e')I_D^9(\psi_1)\,, \qquad (A.47)$$

$$I_D^{10}(\psi_4) = \int_{-\infty}^{\infty}\int_{0}^{\infty}\int_{0}^{\infty} \rho(\frac{{c_1}^2}{2} + \frac{{c_2}^2}{2} + \frac{{c_3}^2}{2} + \epsilon')c_2 f_0 dc_2 dc_1 dc_3$$
$$= \frac{\rho\beta}{2\pi}(I_{10A} + I_{10B}) + (\frac{1}{4\beta} + e')I_D^{10}(\psi_1)\,, \qquad (A.48)$$

$$I_D^{11}(\psi_4) = \int_{-\infty}^{\infty}\int_{-\infty}^{0}\int_{-c_1\alpha}^{\infty} \rho(\frac{{c_1}^2}{2} + \frac{{c_2}^2}{2} + \frac{{c_3}^2}{2} + \epsilon')c_1 f_0 dc_2 dc_1 dc_3$$

$$= \frac{\rho\beta}{2\pi}(I_{11A} + I_{11B}) + (\frac{1}{4\beta} + e')I_D^{11}(\psi_1)\,, \tag{A.49}$$

$$I_D^{12}(\psi_4) = \int_{-\infty}^{\infty}\int_{-\infty}^{0}\int_{-c_1\alpha}^{\infty}\rho(\frac{{c_1}^2}{2} + \frac{{c_2}^2}{2} + \frac{{c_3}^2}{2} + \epsilon')c_2 f_0 dc_2 dc_1 dc_3$$
$$= \frac{\rho\beta}{2\pi}(I_{12A} + I_{12B}) + (\frac{1}{4\beta} + e')I_D^{12}(\psi_1)\,, \tag{A.50}$$

where

$$I_{1A} = -\frac{\sqrt{\pi}}{4\beta^2\sqrt{\beta}}(1 + \beta{u_1}^2)e^{-\beta{u_1}^2}erfc(\sqrt{\beta}u_2)$$
$$+ \frac{\pi}{8\beta^2}(3u_1 + 2\beta{u_1}^3)erfc(\sqrt{\beta}u_1)erfc(\sqrt{\beta}u_2)\,, \tag{A.51a}$$

$$I_{1B} = \frac{u_2}{4\beta^2}e^{-\beta({u_1}^2+{u_2}^2)} - \frac{u_1u_2\sqrt{\pi}}{4\beta\sqrt{\beta}}e^{-\beta{u_2}^2}erfc(\sqrt{\beta}u_1)$$
$$- \frac{\sqrt{\pi}}{8\beta^2\sqrt{\beta}}(1 + 2\beta{u_2}^2)e^{-\beta{u_1}^2}erfc(\sqrt{\beta}u_2)$$
$$+ \frac{u_1\pi}{8\beta^2}(1 + 2\beta{u_2}^2)erfc(\sqrt{\beta}u_2)erfc(\sqrt{\beta}u_1)\,, \tag{A.51b}$$

$$I_{2A} = \frac{u_1}{4\beta^2}e^{-\beta({u_1}^2+{u_2}^2)} - \frac{u_1u_2\sqrt{\pi}}{4\beta\sqrt{\beta}}e^{-\beta{u_1}^2}erfc(\sqrt{\beta}u_2)$$
$$- \frac{\sqrt{\pi}}{8\beta^2\sqrt{\beta}}(1 + 2\beta{u_1}^2)e^{-\beta{u_2}^2}erfc(\sqrt{\beta}u_1)$$
$$+ \frac{u_2\pi}{8\beta^2}(1 + 2\beta{u_1}^2)erfc(\sqrt{\beta}u_1)erfc(\sqrt{\beta}u_2)\,, \tag{A.52a}$$

$$I_{2B} = -\frac{\sqrt{\pi}}{4\beta^2\sqrt{\beta}}(1 + \beta{u_2}^2)e^{-\beta{u_2}^2}erfc(\sqrt{\beta}u_1)$$
$$+ \frac{\pi}{8\beta^2}(3u_2 + 2\beta{u_2}^3)erfc(\sqrt{\beta}u_2)erfc(\sqrt{\beta}u_1)\,, \tag{A.52b}$$

$$I_{3A} = \frac{\sqrt{\pi}}{2\sqrt{\beta}}\Big[\frac{\alpha}{2\beta\sqrt{\beta}\sqrt{\pi}(1+\alpha^2)^2}e^{-\beta({u_1}^2+{u_2}^2)}(2u_1 + \alpha^2u_1 - \alpha u_2)$$
$$+ \frac{\sqrt{\pi}}{4\beta\sqrt{\beta}}(3u_1 + 2\beta{u_1}^3)erfc(\sqrt{\beta}u_1)erf(\sqrt{\beta}u_2)$$

$$
\begin{aligned}
&- \frac{\alpha}{4\beta^2(1+\alpha^2)^{5/2}} e^{\frac{-\mu^2}{1+\alpha^2}} erfc[\frac{\sqrt{\beta}(u_1-\alpha u_2)}{\sqrt{1+\alpha^2}}](3+5\alpha^2+2\alpha^4+6\beta {u_1}^2 \\
&+ 6\alpha^2\beta {u_1}^2 + 2\alpha^4\beta {u_1}^2 - 6\alpha\beta u_1 u_2 - 2\alpha^3\beta u_1 u_2 + 2\alpha^2\beta {u_2}^2) \\
&- \frac{1}{2\beta\sqrt{\beta}}(3u_1+2\beta {u_1}^3)\Omega_2\Big] , \qquad (A.53a)
\end{aligned}
$$

$$
\begin{aligned}
I_{3B} = &- \frac{\alpha}{4\beta^2(1+\alpha^2)^2} e^{-\beta({u_1}^2+{u_2}^2)}(u_1+\alpha^3 u_2) + \frac{u_1 u_2\sqrt{\pi}}{4\beta\sqrt{\beta}} e^{-\beta {u_2}^2} erfc(\sqrt{\beta}u_1) \\
&+ \frac{u_1\pi}{8\beta^2}(1+2\beta {u_2}^2) erf(\sqrt{\beta}u_2) erfc(\sqrt{\beta}u_1) \\
&- \frac{\sqrt{\pi}}{8\beta^{5/2}(1+\alpha^2)^{5/2}} e^{\frac{-\mu^2}{1+\alpha^2}} erfc[\frac{\sqrt{\beta}(u_1-\alpha u_2)}{\sqrt{1+\alpha^2}}](\alpha^3+\alpha^5-2\alpha\beta {u_1}^2 \\
&+ 2\beta u_1 u_2 + 6\alpha^2\beta u_1 u_2 + 2\alpha^5\beta {u_2}^2) \\
&- \frac{\sqrt{\pi}u_1}{4\beta^2}(1+2\beta {u_2}^2)\Omega_2 , \qquad (A.53b)
\end{aligned}
$$

$$
\begin{aligned}
I_{4A} = &- \frac{\alpha^2}{4\beta^2(1+\alpha^2)^2} e^{-\beta({u_1}^2+{u_2}^2)}(2u_1+\alpha^2 u_1 - \alpha u_2) \\
&+ \frac{\sqrt{\pi}}{8\beta^2\sqrt{\beta}}(1+2\beta {u_1}^2) e^{-\beta {u_2}^2} erfc(\sqrt{\beta}u_1) \\
&+ \frac{u_2\pi}{8\beta^2}(1+2\beta {u_1}^2) erf(\sqrt{\beta}u_2) erfc(\sqrt{\beta}u_1) \\
&- \frac{\sqrt{\pi}}{8\beta^{5/2}(1+\alpha^2)^{5/2}} e^{\frac{-\mu^2}{1+\alpha^2}} erfc[\frac{\sqrt{\beta}(u_1-\alpha u_2)}{\sqrt{1+\alpha^2}}](1+\alpha^2+2\beta {u_1}^2 \\
&+ 4\alpha^3\beta u_1 u_2 - 2\alpha^2\beta {u_2}^2 - 4\alpha^4\beta {u_2}^2) - \frac{u_2\sqrt{\pi}}{4\beta^2}(1+2\beta {u_1}^2)\Omega_2 , \qquad (A.54a)
\end{aligned}
$$

$$
\begin{aligned}
I_{4B} = &\frac{\alpha}{4\beta^2(1+\alpha^2)^2} e^{-\beta({u_1}^2+{u_2}^2)}(\alpha u_1 - u_2 - 2\alpha^2 u_2) \\
&+ \frac{\sqrt{\pi}}{4\beta^2\sqrt{\beta}}(1+\beta {u_2}^2) e^{-\beta {u_2}^2} erfc(\sqrt{\beta}u_1) \\
&+ \frac{\pi}{8\beta^2}(3u_2+2\beta {u_2}^3) erf(\sqrt{\beta}u_2) erfc(\sqrt{\beta}u_1) \\
&- \frac{\sqrt{\pi}}{8\beta^{5/2}(1+\alpha^2)^{5/2}} e^{\frac{-\mu^2}{1+\alpha^2}} erfc[\frac{\sqrt{\beta}(u_1-\alpha u_2)}{\sqrt{1+\alpha^2}}](2+5\alpha^2+3\alpha^4+2\alpha^2\beta {u_1}^2 \\
&- 2\alpha\beta u_1 u_2 - 6\alpha^3\beta u_1 u_2 + 2\beta {u_2}^2 + 6\alpha^2\beta {u_2}^2 + 6\alpha^4\beta {u_2}^2) \\
&- \frac{\sqrt{\pi}}{4\beta^2}(3u_2+2\beta {u_2}^3)\Omega_2 , \qquad (A.54b)
\end{aligned}
$$

$$I_{5A} = \frac{\sqrt{\pi}}{2\sqrt{\beta}}\Big[-\frac{\alpha}{2\beta\sqrt{\beta}\sqrt{\pi}(1+\alpha^2)^2}e^{-\beta({u_1}^2+{u_2}^2)}(2u_1+\alpha^2u_1-\alpha u_2)$$
$$+\frac{1}{2\beta^2}(1+\beta{u_1}^2)e^{-\beta{u_1}^2}erfc(\sqrt{\beta}u_2)+\frac{\sqrt{\pi}}{4\beta\sqrt{\beta}}(3u_1+2\beta{u_1}^3)erfc(-\sqrt{\beta}u_1)$$
$$-\frac{\alpha}{4\beta^2(1+\alpha^2)^{5/2}}e^{\frac{-\mu^2}{1+\alpha^2}}erfc[\frac{-\sqrt{\beta}(u_1-\alpha u_2)}{\sqrt{1+\alpha^2}}](3+5\alpha^2+2\alpha^4+6\beta{u_1}^2$$
$$+6\alpha^2\beta{u_1}^2+2\alpha^4\beta{u_1}^2-6\alpha\beta u_1u_2-2\alpha^3\beta u_1u_2+2\alpha^2\beta{u_2}^2)$$
$$-\frac{1}{2\beta\sqrt{\beta}}(3u_1+2\beta{u_1}^3)\Omega_1\Big]\,, \qquad (A.55a)$$

$$I_{5B} = \frac{1}{4\beta^2(1+\alpha^2)^2}e^{-\beta({u_1}^2+{u_2}^2)}(\alpha u_1-u_2-2\alpha^2u_2)$$
$$+\frac{\sqrt{\pi}}{8\beta^2\sqrt{\beta}}(1+2\beta{u_2}^2)e^{-\beta{u_1}^2}erfc(\sqrt{\beta}u_2)+\frac{u_1\pi}{8\beta^2}(1+2\beta{u_2}^2)erfc(-\sqrt{\beta}u_1)$$
$$-\frac{\sqrt{\pi}}{8\beta^{5/2}(1+\alpha^2)^{5/2}}e^{\frac{-\mu^2}{1+\alpha^2}}erfc[\frac{-\sqrt{\beta}(u_1-\alpha u_2)}{\sqrt{1+\alpha^2}}](\alpha^3+\alpha^5-2\alpha\beta{u_1}^2$$
$$+2\beta u_1u_2+6\alpha^2\beta u_1u_2+2\alpha^5\beta{u_2}^2)-\frac{\sqrt{\pi}u_1}{4\beta^2}(1+2\beta{u_2}^2)\Omega_1\,, \qquad (A.55b)$$

$$I_{6A} = -\frac{1}{4\beta^2(1+\alpha^2)^2}e^{-\beta({u_1}^2+{u_2}^2)}(u_1+\alpha^3u_2)$$
$$+\frac{u_1u_2\sqrt{\pi}}{4\beta\sqrt{\beta}}e^{-\beta{u_1}^2}erfc(\sqrt{\beta}u_2)+\frac{u_2\pi}{8\beta^2}(1+2\beta{u_1}^2)erfc(-\sqrt{\beta}u_1)$$
$$-\frac{\sqrt{\pi}}{8\beta^{5/2}(1+\alpha^2)^{5/2}}e^{\frac{-\mu^2}{1+\alpha^2}}erfc[\frac{-\sqrt{\beta}(u_1-\alpha u_2)}{\sqrt{1+\alpha^2}}](1+\alpha^2+2\beta{u_1}^2$$
$$+4\alpha^3\beta u_1u_2-2\alpha^2\beta{u_2}^2-4\alpha^4\beta{u_2}^2)-\frac{u_2\sqrt{\pi}}{4\beta^2}(1+2\beta{u_1}^2)\Omega_1\,, \qquad (A.56a)$$

$$I_{6B} = -\frac{\alpha}{4\beta^2(1+\alpha^2)^2}e^{-\beta({u_1}^2+{u_2}^2)}(\alpha u_1-u_2-2\alpha^2u_2)$$
$$+\frac{\pi}{8\beta^2}(3u_2+2\beta{u_2}^3)erfc(-\sqrt{\beta}u_1)$$
$$-\frac{\sqrt{\pi}}{8\beta^{5/2}(1+\alpha^2)^{5/2}}e^{\frac{-\mu^2}{1+\alpha^2}}erfc[\frac{-\sqrt{\beta}(u_1-\alpha u_2)}{\sqrt{1+\alpha^2}}](2+5\alpha^2+3\alpha^4$$
$$+2\alpha^2\beta{u_1}^2-2\alpha\beta u_1u_2-6\alpha^3\beta u_1u_2+2\beta{u_2}^2+6\alpha^2\beta{u_2}^2+6\alpha^4\beta{u_2}^2)$$
$$-\frac{\sqrt{\pi}}{4\beta^2}(3u_2+2\beta{u_2}^3)\Omega_1\,, \qquad (A.56b)$$

$$I_{7A} = \frac{\sqrt{\pi}}{2\sqrt{\beta}}\Big[\frac{\alpha}{2\beta\sqrt{\beta}\sqrt{\pi}(1+\alpha^2)^2}e^{-\beta({u_1}^2+{u_2}^2)}(2u_1+\alpha^2u_1-\alpha u_2)$$
$$-\frac{\sqrt{\pi}}{4\beta\sqrt{\beta}}(3u_1+2\beta{u_1}^3)erfc(-\sqrt{\beta}u_1)erf(\sqrt{\beta}u_2)$$
$$+\frac{\alpha}{4\beta^2(1+\alpha^2)^{5/2}}e^{\frac{-\mu^2}{1+\alpha^2}}erfc[\frac{-\sqrt{\beta}(u_1-\alpha u_2)}{\sqrt{1+\alpha^2}}](3+5\alpha^2+2\alpha^4+6\beta{u_1}^2$$
$$+6\alpha^2\beta{u_1}^2+2\alpha^4\beta{u_1}^2-6\alpha\beta u_1u_2-2\alpha^3\beta u_1u_2+2\alpha^2\beta{u_2}^2)$$
$$+\frac{1}{2\beta\sqrt{\beta}}(3u_1+2\beta{u_1}^3)\Omega_1\Big]\,, \qquad (A.57a)$$

$$I_{7B} = -\frac{\alpha}{4\beta^2(1+\alpha^2)^2}e^{-\beta({u_1}^2+{u_2}^2)}(u_1+\alpha^3u_2)-\frac{u_1u_2\sqrt{\pi}}{4\beta\sqrt{\beta}}e^{-\beta{u_2}^2}erfc(-\sqrt{\beta}u_1)$$
$$-\frac{u_1\pi}{8\beta^2}(1+2\beta{u_2}^2)erf(\sqrt{\beta}u_2)erfc(-\sqrt{\beta}u_1)$$
$$+\frac{\sqrt{\pi}}{8\beta^{5/2}(1+\alpha^2)^{5/2}}e^{\frac{-\mu^2}{1+\alpha^2}}erfc[\frac{-\sqrt{\beta}(u_1-\alpha u_2)}{\sqrt{1+\alpha^2}}](\alpha^3+\alpha^5-2\alpha\beta{u_1}^2$$
$$+2\beta u_1u_2+6\alpha^2\beta u_1u_2+2\alpha^5\beta{u_2}^2)$$
$$+\frac{\sqrt{\pi}u_1}{4\beta^2}(1+2\beta{u_2}^2)\Omega_1\,, \qquad (A.57b)$$

$$I_{8A} = -\frac{\alpha^2}{4\beta^2(1+\alpha^2)^2}e^{-\beta({u_1}^2+{u_2}^2)}(2u_1+\alpha^2u_1-\alpha u_2)$$
$$-\frac{\sqrt{\pi}}{8\beta^2\sqrt{\beta}}(1+2\beta{u_1}^2)e^{-\beta{u_2}^2}erfc(-\sqrt{\beta}u_1)$$
$$-\frac{u_2\pi}{8\beta^2}(1+2\beta{u_1}^2)erf(\sqrt{\beta}u_2)erfc(-\sqrt{\beta}u_1)$$
$$+\frac{\sqrt{\pi}}{8\beta^{5/2}(1+\alpha^2)^{5/2}}e^{\frac{-\mu^2}{1+\alpha^2}}erfc[\frac{-\sqrt{\beta}(u_1-\alpha u_2)}{\sqrt{1+\alpha^2}}](1+\alpha^2+2\beta{u_1}^2$$
$$+4\alpha^3\beta u_1u_2-2\alpha^2\beta{u_2}^2-4\alpha^4\beta{u_2}^2)+\frac{u_2\sqrt{\pi}}{4\beta^2}(1+2\beta{u_1}^2)\Omega_1\,, \qquad (A.58a)$$

$$I_{8B} = \frac{\alpha}{4\beta^2(1+\alpha^2)^2}e^{-\beta({u_1}^2+{u_2}^2)}(\alpha u_1-u_2-2\alpha^2u_2)$$
$$-\frac{\sqrt{\pi}}{4\beta^2\sqrt{\beta}}(1+\beta{u_2}^2)e^{-\beta{u_2}^2}erfc(-\sqrt{\beta}u_1)$$
$$-\frac{\pi}{8\beta^2}(3u_2+2\beta{u_2}^3)erf(\sqrt{\beta}u_2)erfc(-\sqrt{\beta}u_1)$$

$$+\frac{\sqrt{\pi}}{8\beta^{5/2}(1+\alpha^2)^{5/2}}e^{\frac{-\mu^2}{1+\alpha^2}}erfc[\frac{-\sqrt{\beta}(u_1-\alpha u_2)}{\sqrt{1+\alpha^2}}](2+5\alpha^2+3\alpha^4$$
$$+2\alpha^2\beta {u_1}^2-2\alpha\beta u_1u_2-6\alpha^3\beta u_1u_2+2\beta {u_2}^2+6\alpha^2\beta {u_2}^2+6\alpha^4\beta {u_2}^2)$$
$$+\frac{\sqrt{\pi}}{4\beta^2}(3u_2+2\beta {u_2}^3)\Omega_1\,, \qquad (A.58b)$$

$$I_{9A}=\frac{\sqrt{\pi}}{4\beta^2\sqrt{\beta}}(1+\beta {u_1}^2)e^{-\beta {u_1}^2}erfc(-\sqrt{\beta}u_2)$$
$$+\frac{\pi}{8\beta^2}(3u_1+2\beta {u_1}^3)erfc(-\sqrt{\beta}u_1)erfc(-\sqrt{\beta}u_2)\,, \qquad (A.59a)$$

$$I_{9B}=\frac{u_2}{4\beta^2}e^{-\beta({u_1}^2+{u_2}^2)}+\frac{u_1u_2\sqrt{\pi}}{4\beta\sqrt{\beta}}e^{-\beta {u_2}^2}erfc(-\sqrt{\beta}u_1)$$
$$+\frac{\sqrt{\pi}}{8\beta^2\sqrt{\beta}}(1+2\beta {u_2}^2)e^{-\beta {u_1}^2}erfc(-\sqrt{\beta}u_2)$$
$$+\frac{u_1\pi}{8\beta^2}(1+2\beta {u_2}^2)erfc(-\sqrt{\beta}u_2)erfc(-\sqrt{\beta}u_1)\,, \qquad (A.59b)$$

$$I_{10A}=\frac{u_1}{4\beta^2}e^{-\beta({u_1}^2+{u_2}^2)}+\frac{u_1u_2\sqrt{\pi}}{4\beta\sqrt{\beta}}e^{-\beta {u_1}^2}erfc(-\sqrt{\beta}u_2)$$
$$+\frac{\sqrt{\pi}}{8\beta^2\sqrt{\beta}}(1+2\beta {u_1}^2)e^{-\beta {u_2}^2}erfc(-\sqrt{\beta}u_1)$$
$$+\frac{u_2\pi}{8\beta^2}(1+2\beta {u_1}^2)erfc(-\sqrt{\beta}u_1)erfc(-\sqrt{\beta}u_2)\,, \qquad (A.60a)$$

$$I_{10B}=\frac{\sqrt{\pi}}{4\beta^2\sqrt{\beta}}(1+\beta {u_2}^2)e^{-\beta {u_2}^2}erfc(-\sqrt{\beta}u_1)$$
$$+\frac{\pi}{8\beta^2}(3u_2+2\beta {u_2}^3)erfc(-\sqrt{\beta}u_2)erfc(-\sqrt{\beta}u_1)\,, \qquad (A.60b)$$

$$I_{11A}=\frac{\sqrt{\pi}}{2\sqrt{\beta}}\Big[-\frac{\alpha}{2\beta\sqrt{\beta}\sqrt{\pi}(1+\alpha^2)^2}e^{-\beta({u_1}^2+{u_2}^2)}(2u_1+\alpha^2u_1-\alpha u_2)$$
$$-\frac{1}{2\beta^2}(1+\beta {u_1}^2)e^{-\beta {u_1}^2}erfc(-\sqrt{\beta}u_2)+\frac{\sqrt{\pi}}{4\beta\sqrt{\beta}}(3u_1+2\beta {u_1}^3)erfc(\sqrt{\beta}u_1)$$
$$+\frac{\alpha}{4\beta^2(1+\alpha^2)^{5/2}}e^{\frac{-\mu^2}{1+\alpha^2}}erfc[\frac{\sqrt{\beta}(u_1-\alpha u_2)}{\sqrt{1+\alpha^2}}](3+5\alpha^2+2\alpha^4+6\beta {u_1}^2$$
$$+6\alpha^2\beta {u_1}^2+2\alpha^4\beta {u_1}^2-6\alpha\beta u_1u_2-2\alpha^3\beta u_1u_2+2\alpha^2\beta {u_2}^2)$$

$$+\frac{1}{2\beta\sqrt{\beta}}(3u_1+2\beta {u_1}^3)\Omega_2\Big]\,, \tag{A.61a}$$

$$\begin{aligned} I_{11B} = {} & \frac{1}{4\beta^2(1+\alpha^2)^2}e^{-\beta({u_1}^2+{u_2}^2)}(\alpha u_1-u_2-2\alpha^2 u_2) \\ & -\frac{\sqrt{\pi}}{8\beta^2\sqrt{\beta}}(1+2\beta {u_2}^2)e^{-\beta {u_1}^2}erfc(-\sqrt{\beta}u_2)+\frac{u_1\pi}{8\beta^2}(1+2\beta {u_2}^2)erfc(\sqrt{\beta}u_1) \\ & +\frac{\sqrt{\pi}}{8\beta^{5/2}(1+\alpha^2)^{5/2}}e^{\frac{-\mu^2}{1+\alpha^2}}erfc[\frac{\sqrt{\beta}(u_1-\alpha u_2)}{\sqrt{1+\alpha^2}}](\alpha^3+\alpha^5-2\alpha\beta {u_1}^2 \\ & +2\beta u_1u_2+6\alpha^2\beta u_1u_2+2\alpha^5\beta {u_2}^2)+\frac{\sqrt{\pi}u_1}{4\beta^2}(1+2\beta {u_2}^2)\Omega_2\,, \end{aligned} \tag{A.61b}$$

$$\begin{aligned} I_{12A} = {} & -\frac{1}{4\beta^2(1+\alpha^2)^2}e^{-\beta({u_1}^2+{u_2}^2)}(u_1+\alpha^3u_2) \\ & -\frac{u_1u_2\sqrt{\pi}}{4\beta\sqrt{\beta}}e^{-\beta {u_1}^2}erfc(-\sqrt{\beta}u_2)+\frac{u_2\pi}{8\beta^2}(1+2\beta {u_1}^2)erfc(\sqrt{\beta}u_1) \\ & +\frac{\sqrt{\pi}}{8\beta^{5/2}(1+\alpha^2)^{5/2}}e^{\frac{-\mu^2}{1+\alpha^2}}erfc[\frac{\sqrt{\beta}(u_1-\alpha u_2)}{\sqrt{1+\alpha^2}}](1+\alpha^2+2\beta {u_1}^2 \\ & +4\alpha^3\beta u_1u_2-2\alpha^2\beta {u_2}^2-4\alpha^4\beta {u_2}^2)+\frac{u_2\sqrt{\pi}}{4\beta^2}(1+2\beta {u_1}^2)\Omega_2\,, \end{aligned} \tag{A.62a}$$

$$\begin{aligned} I_{12B} = {} & -\frac{\alpha}{4\beta^2(1+\alpha^2)^2}e^{-\beta({u_1}^2+{u_2}^2)}(\alpha u_1-u_2-2\alpha^2u_2) \\ & +\frac{\pi}{8\beta^2}(3u_2+2\beta {u_2}^3)erfc(\sqrt{\beta}u_1) \\ & +\frac{\sqrt{\pi}}{8\beta^{5/2}(1+\alpha^2)^{5/2}}e^{\frac{-\mu^2}{1+\alpha^2}}erfc[\frac{\sqrt{\beta}(u_1-\alpha u_2)}{\sqrt{1+\alpha^2}}](2+5\alpha^2+3\alpha^4 \\ & +2\alpha^2\beta {u_1}^2-2\alpha\beta u_1u_2-6\alpha^3\beta u_1u_2+2\beta {u_2}^2+6\alpha^2\beta {u_2}^2+6\alpha^4\beta {u_2}^2) \\ & +\frac{\sqrt{\pi}}{4\beta^2}(3u_2+2\beta {u_2}^3)\Omega_2\,, \end{aligned} \tag{A.62b}$$

A.1.5 Approximate Integration Techniques

Approximate integration techniques are needed to evaluate the integral in Eq. (A.2a). In the present analysis, a Gauss-Laguerre quadrature has been utilized.

Here, the the integral rewritten using the change of variables $\xi = z \mp a$ as

$$\Omega_{1,2} = \int_0^\infty e^{-\xi} F(\xi) d\xi \,, \tag{A.63a}$$

where

$$F(\xi) = e^{\xi} e^{-(\xi \pm a)^2} erf[(\pm\xi + a)\alpha + \mu] \,. \tag{A.63b}$$

The integral $\Omega_{1,2}$ may now be approximated as

$$\Omega_{1,2} \approx \sum_{i=0}^{n} \omega_i F(\xi_i) \,, \tag{A.63c}$$

where ω_i are the Gauss-Laguerre coefficients and ξ_i are the quadrature points. Calculations were performed using a 14 point quadrature.

A.2 Moments for MKFS-NDU Scheme

The moments necessary for the MKFS-NDU scheme (see Sec. 7.3.3) can be written in terms of the moments for the NDD-scheme through a change in variables. The relationships are given using a compact notation as follows. For the (l, m) pairs $(1,1)$, $(3,5)$, $(5,7)$, $(7,9)$, $(9,11)$, $(11,3)$,

$$I_U^l(\psi_1)[u_1, u_2] = I_D^m(\psi_1)[\bar{u}_1, \bar{u}_2] \,, \tag{A.64a}$$

$$I_U^l(\psi_2)[u_1, u_2] = I_D^m(\psi_2)[\bar{u}_1, \bar{u}_2] \,, \tag{A.64b}$$

$$I_U^l(\psi_3)[u_1, u_2] = -I_D^m(\psi_3)[\bar{u}_1, \bar{u}_2] \,, \tag{A.64c}$$

$$I_U^l(\psi_4)[u_1, u_2] = I_D^m(\psi_4)[\bar{u}_1, \bar{u}_2] \,, \tag{A.64d}$$

and for the (l, m) pairs $(2,2)$, $(4,6)$, $(6,8)$, $(8,10)$, $(10,12)$, $(12,4)$,

$$I_U^l(\psi_1)[u_1, u_2] = -I_D^m(\psi_1)[\bar{u}_1, \bar{u}_2] \,, \tag{A.65a}$$

$$I_U^l(\psi_2)[u_1, u_2] = -I_D^m(\psi_2)[\bar{u}_1, \bar{u}_2] \,, \tag{A.65b}$$

$$I_U^l(\psi_3)[u_1, u_2] = I_D^m(\psi_3)[\bar{u}_1, \bar{u}_2] \,, \tag{A.65c}$$

$$I_U^l(\psi_4)[u_1, u_2] = -I_D^m(\psi_4)[\bar{u}_1, \bar{u}_2] \,, \tag{A.65d}$$

where $\bar{u}_1 = u_1$ and $\bar{u}_2 = -u_2$.

Vitae

The author was born on March 13, 1963 in Harrisonburg Virginia. He received a Bachelor of Science degree in Aerospace Engineering at VPI&SU in June, 1985. The author remained at VPI&SU and earned a Masters of Science degree in Aerospace Engineering in July, 1987. For the next two years the author was employed by Analytical Services and Materials in Hampton Virginia where he was a contractor in the Computational Methods Branch at NASA Langley Research Center. In July 1989 he returned to VPI&SU in pursuit of a Ph.D. in Aerospace Engineering.